5-2017

Morphology Controlled Synthesis of Copper Based Multimetallic Nanostructures and Their Electrocatalytic Properties for Methanol Oxidation Reaction

Leanne Elizabeth Mathurin
University of Arkansas, Fayetteville

Morphology Controlled Synthesis of Copper Based Multimetallic Nanostructures and Their Electrocatalytic Properties for Methanol Oxidation Reaction

A dissertation submitted in partial fulfillment
of the requirements for the degree of
Doctor of Philosophy in Chemistry

by

Leanne Mathurin
Hendrix College
Bachelor of Arts in Chemistry, 2010

May 2017
University of Arkansas

This dissertation is approved for recommendation to the Graduate Council.

_____
Dr. Jingyi Chen
Dissertation Director

_____
Dr. Bill Durham
Committee Member

_____
Dr. James F. Hinton
Committee Member

_____
Dr. Colin Heyes
Committee Member

_____
Dr. Ryan Tian
Committee Member

Abstract:

This research focuses on the development of shape-controlled synthesis of Cu NM, Cu-based bimetallic and trimetallic nanostructures, and their electrocatalytic properties for methanol oxidation reaction (MOR). Copper nanomaterials (Cu NM) with specific surface facets can tailor their catalytic activity. Understanding reagents responsible for Cu NM growth is important for morphology-controlled synthesis of the nanostructures. This research studies the halide influence on Cu NM growth and morphology in an oil-based synthesis. The morphology of the Cu NM varies with the halide type (i.e., Cl^-, Br^-, I^-), and the halide concentration. Additionally, the type of Cu precursor also influenced the morphology of the resultant Cu NM.

Select Cu nanostructures were utilized as templates for the formation of bimetallic and trimetallic nanostructures in order to study the composition and morphology influence on the electrocatalytic properties. Binary and ternary core-frame and frame nanostructures, composed of Cu, Pt, and Ru, were developed and their electrocatalytic activity was investigated. Multimetallic, branched core-frame nanostructures were formed by co-reducing Pt and Ru onto the vertices and edges of Cu rhombic dodecahedra. The multimetallic frame nanostructures were formed by etching the coreframe nanostructures. Studies over electrocatalytic activity demonstrated the multimetallic coreframe nanostructures decreased MOR activity, while the multimetallic frame nanostructures enhanced MOR activity and stability, due to the alloying at the frame nanostructure's surface. Additionally, the incorporation of Ru into these novel frame nanostructures improved resistance towards CO poisoning.

This research also develops multimetallic nanotubes with synthetically tunable surface morphology and platinum content. CuPt nanotubes with smooth and rough surface morphology were developed through the in situ separation of the galvanic replacement reaction and the co-

reduction mechanisms, during the alloying process with Cu nanowires. Ru was incorporated into the multimetallic nanotubes forming Cu-Pt-Ru smooth and rough surface structure. The influence of nanotube surface morphology and composition on electrocatalytic activity was investigated, which determined the importance of surface roughness for enhanced MOR activity. Rough nanotubes with Ru increased MOR activity, decreased MOR overpotential, and improved resistance towards CO poisoning. This research provides insight into the effects of nanomaterial composition and structure on electrocatalysis of MOR.

Acknowledgements:

I would like to thank Dr. Chen for her guidance throughout my time in graduate school, without these experiences I would not have developed into the person I am. I would also like to thank her for allowing me to complete my three research projects, I greatly appreciate it. I would like to thank Dr. Durham for his advice and mentorship over the years, as well as his willingness to answer my random questions. A Special Thanks to my committee members for their help and guidance with my research projects over the years. Additionally, I would like to thank the inorganic faculty for their assistance in developing my presentation skills & style. I would like to thank David Parette, Dr. Benamara, and Erik Pollock for their instrumentation knowledge and assistance. Without whom, I would not have obtained any characterization results.

A special thanks to my lab mates who were always willing to discuss research issues, TA assignments, and ponder the causes of synthesis failures. The lab windows that reminded me of life outside of lab, and at the end of a long day rewarded me with an excellent view. I would also like to thank my friends for improving my quality of life with running, coffee, and lunch breaks; and reminded me that all of life's issues could be fixed with a cuppa and Doctor Who. Lastly, I would like to thank my family, without whose support and influence, I would not have endured graduate school nor endeavored to successfully achieve my goals.

Dedication:

This dissertation is dedicated to my Mom, Dad, and Matt who have always inspired me to achieve my goals. May this work join the others on the library shelf, hopefully not forgotten, just collecting dust.

Table of Contents:

Chapter I. Introduction……1

Introductory statement…….1

Background:…….3

Direct Methanol Fuel Cells……..……..3

DMFC Anode Limitations……...……..5

Ideal Compositions of Nanomaterial Electrocatalysts for MOR……...6

Structural Benefits of Nanomaterials as Electrocatalysts for MOR……..9

Nanomaterial Growth and Influencing Factors……10

Halide Influence on Noble Metal Nanomaterial Growth…….12

Copper Nanomaterial (Cu NM) Growth and Limitations……14

Halide Influence of Cu NM Facet Selectivity and Cu NM Growth……16

Mechanisms for Alloyed Multimetallic Nanomaterials……...17

Overview of this Research……..……...19

References……..……23

Chapter II. Morphology Control of Copper Nanomaterials & the Influence of Halides on Nanomaterial Growth……32

Abstract…….32

Introduction……33

Part I……...35

Part I: Experimental Methods..……35

Part I: Results and Discussion..…..……..41

Part II…….57

Part II: Experimental Methods……57

Part II: Results and Discussion……..59

Conclusions……67

Appendix A: Part I & II Supporting Information Part 1……68

Appendix B: Reduction Kinetics and ITC Studies……83

Appendix B: Abstract……..……83

Appendix B: Experimental Methods……...……84

Appendix B: Results and Discussion…...……..…….88

Appendix B: Conclusion……..93

References…….94

Chapter III. Synthesis of Branched Core-Frame and Frame Copper-Platinum-Ruthenium Rhombic Dodecahedra and their Electrocatalytic Properties for Methanol Oxidation…...98

Abstract…….....99

Introduction……..100

Experimental Methods.……....102

Results and Discussion……107

Conclusions…….132

Appendix A: Supporting Information, Experimental Methods.……..134

Appendix B: Supporting Information, Results and Discussion.……..137

Appendix C: Supplemental Information, Experimental Methods...……150

Appendix D: Supplemental Information, Results and Discussion..……152

Appendix E: Supplemental Information, Conclusions……159

References……160

Chapter IV. Tailoring the Surface Morphology and Composition of Copper-Platinum-Ruthenium multimetallic nanotubes, and their electrocatalytic properties for MOR……..…….164

Abstract……164

Introduction……..165

Experimental Methods…..……167

Results and Discussion……174

Conclusions……..220

Appendix A: Supporting Information, Experimental Methods…..……..220

Appendix B: Supporting Information, Results and Discussion……...……224

References:……...246

Chapter V. Conclusion and Future Direction…….249

Conclusion……..249

Future Directions…….255

List of Abbreviations:

AA	Atomic Absorption Spectroscopy
A.A.	Glacial Acetic Acid
Ar	Argon
BTA	Butylamine
CA	Chronoamperometry
Cu	Copper
Cu NM	Copper Nanomaterial
Cu NO	Copper Nanooctahedron
Cu NP	Copper Nanoparticle
Cu NPL	Copper Nanoplate
Cu hNPL	Hexagonal Copper Nanoplate
Cu NPH	Copper Nano-Polyhedron
Cu NW	Copper Nanowire
Cu RHD	Copper Nano-Rhombic Dodecahedron
$Cu(acac)_2$	Copper (II) Acetylacetonate
$Cu(ac)_2$	Copper (II) Acetate
$CuBr_2$	Copper (II) Bromide
CuBr	Copper (I) Bromide
$CuCl_2$	Copper (II) Chloride
CuCl	Copper (I) Chloride
CuI	Copper (I) Iodide
CO	Carbon Monoxide

CuPt Coreframe	Copper Platinum Coreframe
CuPt Frame	Copper Platinum Frame
CuPt rNT 10%	Copper Platinum Rough Nanotubes, 10% Platinum
CuPt rNT 20%	Copper Platinum Rough Nanotubes, 20% Platinum
CuPt sNT 10%	Copper Platinum Smooth Nanotubes, 10% Platinum
CuPtRu Coreframe	Copper Platinum Ruthenium Coreframe
CuPtRu Frame	Copper Platinum Ruthenium Frame
CuPtRu rNT 10%	Copper Platinum Ruthenium Rough Nanotubes, 10% Platinum
CuPtRu rNT 20%	Copper Platinum Ruthenium Rough Nanotubes, 20% Platinum
CuPtRu sNT 10%	Copper Platinum Ruthenium Rough Nanotubes, 10% Platinum
CTAB	Cetyltrimetylammounium Bromide
CTAC	Cetyltrimetylammounium Chloride
CV	Cyclic Voltammetry
DMFC	Direct Methanol Fuel Cell
DDA	Dodecylamine
EDX	Energy Dispersive X-ray Spectroscopy
EtOH	Ethanol
HAADF-STEM	High Annular Angular Dark Field – Scanning Transmission Electron Microscopy
HCl	Hydrochloric Acid
$HClO_4$	Perchloric Acid (0.1 M)
HRTEM	High resolution transmission electron microscopy

HNO_3	Nitric acid
ICP-MS	Inductively-coupled mass spectrometry
NM	Nanomaterial (generic)
MeOH	Methanol
MOR	Methanol Oxidation Reaction
Pt	Platinum
Ru	Ruthenium
SEM	Scanning electron microscopy
TBAB	Tetrabutylammonium Bromide
TBAC	Tetrabuylammounium Chloride
TBAI	Tetrabutylammounium Iodide
TEM	Transmission Electron Microscopy
UV-Vis	UV-Visible Spectroscopy
XPS	X-ray Photoelectron Spectroscopy
XRD	X-ray Diffraction

List of Tables and Figures:

Chapter I

Figure 1: Comparison of Energy Storage and Conversion Devices……3

Figure 2: Schematic of a Direct Methanol Fuel Cell……...4

Figure 3: Methanol oxidation pathways……..5

Figure 4: Schematic of the Bifunction Mechanism…….6

Figure 5: Volcano Plot Comparing ΔG Values for CO and OH oxidation…….8

Figure 6: Schematic of Copper Nanomaterial Growth……15

Figure 7: Schematic of NM Growth based on Protected Facets……15

Chapter II

Figure 1: Chloride influence on Cu NM morphology, by different sources…….....46

Figure 2: Schematic of Cu NM growth with chloride as a shape directing additive……47

Figure 3: Bromide influence on Cu NM morphology, by $CuBr_2$……..49

Figure 4: Schematic of Cu NM growth $CuBr_2$……..49

Figure 5: Bromide influence on Cu NM morphology, external bromide source……...51

Figure 6: Schematic of Cu NM growth with external bromide source……..51

Figure 7: Cu NM growth with altered ratios of $Cu(acac)_2$ and $CuBr_2$……..52

Figure 8: Iodide influence on Cu NM morphology……...53

Figure 9: Schematic of Cu NM growth with iodide……..54

Figure 10: Cu NM growth without haldies……55

Figure 11: Cu NM growth with copper (I) halides……57

Figure 12: Chloride influence on Cu NM growth with $Cu(ac)_2$……60

Figure 13: Chloride influence on Cu NM growth with $Cu(ac)_2$, external source……..62

Figure 14: Bromide influence on Cu NM growth with $Cu(ac)_2$……64

Figure 15: Bromide influence on Cu NM growth with $Cu(ac)_2$, external source…….65

Figure 16: Halide influence on Cu NM growth with $Cu(ac)_2$, TBAC and TBAB……...67

Figure S1: Detailed characterization of $Cu(acac)_2$ and $CuCl_2$ syntheses at 50 min……68

Figure S2: Detailed Characterization of Cu NW……..69

Figure S3: Detailed characterization of $Cu(acac)_2$ and $CuCl_2$ syntheses at 72 hours.....……..69

Figure S4: TEM characterization of all $Cu(acac)_2$ and $CuCl_2$.....70

Figure S5: Detailed characterization of $Cu(acac)_2$ and CTAC…….70

Figure S6: Detailed characterization of $Cu(acac)_2$ and TBAC…….71

Figure S7: Detailed characterization of $Cu(acac)_2$ & CTAC
and $Cu(acac)_2$ & TBAC at a ratio of 1:0.25……72

Figure S8: Detailed characterization of $Cu(acac)_2$ and $CuBr_2$ syntheses at 50 min……..73

Figure S9: Detailed characterization of $Cu(acac)_2$ & $CuBr_2$ synthesis for 48 hours …….....74

Figure S10: Detailed characterization of $Cu(acac)_2$ & CTAB synthesis for 50 mins.....75

Figure S11: Detailed characterization of $Cu(acac)_2$ & CTAB synthesis for 48 hours……...75

Figure S12: Detailed characterization of $Cu(acac)_2$ & CTAB at lower ratios……...76

Figures S13: Detailed characterization of $Cu(acac)_2$ & TBAB synthesis for 50 mins……..77

Figure S14: Additional characterization of 1:0.5 ratio synthesis……...77

Figure S15: Detailed characterization of $Cu(acac)_2$ & CTAB
and $Cu(acac)_2$ & TBAB at a ratio of 1:0.25……...78

Figure S16: Detailed characterization of $Cu(acac)_2$ & TBAI at various ratios……..79

Figure S17: Detailed characterization of $Cu(ac)_2$ and $CuCl_2$ synthesis at different ratios……80

Figure S18: Detailed characterization of $Cu(ac)_2$ and CTAC synthesis at different ratios……...81

Figure S19: Detailed characterization of $Cu(ac)_2$ and CTAC at a ratio of 1:0.25…….81

Figure S20: Detailed characterization of $Cu(ac)_2$ and $CuBr_2$ synthesis at different ratios……82

Figure S21: Detailed characterization of $Cu(ac)_2$ and CTAB synthesis at different ratios……..83

Figure S22: Detailed characterization of $Cu(ac)_2$ and CTAB at a ratio of 1:0.25…….83

Figure SI 1: Schematic of ITC and ITC experiments……85

Figure SI 2: ITC results for $Cu(ac)_2$ and amine ligands……90

Figure SI 3: ITC results for $CuCl_2$ and amine ligands……..90

Figure SI 4: ITC results $Cu(acac)_2$ and amine ligands……..91

Figure SI 5: Reduction kinetics for $Cu(acac)_2$ and amine ligands……92

Figure SI 6: Reduction kinetics for $CuCl_2$ and amine ligands……..93

Chapter III

Figure 1: Characterization of CuPtRu branched core-frame rhombic dodecahedra……109

Figure 2: Characterization of CuPtRu branched frame rhombic dodecahedra……112

Figure 3: Characterization of CuPt branched core-frame rhombic dodecahedra……114

Figure 4: Characterization of the CuPt frame rhombic dodecahedra……..115

Figure 5: CO stripping voltammetry study of coreframe and frame nanostructures……...117

Figure 6: Preliminary electrochemical study of coreframe and frame nanostructures……120

Figure 7: XPS Spectra for Pt 4f and Ru 3p photoelectric lines……...122

Figure 8: Electrolyte stability study with MOR scans of frame nanostructures……..125

Figure 9: Analyte stability study for frame nanostructures ….……...129

Figure 10: Characterization of frame nanostructures after analyte stability study……..132

Figure S1: Characterization of CuPtRu coreframe nanostructure growth……...137

Figure S2: Characterization of CuPt coreframe nanostructure growth……138

Figure S3: Schematic of multimetallic coreframe and frame nanostructure growth……...139

Figure S4: CO stripping voltammetry study of the PtRu standard and integrated area.....140

Figure S5: CA study of Frame nanostructures……140

Figure S6: Peak deconvolution of Pt $4f_{7/2}$ and Pt $4f_{5/2}$ for each nanostructure……141

Figure S7: Peak deconvolution of Ru $3p_{3/2}$ for each nanostructure…….142

Figure S8: Peak deconvolution of Cu $2p_{3/2}$ for each nanostructure…….143

Figure S9: Electrolyte stability study MOR for PtRu STND……..144

Figure S10: Electrolyte stability studies of coreframe nanostructures…….…..…..145

Figure S11: Electrolyte stability studies, corresponding MOR CV…….146

Figure S12: Electrolyte stability study for the coreframe nanostructures, initial MOR…..…..…147

Figure S13: Analyte stability study of the coreframe nanostructures……..……148

Figure S14: TEM images of coreframe and frame after electrolyte stability study……149

Figure S15: TEM images of coreframe and frame after analyte stability study……..150

Figure SI 1: phase transfer methods for coreframe nanostructures…….154

Figure SI 2: electrochemical characterization of phase transfer methods……...155

Figure SI 4: Reproducibility studies of coreframe nanostructures…….156

Figure SI 5: Reproducibility studies of frame nanostructures…….157

Table SI 1: chart demonstrating the concentration change
after stability studies for PtCu & RuPtCu coreframe nanostructures…….158

Table SI 2: Chart demonstrating the change in copper content after stability studies……158

Table SI 3: Chart demonstrating the change in ruthenium content after stability studies……...159

Table SI 4: Chart demonstrating the change in platinum content after stability studies…….....159

Chapter IV

Scheme 1: illustration of nanotube growth……..……171

Figure 1: Characterization results for CuPt sNT 10%.....176

Figure 2: Characterization results for CuPt rNT 10%.....177

Figure 3: Characterization results for CuPt rNT 20%.....179

Figure 4: Characterization results for CuPtRu sNT 10%.....182

Figure 5: Characterization results for CuPtRu rNT 10% ……183

Figure 6: Characterization results for CuPtRu rNT 20%.....185

Figure 7: Nanotubes characterization after the phase transfer process……186

Figure 8: Preliminary electrochemical study of multimetallic nanotubes
with varying surface structure, maintaining platinum percentage……188

Figure 9: Preliminary electrochemical characterization of multimetallic nanotubes
Increasing platinum percentage, maintaining surface structure……...190

Table 1: MOR overpotential values from preliminary electrochemical study……....191

Table 2: If/Ir mass current from preliminary electrochemical study……...191

Figure 10: CO stripping study on the rough multimetallic nanotubes…….193

Table 3: Overpotential values from CO stripping study……..193

Table 4: ECSA values from the CO stripping study……194

Figure 11: Electrolyte stability studies for the rough nanotubes with 10% platinum……..196

Figure 12: Electrolyte stability studies for the rough nanotubes with 20% platinum……..198

Table 5: Overpotential values from the electrolyte stability studies……....198

Table 6: If/Ir values from the electrolyte stability study……..…199

Figure 13: Analyte stability study for rough nanotubes with 10% platinum…….…..201

Figure 14: Analyte stability study for rough nanotubes with 20% platinum…….…..203

Table 7: Overpotential values from the analyte stability study……...204

Table 8: If/Ir values from the analyte stability study……...204

Figure 15: Characterization of nanotubes after preliminary electrochemical characterization...207

Figure 16: Characterization of rough nanotubes after electrolyte stability study……...209

Figure 17: Characterization of rough nanotubes after analyte stability study…….210

Table 9: Binding energies for the Pt 4f photoelectric line……...211

Figure 18: XPS Pt 4f photoelectric line of smooth and rough nanotubes, 10% platinum……...212

Table 10: Pt 4f binding energies of the nanotubes…….……..213

Figure 19: XPS Pt 4f photoelectric line of rough nanotubes, 10% and 20% platinum……214

Table 11: Cu 2p binding energies of the nanotubes…….215

Figure 20: XPS Cu 2p photoelectric line of smooth and rough nanotubes, 10% platinum…….216

Figure 21: XPS Cu 2p photoelectric line of rough nanotubes, 10% and 20% platinum……..217

Table 12: Ru 3p binding energies of the nanotubes…….218

Figure 22: XPS characterization of Ru 3p of the ruthenium incorporated nanotubes…….219

Figure S1: CuPt rNT 20% characterization of morphology……....224

Figure S2: Characterization of the in situ optimization of the CuPt NT
by concentration of platinum precursor…….228

Figure S3: Characterization of the in situ optimization of the CuPt rNT by reaction time…….229

Figure S4: Characterization of in situ separation of smooth and rough nanotubes…….230

Figure S5: characterization of the in situ separation of the two mechanisms,
galvanic replacement reaction and the coreduction process……..231

Figure S6: Characterization of Synthetic trials for CuPtRu NT……..……232

Figure S7: Preliminary electrochemical activity results for smooth nanotubes……..233

Figure S8: Preliminary electrochemical characterization of rough nanotubes……234

Figure S9: XPS characterization of the C 1s of all nanotube samples…….235

Figure S10: Peak deconvolution of Pt $4f_{5/2\ \&\ 7/2}$ photoelectric line for nanotubes……..236

Table S1: binding energy values of peak deconvolution for Pt $4f_{7/2}$ photoelectric line.....….237

Table S2: binding energy values of peak deconvolution for Pt $4f_{5/2}$ photoelectric line...…..….237

Figure S11: Peak deconvolution of Cu 2p photoelectric line……..238

Table S2: Binding energy values for peak deconvolution of Cu 2p photoelectric line……...239

Figure S12: peak deconvolution of the Ru $3p_{1/2}$ photoelectron line for nanotubes....……240

Figure S13: peak deconvolution of the Ru $3p_{3/2}$ photoelectron line for nanotubes…….241

Table S3: binding energy values for peak deconvolution of Ru 3p photoelectron lines…….242

Figure S14: peak deconvolution of C 1s photoelectron line for nanotubes…….....243

Table S4: Atomic ratio of the CuPt sNT 10% by ICP-MS……..244

Table S5: Atomic ratio of the CuPt rNT ~10% by ICP-MS……244

Table S6: Atomic ratio of the CuPtRu rNT ~10% by ICP-MS……...……245

Table S7: Atomic ratio of the CuPt rNT ~20% by ICP-MS……....245

Table S8: Atomic ratio of CuPtRu rNT 20% by ICP-MS……245

Figure S15: Electrochemical characterization of nanotubes in H_2SO_4 electrolyte……246

1. Chapter I. Introduction

1.1 Introductory Statement

Fuel cells are one type of energy storage and conversion devices, which generate energy from chemical reactions and demonstrate high specific energy; however, their efficiency is limited by low specific power. Individual types of fuel cells possess additional limitations that pertain to their specific device design, reaction mechanisms of electroactive species.[1] These limitations prevent realistic competition with the combustion engine, which possesses both high specific power and specific density[1a] Developing nanomaterials that improve electrocatalytic efficiency and economic viability, for existing fuel cell devices, could enable the commercialization of fuel cells and improve environmental issues. In the case of direct methanol fuel cells (DMFC), energy is produced from methonal oxidation at the anode, and counterbalanced by the reduction of oxygen on the cathode allowing for continual production of energy. DMFC efficiency is limited by fuel cross over, slow reaction kinetics at the cathode, and anode efficiency.[1b, 2] Bulk platinum is the leading electrocatalyst for the anodic electrode in these fuel cells; however, it is limited by surface area and its propensity for CO poisoning. Platinum based nanostructures overcome surface area limitations, yet the efficiency of these electrocatalysts is still limited by CO poisoning, slow MOR kinetics, and a more positive overpotential. Previous research has shown that developing Pt based nanomaterials alloyed with specific transition metals improves the resistance towards CO poisoning and MOR activity.[3] Additionally, multimetallic nanomaterial's structure and morphology can influence electrochemical activity.[4]

The main objective of this research is to develop multimetallic alloyed nanomaterials that improve electrocatalytic activity for MOR, and eventually function as anodic electrocatalysts in

DMFC that address the anode limitations. These multimetallic nanomaterials could possess increased electrocatalytic properties, due to geometric and synergistic effects that occur in alloyed nanomaterials with unique morphologies. Previous research has shown that platinum based nanomaterials are the leading electrocataysts for MOR, and alloys with copper and ruthenium can simultaneously reduce CO poisoning and increase the oxidation of CO to CO_2 through the bifunctional mechanism.[5-6] Since coinage metals and noble metals are ideal candidates for electrocatalysis, this research focuses on producing bimetallic and trimetallic alloyed nanomaterials with composition of Pt, Cu and Ru. Additionally, altering the percent composition of multimetiallic nanomaterials could affect the electrocatalytic efficiency of MOR, due to the synergistic properties[3, 7,8,9,10] After the successful development of copper-platinum nanomaterials (CuPt NM) and copper-platinum-ruthenium nanomaterials (CuPtRu NM), with varying percent compositions, the electrocatalytic properties will be studied to determine efficiency for methanol oxidation, resistance towards CO poisoning, and stability.

Synthetic tailoring the composition of the multimetallic nanomaterials is a key objective of this research. The multimetallic nanomaterials, for this research, can be formed on Cu NM templates through the following galvanic replacement reaction, co-reduction mechanims and the in situ separation of these mechanisms. Addtionally, these mechanisms are responsible for tailoring the percent composition of the multimetallic nanomaterials.[9, 11] Synthetic control of the multimetallic alloyed nanomaterials could not only result in variation in the nanomaterial composition, but also in the size, morphology, and porosity. Nanomaterials with unique morphologies, hollow structures, and select surface facets could influence catalytic properties.[12,13,14] This research will also study the effect of size, morphology, porosity, surface structure on the CuPt NM and CuPtRu NM MOR efficiency.

Multimetallic nanomaterial morphology and structure can be controlled by the intial Cu NM synthesis. Previous research suggests the influence of halides present in the reaction solution on nanomaterial growth.[15,16] This research will also focus on developing protocols for copper nanomaterials with unique morpholgoies and 1-D structures, as well as studying the influencing factors of Cu NM growth.

1.2 Background:

1.2.1 Background: Direct Methanol Fuel Cells

Energy storage and conversion devices are alternative renewable energy sources that endeavor to be more efficienct and environmentally friendly than the combustion engine.[1a] These devices include capacitors, super capacitors, batteries, and fuel cells. The efficiency of alternative, renewable energy sources is outlined in Figure 1, which provides a Ragone plot of the four most common types of energy storage and conversion devices and the combustion engine.[1a] This plot compares the specific power and specific energy of the combustion engine, fuel cell, battery, and supercapacitor. This plot demonstrates that combustion engines possess the highest specific power and specific energy.

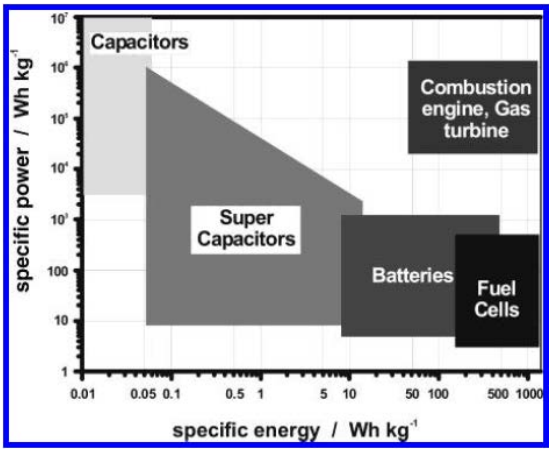

Figure 1: contains a simplified Ragone plot, comparing the efficiency of common energy storage and conversion devices.[1a] (Reprinted with permission from 1a copyright 2004, American Chemical Society).

Capacitors and supercapacitors possess the highest specific power and lowest specific energy, while batteries have lower specific power and higher specific energy. Fuel cells have the highest specific energy and lowest specific power.[1a] In order to develop an alternative energy storage and conversion device that is a commercially viable option instead of the combustion engine, the efficiency of each device needs be improved.

Direct methanol fuel cell is a specific type of proton exchange membrane fuel cell that creates energy from the oxidation of methanol on the anodic electrode, and is replenished by the reduction of oxygen on the cathodic reaction.[17] Figure 2 contains a diagram of a direct methanol fuel cell, which consists of two electrodes, generally composed of platinum. At the anode methanol oxidation occurs, which generates 6 intermediate species and electrons.

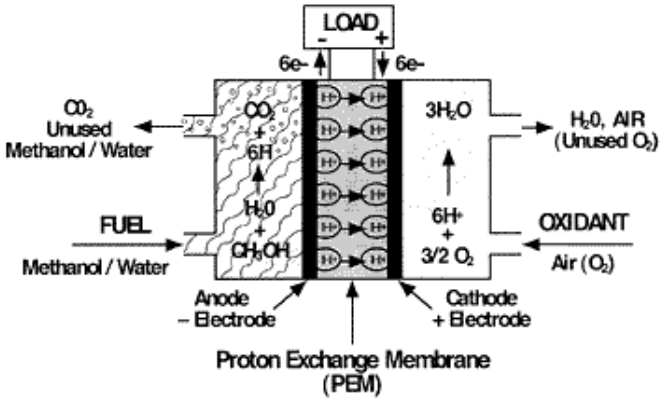

Figure 2: contains a schematic of the electron flow a direct methanol fuel cell.[2]

The intermediate species formed during methanol oxidation is based on the electrolyte pH and electrocatalyst composition.[2] In acidic media, methanol will undergo one of the two following pathways. The first pathway oxidizes methanol to hydroxymethyl, formaldehyde, formic acid, formate, carbon dioxide.[2] In the second pathyway methanol oxidizes methanol ot hydroxymethyl, formaldehyde, aldehyde, carbon monoxide, formate, and carbon dioxide. These pathways were shown in **Figure 3.**

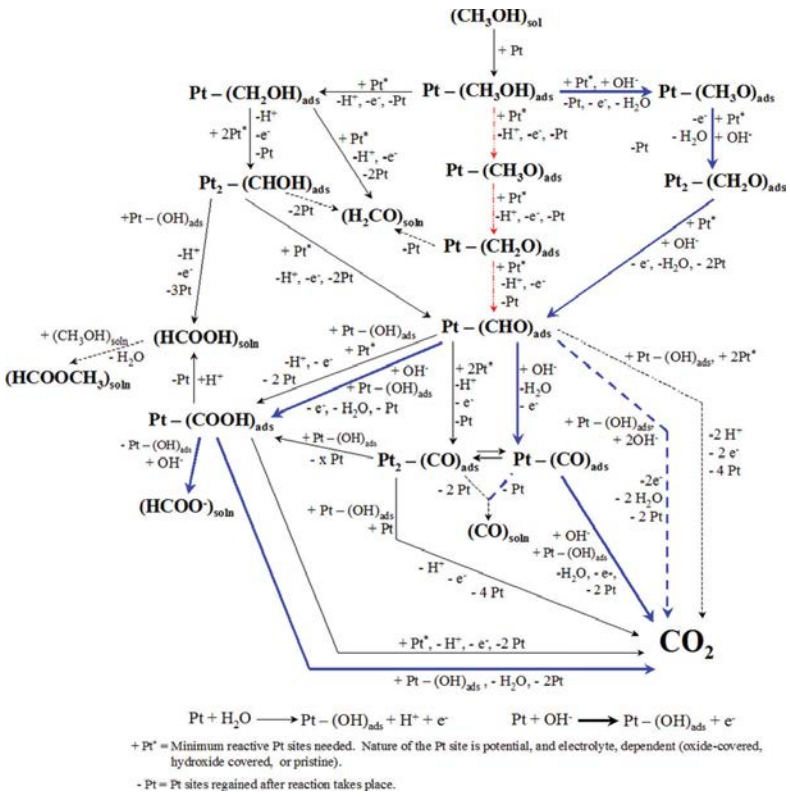

Figure 3: methanol oxidation pathway in acidic media (black), alkaline media (blue), and UHV (red).[2] (Reprinted with permission from 2 copyright 2007, Royal Society of Chemistry).

The electrons from MOR will flow through an external circuit that will generate energy, and then continue to the cathode. At the cathode reaction, oxygen reduction occurs, balancing the overall charge of the fuel cell.[1a] The efficiency of the DMFC is limited by fuel cross over at the proton exchange membrane, and the cathode efficiency limited by the kinetics of oxygen reduction. The efficiency of the anodic electrode is limited by CO poisoning of the electrocatalyst surface, slow MOR kinetics, and high MOR overpotential. [2]

1.2.2 Background: DMFC Anode Limitations

Platinum is generally utilized as an electrocatalyst for oxidation and reduction reactions, in DMFC. The platinum efficiency at the anode is limited by its surface area, CO poisoning, and high MOR onset potential. Previous research suggests that platinum based nanomaterials can increase electrocatalytic activity through synergistic and geometric effects.[18] While platinum can

readily be poisoned by CO, it has been shown that alloying platinum with another group 10 or 11 metal can reduce CO poisoning on the catalyst allowing for an increase the catalytic properties.[3,7,19,20] **Figure 4** provides a schematic of the bifunctional mechanism, in a platinum-alloyed system.[5] In which the formation of the alloys, from group 10 and 11 metals, weakens the bond between the electrocatalyst and adsorbed species, allowing for easier de-adsorption of the species promoting alcohol oxidations and oxophilic reactions.[7, 20] In the bifunctional mechanism, the platinum and the oxophillic metal (Ru, Cu, Sn) will alter the crystal lattice structure of the nanomaterial alloy, resulting in a shift of d-band orbitals. The shifting of the valence orbitals will weaken the bond between the platinum alloy's surface and the adsorbed CO, as well as bonding with adsorbed hydroxyl groups. This causes the adsorbed CO and an oxophillic species (OH-) to desorb, and react to form CO_2. This process prevents readsorption of CO onto the platinum alloys surface, and frees reactive sites at the electrocatalyst surface for MOR. [5-6, 21, 22]

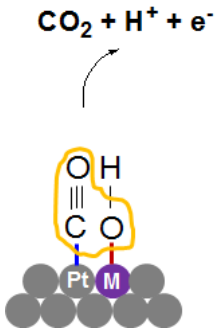

Figure 4: schematic of bifunctional mechanism in a platinum alloy. [5]

1.2.3 Ideal Compositions of Nanomaterial Electrocatalysts for MOR

While platinum is the most efficient electrocatalyst for MOR, efficiency is limited by CO poisoning. The oxidation of methanol in acidic media forms 6 different intermediates, including CO.[2, 23] Once formed CO will strong onto platinum, which reduces the number of active sites for methanol oxidation lowering the MOR efficiency. Previous research has shown that alloying

platinum with another metal can reduce CO poisoning through the bifunctional mechanism.[21] Multimetallic nanomaterials comprised of platinum and copper have unique optical and catalytic properties, which are reliant on their size, shape, and composition.[7, 24] $PtCu_3$ NMs of basic morphologies have proven successful in increasing the catalytic activity of the following reactions: methanol oxidation reaction, CO oxidation reactions, and oxygen reduction reactions. [7]

Density functional theory and volcano plots comparing the energy required to oxidize CO and OH of various platinum based alloys, demonstrates which alloys are the most efficient for the bifunctional mechanism to occur. These studies determined that platinum alloys with ruthenium, copper, and tin are the most efficient for the oxidation of CO & OH. [5, 25] The ideal composition of the bimetallic alloy was computationally determined and represented by a volcano plot, found in **Figure 5**.[5] This plot compares the energy required to remove adsorbed hydroxyl groups, and CO groups, the alloys shown in the blue region shows alloys that possess a lower potential for the removal of the adsorbed species. This plot suggests that alloys between platinum and copper as well as platinum and ruthenium are ideal compositions for the removal of adsorbed species.[5]

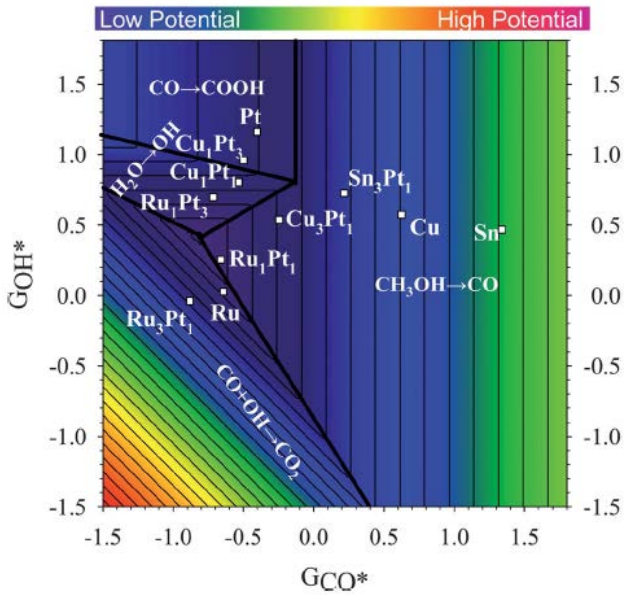

Figure 5: contains a volcano plot comparing alloyed compositions and their reactivity for adsorbed species.[4] (Reprinted with permission from 4 copyright 2012, Royal Society of Chemistry).

It was determined that alloying platinum with an oxophillic metal, such as Ru, Sn, Cu, would alter the crystal structure weaken the bound CO on the platinum surface.[5-6, 21] Additionally, CO would further oxidize to CO_2 preventing the re-adsorption of CO.[22] It has been determined that alloys between Pt & Ru or Pt & Cu cause the greatest resistance towards CO poisoning, forming a more efficient electrocatalyst.[26] Additional studies have been completed over altering the composition of nanomaterials and improved electrocatalytic activity.[27] It has been determined that electrocatalytic activity can be influenced by composition, as well as atomic ratio within the nanomaterial.[9, 28] The atomic ratio at the surface of the nanomaterial can influence the methanol oxidation pathway, resulting in a volcano like influence on electrocatalytic activity.[9] Additional studies have been completed that suggest the formation of a trimetallic nanomaterial, can improve the electrocatalytic activity.[29]

1.2.4 Structural Benefits of Nanomaterials as Electrocatalysts for MOR

Multimetallic nanostructures have emerged as a route for improving fuel cell electrocatlaysts, due nanomaterial's tailorable composition, size, and morphology of nanomaterials, which synthetically designed to improve catalytic properties.[30] Previous research has shown that nanomaterial surface structure, morphology, and high index facets can improve electrocatalytic activity through multiple routes.[7, 29a, 25] Nanomaterials with high index facets on the surface have shown to improve electrocatalytic activity.[31] Previous studies have shown that electrochemical reactions can be influenced by surface facets and surface structure can improve MOR activity and CO oxidation.[32] Crystal overgrowth at the nanomaterials surface can influence the electrocatalytic activity by increasing surface area as well as providing high index facets.[6, 24b]

Nanomaterials of unique morphologies can influence electrocatalytic activity, by increasing the surface area and providing surface facets that will favorably influence electrochemical reactions.[33] Recent studies have been completed to determine the effect of geometry/shape,e.g., nanocubes,[34] nanocages,[7, 35] hexapod concave structures,[36] and nanodendrites[37], on the catalytic activity of PtCu alloy for MOR. These PtCu binary nanostructures exhibit higher catalytic activity compared to their corresponding nanoparticles due to the presence of more active sites. PtCu nanocubes can improve formic acid oxidation.[4, 33c] Nanodendrites exhibit high catalytic activities for electrochemical reactions, due to ultrafine branches confined within the relatively-large assemblies.[37a, 38] Porous nanomaterials, such as nanoframes and nanocages, have also shown to improve electrocatalytic activity, by increasing the nanomaterial's surface area increasing reactive sites.[7, 39] Frame nanostructures possess a thin surface structure, or skeleton, with a large overall structure size. These structures enhance electrochemical reactions by increasing the surface area of the overall structure, the maintaining

the stability of the ultrafine surface by framework structure, and providing the extremely thin surface structure that contians a large quantity of surface atoms for catalytic reaction.[7, 35a, 40] [7, 35a, 40a-e]

Previous research has shown that altering nanomaterial structure from 0-D to 1-D can improve electrocatalytic activity and the onset potential of MOR, by providing a combination of nanomaterial attributes that are responsible for enhancement of electrocatalytic properties. In research completed by Yan et al., nanotubes improved MOR activity by providing a high surface area based on morphology, and unique surface structure that is "decorated" with crystal overgrowth and high index facets.[32b] 1-D structures can be synthetically tailored, through the galvanic replacement reaction, to possess varying degrees of porosity on the surface.[41] This can increase the electrocatalytic surface area and improve MOR activity, as shown by Feng et al.[41] Additional examples of 1-D structures improving the electrochemical activity include carbon nanotubes decorated with Pt & Ru, which function as the electro-active species that improve electrocatalytic activity. [42, 43] 2-D structures, such as Pt-Cu alloyed nanosheets and nanocones, have also improved electrocatalytic activity by providing unique morphologies and crystal planes along the 2-D structures that enhance electrochemical reactions.[7, 44]

1.2.5 Background: Nanomaterial Growth and Influencing Factor

Crystal growth of nanomaterials is formed through two main methods, the top down approach where bulk materials are broken down into uniform morphologies through etching, micropatterning or photolithography, or the bottom up synthesis which generally involves chemical synthesis to generate nanomaterials. The bottom up synthesis occurs through two main mechanisms that result in nucleation and the nanocrystals growth are the Finke-Watzy mechanism and the LaMer mechanism. The Finke-Watzy mechanism is defined as a slow nucleation of monomers and then a fast autocatalytic growth. The LaMer mechanism is defined as a fast single

nucleation event, this occurs when there is a high concentration of monomers, and these simultaneously form nuclei and nanocrystals growth. The LaMer mechanism is responsible for the nanomaterial growth in this research.[45] Nanomaterial synthesis, crystal growth, and resulting morphology is influenced by the metal precursor, reduction kinetics, additives and capping ligands. In a typical synthesis, metal precursors are combined with a reducing agent, reaction additives and capping ligands and solvent present in the reaction solution.[46,45] The metal percursors will be reduced by reducing agents to a neutral valent state. After the concentration of neutral valent metal atoms reaches a super saturation point, the atoms will nucleate and form a crystal seed. Metallic seeds will continue to form until the concentration of metal atoms falls beneath the super saturation concentration, after which any remaining metal atoms will adsorb onto the nucleated seed. The nanomaterial growth and morphology can be directed from the seed, when specific additives are added to the reaction solution, including halogens, capping ligands, or etching agents. Capping ligands (or halogens) will selectively adsorb onto specific facets, the metal adsorb onto unprotected facets directing growth along that direction.[16, 52] There are numerous studies that discuss the influence from the capping ligands that will selectively bind to facets.[47] Specifically, PVP with the {100} forming nanocubes or citrate with {111} forming nanoplate.[47b] Neutral valent metallic atoms could also adsorb on the surface with high surface energy to reduce the energy, and form a more stable particle. Crystal growth will continue until a nanomaterial has formed the desired morphology.[47a]

Nanomaterial growth can be affected by the reduction kinetics and thermodynamics. For example Younan Xia's group was able to synthesize palladium nanocrystals (Pd NC) using a seed mediated growth mechanism into a variety of shapes, including cubes, octahedrons, as well as cubes and octahedrons with varying degree of truncation.[48] The capping ligand influenced nanomaterial growth; however, it was not the sole explanation for the growth of the Pd NC.[48a, 49]

Their research determined that the metal precursor, either Na_2PdCl_4 and $Pd(acac)_2$, utilized would influence the quickest growing facet, this ultimately affected the final morphology.[31a] They determined that Na_2PdCl_4 favored growth along the <100> plane leading to the formation of nanocubes, while $Pd(acac)_2$ had growth along the {100} The resulting shapes were attributed to the ligands that present in the metal precursor and their effect on reaction kinetics. Low index morphologies are influenced by the reaction parameters, their metal precursors, as well as their capping ligands. Generally these processes are thermodynamically favorable, which makes them easier to synthesize than complex nanostructures.

1.2.6 Background: Halide Influence on Noble Metal Nanomaterial Growth

Halides have proven to direct noble metal synthesis and distinct morphologies. Previous studies have been completed on the formation of noble metal nanoparticles, with varying morphologies. When halides are utilized as a shape directing additive, unique morphologies can be developed. Some examples of morphologies develop by shape directing halogens include nanocubes, nano-rhombic dodecahedra, nanoplates, nanopyraminds, nano-bipyramids, and nanowires.[47a, 50]

Additional studies have been completed to determine the halides function as a shape directing additives. Previous research has investigated the influence of chloride and bromide on nanomaterial growth and resulting morphology. Research completed by Murphy et al. determined that halides in the reaction solution can influence morphology as well as size.[16] Altering the halide present in the synthesis can varying the noble metal nanomaterial shape.[16] Studies have determined that the morphology of noble metals nanomaterials, mainly gold and silver, can be tailored based on the halogen present in solution in addition to the amount of precursor present in solution. Research completed by personick et al. studied the influence of

halides and silver ions on seed mediated synthesis. This work determined that the silver ions and halides present in the reaction solution can tailor gold nanomaterials's morphology by reduction kinetics, the under deposition potential, and synergistic effects. The role of halides on the reduction kinetics, facet selectivity, and noble metal nanomaterial growth was elucidated.[15] It was determined that halides will bind to the gold surface with varying degrees of strength (Cl-, Br-, I-), and this can then inhibit the nanomaterial growth, and that bromide and iodide halides can slow the rate of gold nanomaterial growth and result in different morphologies.[15] Additionally, this group was able to alter the concentration of the various halides (Cl- & Br-) in the growth solution to obtain the various shapes.[15] Research completed by Mirkin et al., has shown that by changing the capping ligand between CTAC and CTAB two different morphologies are synthesized, and they attribute this to exchanging the Cl^- with Br^- in their reaction solution.[15, 51] Chloride has also been used as an oxidative etchant in order to develop nanomaterials of unique morphology.[52] There are multiple studies that attribute oxidative etching to the formation of noble metal nanoplates of varying morphology including, hexagons, traingles, and disks.[53] The halide facet selectivity and nanomaterial shape directing properties can also extend to bimetallic nanomaterials.[54]

Additional studies have determined that halides possess shape directing properties for noble metal nanomaterial synthesis, due to their preferential binding of specific facets. Previous research has determined that bromide will selectively adsorb onto the {100}, influencing growth along different facets present on the nanomaterial.[47b] This study also discussed the influence from the capping ligands that will selectively bind to facets. Specifically, PVP with the {100} forming nanocubes or citrate with {111} forming nanoplate.[47b] Gold nanomaterials that possessed the following shapes: rhombic dodecahedra (RD) and bipyramids (BP). Both

structures were found in one synthesis, in which CTAC was utilized as the reducing agent. This research also reviewed the energetically favorable surface facets order: {111}, {100}, {110}. The {111} facet is thermodynamically favorable, while the {110} facet has the highest surface energy. Since the {110} facet has the highest surface energy.[55] The influence of CTAB vs CTAC on gold nanomaterials was studied, which created concave nanocubes or convex nanocubes, respecivtely. The alteration in the morphology of the nanocubes is attributed to the presence of either chloride or bromide selectively binding to facets.[56] Other studied determined the influence of Br- anion on the aspect ratio of Au NRs for aqueous syntheses. Changing the concentrations of CTAB on the resulted the a change in aspect ratio of the gold nanorods.[51] Additionally, the Br^- anion protects the {111} and {100} surface facets, while promoting growth in the [110] direction. CTA^+ and Br^- independently influence on the growth of the nanorods. It was determined that CTA^+ protects the sides and {110}, while Br^- anion will protect the {100} & {111} facets, which correlates to the surface energy. [51]

1.2.7 Copper Nanomaterial (Cu NM) Growth and Limitiations

Copper nanomaterials have applications in catalysis, electrocatalysis, photocatalysis SERS, optics and imaging.[47a, 57] Copper nanomaterials with specific morphologies and surface facets can enhance the activity. Understanding the synthetic additives responsible for copper nanomaterial growth is important to determine methods for synthetic tuning of nanomaterial structure. The growth processes for copper nanomaterials function similarly to noble metal nanomaterials. Previous work has determined that the crystal growth of the Cu NM can form nanospheres, nanowires, nanoplates, and nanodendrites.[58] Copper nanomaterial structure is synthetically tailored through facet selective binding of capping ligand, reduction kinetics, pH,

and various other reaction parameters.[59] **Figure 6** provides a schematic of Cu NM nucleation and growth, while **Figure 7** provides a schematic of Cu NM facet specific growth.

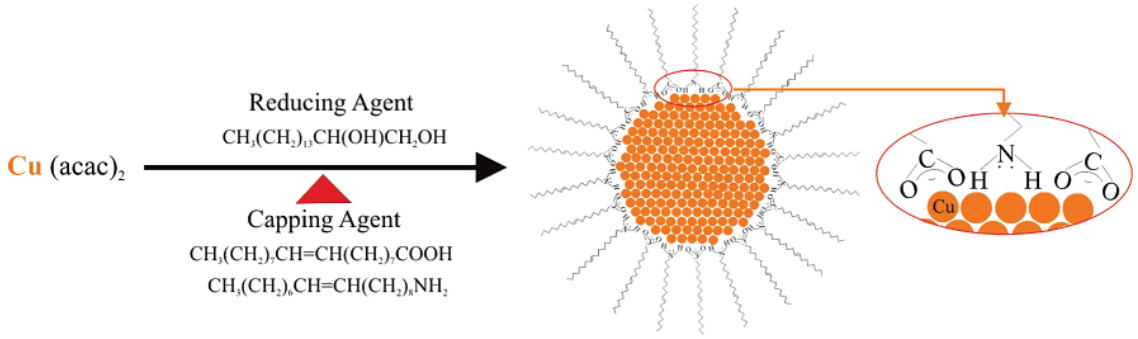

Figure 6: a schematic of the basics of Cu NP growth, showing the progression from the starting materials to nucleation to Cu NP.[46a] (Reprinted with permission from 46a copyright 2007, American Chemical Society).

Copper is a face centered cubic crystal (FCC), which means that crystal growth in the {111} and {100} facets are favored, and shown in **Figure 7**.[46a] Growth in these directions will lead to the formation of cubes, octahedrons, rods/wires and in cases where twin defects are present icosahedra and decahedra morphologies will be formed. Variations in the reaction parameters can influence surface energies, and are responsible for the growth of specific morphologies and sizes. These parameters include reaction temperature, concentration of reducing agents, and the capping ligand.[46a] Previous research has shown that reaction temperature directly correlates to the size of a nanoparticle, increasing the temperature results in an increased size copper nanoparticle.[46a]

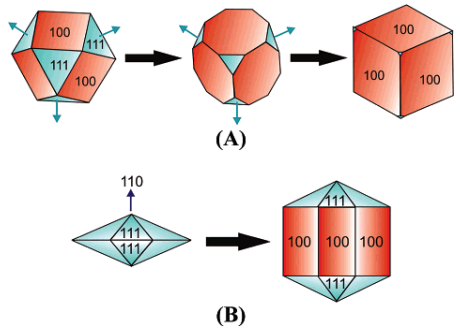

Figure 7: Preferential facets present in copper and copper oxide nanomaterial growth.[46a] (Reprinted with permission from 46a copyright 2007, American Chemical Society).

Forming uniform copper nanomaterials has proven challenging, due to the strength of the capping ligands on noble metal nanomaterials as opposed to coinage metals.[46a] The morphology of copper nanomaterials are challenging to control morphologically due to the oxidation at the surface once capping ligands have been removed.[46a] When this occurs the Cu NM can form copper oxide, and the morphology of the Cu NM can be altered from solid to hollow particles.[58b, 60] In order to increase the stability of the copper nanomaterials of this research, these syntheses will occur in organic phase, and the reaction phase will take place in an inert atmosphere.

1.2.8 Background: Halide influence of Cu NM facet selectivity and Cu NM growth

The growth processes for copper nanomaterials function similarly to noble metal nanomaterials. Forming uniform copper nanomaterials has proven to be more challenging than the noble metal nanomaterials, which could be due to the strength of the capping ligands on noble metal nanomaterials as opposed to coinage metals.[46a] Previous work has determined that the crystal growth of the Cu NM can form nanospheres, nanowires, nanoplates, and nanodendrites.[58] Copper nanomaterial structure is synthetically tailored through facet selective binding of capping ligand, reduction kinetics, pH, and various other reaction parameters.[59] Generally, the morphology of copper nanomaterials are challenging to control morphologically due to the oxidation. When this occurs the Cu NM can form copper oxide, and the morphology of the Cu NM can be altered from solid to hollow particles.[58b, 60] In order to increase the stability of the copper nanomaterials of this research, these syntheses will occur in organic phase, and the reaction phase will take place in an inert atmosphere.

Few studies have been completed on the halide influence of copper nanomaterial growth and resulting copper nanomaterial morphologies. Pileni et at., studied copper nanomaterial growth with the micelle method, and the influence of various halides on the resulting

morphologies.[61] This group also studied the reaction parameters influencing the size of the nanomaterials. [62 63] The following halides were studied included NaCl, NaBr, NaF, NaI, $CuCl_2$, CTAC, CTAB influence on Cu NM growth with the micelle. For the most part only Cl^- and Br^- had the most impact on nanomaterial growth, while the rest of the anions did not. Corresponding CTA^+ also had an impact on nanomaterial shape, similar to other studies on noble metal nanomaterials. determined Cl^- selective binds to the {111} & {100} based on the concentration and CTA^+. Br^- selectively binds to the {111} facet over the {100}, explains why in their research plates were generally formed.[61]

1.2.9 Background: Mechanisms for Alloyed Multimetallic Nanomaterials

The formation of multimetallic alloyed nanomaterial, that consists of an alloy between two metals in group 10 and group 11, can not only produce bimetallic nanostructures that possess synergistic effects, but also form a more stable nanomaterial with unique optical and catalytic properties.[3, 6-7, 19-20, 64] Previous research has shown that alloying copper with other group 10 or 11 metals could potentially increase the stability of copper nanocrystal.[11, 65]

Tailoring the composition of the multimetallic nanomaterials can be completed by altering reaction parameters including precursor concentration, pH, temperature, and kinetics.[28b] Multimetallic nanotubes were developed by alloying Pt & Ru along the vertices of the Cu NW through the galvanic replacement reaction and the coreduction mechanism. These two growth mechanisms are responsible for the development of the nanotube surface structure. The galvanic replacement reaction developed binary and ternary nanotubes with smooth surface structure, while the multimetallic nanotubes with rough surface structure are developed through the galvanic replacement reaction and coreduction mechanism.

The galvanic replacement reaction process occurs when atoms on the surface of a nanomaterial template are exchanged with atoms from a secondary metal.[66] In this process, a secondary metal precursor is injected into the reaction solution with the previously formed nanomaterial template. Metal atoms are reduced and will replace atoms at the surface of the nanomaterial template, based on the difference in reduction potential of the two metals.[11, 66] This process will continue until the surface has formed an alloy between the two metals. Additionally, the replacement process will cause metal atoms from the template interior to diffuse out of the nanomaterial, forming a porous nanomaterial.[66] This will continue until an alloyed frame has been developed. This growth mechanism was studied by Xia et al., with the transformation of silver nanocubes into gold nanocages.[66] The galvanic replacement reaction has proven to be applicable in trimetallic syntheses and the development of core-shell nanomaterials.[67] Previous research has shown that the stability of group 10 and 11 metals can be increased by forming an alloyed nanostructure between two of the metals. Previous research has focused on forming stable noble-metal bimetallic nanoparticles through the galvanic replacement reaction. This includes silver and gold nanoparticles (AgAu NC), platinum and gold nanoparticles (PtAu NC), gold with palladium nanoparticles (AuPd NC), and lastly platinum and copper nanoparticles (PtCu3 NCs).[7-8, 11, 68, 69]

There are two main alloying methods that are utilized to form hollow bimetallic alloys, the galvanic replacement reaction and the kirkendall effect. Bimetallic nanoparticles are generally produced through a galvanic replacement reaction and a simultaneous Kirkendall effect, the end result is an alloyed bimetallic nanoparticle that is generally uniform and hollow in shape. [66a, 68, 70, 71] The Kirkendall effect is responsible for the development of an alloy between two metals that occurs on the interior of the nanostructure. Once the surface has been covered

with the alloying metal, a small cavity will begin to form in the interior of the nanostructure, by the diffusion of the metal forming the nanostructure out of the interior and the diffusion the alloying metal into the center of the nanostructure. This diffusion in and out between the two metals will continue until a completely alloyed structure is formed.

The coreduction mechanism is responsible for the formation of crystal overgrowth along the vertices and edges of the nanotubes. In the seeded coreduction mechanism, a nanomaterial seed is developed, and a secondary metal precursor will coreduce and adsorb onto the surface of the seed influencing nanomaterial structures.[71a] The secondary metal will favorably adsorb on the template areas with high surface energy, such as the vertices and edges, in order to stabilize the nanomaterial.[49, 72] This influences nanomaterial growth resulting in overgrowth along the vertices and edges.[54, 71a]

1.3 Overview of this Research

1.3.1 Chapter II: Morphology Control of Copper Nanomaterials & the Influence of Halides on Nanomaterial Growth

Since previous research has determined halogens can function as shape directing additives in aqueous, micelle, nanomaterial synthesis, the focus of this research is to determine the influence of copper (II) halides on oil-based copper nanomaterial growth and resulting nanomaterial structure. The oil-based copper nanomaterials developed with copper (II) chloride included copper nanoparticles (Cu NP), copper nano-rhombic dodecahedron, (Cu RDH), copper nanowires (Cu NW), and copper nanoplates. These morphologies were obtained by varying the concentration of the two copper precursors present in the reaction solution, and the resulting morphologies were characterized. It was determined that the copper precursor, $CuCl_2$, was responsible for the nanomaterials morphology. In an effort to understand the influence of the chloride anion on nanomaterial growth in an oil-based synthesis, the chloride source was altered

and the synthetic protocol repeated. Synthetic studies were completed with external sources of chloride (CTAC & TBAC), and the resulting morphology remained the same with the external chloride source. This suggested that the chloride selectively bound to the (110) facet and directed nanomaterial growth and structure.

Since chloride halides directed nanomaterial growth in an oil-based synthesis, the shape directing properties of other halides (Br-, I-) were investigated. The influence of bromide on nanomaterial growth in an oil-based, dual copper precursor system was studied utilizing the same synthetic protocols. Utilizing $CuBr_2$ instead of $CuCl_2$ in the synthesis resulted in the formation of copper nanomaterials with different morphologies. Additionally, the concentration $CuBr_2$ utilized in the synthesis influenced the nanomaterial's morphology. The nanomaterials produced with bromide included nanospheres, nanopyramids, nanooctahedra, and nanoplates. Additional synthesis studies were completed with an external source of bromide (CTAB & TBAB). The nanostructures developed with various bromide sources were similar in structure. Based on nanomaterial morphology the oil-based nanomaterial growth is affected not only by Br- concentration but also the source of bromide. This suggests that bromide does not function less effectively than chloride as a shape directing additive.

The influence of iodine on oil-based copper nanomaterial growth was also investigated. When iodide was utilized in the synthesis, the Cu NM formed spherical and hexagonal nanoplates. This morphological structure was formed regardless of iodide concentration, suggesting that iodine was not as effective at directing nanomaterial growth compared to chloride or bromide. Each halogen produced uniform nanomaterials of distinct morphologies, in contrast to the nanomaterials formed in the absence of this shape directing additive. These results

may correlate to either Cl-, Br-, I- selectively binding to a nanomaterial facet, protecting that facet while directing growth a different facet.

1.3.2 Chapter III: Synthesis of Branched Core-Frame and Frame Copper-Platinum-Ruthenium Rhombic Dodecahedra and their Electrocatalytic Properties for Methanol Oxidation

This research developed binary and ternary coreframe and frame nanostructures, composed of Cu, Pt, and Ru, and investigated their activity for methanol oxidation reaction (MOR). Multimetallic, branched core-frame nanostructures were formed by coreducing Pt & Ru onto the vertices and edges of copper rhombic dodecahedra (Cu RHD). The multimetallic frame nanostructures were formed by etching the coreframe nanostructures.

Studies over electrocatalytic activity determined that the multimetallic frame nanostructures enhance MOR activity and stability, based on the alloying at the frame nanostructure's surface. Additionally, the incorporation of Ru into the nanostructures improved resistance towards CO poisoning, and the nanostructure's morphology and composition was maintained during the stability studies.

1.3.3 Chapter IV: Synthesis of Multimetallic nanotubes with rough and smooth surface structure and their Electrocatalytic Activity for Methanol Oxidation

This research develops multimetallic nanotubes with synthetically tunable surface structure and platinum content. The bimetallic and trimetallic nanotubes with varying surface structure were developed utilizing similar methods as the coreframe nanostructures. Copper platinum nanotubes (CuPt NT) were developed by forming Cu NW and then alloying with Pt. Synthetically tuning the alloying mechanisms, the galvanic replacement reaction and seeded co-reduction mechanism controlled the binary nanotube surface morphology. Copper platinum nanotubes with smooth surface structure (CuPt sNT10%) were formed through the galvanic

replacement reaction. Copper platinum nanotubes with rough surface structure (CuPt rNT 10%) were developed through both the galvanic replacement reaction and the coreduction mechanism. Ru was incorporated into the smooth and rough nanotubes. Copper platinum ruthenium smooth nanotubes (CuPtRu sNT 10%) were formed through solely the galvanic replacement reaction, while copper platinum ruthenium rough nanotubes (CuPtRu rNT 10%) were formed through both reaction mechanisms. The atomic ratio of platinum present in the rough nanotubes was also tailored by varying the precursor concentration and reaction time. The rough nanotubes were synthetically tailored to possess atomic ratios of 20% platinum, forming CuPt rNT 20% and CuPtRu rNT 20%.

The synthetic variations of the nanotubes enabled an electrochemical comparison of the multimetallic nanotubes based on surface structure and composition. The electrochemical study completed on multimetallic nanotubes with varying surface structure with an atomic ratio of 10% platinum. The multimetallic nanotubes with rough surface structure possessed increased the MOR activity compared to the smooth nanotubes. The trimetallic nanotubes with rough surface also lowered the MOR overpotential to a voltage comparable to the PtRu standard, as well as improving resistance towards CO poisoning. An electrochemical study was completed on the multimetallic rough surface structure with different atomic ratios of platinum. It was determined that by increasing the content of platinum in the binary and ternary rough nanotubes, the electrocatalytic activity for MOR increased, while the resistance to CO poisoning and lowered onset potential was maintained. The improved electrocatalytic activity, improved resistance for CO poisoning, and lowered MOR overpotential, can be attributed to the 1-D structure, composition, and surface morphology of the multimetallic nanotubes.

References

1. (a) Winter, M.; Brodd, R. J., What Are Batteries, Fuel Cells, and Supercapacitors? *Chemical Reviews* **2004,** *104* (10), 4245-4270; (b) Guo, S.; Wang, E., Noble metal nanomaterials: Controllable synthesis and application in fuel cells and analytical sensors. *Nano Today* **2011,** *6* (3), 240-264.

2. Cohen, J. L.; Volpe, D. J.; Abruna, H. D., Electrochemical determination of activation energies for methanol oxidation on polycrystalline platinum in acidic and alkaline electrolytes. *Physical Chemistry Chemical Physics* **2007,** *9* (1), 49-77.

3. Dimitratos, N.; Villa, A.; Wang, D.; Porta, F.; Su, D.; Prati, L., Pd and Pt catalysts modified by alloying with Au in the selective oxidation of alcohols. *Journal of Catalysis* **2006,** *244* (1), 113-121.

4. Xu, D.; Liu, Z.; Yang, H.; Liu, Q.; Zhang, J.; Fang, J.; Zou, S.; Sun, K., Solution-Based Evolution and Enhanced Methanol Oxidation Activity of Monodisperse Platinum–Copper Nanocubes. *Angewandte Chemie International Edition* **2009,** *48* (23), 4217-4221.

5. Rossmeisl, J.; Ferrin, P.; Tritsaris, G. A.; Nilekar, A. U.; Koh, S.; Bae, S. E.; Brankovic, S. R.; Strasser, P.; Mavrikakis, M., Bifunctional anode catalysts for direct methanol fuel cells. *Energy & Environmental Science* **2012,** *5* (8), 8335-8342.

6. Lim, B.; Yu, T.; Xia, Y., Shaping a Bright Future for Platinum-Based Alloy Electrocatalysts. *Angewandte Chemie International Edition* **2010,** *49* (51), 9819-9820.

7. Xia, B. Y.; Wu, H. B.; Wang, X.; Lou, X. W., One-Pot Synthesis of Cubic PtCu3 Nanocages with Enhanced Electrocatalytic Activity for the Methanol Oxidation Reaction. *Journal of the American Chemical Society* **2012,** *134* (34), 13934-13937.

8. Yang, R.; Leisch, J.; Strasser, P.; Toney, M. F., Structure of Dealloyed PtCu3 Thin Films and Catalytic Activity for Oxygen Reduction. *Chemistry of Materials* **2010,** *22* (16), 4712-4720.

9. Suntivich, J.; Xu, Z.; Carlton, C. E.; Kim, J.; Han, B.; Lee, S. W.; Bonnet, N.; Marzari, N.; Allard, L. F.; Gasteiger, H. A.; Hamad-Schifferli, K.; Shao-Horn, Y., Surface Composition Tuning of Au–Pt Bimetallic Nanoparticles for Enhanced Carbon Monoxide and Methanol Electro-oxidation. *Journal of the American Chemical Society* **2013,** *135* (21), 7985-7991.

10. Wang, D.; Yu, Y.; Xin, H. L.; Hovden, R.; Ercius, P.; Mundy, J. A.; Chen, H.; Richard, J. H.; Muller, D. A.; DiSalvo, F. J.; Abruña, H. D., Tuning Oxygen Reduction Reaction Activity via Controllable Dealloying: A Model Study of Ordered Cu3Pt/C Intermetallic Nanocatalysts. *Nano Letters* **2012,** *12* (10), 5230-5238.

11. Sun, Y.; Xia, Y., Alloying and Dealloying Processes Involved in the Preparation of Metal Nanoshells through a Galvanic Replacement Reaction. *Nano Letters* **2003,** *3* (11), 1569-1572.

12. Guo, S.; Zhang, S.; Sun, X.; Sun, S., Synthesis of Ultrathin FePtPd Nanowires and Their Use as Catalysts for Methanol Oxidation Reaction. *Journal of the American Chemical Society* **2011,** *133* (39), 15354-15357.

13. Quan, Z.; Wang, Y.; Fang, J., High-Index Faceted Noble Metal Nanocrystals. *Accounts of Chemical Research* **2012,** *46* (2), 191-202.

14. Tian, N.; Xiao, J.; Zhou, Z.-Y.; Liu, H.; Deng, Y.-J.; Huang, L.; Xu, B.; Sun, S.-G., Pt-group bimetallic nanocrystals with high-index facets as high performance electrocatalysts. *Faraday Discussions* **2013**.

15. Langille, M. R.; Personick, M. L.; Zhang, J.; Mirkin, C. A., Defining Rules for the Shape Evolution of Gold Nanoparticles. *Journal of the American Chemical Society* **2012,** *134* (35), 14542-14554.

16. Lohse, S. E.; Burrows, N. D.; Scarabelli, L.; Liz-Marzán, L. M.; Murphy, C. J., Anisotropic Noble Metal Nanocrystal Growth: The Role of Halides. *Chemistry of Materials* **2014,** *26* (1), 34-43.

17. Antolini, E., Catalysts for direct ethanol fuel cells. *Journal of Power Sources* **2007,** *170* (1), 1-12.

18. Kakati, N.; Maiti, J.; Lee, S. H.; Jee, S. H.; Viswanathan, B.; Yoon, Y. S., Anode Catalysts for Direct Methanol Fuel Cells in Acidic Media: Do We Have Any Alternative for Pt or Pt–Ru? *Chemical Reviews* **2014,** *114* (24), 12397-12429.

19. Mallat, T.; Baiker, A., Oxidation of Alcohols with Molecular Oxygen on Solid Catalysts. *Chemical Reviews* **2004,** *104* (6), 3037-3058.

20. Li, W.; Wang, A.; Liu, X.; Zhang, T., Silica-supported Au–Cu alloy nanoparticles as an efficient catalyst for selective oxidation of alcohols. *Applied Catalysis A: General* **2012,** *433–434* (0), 146-151.

21. Mavrikakis, M.; Hammer, B.; Nørskov, J. K., Effect of Strain on the Reactivity of Metal Surfaces. *Physical Review Letters* **1998,** *81* (13), 2819-2822.

22. Wang, H.; Chen, S.; Wang, C.; Zhang, K.; Liu, D.; Haleem, Y. A.; Zheng, X.; Ge, B.; Song, L., Role of Ru Oxidation Degree for Catalytic Activity in Bimetallic Pt/Ru Nanoparticles. *The Journal of Physical Chemistry C* **2016,** *120* (12), 6569-6576.

23. Chen, Y. X.; Miki, A.; Ye, S.; Sakai, H.; Osawa, M., Formate, an Active Intermediate for Direct Oxidation of Methanol on Pt Electrode. *Journal of the American Chemical Society* **2003,** *125* (13), 3680-3681.

24. (a) Camara, G. A.; de Lima, R. B.; Iwasita, T., Catalysis of ethanol electrooxidation by PtRu: the influence of catalyst composition. *Electrochemistry Communications* **2004,** *6* (8), 812-

815; (b) Lim, B.; Jiang, M.; Camargo, P. H. C.; Cho, E. C.; Tao, J.; Lu, X.; Zhu, Y.; Xia, Y., Pd-Pt Bimetallic Nanodendrites with High Activity for Oxygen Reduction. *Science* **2009,** *324* (5932), 1302-1305.

25. Tritsaris, G. A.; Rossmeisl, J., Methanol Oxidation on Model Elemental and Bimetallic Transition Metal Surfaces. *The Journal of Physical Chemistry C* **2012,** *116* (22), 11980-11986.

26. (a) Marković, N. M.; Gasteiger, H. A.; Ross, P. N.; Jiang, X.; Villegas, I.; Weaver, M. J., Electro-oxidation mechanisms of methanol and formic acid on Pt-Ru alloy surfaces. *Electrochimica Acta* **1995,** *40* (1), 91-98; (b) Marković, N. M.; Gasteiger, H. A.; Ross, P. N.; Jiang, X.; Villegas, I.; Weaver, M. J., Surface Structure and Electrochemical ReactivityElectro-oxidation mechanisms of methanol and formic acid on Pt-Ru alloy surfaces. *Electrochimica Acta* **1995,** *40* (1), 91-98.

27. (a) Ávila-García, I.; Plata-Torres, M.; Domínguez-Crespo, M. A.; Ramírez-Rodríguez, C.; Arce-Estrada, E. M., Electrochemical study of Pt–Pd, Pt–Ru, Pt–Rh and Pt–Sn/C in acid media for hydrogen adsorption–desorption reaction. *Journal of Alloys and Compounds* **2007,** *434–435*, 764-767; (b) Wiltshire, R. J. K.; King, C. R.; Rose, A.; Wells, P. P.; Davies, H.; Hogarth, M. P.; Thompsett, D.; Theobald, B.; Mosselmans, F. W.; Roberts, M.; Russell, A. E., Effects of composition on structure and activity of PtRu/C catalysts. *Physical Chemistry Chemical Physics* **2009,** *11* (13), 2305-2313; (c) Poh, C. K.; Tian, Z.; Gao, J.; Liu, Z.; Lin, J.; Feng, Y. P.; Su, F., Nanostructured trimetallic Pt/FeRuC, Pt/NiRuC, and Pt/CoRuC catalysts for methanol electrooxidation. *Journal of Materials Chemistry* **2012,** *22* (27), 13643-13652.

28. (a) Stamenkovic, V. R.; Mun, B. S.; Mayrhofer, K. J. J.; Ross, P. N.; Markovic, N. M., Effect of Surface Composition on Electronic Structure, Stability, and Electrocatalytic Properties of Pt-Transition Metal Alloys: Pt-Skin versus Pt-Skeleton Surfaces. *Journal of the American Chemical Society* **2006,** *128* (27), 8813-8819; (b) Yuan, Q.; Huang, D.-B.; Wang, H.-H.; Zhou, Z.-Y., RhPt Flowerlike Bimetallic Nanocrystals with Tunable Composition as Superior Electrocatalysts for Methanol Oxidation. *Langmuir* **2014,** *30* (20), 5711-5715.

29. (a) Wanjala, B. N.; Fang, B.; Luo, J.; Chen, Y.; Yin, J.; Engelhard, M. H.; Loukrakpam, R.; Zhong, C.-J., Correlation between Atomic Coordination Structure and Enhanced Electrocatalytic Activity for Trimetallic Alloy Catalysts. *Journal of the American Chemical Society* **2011,** *133* (32), 12714-12727; (b) Sun, X.; Li, D.; Ding, Y.; Zhu, W.; Guo, S.; Wang, Z. L.; Sun, S., Core/Shell Au/CuPt Nanoparticles and Their Dual Electrocatalysis for Both Reduction and Oxidation Reactions. *Journal of the American Chemical Society* **2014,** *136* (15), 5745-5749.

30. (a) Wang, D.; Li, Y., Bimetallic nanocrystals: liquid-phase synthesis and catalytic applications. *Advanced Materials* **2011,** *23* (9), 1044-1060; (b) Zhang, H.; Jin, M.; Xia, Y., Enhancing the catalytic and electrocatalytic properties of Pt-based catalysts by forming bimetallic nanocrystals with Pd. *Chemical Society Reviews* **2012,** *41* (24), 8035-8049; (c) Wu, J.; Yang, H., Platinum-based oxygen reduction electrocatalysts. *Accounts of chemical research* **2013,** *46* (8), 1848-1857; (d) Weiner, R. G.; Kunz, M. R.; Skrabalak, S. E., Seeding a new kind of garden: synthesis of architecturally defined multimetallic nanostructures by seed-mediated co-

reduction. *Accounts of chemical research* **2015,** *48* (10), 2688-2695; (e) Gilroy, K. D.; Ruditskiy, A.; Peng, H.-C.; Qin, D.; Xia, Y., Bimetallic nanocrystals: syntheses, properties, and applications. *Chemical Reviews* **2016,** *116* (18), 10414-10472.

31. (a) Chrzanowski, W.; Wieckowski, A., Surface Structure Effects in Platinum/Ruthenium Methanol Oxidation Electrocatalysis. *Langmuir* **1998,** *14* (8), 1967-1970; (b) Zhou, Z.-Y.; Huang, Z.-Z.; Chen, D.-J.; Wang, Q.; Tian, N.; Sun, S.-G., High-Index Faceted Platinum Nanocrystals Supported on Carbon Black as Highly Efficient Catalysts for Ethanol Electrooxidation. *Angewandte Chemie International Edition* **2010,** *49* (2), 411-414.

32. (a) Lee, S. W.; Chen, S.; Sheng, W.; Yabuuchi, N.; Kim, Y.-T.; Mitani, T.; Vescovo, E.; Shao-Horn, Y., Roles of Surface Steps on Pt Nanoparticles in Electro-oxidation of Carbon Monoxide and Methanol. *Journal of the American Chemical Society* **2009,** *131* (43), 15669-15677; (b) Zheng, J.; Cullen, D. A.; Forest, R. V.; Wittkopf, J. A.; Zhuang, Z.; Sheng, W.; Chen, J. G.; Yan, Y., Platinum–Ruthenium Nanotubes and Platinum–Ruthenium Coated Copper Nanowires As Efficient Catalysts for Electro-Oxidation of Methanol. *ACS Catalysis* **2015,** *5* (3), 1468-1474.

33. (a) Chen, S.; Si, R.; Taylor, E.; Janzen, J.; Chen, J., Synthesis of Pd/Fe3O4 Hybrid Nanocatalysts with Controllable Interface and Enhanced Catalytic Activities for CO Oxidation. *The Journal of Physical Chemistry C* **2012,** *116* (23), 12969-12976; (b) Taylor, E.; Chen, S.; Tao, J.; Wu, L.; Zhu, Y.; Chen, J., Synthesis of Pt–Cu Nanodendrites through Controlled Reduction Kinetics for Enhanced Methanol Electro-Oxidation. *ChemSusChem* **2013,** *6* (10), 1863-1867; (c) Xu, D.; Bliznakov, S.; Liu, Z.; Fang, J.; Dimitrov, N., Composition-Dependent Electrocatalytic Activity of Pt-Cu Nanocube Catalysts for Formic Acid Oxidation. *Angewandte Chemie International Edition* **2010,** *49* (7), 1282-1285.

34. (a) Xu, D.; Liu, Z.; Yang, H.; Liu, Q.; Zhang, J.; Fang, J.; Zou, S.; Sun, K., Solution-Based Evolution and Enhanced Methanol Oxidation Activity of Monodisperse Platinum–Copper Nanocubes. *Angewandte Chemie International Edition* **2009,** *48* (23), 4217-4221; (b) Yin, A. X.; Min, X. Q.; Zhu, W.; Liu, W. C.; Zhang, Y. W.; Yan, C. H., Pt □ Cu and Pt□ P Nanocubes with High-Index Facets and Superior Electrocatalytic Activity. *Chemistry–A European Journal* **2012,** *18* (3), 777-782; (c) Qi, Y.; Bian, T.; Choi, S.-I.; Jiang, Y.; Jin, C.; Fu, M.; Zhang, H.; Yang, D., Kinetically controlled synthesis of Pt–Cu alloy concave nanocubes with high-index facets for methanol electro-oxidation. *Chemical Communications* **2014,** *50* (5), 560-562.

35. (a) Nosheen, F.; Zhang, Z.-c.; Zhuang, J.; Wang, X., One-pot fabrication of single-crystalline octahedral Pt–Cu nanoframes and their enhanced electrocatalytic activity. *Nanoscale* **2013,** *5* (9), 3660-3663; (b) Zhang, Z.; Luo, Z.; Chen, B.; Wei, C.; Zhao, J.; Chen, J.; Zhang, X.; Lai, Z.; Fan, Z.; Tan, C., One-Pot Synthesis of Highly Anisotropic Five-Fold-Twinned PtCu Nanoframes Used as a Bifunctional Electrocatalyst for Oxygen Reduction and Methanol Oxidation. *Advanced Materials* **2016,** *28* (39), 8712-8717.

36. (a) Liu, X.; Wang, W.; Li, H.; Li, L.; Zhou, G.; Yu, R.; Wang, D.; Li, Y., One-pot protocol for bimetallic Pt/Cu hexapod concave nanocrystals with enhanced electrocatalytic

activity. *Scientific reports* **2013,** *3*; (b) Xiong, Y.; Ma, Y.; Lin, Z.; Xu, Q.; Yan, Y.; Zhang, H.; Wu, J.; Yang, D., Facile synthesis of PtCu 3 alloy hexapods and hollow nanoframes as highly active electrocatalysts for methanol oxidation. *CrystEngComm* **2016,** *18* (40), 7823-7830.

37. (a) Taylor, E.; Chen, S.; Tao, J.; Wu, L.; Zhu, Y.; Chen, J., Synthesis of Pt–Cu Nanodendrites through Controlled Reduction Kinetics for Enhanced Methanol Electro-Oxidation. *ChemSusChem* **2013,** *6* (10), 1863-1867; (b) Cao, Y.; Yang, Y.; Shan, Y.; Huang, Z., One-Pot and Facile Fabrication of Hierarchical Branched Pt–Cu Nanoparticles as Excellent Electrocatalysts for Direct Methanol Fuel Cells. *ACS applied materials & interfaces* **2016,** *8* (9), 5998-6003.

38. (a) Lim, B.; Jiang, M.; Camargo, P. H.; Cho, E. C.; Tao, J.; Lu, X.; Zhu, Y.; Xia, Y., Pd-Pt bimetallic nanodendrites with high activity for oxygen reduction. *Science* **2009,** *324* (5932), 1302-1305; (b) Wang, L.; Nemoto, Y.; Yamauchi, Y., Direct synthesis of spatially-controlled Pt-on-Pd bimetallic nanodendrites with superior electrocatalytic activity. *Journal of the American Chemical Society* **2011,** *133* (25), 9674-9677; (c) Wang, W.; Wang, D.; Liu, X.; Peng, Q.; Li, Y., Pt–Ni nanodendrites with high hydrogenation activity. *Chemical Communications* **2013,** *49* (28), 2903-2905.

39. (a) Chen, C.; Kang, Y.; Huo, Z.; Zhu, Z.; Huang, W.; Xin, H. L.; Snyder, J. D.; Li, D.; Herron, J. A.; Mavrikakis, M.; Chi, M.; More, K. L.; Li, Y.; Markovic, N. M.; Somorjai, G. A.; Yang, P.; Stamenkovic, V. R., Highly Crystalline Multimetallic Nanoframes with Three-Dimensional Electrocatalytic Surfaces. *Science* **2014,** *343* (6177), 1339; (b) Guo, S.; Fang, Y.; Dong, S.; Wang, E., High-Efficiency and Low-Cost Hybrid Nanomaterial as Enhancing Electrocatalyst: Spongelike Au/Pt Core/Shell Nanomaterial with Hollow Cavity. *The Journal of Physical Chemistry C* **2007,** *111* (45), 17104-17109; (c) You, H.; Zhang, F.; Liu, Z.; Fang, J., Free-Standing Pt–Au Hollow Nanourchins with Enhanced Activity and Stability for Catalytic Methanol Oxidation. *ACS Catalysis* **2014,** *4* (9), 2829-2835.

40. (a) Zeng, J.; Zhang, Q.; Chen, J.; Xia, Y., A comparison study of the catalytic properties of Au-based nanocages, nanoboxes, and nanoparticles. *Nano letters* **2009,** *10* (1), 30-35; (b) Chen, C.; Kang, Y.; Huo, Z.; Zhu, Z.; Huang, W.; Xin, H. L.; Snyder, J. D.; Li, D.; Herron, J. A.; Mavrikakis, M., Highly crystalline multimetallic nanoframes with three-dimensional electrocatalytic surfaces. *Science* **2014,** *343* (6177), 1339-1343; (c) Li, J.; Sun, X.; Qin, D., Ag-Enriched Ag-Pd Bimetallic Nanoframes and Their Catalytic Properties. *ChemNanoMat* **2016,** *2* (6), 494-499; (d) Luo, S.; Shen, P. K., Concave Platinum–Copper Octopod Nanoframes Bounded with Multiple High-Index Facets for Efficient Electrooxidation Catalysis. *ACS Nano* **2016**; (e) Becknell, N.; Zheng, C.; Chen, C.; Yu, Y.; Yang, P., Synthesis of PtCo3 polyhedral nanoparticles and evolution to Pt3Co nanoframes. *Surface Science* **2016,** *648*, 328-332; (f) Fang, Z.; Wang, Y.; Liu, C.; Chen, S.; Sang, W.; Wang, C.; Zeng, J., Rational design of metal nanoframes for catalysis and plasmonics. *Small* **2015,** *11* (22), 2593-2605.

41. Lou, Y.; Li, C.; Gao, X.; Bai, T.; Chen, C.; Huang, H.; Liang, C.; Shi, Z.; Feng, S., Porous Pt Nanotubes with High Methanol Oxidation Electrocatalytic Activity Based on Original Bamboo-Shaped Te Nanotubes. *ACS Applied Materials & Interfaces* **2016,** *8* (25), 16147-16153.

42. Lee, H.-Y.; Vogel, W.; Chu, P. P.-J., Nanostructure and Surface Composition of Pt and Ru Binary Catalysts on Polyaniline-Functionalized Carbon Nanotubes. *Langmuir* **2011,** *27* (23), 14654-14661.

43. Lin, Y.; Cui, X.; Yen, C. H.; Wai, C. M., PtRu/Carbon Nanotube Nanocomposite Synthesized in Supercritical Fluid: A Novel Electrocatalyst for Direct Methanol Fuel Cells. *Langmuir* **2005,** *21* (24), 11474-11479.

44. Saleem, F.; Zhang, Z.; Xu, B.; Xu, X.; He, P.; Wang, X., Ultrathin Pt–Cu Nanosheets and Nanocones. *Journal of the American Chemical Society* **2013,** *135* (49), 18304-18307.

45. Lignier, P.; Bellabarba, R.; Tooze, R. P., Scalable strategies for the synthesis of well-defined copper metal and oxide nanocrystals. *Chemical Society Reviews* **2012,** *41* (5), 1708-1720.

46. (a) Mott, D.; Galkowski, J.; Wang, L.; Luo, J.; Zhong, C. J., Synthesis of size-controlled and shaped copper nanoparticles. *Langmuir : the ACS journal of surfaces and colloids* **2007,** *23* (10), 5740-5745; (b) Nam, K. M.; Shim, J. H.; Ki, H.; Choi, S.-I.; Lee, G.; Jang, J. K.; Jo, Y.; Jung, M.-H.; Song, H.; Park, J. T., Single-Crystalline Hollow Face-Centered-Cubic Cobalt Nanoparticles from Solid Face-Centered-Cubic Cobalt Oxide Nanoparticles. *Angewandte Chemie International Edition* **2008,** *47* (49), 9504-9508; (c) Mourdikoudis, S.; Liz-Marzán, L. M., Oleylamine in Nanoparticle Synthesis. *Chemistry of Materials* **2013,** *25* (9), 1465-1476.

47. (a) Xia, Y.; Xiong, Y.; Lim, B.; Skrabalak, S. E., Shape-Controlled Synthesis of Metal Nanocrystals: Simple Chemistry Meets Complex Physics? *Angewandte Chemie International Edition* **2009,** *48* (1), 60-103; (b) Zeng, J.; Zheng, Y.; Rycenga, M.; Tao, J.; Li, Z.-Y.; Zhang, Q.; Zhu, Y.; Xia, Y., Controlling the Shapes of Silver Nanocrystals with Different Capping Agents. *Journal of the American Chemical Society* **2010,** *132* (25), 8552-8553.

48. (a) Wang, Y.; Xie, S.; Liu, J.; Park, J.; Huang, C. Z.; Xia, Y., Shape-Controlled Synthesis of Palladium Nanocrystals: A Mechanistic Understanding of the Evolution from Octahedrons to Tetrahedrons. *Nano Letters* **2013,** *13* (5), 2276-2281; (b) Bachman, R. E.; Fioritto, M. S.; Fetics, S. K.; Cocker, T. M., The Structural and Functional Equivalence of Aurophilic and Hydrogen Bonding: Evidence for the First Examples of Rotator Phases Induced by Aurophilic Bonding. *Journal of the American Chemical Society* **2001,** *123* (22), 5376-5377.

49. Lim, B.; Xia, Y., Metal Nanocrystals with Highly Branched Morphologies. *Angewandte Chemie International Edition* **2011,** *50* (1), 76-85.

50. Lu, X.; Yavuz, M. S.; Tuan, H.-Y.; Korgel, B. A.; Xia, Y., Ultrathin Gold Nanowires Can Be Obtained by Reducing Polymeric Strands of Oleylamine−AuCl Complexes Formed via Aurophilic Interaction. *Journal of the American Chemical Society* **2008,** *130* (28), 8900-8901.

51. Zhang, J.; Langille, M. R.; Personick, M. L.; Zhang, K.; Li, S.; Mirkin, C. A., Concave Cubic Gold Nanocrystals with High-Index Facets. *Journal of the American Chemical Society* **2010,** *132* (40), 14012-14014.

52. (a) Xiong, Y.; McLellan, J. M.; Chen, J.; Yin, Y.; Li, Z.-Y.; Xia, Y., Kinetically Controlled Synthesis of Triangular and Hexagonal Nanoplates of Palladium and Their SPR/SERS Properties. *Journal of the American Chemical Society* **2005,** *127* (48), 17118-17127; (b) Wiley, B.; Sun, Y.; Xia, Y., Synthesis of Silver Nanostructures with Controlled Shapes and Properties. *Accounts of Chemical Research* **2007,** *40* (10), 1067-1076.

53. (a) Chen, L.; Ji, F.; Xu, Y.; He, L.; Mi, Y.; Bao, F.; Sun, B.; Zhang, X.; Zhang, Q., High-Yield Seedless Synthesis of Triangular Gold Nanoplates through Oxidative Etching. *Nano Letters* **2014,** *14* (12), 7201-7206; (b) Zhang, Q.; Yang, Y.; Li, J.; Iurilli, R.; Xie, S.; Qin, D., Citrate-Free Synthesis of Silver Nanoplates and the Mechanistic Study. *ACS Applied Materials & Interfaces* **2013,** *5* (13), 6333-6345.

54. Bower, M. M.; DeSantis, C. J.; Skrabalak, S. E., A Quantitative Analysis of Anions and pH on the Growth of Bimetallic Nanostructures. *The Journal of Physical Chemistry C* **2014,** *118* (32), 18762-18770.

55. Personick, M. L.; Langille, M. R.; Zhang, J.; Harris, N.; Schatz, G. C.; Mirkin, C. A., Synthesis and Isolation of {110}-Faceted Gold Bipyramids and Rhombic Dodecahedra. *Journal of the American Chemical Society* **2011,** *133* (16), 6170-6173.

56. Garg, N.; Scholl, C.; Mohanty, A.; Jin, R., The Role of Bromide Ions in Seeding Growth of Au Nanorods. *Langmuir* **2010,** *26* (12), 10271-10276.

57. Darugar, Q.; Qian, W.; El-Sayed, M. A.; Pileni, M.-P., Size-Dependent Ultrafast Electronic Energy Relaxation and Enhanced Fluorescence of Copper Nanoparticles. *The Journal of Physical Chemistry B* **2005,** *110* (1), 143-149.

58. (a) Yang, H.-J.; He, S.-Y.; Chen, H.-L.; Tuan, H.-Y., Monodisperse Copper Nanocubes: Synthesis, Self-Assembly, and Large-Area Dense-Packed Films. *Chemistry of Materials* **2014,** *26* (5), 1785-1793; (b) Kuo, C.-H.; Huang, M. H., Fabrication of Truncated Rhombic Dodecahedral Cu2O Nanocages and Nanoframes by Particle Aggregation and Acidic Etching. *Journal of the American Chemical Society* **2008,** *130* (38), 12815-12820.

59. (a) Hua, Q.; Chen, K.; Chang, S.; Ma, Y.; Huang, W., Crystal Plane-Dependent Compositional and Structural Evolution of Uniform Cu2O Nanocrystals in Aqueous Ammonia Solutions. *The Journal of Physical Chemistry C* **2011,** *115* (42), 20618-20627; (b) Hua, Q.; Shang, D.; Zhang, W.; Chen, K.; Chang, S.; Ma, Y.; Jiang, Z.; Yang, J.; Huang, W., Morphological Evolution of Cu2O Nanocrystals in an Acid Solution: Stability of Different Crystal Planes. *Langmuir* **2010,** *27* (2), 665-671; (c) Salzemann, C.; Lisiecki, I.; Urban, J.; Pileni, M. P., Anisotropic Copper Nanocrystals Synthesized in a Supersaturated Medium: Nanocrystal Growth. *Langmuir* **2004,** *20* (26), 11772-11777.

60. (a) Siegfried, M. J.; Choi, K.-S., Elucidating the Effect of Additives on the Growth and Stability of Cu2O Surfaces via Shape Transformation of Pre-Grown Crystals. *Journal of the American Chemical Society* **2006,** *128* (32), 10356-10357; (b) Hung, L.-I.; Tsung, C.-K.; Huang,

W.; Yang, P., Room-Temperature Formation of Hollow Cu2O Nanoparticles. *Advanced Materials* **2010,** *22* (17), 1910-1914.

61. Filankembo, A.; Giorgio, S.; Lisiecki, I.; Pileni, M. P., Is the Anion the Major Parameter in the Shape Control of Nanocrystals? *The Journal of Physical Chemistry B* **2003,** *107* (30), 7492-7500.

62. Salzemann, C.; Urban, J.; Lisiecki, I.; Pileni, M. P., Characterization and Growth Process of Copper Nanodisks. *Advanced Functional Materials* **2005,** *15* (8), 1277-1284.

63. Pileni, M. P., Control of the Size and Shape of Inorganic Nanocrystals at Various Scales from Nano to Macrodomains. *The Journal of Physical Chemistry C* **2007,** *111* (26), 9019-9038.

64. (a) Hou, W.; Dehm, N. A.; Scott, R. W. J., Alcohol oxidations in aqueous solutions using Au, Pd, and bimetallic AuPd nanoparticle catalysts. *Journal of Catalysis* **2008,** *253* (1), 22-27; (b) Liu, X.; Wang, A.; Zhang, T.; Su, D.-S.; Mou, C.-Y., Au–Cu alloy nanoparticles supported on silica gel as catalyst for CO oxidation: Effects of Au/Cu ratios. *Catalysis Today* **2011,** *160* (1), 103-108; (c) Koh, S.; Strasser, P., Electrocatalysis on Bimetallic Surfaces: Modifying Catalytic Reactivity for Oxygen Reduction by Voltammetric Surface Dealloying. *Journal of the American Chemical Society* **2007,** *129* (42), 12624-12625.

65. Sun, Y.; Xia, Y., Mechanistic Study on the Replacement Reaction between Silver Nanostructures and Chloroauric Acid in Aqueous Medium. *Journal of the American Chemical Society* **2004,** *126* (12), 3892-3901.

66. (a) Chen, J.; McLellan, J. M.; Siekkinen, A.; Xiong, Y.; Li, Z.-Y.; Xia, Y., Facile Synthesis of Gold−Silver Nanocages with Controllable Pores on the Surface. *Journal of the American Chemical Society* **2006,** *128* (46), 14776-14777; (b) Lu, X.; Chen, J.; Skrabalak, S. E.; Xia, Y., Galvanic replacement reaction: a simple and powerful route to hollow and porous metal nanostructures. *Proc. IMechE* **2007,** *221*, 1-16.

67. Xu, C.; Liu, Y.; Wang, J.; Geng, H.; Qiu, H., Fabrication of nanoporous Cu–Pt(Pd) core/shell structure by galvanic replacement and its application in electrocatalysis. *ACS Applied Materials & Interfaces* **2011,** *3* (12), 4626-4632.

68. González, E.; Arbiol, J.; Puntes, V. F., Carving at the Nanoscale: Sequential Galvanic Exchange and Kirkendall Growth at Room Temperature. *Science* **2011,** *334* (6061), 1377-1380.

69. Lim, B.; Kobayashi, H.; Yu, T.; Wang, J.; Kim, M. J.; Li, Z.-Y.; Rycenga, M.; Xia, Y., Synthesis of Pd−Au Bimetallic Nanocrystals via Controlled Overgrowth. *Journal of the American Chemical Society* **2010,** *132* (8), 2506-2507.

70. (a) Yin, Y.; Rioux, R. M.; Erdonmez, C. K.; Hughes, S.; Somorjai, G. A.; Alivisatos, A. P., Formation of Hollow Nanocrystals Through the Nanoscale Kirkendall Effect. *Science* **2004,** *304* (5671), 711-714; (b) Liu, B.; Zeng, H. C., Fabrication of ZnO "Dandelions" via a Modified Kirkendall Process. *Journal of the American Chemical Society* **2004,** *126* (51), 16744-16746.

71. (a) DeSantis, C. J.; Peverly, A. A.; Peters, D. G.; Skrabalak, S. E., Octopods versus Concave Nanocrystals: Control of Morphology by Manipulating the Kinetics of Seeded Growth via Co-Reduction. *Nano Letters* **2011,** *11* (5), 2164-2168; (b) Zeng, J.; Zhu, C.; Tao, J.; Jin, M.; Zhang, H.; Li, Z.-Y.; Zhu, Y.; Xia, Y., Controlling the Nucleation and Growth of Silver on Palladium Nanocubes by Manipulating the Reaction Kinetics. *Angewandte Chemie International Edition* **2012,** *51* (10), 2354-2358.

72. Chen, S.; Jenkins, S. V.; Tao, J.; Zhu, Y.; Chen, J., Anisotropic Seeded Growth of Cu–M (M = Au, Pt, or Pd) Bimetallic Nanorods with Tunable Optical and Catalytic Properties. *The Journal of Physical Chemistry C* **2013,** *117* (17), 8924-8932.

Chapter II. Morphology Control of Copper Nanomaterials & the Influence of Halides on Nanomaterial Growth

2.1. Abstract:

Copper nanomaterials (Cu NM) with specific surface facets can tailor their chemical and physical properties. Understanding reagents responsible for Cu NM growth is important for morphology-controlled synthesis of the nanostructures. This work studies the halide influence on Cu NM growth and morphology in an oil-based synthesis. The morphology of the Cu NM varies with the halide type (i.e., Cl^-, Br^-, I^-), and the halide concentration. By varying the molar ratio of copper (II) acetylacetonate ($Cu(acac)_2$) and $CuCl_2$, Cu nanoparticles, Cu rhombic dodecahedra, Cu nanowires, and Cu nanoplates were obtained. Further study of chloride influence on Cu NM growth was completed by switching $CuCl_2$ with CTAC and TBAC as external chloride sources. The morphologies remain the same as those resulting from $CuCl_2$, suggesting Cl^- is responsible for the shape-controlled synthesis of Cu NM. For $Cu(acac)_2$ and $CuBr_2$, different molar ratios yielded Cu nanospheres, Cu nanopyramides, Cu nanooctahedra, and Cu nanoplates.

Additional studies over the bromide influence on Cu NM were completed by replacing $CuBr_2$ with CTAB and TBAB as external chloride sources. The morphologies remain the same as those resulting from $CuBr_2$, suggesting Br^- plays an important role for this shape-controlled synthesis of Cu.$Cu(acac)_2$ and TBAI were combined to determine the influence of idodine, and the primary products were circular and hexagonal Cu nanoplates. These studies demonstrated that halides (Cl-, Br-, I-) can be utilized as additives in oil phase synthesis for shape-controlled synthesis of Cu NM.

2.2. **Introduction:**

Copper nanomaterials have applications in catalysis, electrocatalysis, photocatalysis SERS, and optical imaging.[1] Copper nanomaterials with specific morphologies and surface facets can tailor their chemical, physical, and optical properties. Understanding the additives responsible for Cu nanomaterial growth is important to develop methods for shape-controlled synthesis of the Cu nanostructures. Bottom-up solution-based methods have been developed for synthesis of Cu nanoparticles; however, a systematically study of oil-phase shape-controlled synthesis has not yet been completed.[2] This research develops oil-based syntheses in which the Cu precursors were reduced by aliphatic amines in the presence of halides. Different reaction conditions were studied to determine the particular the role of halides for the morphology control of Cu nanostructures.

Halides have proven to control the growth of noble metals with distinct morphologies including nanocubes, nano-rhombic dodecahedra, nanoplates, nanopyraminds, nano-bipyramids, and nanowires.[1b, 3] For example, Murphy and co-workers reported that halides in the reaction solution can influence morphology as well as size.[4] Mirkin and co-workers reported the influence of halides and silver ions on seed-mediated synthesis of Au nanostructures including reduction kinetics, the under deposition potential, and synergistic effects.[5,6] It was found that halides bind to the Au surface with different strength depending on the types (Cl^-, Br^-, or I^-), which can then inhibit the nanomaterial growth.[5] Additionally, different morphologies could be obtained by altering the concentration of the various halides (Cl^- and Br^-).[5] A study reported that the Cl^- (CTAC) or Br^- (CTAB) could selectively binding to facets, resulting in concave or convex nanocubes, respectively. Another study reported that Br^- could influence the aspect ratio of Au NRs and protects the {111} and {100} surface facets, while promoting growth in the [110] direction.[7] Chloride has also been used as an oxidative etchant in order to achieve shape-

controlled synthesis for Ag and Pd.[8] The halide influence on facet selectivity shapecontrolled synthesis can also extend to bimetallic nanomaterials.[9] Shape-controlled synthesis of Cu is more challenging than noble metals because of their high reactivity.The growth processes for copper nanomaterials function similarly to noble metal nanomaterials. Forming uniform copper nanomaterials has proven to be more challenging than the noble metal nanomaterials, which could be due to the strength of the capping ligands on noble metal nanomaterials as opposed to coinage metals.[10] Research has been completed to from Cu nanospheres, nanowires, nanoplates, and nanodendrites.[11] Different morphologies could be synthetically tailored through capping ligands, reduction kinetics, pH, and other reaction parameters.[12] The morphology of Cu nanoparticles are challenging to maintain due to oxidation; once Cu NM are exposed to atmosphere solid particles will become hollow.[11b, 13, 11b, 13] In order to increase the stability of the Cu nanostructures, this research's syntheses were performed in organic phase under an inert atmosphere. The halides were used to control the shape of the resulting Cu nanostructures. Few studies have been reported on the halide influence of Cu nanoparticle growth and the resulting morphologies. Pileni et. al. studied the synthesis of Cu nanoparticles with the micelle method in the presence of various halides.[14] It was found that the size of the nanoparticles varied with the reaction parameters.[15, 16] Among all the halides (NaCl, NaBr, NaF, NaI, $CuCl_2$, CTAC, and CTAB) studied, only Cl^- and Br^- had an impact on nanocrystal growth. It was determined that Cl^- selectively binds to the {111} and {100} depending on the halide concentration. Br^- selectively binds to the {111} facet resulting in the growth of nanoplates.[14]

This research studied the influence of halides on oil-based synthesis of Cu NM morphologies. The morphology of the Cu NM varies with the halide type (i.e., Cl^-, Br^-, I^-), and the halide concentration. The influence of Cl^- by varying the molar ratio of copper (II)

acetylacetonate ($Cu(acac)_2$) and $CuCl_2$, Cu nanoparticles (Cu NP), Cu rhombic dodecahedra (Cu NPH or Cu RDH), Cu nanowires (Cu NW), and Cu nanoplates (Cu NPL) were obtained. Exchanging $CuCl_2$ with an external source, CTAC and TBAC, formed Cu NM with the same morphologies as syntheses with $CuCl_2$. This suggests that Cl^- is responsible for this shape control in these Cu NM syntheses.

The influence of Br^- was investigated by combining $Cu(acac)_2$ and $CuBr_2$ at different molar ratios yielded Cu nanospheres, nanopyramides, nanooctahedra (Cu NO), and nanoplates. Replacing $CuBr_2$ with an external bromide source, CTAB and TBAB, the morphologies remain similar as those resulting from $CuBr_2$. This suggests that Br^- directs Cu NM growth in these shape-controlled syntheses.

The influence of iodine on oil-based Cu NM was investigated with $Cu(acac)_2$ and TBAI were used. The primary products were circular and hexagonal Cu nanoplates. Additionally, nanoplates were formed regardless of iodide concentration. . These studies demonstrated that halides (Cl-, Br-, I-) can be utilized as additives in oil phase synthesis for shape-controlled synthesis of Cu NM, in contrast to Cu NM formed in the absence of this shape directing additive.

2.3. **Part 1: Experimental Methods, $Cu(acac)_2$ as the Primary Copper Precursor**

Chemicals. Copper 2,4-pentanedionate ($Cu(acac)_2$, 98%), copper chloride ($CuCl_2$), copper (II) bromide ($CuBr_2$), dodecylamine (DDA, 98%), Cu (II) acetate ($Cu(ac)_2$, 98%), hexadecytrimetylammonium chloride (CTAC), hexadecyltrimetylammonium bromide (CTAB), and Tetrabutylammonium bromide (TBAB) were purchased from Alfa Aesar. Tetrabutylammounium chloride (TBAC) was purchased from TCI. All chemicals were used as received unless specified otherwise.

2.3.1. The influence of $CuCl_2$ (Synthesis set 1)

Different morphologies, including Cu NP, Cu NPH, Cu NW, Cu H-NPL, and Cu NP were obtained by the following $Cu(acac)_2$ to $CuCl_2$ precursor ratios including; 1:0, 1:0.5, 1:1, 1:1.5, and 0:1.

Synthesis of Cu nanoparticles (Cu NP): Cu NP were synthesized by reducing $Cu(acac)_2$ with DDA. $Cu(acac)_2$ (0.2 mmol, 52.5 mg) and DDA (5 g) were combined in a 25 mL three-neck round bottom flask equipped with astir bar. The solid mixture was degassed with Ar for 15 min to remove excess O_2 (g), and then gradually heated to 220 °C. The solid reactants began to melt at 27 °C and were completely liquid at 45 °C, as the solid mixture melted the stir rate is gradually increased to setting 5.5. The reaction solution generally heats to 220 °C within 10 minutes, during which the reaction solution color will change from teal to dark blue, to orange, and finally to metallic red. Once the reaction solution temperature reaches 220 °C, the temperature is held for 25 min. The reaction solution is quenched, purified, and prepared for characterization by the following method. Cu NP are removed from the flask, and placed in a 15 ml centrifuge with 2 ml ethanol. The tube was filled to 15 mL with ethanol, and the nanoparticles were separated out by centrifuge at 6,000 rpm for 4 min. The nanomaterials were purified by ethanol/toluene (1:10 v/v) mixture twice and Cu NP were redispersed in 2 ml of toluene for further characterization.

Synthesis of Cu rhombic dodecahedra (Cu NPH or Cu RDH): Cu RHD were formed in a similar procedure as the. Cu RDH were synthesized by using $Cu(acac)_2$ to $CuCl_2$ at a copper precursor ratio of 1 to 0.5. In a typical synthesis, DDA (5 g), $Cu(acac)_2$ (0.200 mmol, 52.5 mg), and $CuCl_2$ (0.098 mmol, 15.6 mg) were combined, degassed, and heated by a similar method to the Cu NP synthesis. During the temperature increase the color of reaction solution changed

from light blue to teal (25-45 ºC), dark green (120 ºC), yellow (160 ºC), orange (180 ºC), black (200 ºC), and greenish black (220). After 5 min at 220 ^{o}C, the reaction changes to reddish black and the reaction was kept at 220 ºC for 50 min. The same purification procedure and characterization method was used as that for Cu NP synthesis.

Synthesis of Cu nanowires (Cu NW): Cu NW were obtained by increasing the copper precursor ratio of 1:1, $Cu(acac)_2$ and $CuCl_2$. Cu NW are synthesized by reducing two copper precursors with an amine, with continual heating the reduced copper nucleated and formed into copper nanowires. The synthetic protocol is as follows: DDA (5 g), $Cu(acac)_2$ (0.2005 mmol, 0.525 g), and $CuCl_2$ (0.196 mmol 0.0264 g) are combined, degassed, and heated in a similar procedure was used as that for Cu NP. During the heating process, the color of the reaction solution changed from light blue to teal (25-45 ºC), dark green (120 ºC), yellow (160 ºC), orange (180 ºC), reddish (200 ºC), and metallic reddish-black (220 ºC), which took 10 min The reaction temperature was held at 220 ºC for 50 min, and then Cu NW were quenched and purified by the protocol described above.

Synthesis of hexagonal copper nanoplates (Cu hNPL) were synthesized by combining $Cu(acac)_2$ and $CuCl_2$ at a ratio of 1 to1.5. The Cu hNPL were synthesized by combining DDA (5.5 g), $Cu(acac)_2$ (0.200 mmol 0.525g), and $CuCl_2$ (0.301 mmol, 0.0430 g). The reaction mixture was degassed and heated in a method similar method to Cu NP. The reaction solution undergoes the following color change during the temperature increase: light blue (27 ºC), teal (32 ºC), dark blue (62 ºC), dark blue-green (110 ºC), dark green (133 ºC), lighter green (144 ºC), lime green (149 ºC), yellow (152 ºC), and the reaction remained yellow until 220 ºC was reached. The reaction solution was kept at 220 ºC for72 hours, during this time Cu hNPL formed

in the reaction solution and on the stir bar. Cu h nPL were then quenched, purified, and characterized by the previously outlined protocol.

Cu nanoplates (Cu NPL): Cu NPL of circular morphology were prepared utilizing only $CuCl_2$. Cu NPL were synthesized by combining DDA (5.5 g) and $CuCl_2$ (0.1964 mmol, 0.0264 g), and degassing and heating in a similar manner as the Cu NW synthesis. The reaction solution underwent the following color change: royal blue 55 ºC, dark blue 90 ºC, 113 ºC periwinkle blue, 173 ºC transparent pale yellow, and remained this color until 220 ºC. The reaction temperature is held at 220 ºC for 1.5 days, during this time the solution remains clear, and brown nucleated particles formed on the stir bar. Once the reaction has been preceded for 1.5 days the reaction solution is quenched, purified, and characterized by the previously outlined procedures.

2.3.2. The influence of hexadecyltrimethylammounium chloride (CTAC) (Synthesis set 2)

Synthesis set 2 studies the influence of chloride on nanomaterial growth, utilizing an external source of chloride. $CuCl_2$ was replaced with CTAC for syntheses completed in *2.3.2*. The molar ratios of $Cu(acac)_2$ to CTAC included 1:0.25, 1:0.5, 1:1, and 1:1.5, in which $Cu(acac)_2$ (0.2 mmol) and 5 g of DDA was utilized. In the 1:0.25 ratio, 0.053 g$Cu(acac)_2$ was combined with 0.049 mmol CTAC and 5 g of DDA. In the 1:0.5 ratio, 0.200 mmol $Cu(acac)_2$ was combined with 0.098 mmol CTAC and DDA (5 g). These reactions were degassed, heated by the same method as Cu NP. The reactions for these ratios were held for 50 min, and then quenched and purified by the previously outlined method.

The 1:1 ratio combined 0.200 mmol $Cu(acac)_2$ and 0.196 mmol CTAC with DDA (5 g). The 1:1.5 ratio combined 0.2 mmol $Cu(acac)_2$ and 0.294 mmol CTAC with DDA (5 g). These

reactions were degassed and heated in a similar method to Cu NPL. These reactions were held at 220 ˚C for 72 hours, then quenched and purified.

2.3.3. The influence of Tetrabutylammounium Chloride (TBAC) (Synthesis set 3)

Synthesis set 3 determines if the cation of the chloride external source has an influence on the resulting nanomaterial's morphology. $CuCl_2$ was replaced with TBAC for syntheses in *2.3.3*. The molar ratios of $Cu(acac)_2$ to TBAC included 1:0.5, 1:1, and 1:1.5, and the concentrations of $Cu(acac)_2$, TBAC, and DDA remained the same as synthesis set 2, section *2.3.2*. Starting precursors, degassing, heating, and reaction time for each ratio followed the protocols outlined in section *2.3.2*, synthesis set 2.

2.3.4. The Influence of bromide: $CuBr_2$ (Synthesis set 4)

$CuCl_2$ was replaced with $CuBr_2$ for syntheses completed in *2.3.4.*, which were completed to determine the influence of bromide on Cu NM morphology. The ratios of $Cu(acac)_2$ to $CuBr_2$ were A)1:0.5, B) 1:1, C) 1:1.5, and D) 0:1 with a fixed amount of $Cu(acac)_2$ (0.200 mmol) and 5 g of DDA. These ratios corresponded to the following amounts of $CuBr_2$: A) 0.1041 mmol (0.0233g), B) 0.1964 mmol (0.0439 g), C) 0.2945 mmol (0.0657 g), and D) 0.196 mmol (0.0438 g). The reaction parameters, purification process, and characterization methods remained the same as section *2.3.1*, synthesis set 1.

2.3.5. The Influence of hexadecyltrimethylammounium bromide (CTAB) (Synthesis set 5)

$CuBr_2$ was replaced with CTAB for syntheses completed in *2.3.5*. The molar ratios of $Cu(acac)_2$ to CTAB were A) 1:0.25, B) 1:0.5, C) 1:1, and D) 1:1.5 with a fixed amount of $Cu(acac)_2$ (0.200 mmol) and 5 g of DDA. These ratios corresponded to the following amounts of CTAB: A) 0.049 mmol (0.0358 g), B) 0.098 mmol (0.0715 g), C) 0.196 mmol (0.143 g), and D) 0.0294 mmol (0.2146 g).The reaction set up, degassing and heating were the same as section

2.3.4, synthesis set 4. The reaction time was based on nanomaterial growth. Syntheses A & B were held for 50 min, and syntheses C & D were held for 48 hours. The purification and characterization process was the same as previously outlined.

2.3.6. The influence of tetrabutylammounium bromide (TBAB) (Synthesis set 6)

Synthesis set 6 was completed to determine if the cation in the external bromide source influences Cu NM growth. $CuCl_2$ was replaced with TBAB for syntheses done in *2.3.2*. The molar ratios of $Cu(acac)_2$ to TBAC were 1:0.5, 1:1, and 1:1.5 with a fixed amount of $Cu(acac)_2$ (0.2 mmol) and 5 g of DDA. These ratios corresponded the following amounts of TBAB: A) 0.049 mmol (0.0316 g), B) 0.098 mmol (0.0633 g), C) 0.196 mmol (0.127 g), and D) 0.0294 mmol (0.189 g). The reaction set up, degassing, and heating remained the same as synthesis set 4, section *2.3.4*. The reaction time was based on Cu NM nucleation. Syntheses A, B, C were held for 50 min, while synthesis D was held for 48 hours. The purification and characterization protocol was the same as previously outlined.

2.3.7. The influence of tetrabutylammounium bromide (TBAI) (Synthesis set 7)

Synthesis set 7 studied the influence of iodine on Cu NM growth. $Cu(acac)_2$ was combined with TBAI for syntheses completed in *2.3.7*. The molar ratios of $Cu(acac)_2$ to CTAC were A) 1:0.25, B) 1:0.5, C) 1:1, and D) 1:1.5 with a fixed amount of $Cu(acac)_2$ (0.200 mmol) and 5 g of DDA. These ratios corresponded the following amounts of TBAI: A) 0.049 mmol, B) 0.098 mmol, C) 0.196 mmol, and D) 0.0294 mmol. These syntheses were combined, degassed, and heated by the previously outlined protocols. The reactions were held at 220 ^{o}C for 96 hours. After which, the reaction solution were purified and characterized by the previously outlined protocols.

2.3.8. Synthesis without Halogens (Synthesis set 8)

$CuCl_2$ was replaced with copper (II) acetate ($Cu(ac)_2$) for syntheses done in *2.3.8*. The molar ratios of $Cu(acac)_2$ to $Cu(ac)_2$ were A) 0:1, B) 1:0.5, and C) 1:1 with a fixed amount of $Cu(acac)_2$ (0.2 mmol) and 5 g of DDA. These ratios had the following concentrations of $Cu(ac)_2$ A) 0.0196 mmol (0.0364 g), B) 0.0982 mmol (0.0178 g), C) 0.1964 mmol (0.0357 g). Each reaction was combined, degassed, and heated by the previously outlined protocols in section *2.3.1*. For each synthesis, the reaction was held at 220 ˚C for 50 min, then purified and characterized by the previously outlined protocols.

2.3.9. The Influence of Cu (I) halide (Synthesis set 9)

$CuCl_2$ was replaced with CuCl, CuBr, or CuI for syntheses done in *2.3.9*. The molar ratio was 1:0.5 for $Cu(acac)_2$ and the Cu (I) halide. In these syntheses, $Cu(acac)_2$ (0.2 mmol) and Cu(I) halide (0.1 mmol) was combined with 5 g of DDA. The reaction protocol was the same process as synthesis set1, section *2.3.1*.

2.4. Part 1: Results and Discussion

2.4.1. Influence of chloride on the synthesis of Cu NM

2.4.1.1. Varying the chloride ratio of $Cu(acac)_2$ and $CuCl_2$ (synthesis set 1)

Cu NP were formed in the absence of $CuCl_2$ in the synthesis. TEM image in **Figure S1A** demonstrates the spherical morphology of the Cu NP, with a diameter of ~10-15 nm. UV-Vis spectrum in **Figure S1B** possessed a copper sharp LSPR peak at 582 nm, which is indicative of Cu NP formation. Metallic Cu composition was determined by XRD pattern in **Figure S1C**. The peaks at 43˚, 50˚, 74˚, and 90˚ can be indexed to {111}, {200}, {220}, and {311} planes of face-centered cubic (fcc) Cu crystal structure.

Cu RDH were formed by the 1:0.5 ratio of $Cu(acac)_2$ to $CuCl_2$. TEM Image in **Figure S1D** demonstrates that most Cu NM are hexagonal 2-D projection of Cu RHD nanostructure, as well as the presence of ~1.2 % nanorods. The average edge length of the Cu RHD is 24 nm, and the Cu nanorods have a length of 52 nm and a width of 21 nm. UV-Vis spectrum in **Figure S1E** possessed a broad LSPR peak at 586 nm, which could result from the size of Cu RDH and presence of Cu nanorods. XRD pattern in **Figure S1F** showspeaks at 43˚, 50˚, 74˚, and 90˚ can be indexed to {111}, {200}, {220}, and {311} planes of face-centered cubic (fcc) Cu crystal structure, suggesting the metallic Cu composition of Cu RDH.

The Cu NW were formed by the 1:1 ratio of $Cu(acac)_2$ to $CuCl_2$. TEM image in **Figure S1G** demonstrates the Cu NW with an average diameter was ~ 20 nm. The SEM characterization in **Figure S2, A-D** demonstrates the length of Cu NW varies from 5 to 10 μm. The UV-Vis spectrum in **Figure S1H** possessed a broad LSPR peak at 594 nm due to the 1-D morphology of Cu NW. Metallic Cu composition was determined by XRD pattern in **Figure S1I**. The peaks at 43˚, 50˚, 74˚, and 90˚ can be indexed to {111}, {200}, {220}, and {311} planes of face-centered cubic (fcc) Cu crystal structure.

Additional ratios of $Cu(acac)_2$ and $CuCl_2$ include 1:1.5 and 0:1. For the 1:1.5 ratio synthesis of $Cu(acac)_2$ to $CuCl_2$, TEM image in **Figure S3A** determined the Cu NM morphology to be hexagonal Cu NPL with an average diameter of ~150 nm and an average thickness of ~10 nm. The UV-Vis spectrum in **Figure S3B** exhibits a board peak at 507 nm. The XRD pattern in **Figure S3C** has peaks at 43˚, 50˚, 74˚, which correlates to the {111}, {200}, and {220} planes of face-centered cubic (fcc) Cu crystal structure. The peaks at 27^0 and 55^0 suggest the Cu NPL contains an impurity, which will require additional characterization to identify the impurity source. Additionally, the hexagonal shape of the nanoplate may be a result of the increased

concentration of chloride present in the reaction solution.[17] For the synthesis with 0:1 ratio of $Cu(acac)_2$ to $CuCl_2$, TEM image in **Figure S3D** shows the morphology to be spherical Cu NPL. The spherical Cu NPL possess an average length of 50-100 nm, which also appear to be overlaid each other and vertically stacked. The UV-Vis spectrum in **Figure S3E** exhibits a very broad peak at 507 nm. XRD pattern in **Figure S3F** only demonstrates one small sharp peak at 43^0. This may correspond to to the {111} plane in face centered cubic Cu, however, it is challenging to fullyindexed and additional characterization is required.

Figure S4 summarized the 5 different morphologies that were obtained by varying the ratios of $Cu(acac)_2$ to $CuCl_2$. With increasing concentrations of $CuCl_2$, the Cu NM morphologies become more defined along the {110} and {111} facets. When no $CuCl_2$ is present, the synthesis forms Cu NP. At a ratio of 1:0.5 forms Cu RDH. Increasing $CuCl_2$ concentration to a ratio of 1:1, forms Cu NW. When the ratio is increased to 1:1.5, this synthesis forms hexagonal Cu NPL.Spherical Cu NPL are formed when only $CuCl_2$ is present at the 0:1 ratio.

These results demonstrate that the Cu precursor ratio of $Cu(acac)_2$ to $CuCl_2$ influences the resulting morphology. In order to determine whether Cu NM morphology is due to the presence of the chloride anion, the synthetic protocols will be completed by replacing the $CuCl_2$ with external chloride sources, specifically CTAC and TBAC.

2.4.1.2. Varying the chloride ratio of $Cu(acac)_2$ and CTAC (synthesis set 2)

Synthesis set 2 investigated the influence of chloride, using CTAC, on Cu NM growth In these studies, CTAC replaces $CuCl_2$ in the previous study of synthesis set 1, while other reaction parameters remained constant. The ratios between the amount of $Cu(acac)_2$ and CTAC included 1:0.5, 1:1, 1:1.5. For each synthesis ratio, the resulting Cu NM were characterized by TEM and UV-Vis spectroscopy as demonstrated in **Figure S5**. At the ratio of 1:0.5, the Cu NM possessed

rhombic dodecahedral morphology, as seen in **Figure S5A.** Spectrum in **Figure S5B** demonstrates the Cu LSPR peak at 575 nm. At the ratio of 1:1, the Cu NM formed 1-D NW morphology, as determined in **Figure S5B.** The 1:1.5 ratio formed a mixture of hexagonal and spherical Cu NPL. The UV-Vis spectrum exhibits two broad peaks at 481 nm and 612 nm. Cu NM with similar morphologies to synthesis set 1 was formed when $CuCl_2$ was replaced by CTAC, as shown in **Figure S1.** These results suggest that the chloride anion may direct nanomaterial growth. An additional study needs to be completed to determine if the cation in the external Cl- source (CTA-) influences copper nanomaterial growth.

2.4.1.3. Varying the chloride ratio of $Cu(acac)_2$ and TBAC (synthesis set 3)

When CTAC was replaced with TBAC, the syntheses were carried out again to determine if the chloride anion is the major factor for the growth of Cu NM, and if the cation of the external source influences Cu NM growth. The molar ratios between $Cu(acac)_2$ and TBAC included: 1:0.5, 1:1, and 1:1.5. For each synthetic ratio, the resulting Cu NM were characterized by TEM and UV-Vis spectroscopy as shown in **Figure S6**. Synthesis ratio of 1:0.5 formed Cu RHD as shown in the TEM image (**Fig. S6A**). The UV-Vis spectrum possessed a sharp peak at 576 nm, which corresponds to the LSPR peak of Cu NM. Based on TEM image (**Fig. S6B**) the 1:1 ratio synthesis formed Cu NW, and the UV-Vis spectrum possessed a narrow copper, LSPR peak at 579 nm. Synthesis ratio of 1:1.5 formed spherical Cu NPL as shown in TEM image (**Fig. S6C**). Cu NPH, Cu NW, and Cu NPL were formed in synthesis set 3, which are similar to the morphological results at the corresponding ratios in synthesis set 2. These results support the concept that chloride is responsible for the shape-controlled synthesis of Cu NM.

2.4.1.4. Summary of the chloride influence

The results from the study of the chloride influence on Cu NM growth and morphology were summarized in **Figure 1 and 2**. **Figure 1**, **A-C**, demonstrates the morphology characterization of the products when $Cu(acac)_2$ to $CuCl_2$ ratios are 1:0.5; 1:1; and 1:1.5, respectively, corresponding to synthesis set 1. **Figure 1**, **D-E**, characterizesthe morphology of the Cu NM when $Cu(acac)_2$ to CTAC ratios are 1:0.5; 1:1; and 1:1.5, which corresponds to synthesis set 2. **Figure 1**, **F-H**, shows the Cu NM morphology when $Cu(acac)_2$ to TBAC ratios are 1:0.5; 1:1; and 1:1.5, respectively, correlating to synthesis set 3. Cu NM morphologies remain unaltered at the same ratios of $Cu(acac)_2$ to chloride source, which suggests that the chloride anion concentration is important for the growth of Cu NM regardless of chloride source.

While the morphology of each Cu NM remained the same, the uniformity of the Cu NM was the best when $CuCl_2$ was used as the chloride source. Additional synthetic studies were completed with bromide and iodine sources, in order to determine if the Cl- shape directing trend is also observed by additional halides.

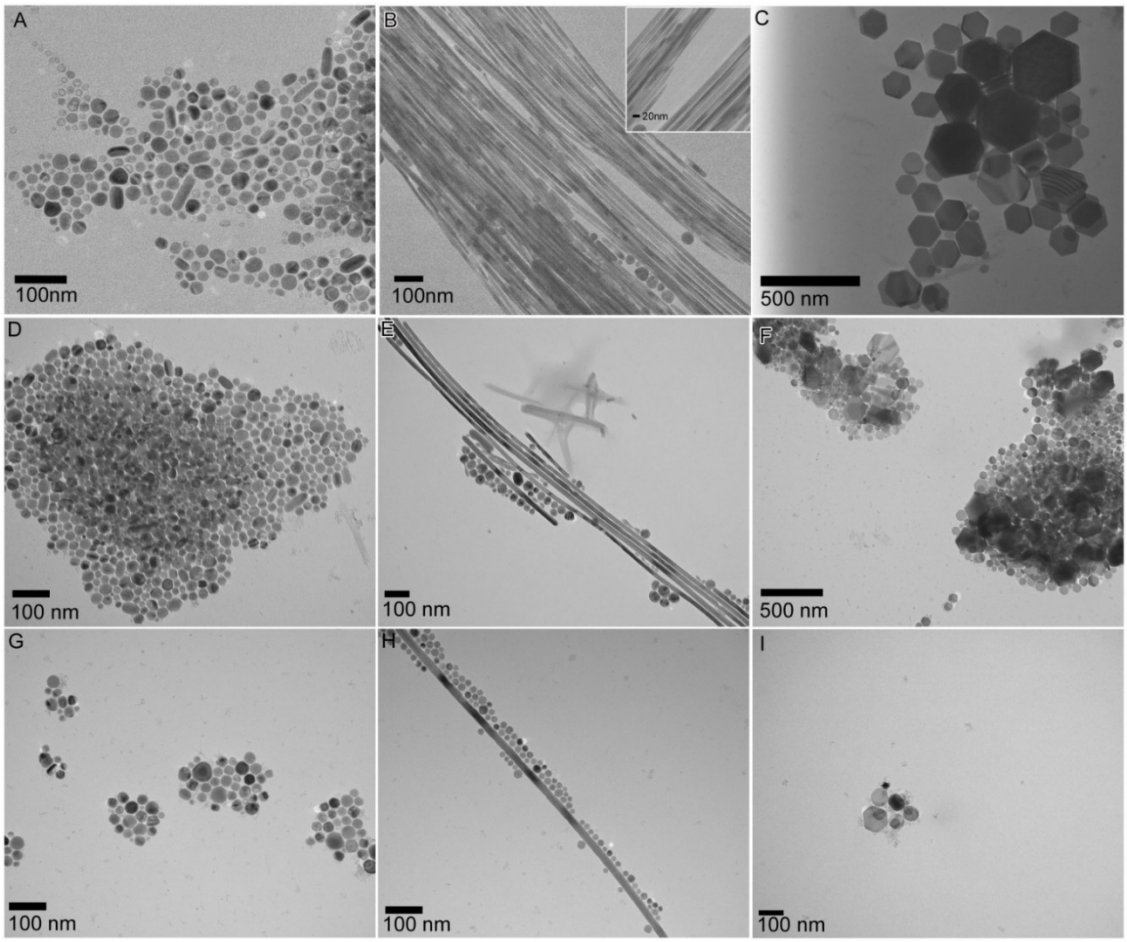

Figure 1. TEM characterization of Cu NM synthesized by using $Cu(acac)_2$ with various chloride sources at different ratios: (A-C) $Cu(acac)_2$ to $CuCl_2$ at 1:0.5, 1:1, and 1:1.5 ratios; (D-E) $Cu(acac)_2$ to CTAC at 1:0.5, 1:1, and 1:1.5 ratios; and (G-I) $Cu(acac)_2$ to TBAC at 1:0.5, 1:1, and 1:1.5 ratios.

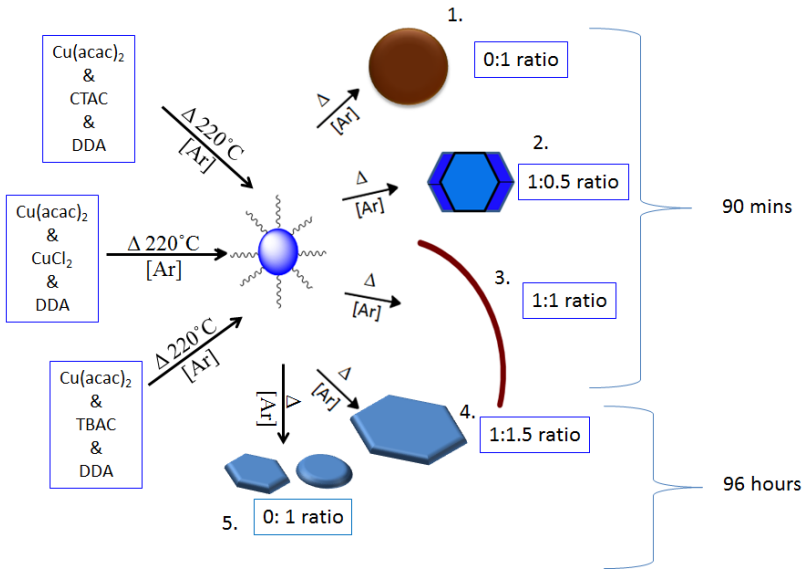

Figure 2. Schematic of Cu NM synthesis at varying ratios of $Cu(acac)_2$ with chloride present in the reaction solution. The chloride sources include $CuCl_2$, CTAC, and TBAC.

2.4.2. Influence of bromide on the synthesis of Cu NM

2.4.2.1. Varying the ratio of $Cu(acac)_2$ and $CuBr_2$ (synthesis set 4)

Synthesis set 4 investigated the influence of bromide on Cu NM growth by using $CuBr_2$.These studies followed synthesis set 1, however, $CuBr_2$ was utilizes instead of $CuCl_2$ while other reaction parameters remained unchanged. The $Cu(acac)_2$ and $CuBr_2$ ratios included: 1:0.5, 1:1, 1:1.5, and 0:1. For each synthetic ratio, the resulting Cu NM were characterized by TEM, UV-Vis spectroscopy, and XRD as shown in **Figure S8**.

At the ratio of 1:0.5, the Cu NM formed a mixture of truncated nanocubes, pyramids, and nanorods of various sizes, as shown in **Figure S8A.** The UV-Vis spectrum in **Figure S8B** shows the Cu LSPR peak at 606 nm. Metallic Cu composition was determined by XRD pattern in **Figure S8C**. The peaks at 43˚, 50˚, 74˚, and 90˚ can be indexed to {111}, {200}, {220}, and {311} planes of face-centered cubic (fcc) Cu crystal structure. At the ratio of 1:1, the Cu NM developed pyramids and ~1% rhombic dodecahedrons, with an average size of 100 nm was seen in **Figure S8D.** The UV-Vis spectrum in **Figure S8E** exhibits the a broad LSPR peak of Cu at

672nm due to large size of the pyramids. XRD pattern in **Figure S9F** possessesone small sharp peak at 43°, which is difficult to fully indexed.

The 1:1.5 ratio formed Cu NM with octahedral shape, and average edge length of ~45 nm as seen in **Figure S9A. The UV-Vis** spectrum in **Figure S9B** shows a broad peak at 447 nm. XRD pattern in **Figure S9C** demonstrates one small sharp peak at 43°, which is challenging to indexed. This sample requires additional characterization to determine the crystal structure. At the ratio of 0:1, the Cu NM with hexagonal and spherical NPL and size from 56-155 nm and thickness of 14 nm was seen in **Figure S9D**. The UV-Vis spectrum in **Figure S9E** exhibits a broad peak at 380 nm. XRD pattern **Figure S9F** does not demonstrate a well defined diffraction pattern, additional characterization is required to elucidate the crystal structure.

In summary, **Figure 3, A–D** provides TEM images of the resulting Cu NM obtained at different ratios of $Cu(acac)_2$ to $CuBr_2$. **Figure 4** illustrates the morphologies and the corresponding reaction conditions from synthesis set 4. The ratio of $Cu(acac)_2$ and $CuBr_2$ varies the resulting morphology, which suggests that bromide may be important for Cu NM growth. Cu NM morphology varies with the molar ratio and copper (II) halide.

The difference between the Cl- anion and the Br- anion on the resulting shapes of the nanostructures could be due to the facet selectivity by these two anions. Previous research on shape control by specific halides in noble metal syntheses, has shown that chloride will direct growth along the (1,1,1).[14] Additionally, the bromide protects the {1,1,1} and {1,0,0} for the crystal growth along the [1,1,0] direction.[18] The main results from these studies suggest the amount of precursor as well as the presence of a specific halide in the reaction solution influence nanomaterial growth and resulting morphology. In order to determine if the various

morphologies are dependent on precursor ratio versus the presence of bromide, an external source of bromide was studied for synthesis set 5.

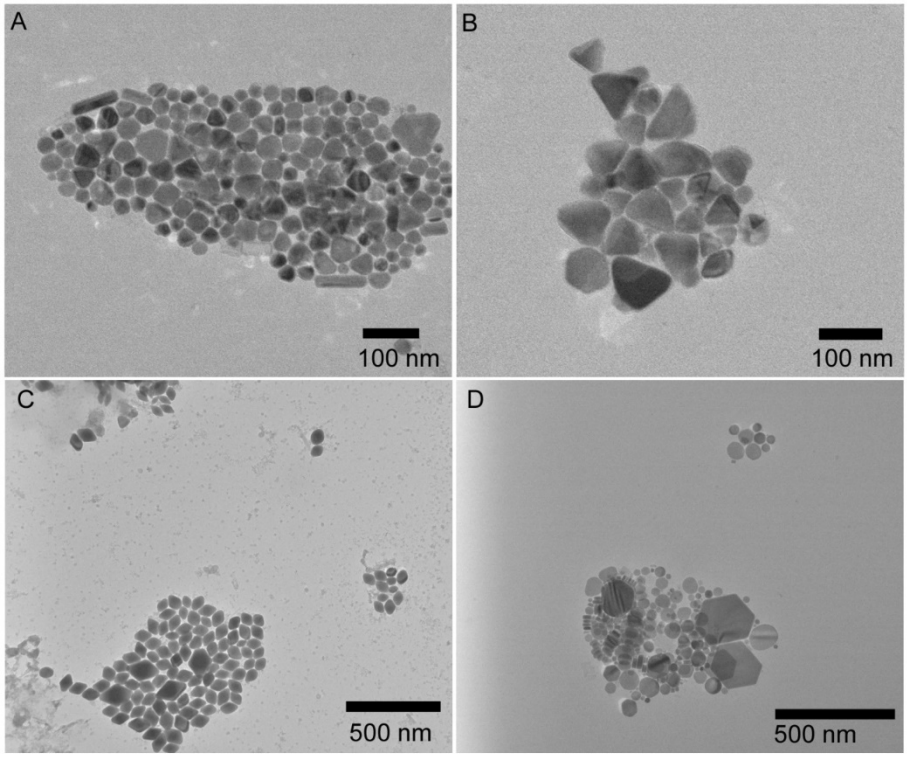

Figure 3. TEM characterization of the Cu NM synthesized using different ratios of $Cu(acac)_2$ to $CuBr_2$: (A) 1:0.5; (B) 1:1; (C) 1:1.5; and (D) 0:1.

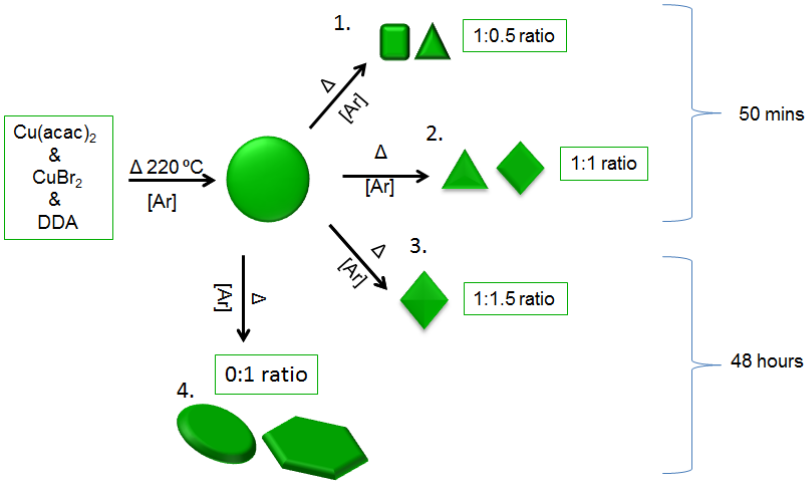

Figure 4. Schematic illustration of Cu NM synthesis at varying ratios of $Cu(acac)_2$ to $CuBr_2$.

2.4.2.2. Varying the ratio of $Cu(acac)_2$ and CTAB (synthesis set 5)

Synthesis set 5 investigated the influence of bromide on Cu NM growth utilizing an external source CTAB. In these studies, CTAB replaces $CuBr_2$ in the previous study of synthesis set 4, while maintaining other reaction parameters remained unchanged. The ratios between $Cu(acac)_2$ and CTAB is as follows : 1:0.25,1:0.5, 1:1, 1:1.5. **Fig. S10 (A, C ,E)** characterizes the ratios of 1:0.25, 1:0.5, and 1:1, by TEM. These reactions yielded the Cu NM with pyramids, nanorods, truncated cubes, and nanospheres with optical spectrum having a Cu LSPR peak at ~585 nm (**Fig. S10 B, D, F**). Additional experiments at lower ratios of 1:0.1 and 1:0.05, the morphology and optical property of the products remained the same (**Fig. S12**). When $Cu(acac)_2$ to CTAB ratio increased to 1:1.5, the synthesis resulted in the formation of hexagonal nanoplates with an average size of 150 nm, with some Cu hNPL as large as 300 nm. UV-Vis spectrum B demonstrates a broad copper LSPR peak at 521 nm (**Fig. S11**).

The results were summarized in **Figure 5 and 6.** The morphologies from synthesis set 5 vary from the morphologies formed in synthesis set 4. This suggests that the type of Cu precursor, for bromide ion study, may contribute to resulting Cu NM morphology.

These results support the findings that halides in the reaction influence Cu NM morphology. Previous studies have been completed on noble metal nanoplates, that attribute the formation of nanoplates to the presence of CTAB, due to CTA^+ favorable adsorption to the {111} facet.[19] An additional study needs to be performed to determine if the cation from the external source influences the Cu NM growth and ultimate morphology. This may explain the variation in the shape when using $CuBr_2$ versus CTAB.

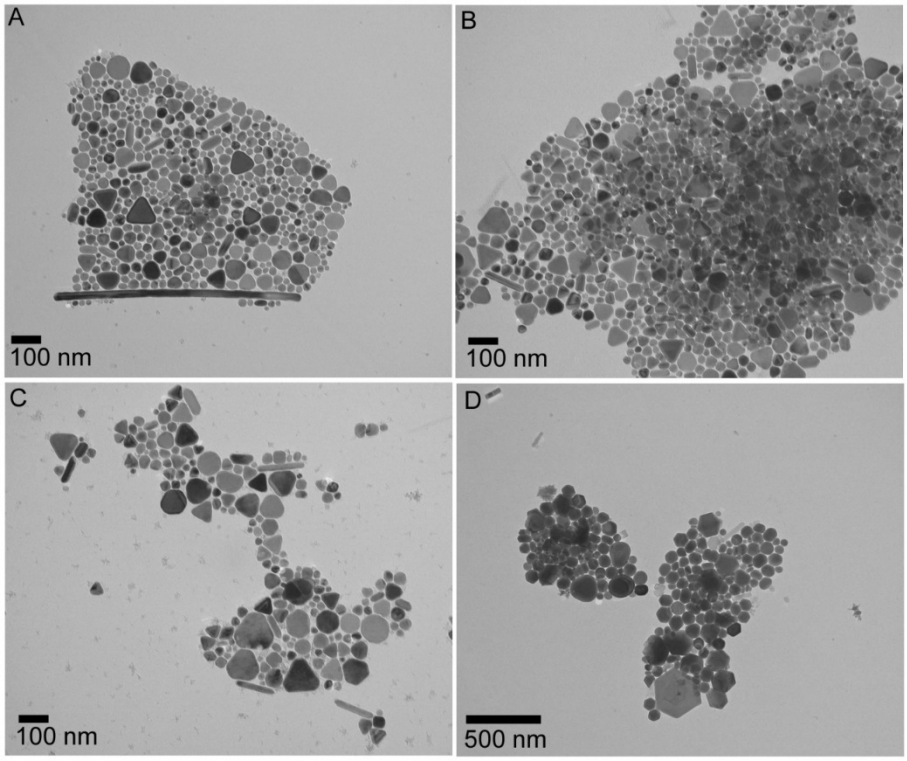

Figure 5. TEM characterization of the Cu NM synthesized using different ratios of $Cu(acac)_2$ to CTAB: (A) 1:0.25; (B) 1:0.5; (C) 1:1; and (D) 0:1.5.

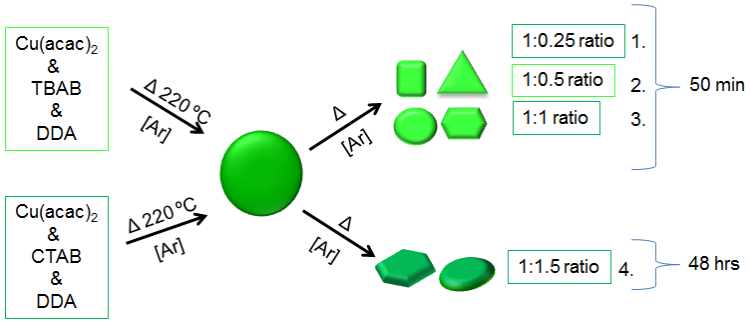

Figure 6. Schematic illustration of Cu NM synthesis at varying ratios of $Cu(acac)_2$ to CTAB and TBAB.

2.4.2.3. Varying the ratio of $Cu(acac)_2$ and TBAB (synthesis set 6)

Synthesis set 6 investigated the influence of bromide on Cu NM growth by using TBAB. In these studies, TBAB is instead of $CuBr_2$, while other reaction parameters remained unchanged. The ratio between the amount of $Cu(acac)_2$ and TBAB was used at the following ratios: 1:0.25 and 1:0.5 as illustrated in **Figure 6**. For both ratios of 1:0.25 and 1:0.5, the reactions yielded the Cu NM with pyramids, nanorods, truncated cubes, and spheres with optical

spectrum having a Cu LSPR peak at ~590 nm (**Fig. S13 and S14**). These results are similar to the Cu NM from reactions with CTAB. The comparison of the morphologies formed at the 1:0.25 ratio when CTAB and TBAB were utilized can be found in **Figure S15.** These results indicatethe two reactions yielded similar products, Cu NM with pyramids, nanorods, truncated cubes, and spheres. The TEM characterization, of the TBAB syntheses, was summarized in **Figure 7.**

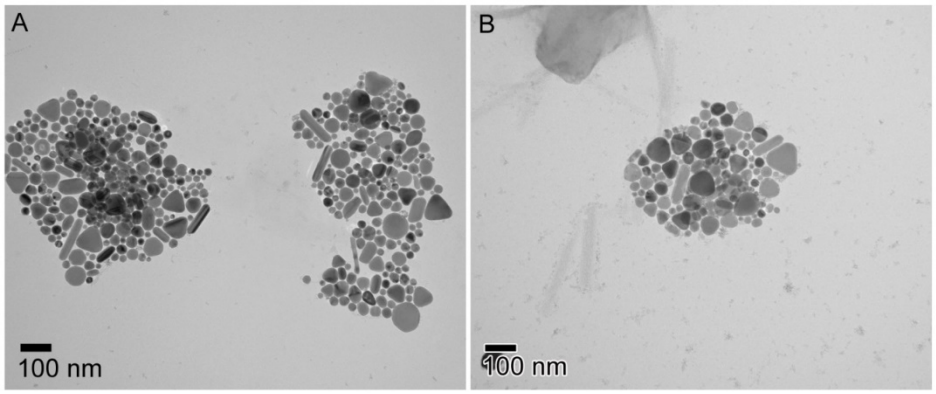

Figure 7. TEM characterization of the Cu NM synthesized using different ratios of $Cu(acac)_2$ to TBAB: (A) 1:0.25; and (B) 1:0.5.

2.4.2.4. Summary of the bromide influence

Comparing the morphology differences among synthesis sets 4, 5, and 6, the Cu NM growth is influenced not only by the presence and concentration of bromide, but also the counter ion bound to the external bromide source. The bromide affects the Cu NM growth and the resulting morphology. This difference could be attributed to the binding strength of the Br^- to the counter ions and reduction kinetics of the metal precursors. The presence of bromide, in the reaction, can partially influence Cu NM morphology during the growth. Since Cl^- consistently formed well defined morphologies and bromide partially influenced Cu NM growth, these observations suggest chloride may selectively bind to facets more favorably than bromide, ultimately functioning as a better shape directing additive in nanomaterial synthesis.

2.4.3. Varying the ratio of $Cu(acac)_2$ and TBAI (synthesis set 7)

Synthesis set 7 investigated the influence of iodide on Cu NM growth..

In these studies, TBAI is used as the halide source, and the reaction parameters were the same as synthesis set 6.The ratios between $Cu(acac)_2$ and TBAIincludes: 1:0.25, 1:0.5, 1:1, and 1:1.5. TEM characterization shown in **Figure 8** indicates these syntheses produced nanoplates. Spherical Cu NPL were formed by the 1:0.25 and 1:0.5 ratios, while hexagonal Cu NPL were formed by the 1:1 and 1:1.5 ratio syntheses. The UV-vis spectra exhibit a broad peak at 476 and 423 nm, for the 1:0.25 and 1:1 ratio synthesis, respectively (**Fig. S16**). These results suggest the iodide ligand led to the growth of Cu NPL, and the increase in iodine concentration could slightly alter the shapeof the Cu NPL, as illustrated in **Figure 9**.

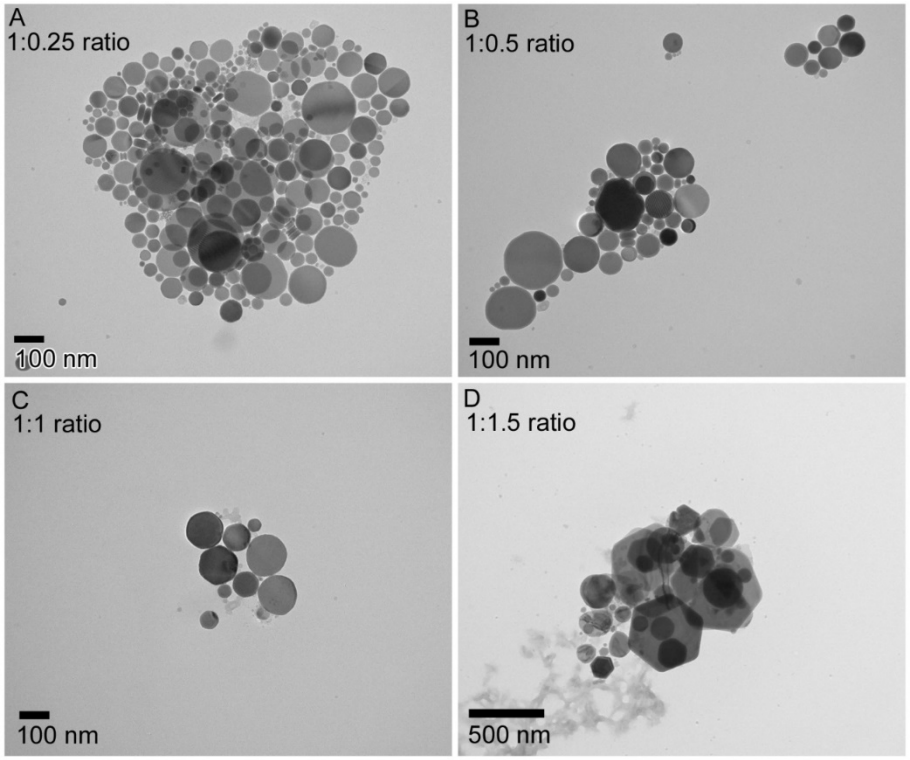

Figure 8. TEM characterization of the Cu NM synthesized using different ratios of $Cu(acac)_2$ to TBAI: (A) 1:0.25; (B) 1:0.5; (C) 1:1; and (D) 0:1.5.

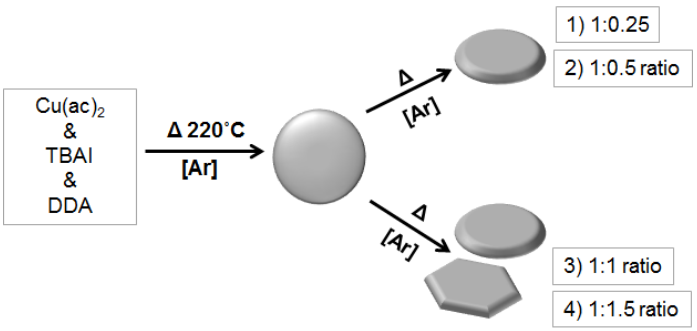

Figure 9. Schematic illustration of Cu NM synthesis at varying ratios of $Cu(acac)_2$ to TBAI.

2.4.4. Synthesis without the presence of a halide (synthesis set 8)

Synthesis set 8 investigated the influence of other Cu precursor, Cu(ac)2, coupled with Cu(acac)2, without the presence of a halide. In these studies, $Cu(ac)_2$ is used instead of the halide sources in the previous studies of synthesis set 1-7, while other reaction parameters remained unchanged. The ratio between the amount of $Cu(acac)_2$ and $Cu(ac)_2$ was used at the following ratios: 0:1, 1:0.5, and 1:1. The results were shown in **Figure 10**, and **Figure 10 G** illustrates nanomaterial growth in the syntheses without halides present. Based on the TEM images, the resulting Cu NM possessed a string-like morphology when only $Cu(ac)_2$ is used (**Fig. 10A**), while polydispersed, round, polycrystalline nanoparticles were obtained at the ratios of 1:0.5 and 1:1 (**Fig. 10, C and E**). When only $Cu(ac)_2$ (0:1 ratio) was utilized as the copper precursor, the resulting Cu NM structure was non-uniform string-like structure as shown in **Figure 10** TEM image A. The UV-Vis spectra (**Fig 10 B, D, F)** show a broad feature for the LSPR. In the synthesis with only $Cu(ac)_2$ there was a slight peak around 495nm, and a shorter peak around 713nm. The syntheses with $Cu(acac)_2$ and $Cu(ac)_2$ as starting precursors possessed similar UV-Vis spectra exhibiting one small peak around 470 nm and a more distinct peak around 590 nm. The result from the syntheses without halide to control Cu NM morphology, supports the previous findings. In which, copper halide precursors, as well as halides from an external source, can selectively direct nanomaterial growth resulting in the formation of unique morphologies.

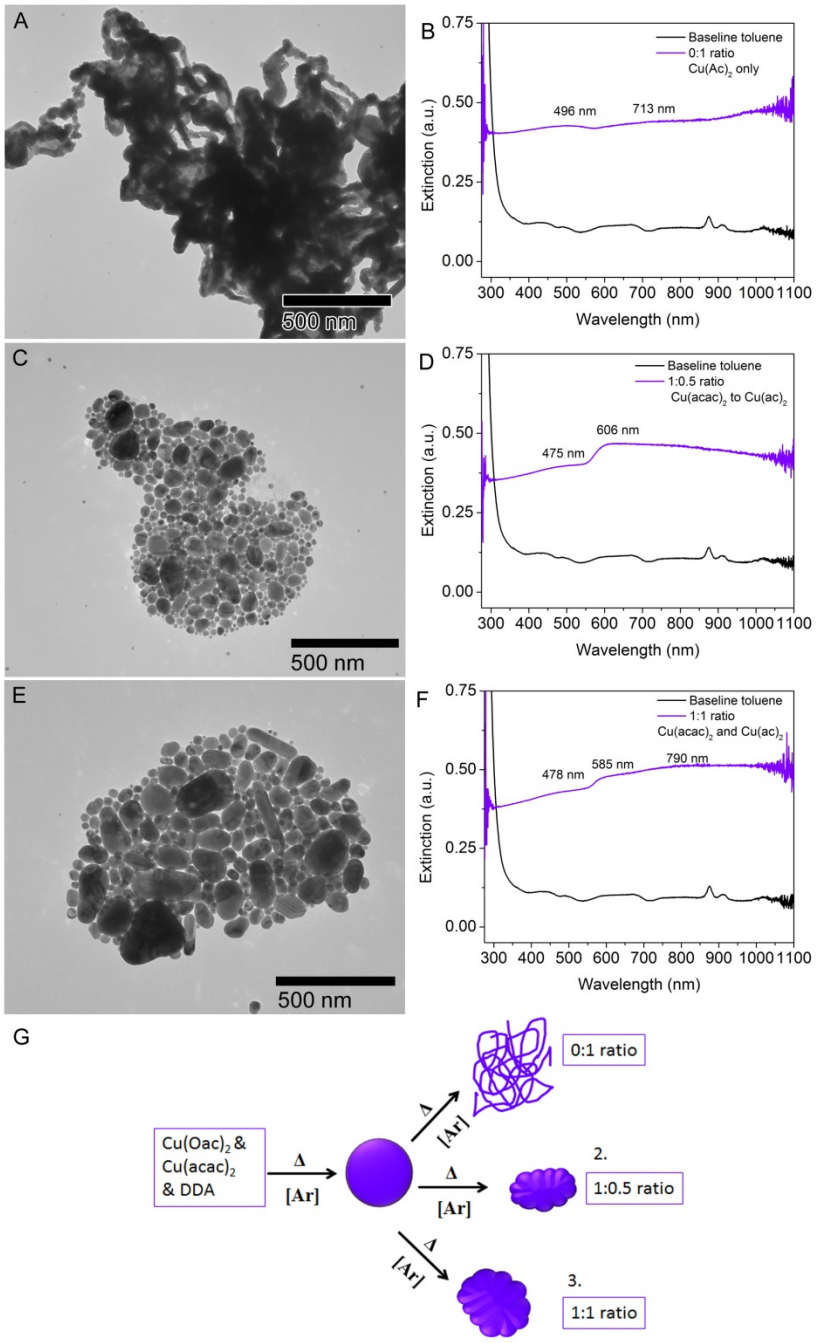

Figure 10: TEM and UV-vis characterization of the Cu NM synthesized using different ratios of $Cu(acac)_2$ to $Cu(ac)_2$: (A,B) 0:1; (C,D) 1:0.5; and (E,F) 1:1. (G) Schematic illustration of Cu NM synthesis at varying ratios of $Cu(acac)_2$ to $Cu(ac)_2$.

2.4.5. Varying the oxidation state of the copper halide (synthesis set 10)

Synthesis set 8 investigated the influence of oxidation state of Cu halide, and the corresponding molecular structures of the copper precursors. In these studies, Cu(I) halides

utilized as the halide source, while other reaction parameters remained unaltered. . The 1:0.5 ratio of $Cu(acac)_2$ to Cu(I) halides was studied, and the results were demonstrated in **Figure 11.**

Based on the TEM images, the resulting morphologies from these syntheses, which utilize Cu (I) halides appear to be similar to their Cu (II) counterparts, in syntheses 1 and 4. The synthesis with CuCl results in the formation of rhombic dodecahedra (**Fig. 11A**). The CuBr synthesis produces Cu NM with a mixture of morphologies including: nanorods, pyramids, spheres, and cubes/truncated cubes (**Fig. 11B**).the CuI synthesis only forms small Cu seeds as shown in **Figure 11C**, which differs from Cu NM from synthesis set 7. The UV-Vis spectra exhibit a Cu LSPR around 590nm for each of the syntheses. These results suggest that the in oxidation state of the Cu halides does not affect the resulting morphology, while the Cu NM morphology is affected by the type and concentration of halide.

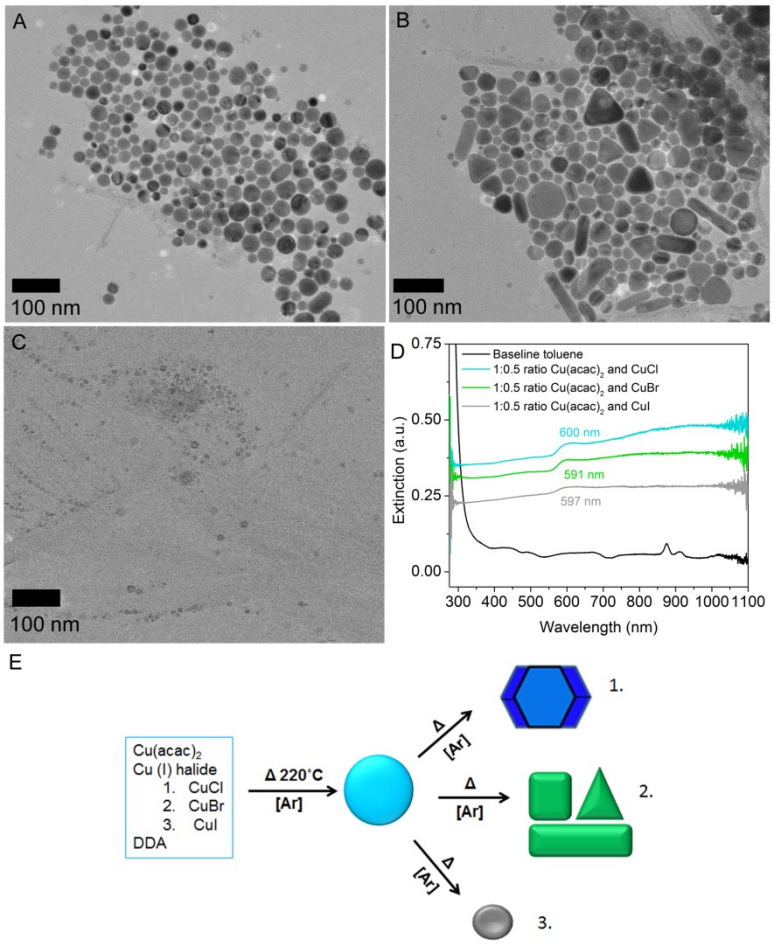

Figure 11. TEM characterization of the Cu NM synthesized using $Cu(acac)_2$ and Cu(I) halides at the ratio of 1:0.5: (A) CuCl; (B) CuBr; and (C) CuI. (D) UV-Vis spectra of the corresponding samples in A-C. (G) Schematic illustration of Cu NM synthesis at the 1:0.5 ratio of $Cu(acac)_2$ to Cu(I) halides.

2.5. Part II: Experimental Methods, $Cu(ac)_2$ as the Primary Copper Precursor

2.5.1. Replacement of $Cu(acac)_2$ with $Cu(ac)_2$ as primary copper precursors (synthesis set 10)

In this study, $Cu(ac)_2$ was used as the primary Cu (II) precursor, and the syntheses completed in synthesis set 1 were repeated to determine if the halide influence Cu NM growth with a different Cu precursor. The experimental protocols remained the same as synthesis set 1, section *2.3.1*, except $Cu(ac)_2$ (0.2 mmol, 0.364 g) was utilized as the starting precursor.

2.5.2. Varying the ratio of $Cu(ac)_2$ and CTAC (synthesis set 11)

In this synthesis set, $Cu(ac)_2$ was combined with CTAC to determine the external chloride source would produce similar copper nanomaterials as synthesis set 2, section *2.3.2*. The molar ratios studied included A) 1:0.25, B) 1:0.5, C) 1:1, and D) 1:1.5. The synthetic protocol remained the same as synthesis set 2, section *2.3.2*; however, the reaction time varied by ratio. The reaction solution was held at 220 ˚C the following time scales 50 mins (A, B), 24 hours (C), and 96 hours (D). The purification and characterization processes remained the same as section *2.3.3*.

2.5.3. Varying the ratio of $Cu(ac)_2$ and TBAC – external source (synthesis set 12)

Synthesis set 7 determines if the cation in the external bromide source influence Cu NM growth. In synthesis set 12, TBAC was the external source of chloride, and the 1:1.5 ratio of $Cu(ac)_2$ to TBAC was investigated.The experimental set up was the same as synthesis set 3, however, the reaction time was held for 96 hours. The purification and characterization processes were the same as section *2.3.3*, synthesis set 3.

2.5.4. Varying the ratio of $Cu(ac)_2$ and $CuBr_2$ (synthesis set 13)

$Cu(ac)_2$ was combined with $CuBr_2$ to determine if bromide would influence Cu NM growth with a different Cu precursor. In synthesis set 13 $Cu(ac)_2$ was combined with $cuBr_2$ at the following ratio: 1:0.5, 1:1, 1:1.5, 0:1. The synthetic protocol, purification, and characterization was the same as synthesis set 4, in section *2.3.4*.

2.5.5. Varying the ratio of $Cu(ac)_2$ and CTAB – external source (synthesis set 14)

In this synthesis set, $Cu(ac)_2$ was combined with CTAB to determine if the external bromide source will influence Cu NM. The molar ratios studied include A) 1:0.25, B) 1:0.5, C) 1:1), and D) 1:1.5. The experimental parameters were similar to synthesis set 5 section *2.3.5*;

however, the reaction time varied by ratio and Cu NM nucleation. The reaction temperature was held at 220 ^{o}C for the following time scales 50 mins (A, B), 24 hours (C), and 96 hours (D). The purification and characterization process remained the same as synthesis set 5, section *2.3.5*.

2.5.6. Varying the ratio of $Cu(ac)_2$ and TBAB – external source (synthesis set 15)

Synthesis set 15, utilizes TBAB as the external source of bromide, in order to determine if the cation of the external bromide source influences Cu NM growth. The only ratio studied was 1:1.5.This synthesis has the same method, purification procoess, and characterization protocol as synthesis set 12, section *2.5.3.*

Part II Results and Discussion: Cu NM with $Cu(ac)_2$ as the primary precursor

2.6.1 Characterization of Cu NM from Synthesis set 10

Varying the ratio of $Cu(ac)_2$ to $CuCl_2$ (synthesis set 10) investigated the influence of chloride on Cu NM growth by using $CuCl_2$. TEM characterization, for synthesis set 10, can be found in **Figure 12**, **A-C. Figure 12D** provides an illustration of the growth conditions and corresponding nanomaterial morphology. Additional characterization, of synthesis set 10 Cu NM, by TEM, UV-Vis, and XRD is demonstrated in **Figure S17.** Based on the TEM images, non-uniform string-like Cu NW (**Fig. 12A**), a mixture of Cu NWs and nanocubes (**Fig. 12B**), and a mixture of Cu NW, truncated cubes, and spheres (**Fig. 12C**), were obtained at ratios of 1:0.5, 1:1, and 1:1.5, respectively.

The UV-Vis spectra exhibit a peak at 620, 620, and 596 nm for ratios of 1:0.5, 1:1, and 1:1.5, respectively (**Fig. S17**, **D-F**). The XRD patterns are in **Figure S17, G-I**, demonstrate peaks at 43˚, 50˚, 74˚, and 90˚, which can be indexed to {111}, {200}, {220}, and {311} planes of face-centered cubic (fcc) Cu crystal structure. The XRD pattern in **Figure S17H** demonstrates a peak at 52^{o} assigned to {2,0,0} planes is more intense than the peak at 43^{o} attributed {1,1,1}

planes, indicating the presence of nanocubes.[11a, 20] This result is in agreement with the TEM observation in Figure **S17B**. When $Cu(ac)_2$ replaced $Cu(acac)_2$, different morphologies are formed, suggesting that different coordinate ligands in the Cu precursors influence the resulting shapes of the products. Although the resulting Cu NM morphologies were not similar, the results of synthesis set 10 are in agreement to those of synthesis set 1. These results support the findings that the chloride anion functions as a facet specific protector, which ultimately directs nanomaterial growth.

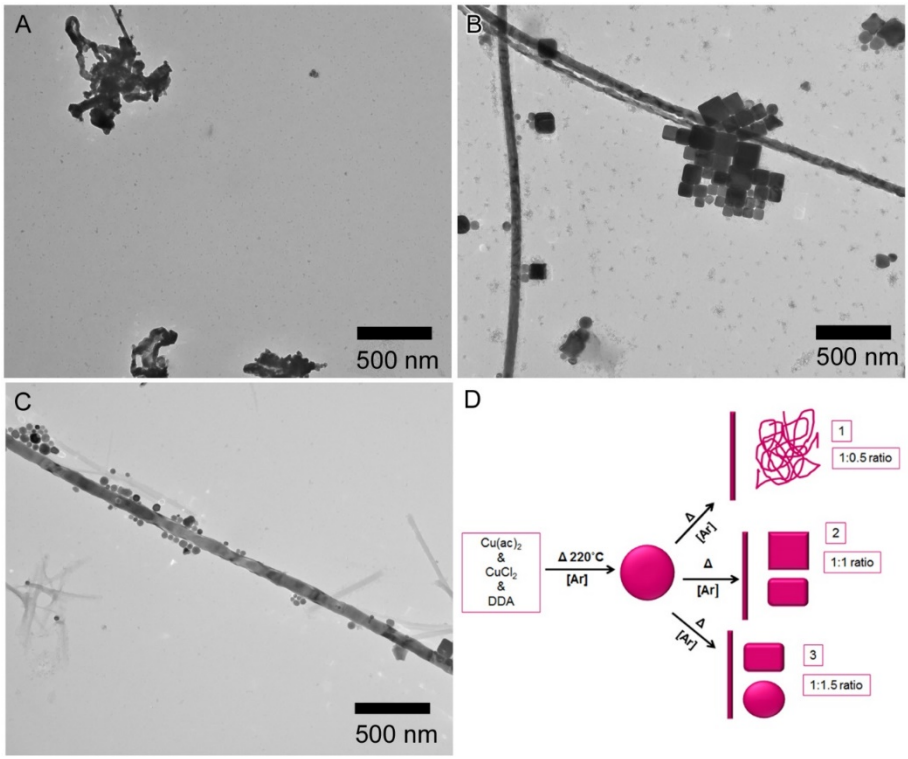

Figure 12: TEM characterization of the Cu NM synthesized using $Cu(ac)_2$ and $CuCl_2$ at different ratios: (A) 1:0.5; (B) 1:1; (C) 1:1.5. (D) Schematic illustration of Cu NM synthesis at varying ratios of $Cu(ac)_2$ to $CuCl_2$.

2.6.2 Varying the ratio of $Cu(ac)_2$ to CTAC (synthesis set 11)

Synthesis set 11 investigated the influence of external chloride (CTAC) on Cu NM growth. The ratios between the amount of $Cu(ac)_2$ and CTAC included 1:0.5, 1:1, and 1:1.5. The results of TEM characterization can be found in **Figure 13**, **A-C** and **Figure 13D** provides an

illustration of the growth conditions and corresponding nanomaterial morphology. Additional characterization of the resulting Cu NM from synthesis set 11 were shown in **Figure S18**, including TEM and UV-Vis. Based on the TEM images, a mixture of hexagonal, triangular, and cubes (**Fig. 13A and S18A**), a mixture of hexagonal, triangular, and cubes (**Fig. 13B and S18B**), and hexagonal nanoplates (**Fig. 13C and S18C**), were obtained at ratios of 1:0.5, 1:1, and 1:1.5, respectively. The UV-Vis spectra exhibits a peak at 612, 416, and 514 nm for ratios of 1:0.5, 1:1, and 1:1.5, respectively (**Fig. S18**, **D-F**).

A lower ratio of $Cu(ac)_2$ to CTAC (1:0.25) was also studied, and characterized in **Figure S19.** TEM image shows the presence of thin nanowires and non-uniform string-like nanomaterials (**Fig. S19A**). UV-Vis spectrum demonstrates a small, copper, LSPR peak at 579 nm (**Fig. S19B**). The resulting Cu NM morphologies in synthetic set 11 deviated from the morphologies produced by synthesis set 10. This result suggests that the cation present in the external source may influence nanomaterial growth; further studies would be required to determine the cation influence.

Different Cu NM resulted when $Cu(ac)_2$ was used instead of $Cu(acac)_2$ in the previous section, suggesting that the chloride influence on morphology is dependent on Cu precursor. This suggests that the reduction and nucleation process of the copper precursor may influence nanomaterial structure, in addition to the halide ion capping effect. A study by Li et al, suggested that reduction rates of metal precursors influence the size and shape of nanomaterial. They studied the reduction of Cu^{2+} and the corresponding cations acetate and chloride. They observed a faster reduction rate for the binding ligand (acetate) and a slower reduction rate for the stronger binding ligands (chloride), resulting in two different morphologies.[21] The variations in morphology from part 1 and part 2, may be a result of the Cu reduction rate and the strength of

the binding ligand for the Cu precursors. In this study, $Cu(acac)_2$ and $Cu(ac)_2$ are utilized, and acetylacetonate is a stronger ligand than acetate due to its bidentate structure, which could influence the reduction rate and morphology.

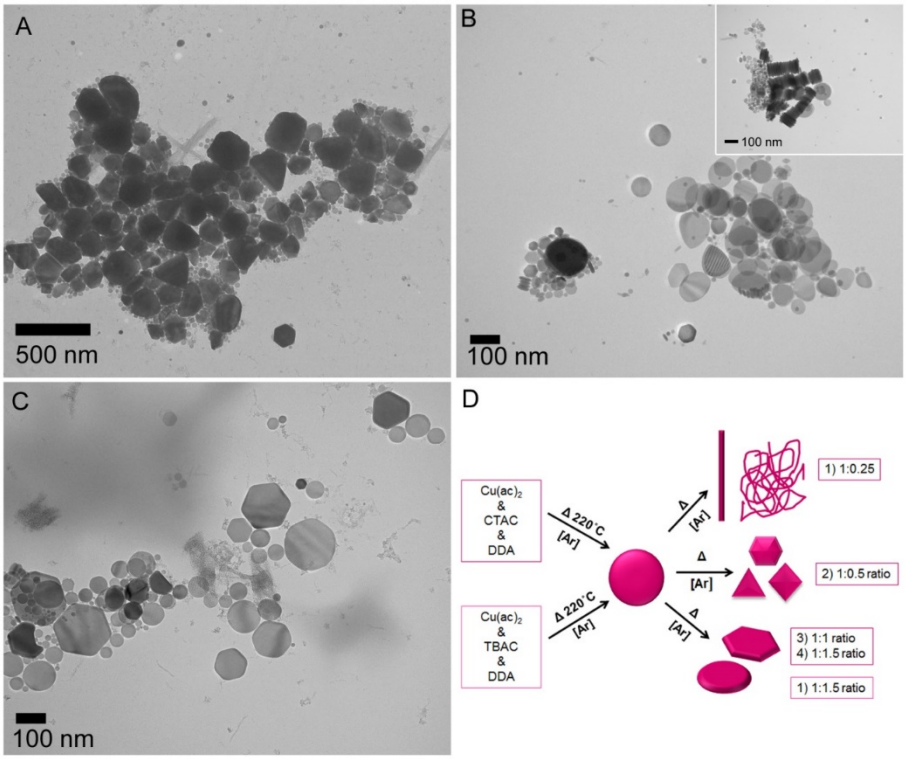

Figure 13: TEM characterization of the Cu NM synthesized using $Cu(ac)_2$ and CTAC at different ratios: (A) 1:0.5; (B) 1:1; (C) 1:1.5. Schematic illustration of Cu NM synthesis at varying ratios of $Cu(ac)_2$ to CTAC.

2.6.3 Varying the ratio of $Cu(ac)_2$ to $CuBr_2$ (synthesis set 13)

Synthesis set 13 investigated the influence of external bromide on Cu NM growth by using $CuBr_2$. The ratio between the amount of $Cu(ac)_2$ and $CuBr_2$included: 1:0.5, 1:1, 1:1.5. Characterization by TEM can be found in **Figure 14**, **A-C;Figure 14 D** provides an illustration of the growth conditions and corresponding nanomaterial morphology. Additional characterization of Cu NM, from synthesis set 13, was demonstrated in **Figure S20**, which included TEM, UV-Vis, and XRD. Based on the TEM images, a mixture of wires, bipyramids and pyramids (**Fig. 14A and S20A**), a mixture of wires, bipyramids and pyramids (**Fig. 14B and**

S20B), and hexagonal nanoplates and bipyramids (**Fig. 14C and S20C**), were obtained at ratios of 1:0.5, 1:1, and 1:1.5, respectively. The UV-Vis spectra exhibits a peak at 603, 590, and 467 nm for ratios of 1:0.5, 1:1, and 1:1.5, respectively (**Fig. S20**, **D-F**). The XRD patterns are in **Figure S20, C & F.**. , which can be indexed to {111}, {200}, {220}, and {311} planes of face-centered cubic (fcc) Cu crystal structure. XRD pattern C possess peaks at 42.2˚, 49.6˚, 73.5˚, and 89.34˚, which are downshifted from the {111}, {200}, {220}, and {311} planes of face-centered cubic (fcc) Cu crystal structure. The shift in peak position may be due to sample preparation, and additional characterization is required. XRD pattern F demonstrates peaks at 42.59˚, 49.6˚, 73.5˚, and 89.34˚. These 2θ values are downshifted from the Cu^0standard, {111}, {200}, {220}, and {311} planes of face-centered cubic (fcc) Cu crystal structure.

The difference in morphology, when varying the ratio, supports the previous findings that the bromide anion functions as a facet specific protector, which ultimately directs nanomaterial growth.

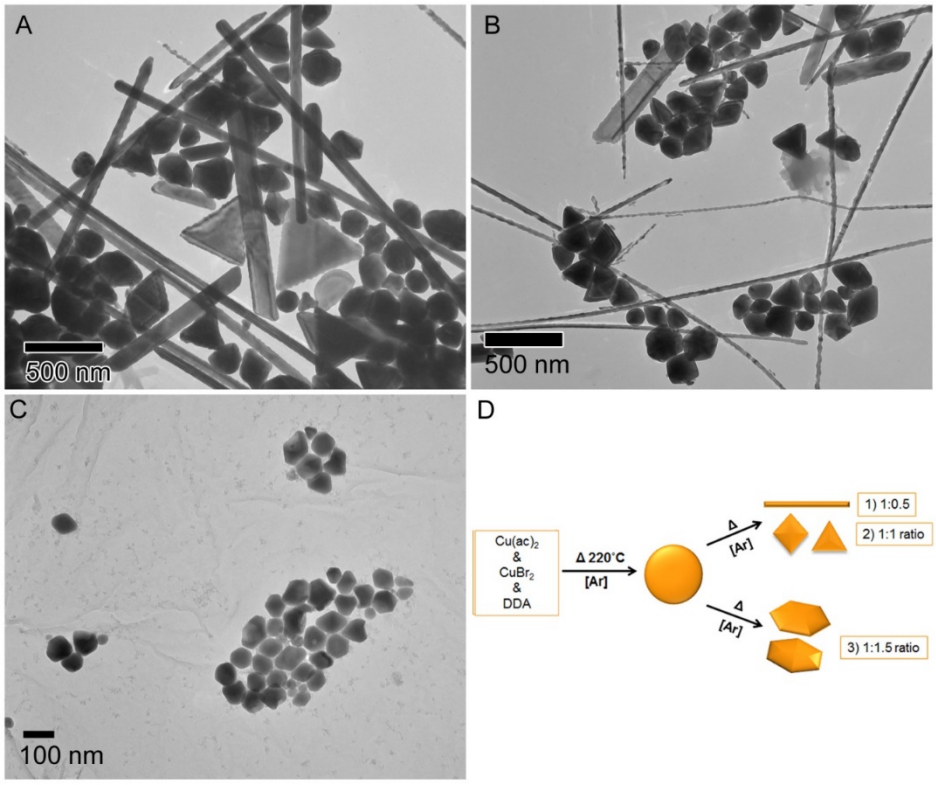

Figure 14: TEM characterization of the Cu NM synthesized using $Cu(ac)_2$ and $CuBr_2$ at different ratios: (A) 1:0.5; (B) 1:1; (C) 1:1.5. Schematic illustration of Cu NM synthesis at varying ratios of $Cu(ac)_2$ to $CuBr_2$.

2.6.4 Varying the ratio of $Cu(ac)_2$ to CTAB (Synthesis set 14)

Synthesis set 14 investigated the influence of external bromide on Cu NM growth by using CTAB. The ratio between the amount of $Cu(ac)_2$ and CTAB included: 1:0.5, 1:1, 1:1.5. The results of TEM characterization can be found in **Figure 15**, **A-C**, while**Figure 15 D** provides an illustration of the growth conditions and corresponding nanomaterial morphology. Additional characterization of synthesis set 14 Cu NM, by TEM, UV-Vis, and XRD was provided in **Figure S21.** The TEM images determined the Cu NM morphologies obtained at ratios of 1:0.5, 1:1, 1:1.5. These syntheses formed a mixture of nanowires and non-uniform polyhedra (**Fig. 15A and S21A**), a mixture of nanowires and pyramids, with spheres (**Fig. 15B and S21B**), and hexagon and spherical Cu NPL (**Fig. 15C and S20C**), respectively. The UV-Vis spectra, for ratios of 1:0.5, 1:1, and 1:1.5, exhibit peaks at 588, 616, and 539nm, respectively

(**Fig. S20**, **D-F**). Different morphologies formed when the ratio was varied. This supports the previous results that the bromide anion selectively binds to facets, directing Cu NM growth. Additionally, the Cu NM morphologies from part I differ from part II. This suggests that the copper precursors, specifically the reduction and nucleation process, may influence the crystal growth. This could relate to different reduction rates between $Cu(acac)_2$ and $Cu(ac)_2$ and the binding strength of the ligands acetylacetonate vs acetate. [21]

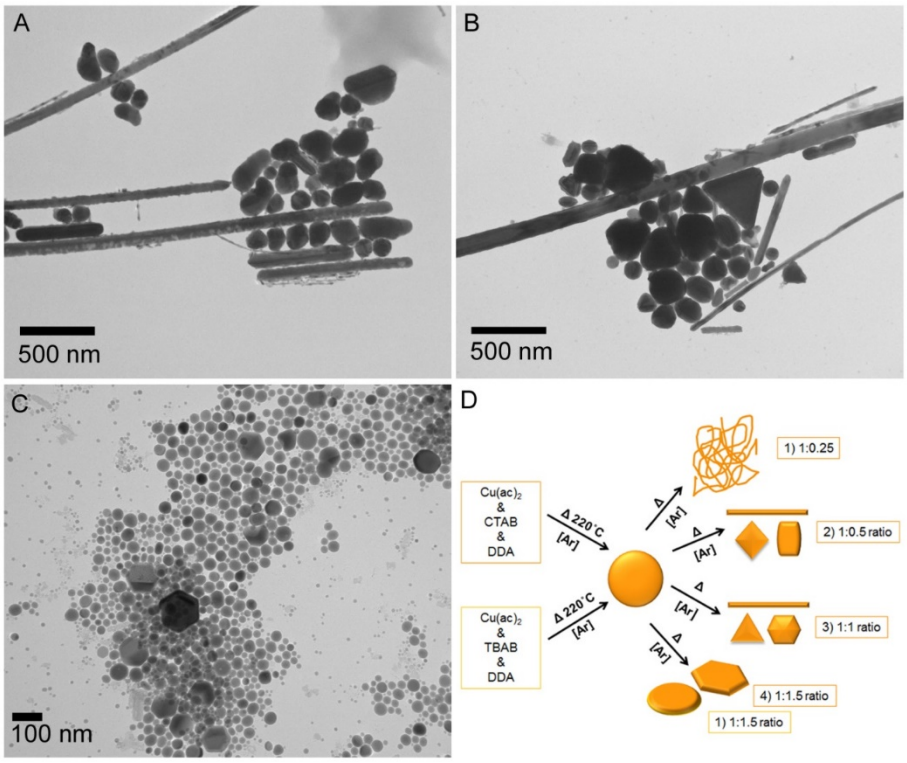

Figure 15. TEM characterization of the Cu NM synthesized using $Cu(ac)_2$ and CTAB at different ratios: (A) 1:0.5; (B) 1:1; (C) 1:1.5. Schematic illustration of Cu NM synthesis at varying ratios of $Cu(ac)_2$ to CTAB.

2.6.5 Determining the morphology of $Cu(ac)_2$ with TBAC or TBAB at a 1:1.5 ratio (synthesis set 13 & 15)

Synthesis sets 13 and 15 investigated the influence of external chloride or bromide on Cu NM growth by using TBAC or TBAB. This studied determined if the cation on the external halide source influenced Cu NM growth. The 1:1.5 ratio between the amount of $Cu(ac)_2$ and

TBAC or TBAB was used for this study. Based on the TEM images (**Fig. 16, A and B**), both syntheses formed a mixture of hexagon and spherical Cu NPL. The UV-Vis spectra exhibit a peak at 401 and 566 nm, for TBAC and TBAB, respectively (**Fig. 16**, **C and D**). These results suggest that the corresponding cation to the bromide source does not influence nanomaterial growth. Since only the 1:1.5 ratio was studied, additional ratios and the resulting morphologies need to be investigated in order to complete the study.

The structures formed by synthesis set 12, is similar to synthesis set 11, which supports the results that chloride will direct Cu NM growth and the corresponding cation does not influence growth. These results differ from synthesis set 10, which suggests that the dual copper precursor may influence nanomaterial growth. Synthesis set 15 forms similar nanostructures as synthesis set 13 and 14, which suggests that bromide directs nanomaterial growth. Additionally, these results suggest that the corresponding cation to the bromide source does not influence nanomaterial growth.

Based on the variations of Cu NM morphologies, the Cu precursor used may be responsible for the formation of different types of copper seeds and nanomaterial morphologies. In order to determine if the two copper precursors influence reduction rate, additional studies were completed by ITC (**Figures SI 1-4),** as well as the reduction kinetics (**Figures SI 5 & 6).** Each Cu precursor utilized in the synthetic process was studied by these methods. These studies could determine the strength of each Cu salt, as well as the reduction process for these individual precursors. This could provide insight into the reduction kinetics, seed formation, and Cu NM growth.

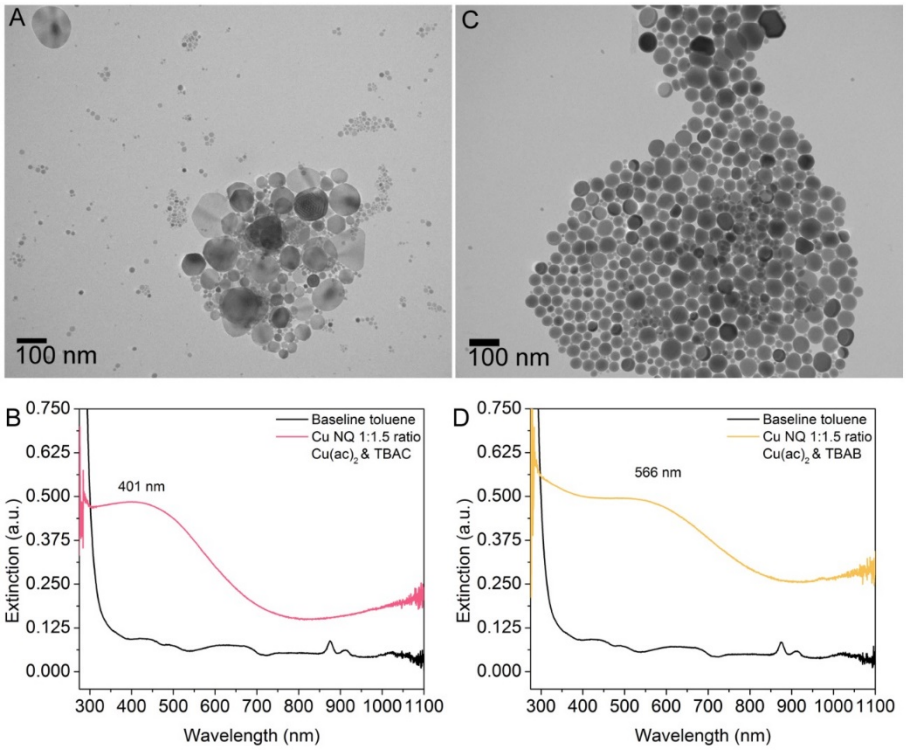

Figure 16: TEM (top row) and UV-vis (bottom row) characterization of the Cu NM synthesized using a 1:1.5 ratio of $Cu(ac)_2$ to different halides: (A,B) TBAC; and (C,D) TBAB.

2.7. **Conclusion:**

This study demonstrated that Cu NM with specific morphologies could be synthesized by the use of halides in the synthesis. The morphology of the Cu NM varies with the halide type (i.e., Cl^-, Br^-, I^-), and the halide concentration. By varying the molar ratio of $Cu(acac)_2$ and $CuCl_2$, Cu nanoparticles, rhombic dodecahedra, nanowires, and Cu nanoplates were obtained. Utilizing external chloride sources (CTAC and TBAC), did not alter the Cu NM morphologies, suggesting Cl^- is responsible for controlling Cu NM morphology. Different molar ratios of $Cu(acac)_2$ and $CuBr_2$, yielded Cu nanospheres, nanopyramides, nanooctahedra, and nanoplates. When external sources of bromide were used Cu NM morphologies remained unaltered, suggesting Br^- functions as a growth directing additive, for Cu NM shape-controlled synthesis. When $Cu(acac)_2$ and TBAI were utilized, the primary products were Cu nanoplates in circular and hexagonal shapes.

The halide influence on morphology was observed when the primary precursor was $Cu(ac)_2$ in part II; however, the resulting morphologies differed from Part I. This suggests that the reactivity of Cu precursors also play a role in the shape-controlled synthesis of Cu NM, due to the binding affinity of ligands to Cu in the precursor complex. The use of halides provides a method to control the morphologies of oil phase Cu NM, which enables the further study of Cu NM for various applications.

2.8. **Appendix A: Supporting Information Part 1:**

Synthesis set 1: detailed characterization of $Cu(acac)_2$ and $CuCl_2$ syntheses at 50 min

.

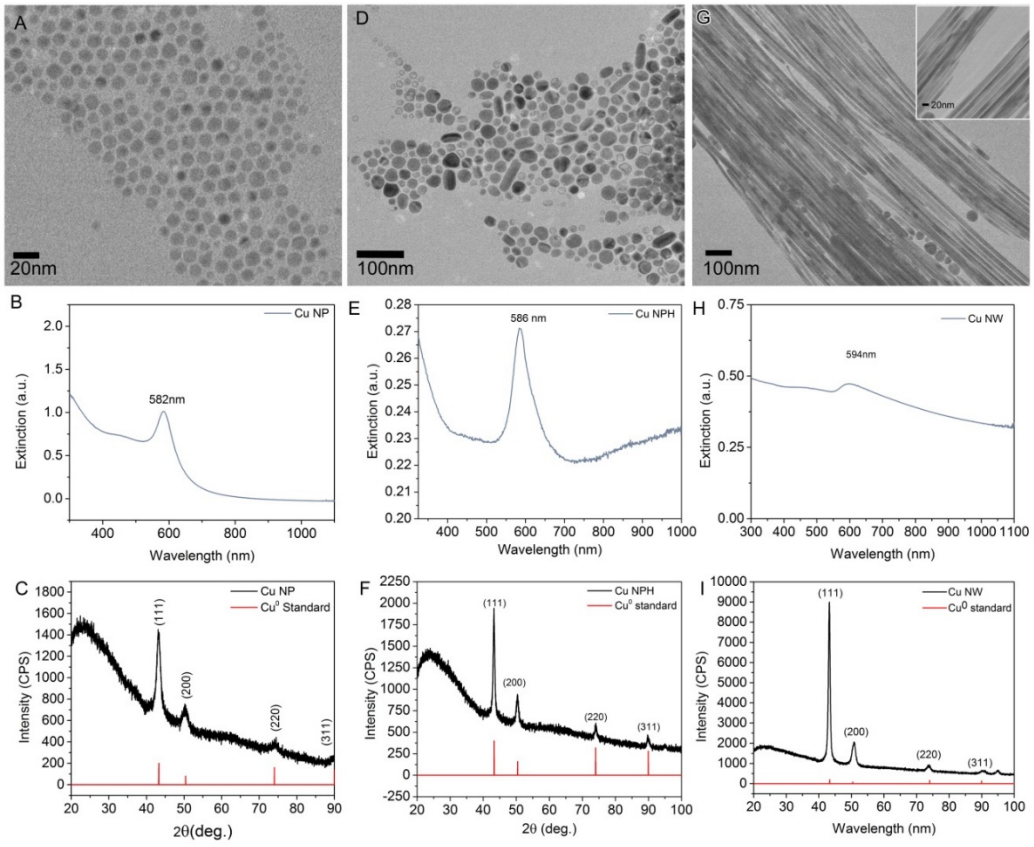

Figure S1. TEM (top row), UV-Vis (middle row), and XRD (bottom row) characterization of the Cu NM synthesized using $Cu(acac)_2$ and $CuCl_2$ at different ratios: (A-C) 1:0.5; (B-F) 1:1; and (G-I) 1:1.5.

Synthesis set 1: detailed characterization of Cu NW.

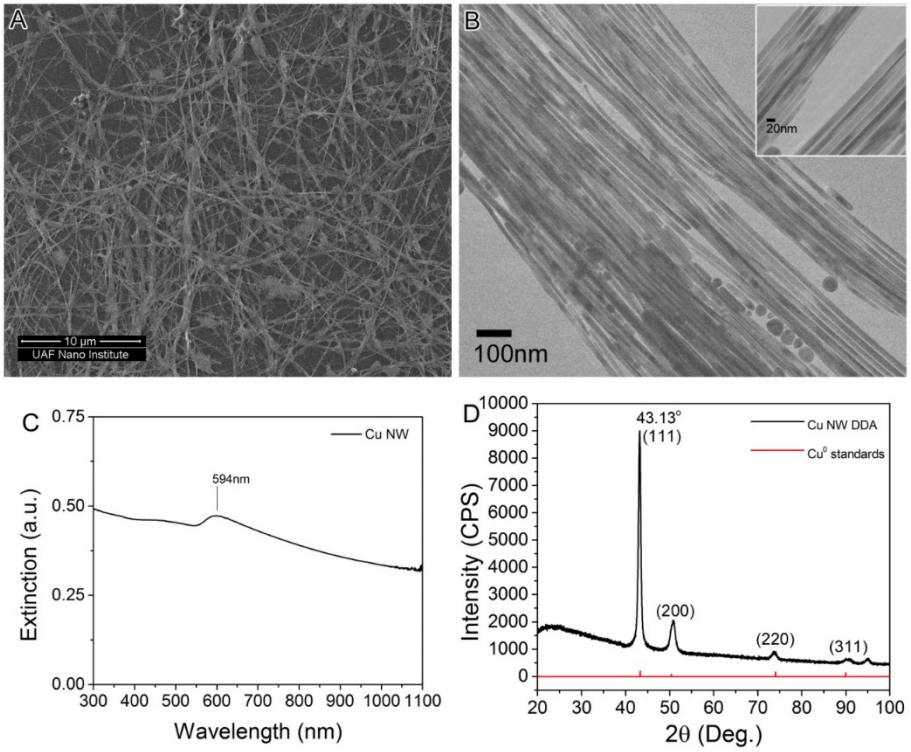

Figure S2. Characterization of Cu NW: (A) SEM image; (B) TEM image with a magnified inset; (C) UV-vis spectrum; and (D) XRD pattern.

Synthesis set 1: detailed characterization of $Cu(acac)_2$ and $CuCl_2$ syntheses at 72 hours.

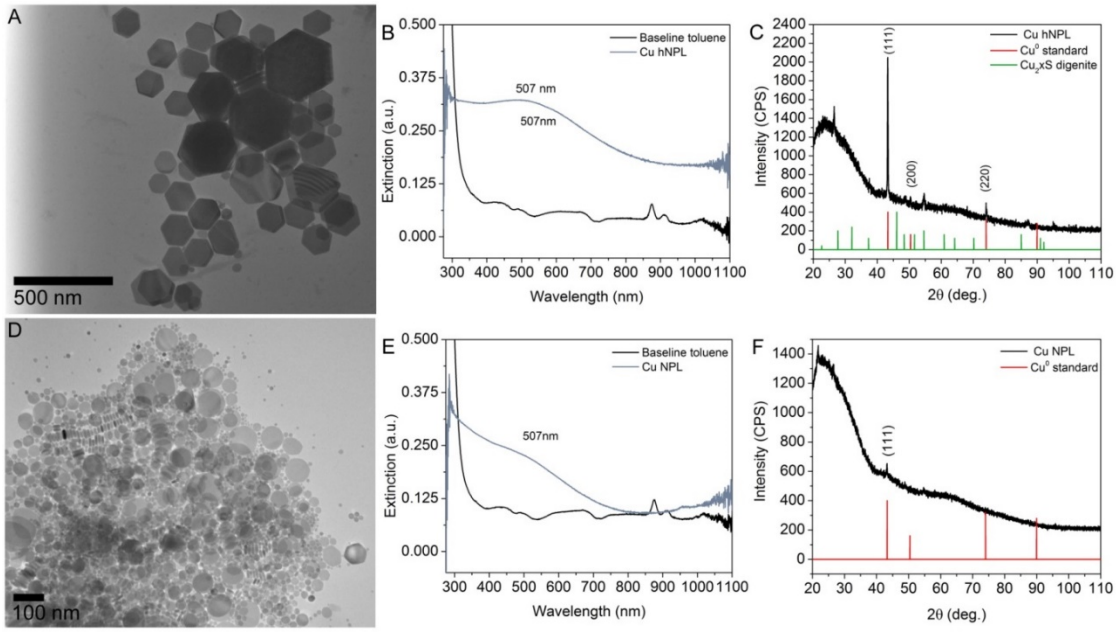

Figure S3. Characterization of Cu hNPL and Cu NPL in synthesis set 1: (A, D) TEM images; (B, E) UV-Vis spectra, and (C, F) XRD patterns.

Synthesis set 1: TEM characterization of all $Cu(acac)_2$ and $CuCl_2$, comparing morphology.

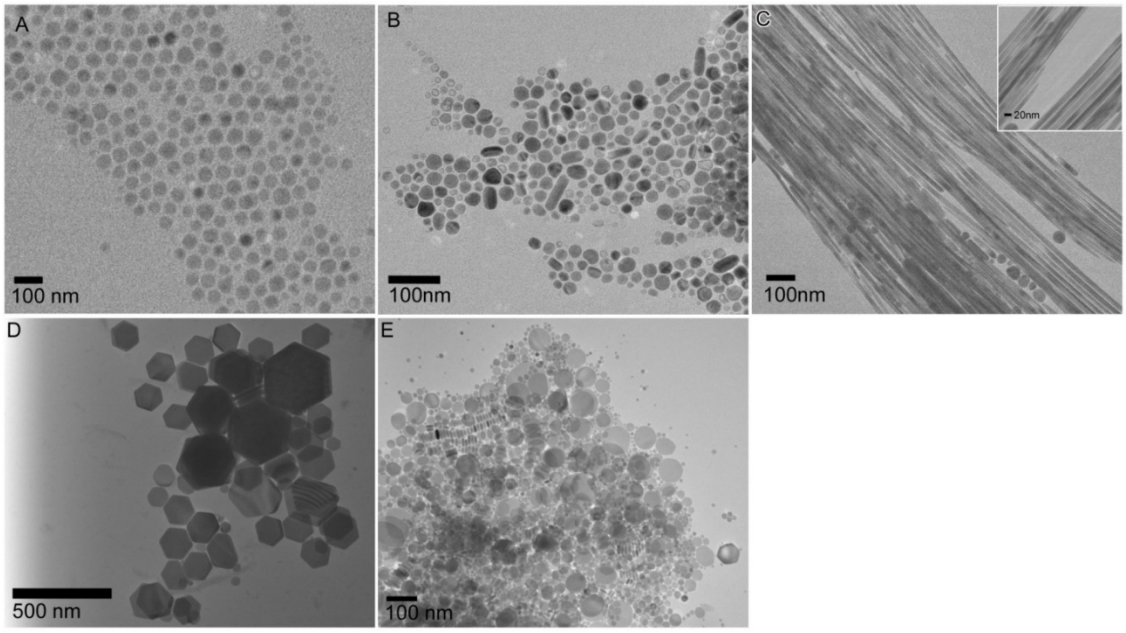

Figure S4. TEM characterization of synthesis set 1 at different ratios of $Cu(acac)_2$ to $CuCl_2$: (A) 1:0, (B) 1:0.5, (C) 1:1, (D) 1:1.5, and (E) 0:1.

Synthesis set 2: detailed characterization of $Cu(acac)_2$ and CTAC.

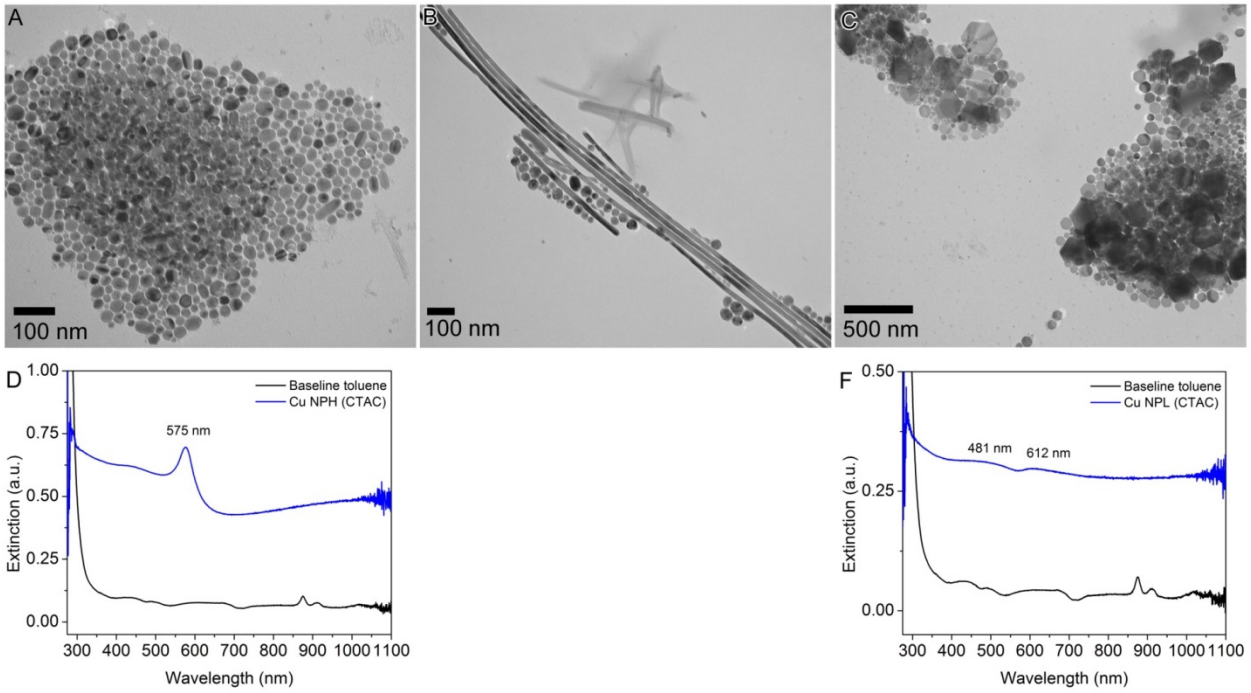

Figure S5. TEM (top row) and UV-vis (bottom row) characterization of synthesis set 2 at different ratios of $Cu(acac)_2$ to CTAC: (A, D) 1:0.5 1:1; and (C, F) 1:1.5.

Synthesis set 3: Detailed characterization of $Cu(acac)_2$ and TBAC.

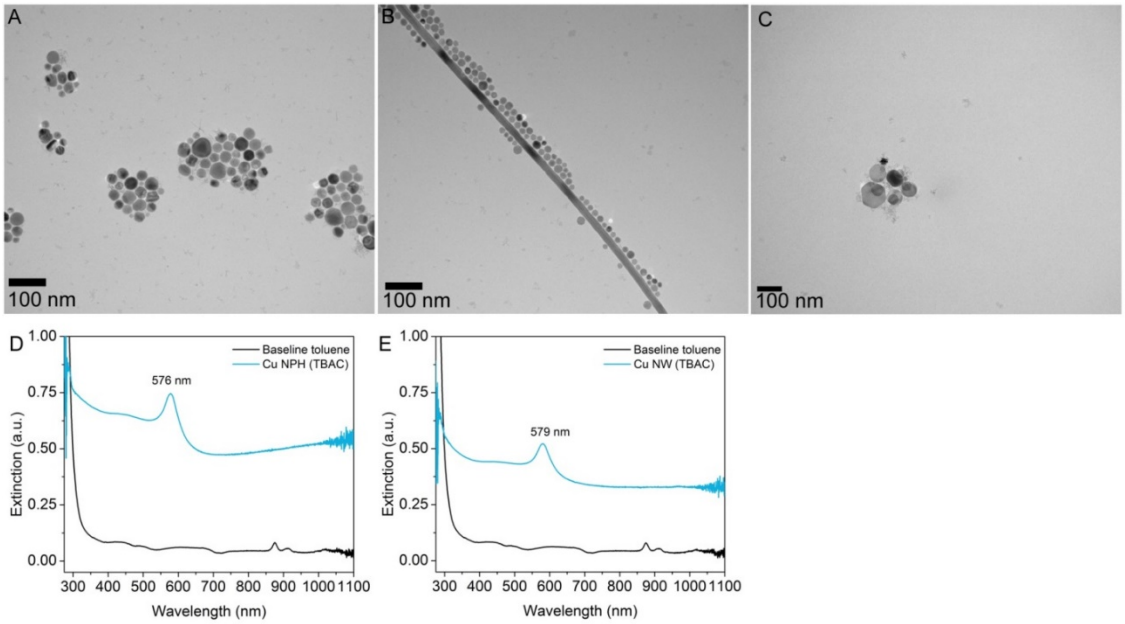

Figure S6. TEM (top row) and UV-vis (bottom row) characterization of synthesis set 2 at different ratios of $Cu(acac)_2$ to TBAC: (A,D) 1:0.5; (B) 1:1; and (C,F) 1:1.5.

Synthesis set 2 and 3: detailed characterization of $Cu(acac)_2$ & CTAC and $Cu(acac)_2$ and TBAC at a ratio of 1:0.25.

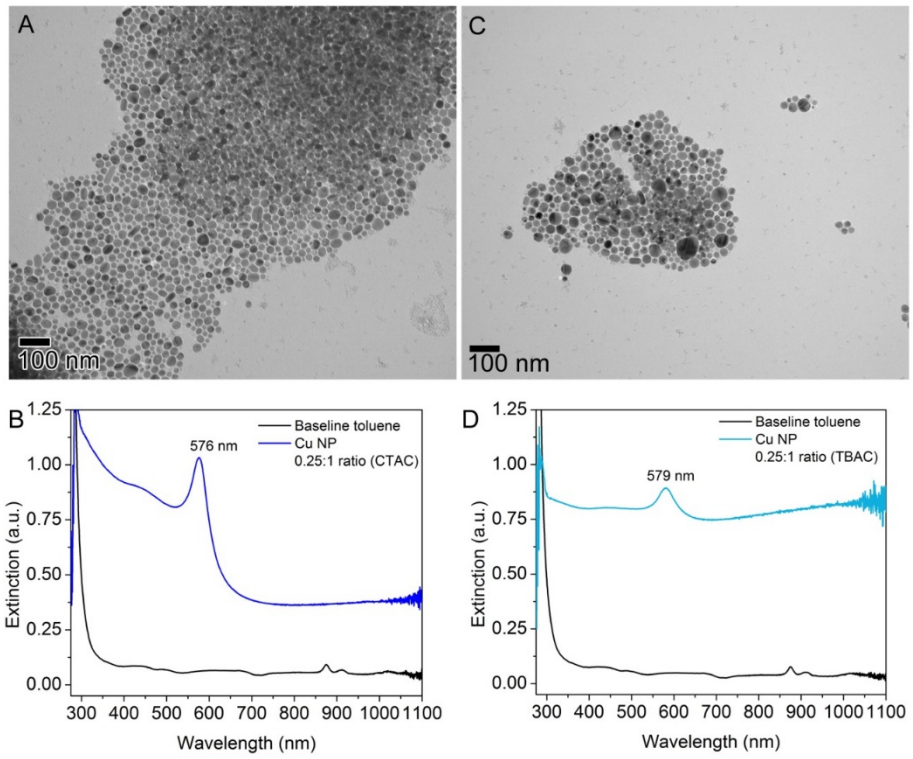

Figure S7. TEM (top row) and UV-vis (bottom row) characterization of synthesis set 2 and 3 at a 1:0.25 ratio of $Cu(acac)_2$ to different halides: (A,B) CTAC; and (C,D) TBAC.

Synthesis set 4: detailed characterization of $Cu(acac)_2$ and $CuBr_2$ synthesis for 50 min.

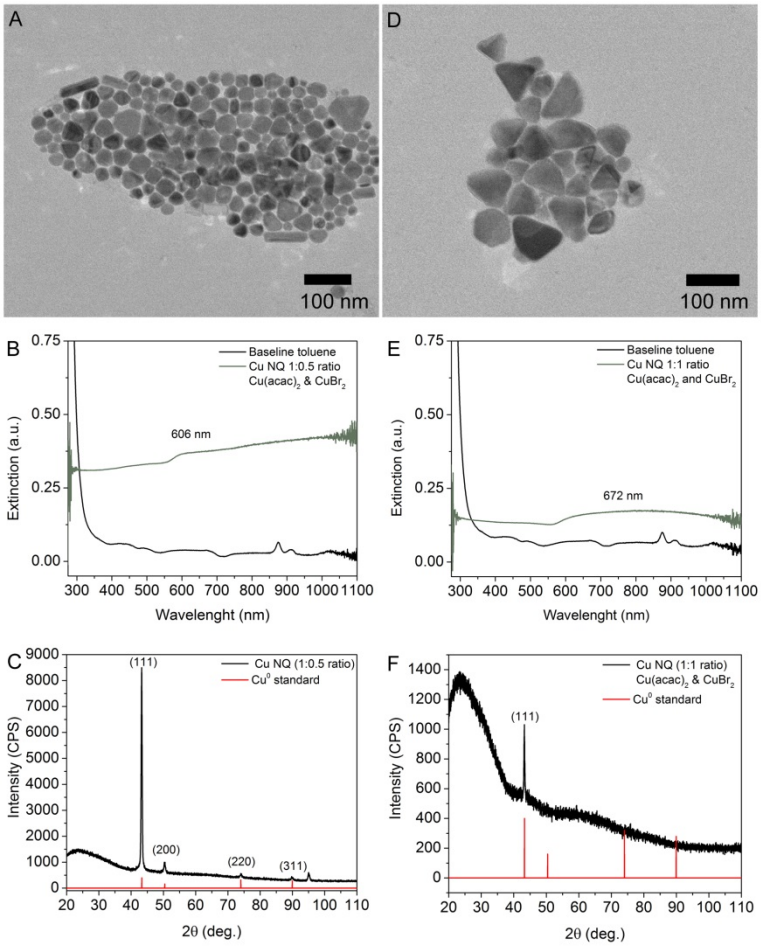

Figure S8. TEM (top row), UV-vis (middle row), and XRD (bottom row) characterization of synthesis set 4 at different ratios of $Cu(acac)_2$ to CTAC: (A-C) 1:0.5; and (D-F) 1:1.

Synthesis set 4: detailed characterization of $Cu(acac)_2$ & $CuBr_2$ synthesis for 48 hours.

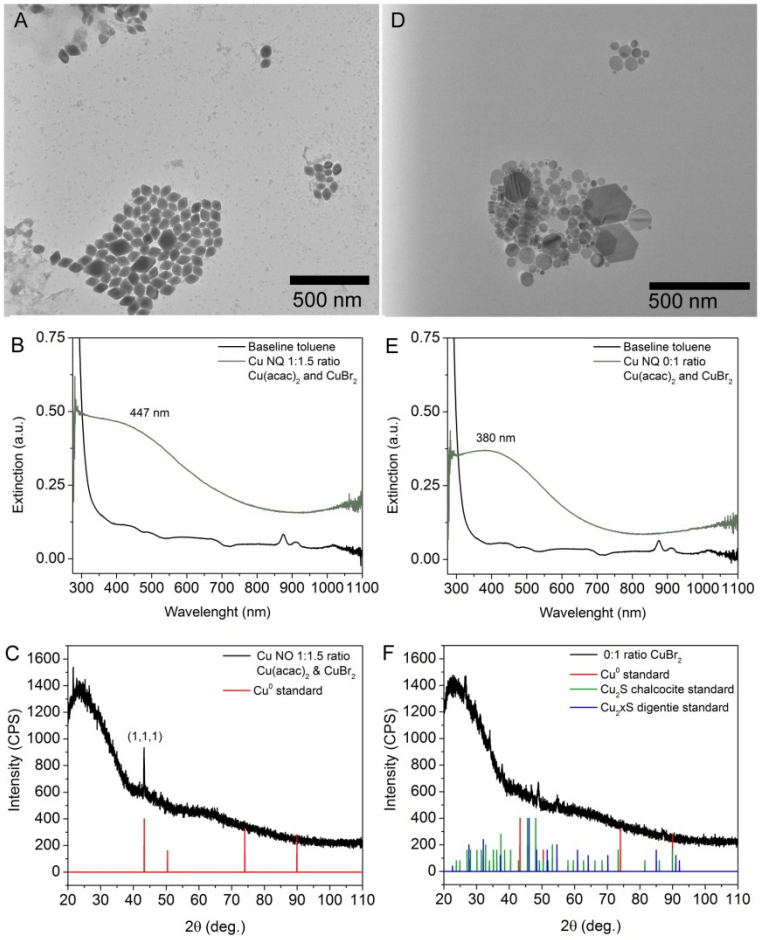

Figure S9. TEM (top row), UV-vis (middle row), and XRD (bottom row) characterization of synthesis set 4 at different ratios of $Cu(acac)_2$ to CTAC: (A-C) 1:1.5; and (D-F) 0:1.

Synthesis set 5: detailed characterization of $Cu(acac)_2$ & CTAB synthesis for 50 min.

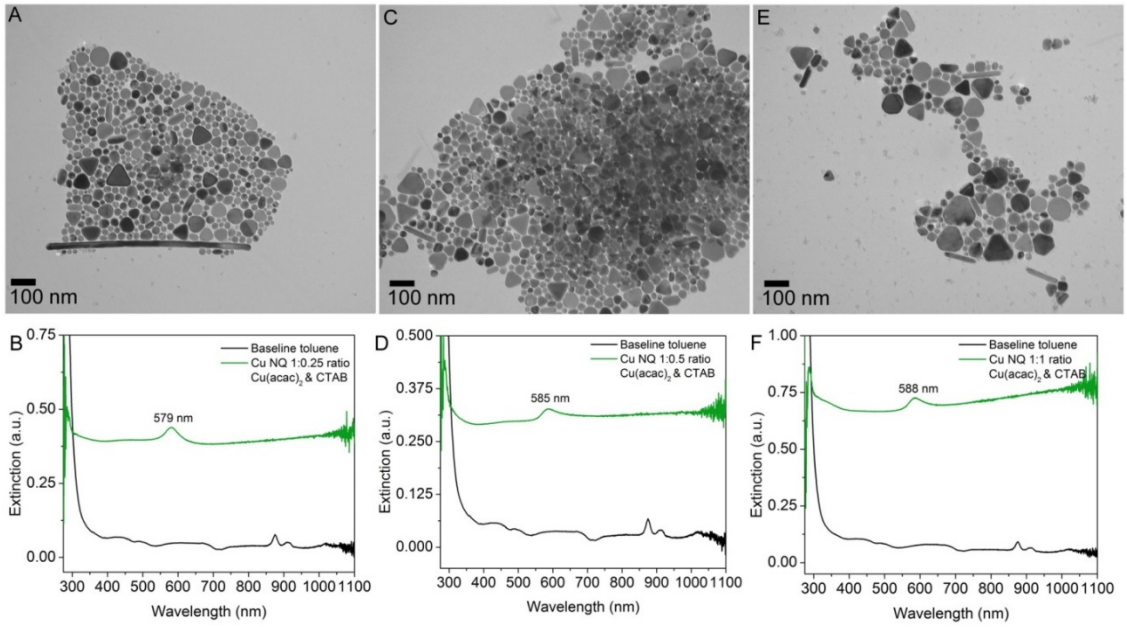

Figure S10. TEM (top row) and UV-vis (bottom row) characterization of synthesis set 5 at different ratios of $Cu(acac)_2$ to CTAB: (A,B) 1:0.5; (C,D) 1:1; and (E,F) 1:1.5.

Synthesis set 5: detailed characterization of $Cu(acac)_2$ & CTAB synthesis for 48 hours.

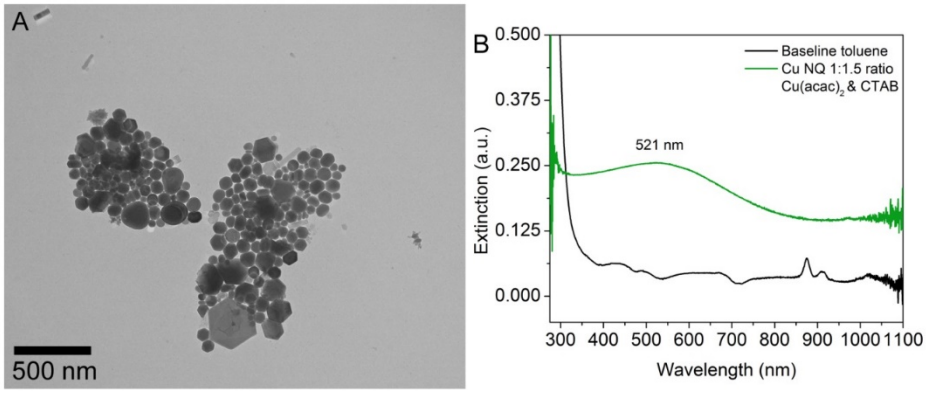

Figure S11. Characterization of synthesis set 5 at a 1:1.5 ratio of $Cu(acac)_2$ to CTAB: (A) TEM image; and (B) UV-Vis spectrum.

Synthesis set 5: detailed characterization of $Cu(acac)_2$ & CTAB at lower ratios of 1:0.1 and 1:0.05.

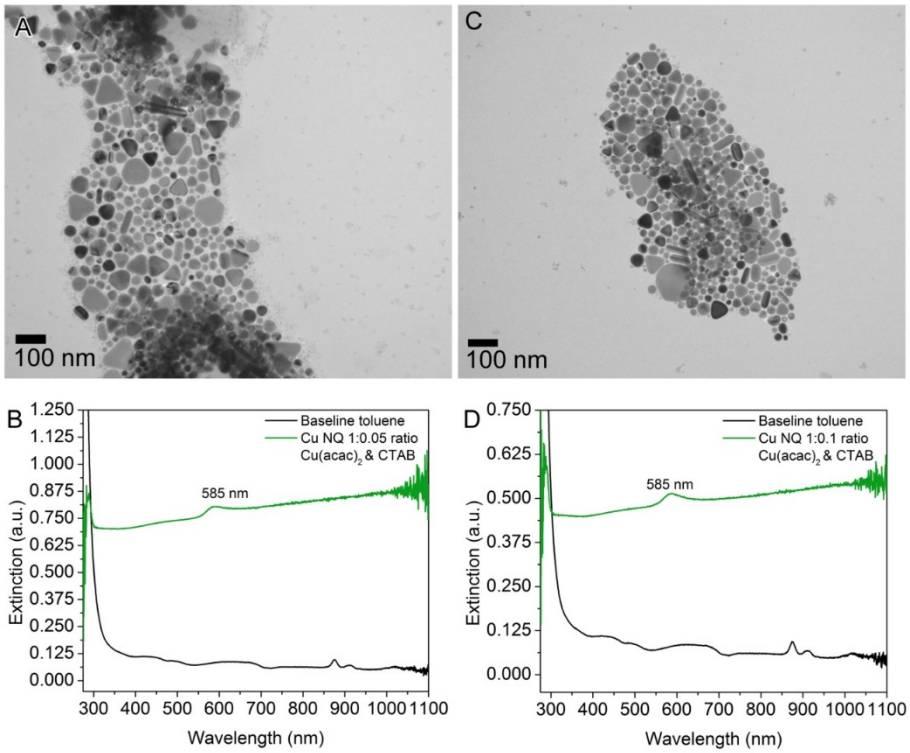

Figure S12. TEM (top row) and UV-vis (bottom row) characterization of synthesis set 5 at different ratios of $Cu(acac)_2$ to CTAB: (A,B) 1:0.1; and (C,D) 1:0.05.

Synthesis set 6: detailed characterization of $Cu(acac)_2$ & TBAB synthesis for 50 min.

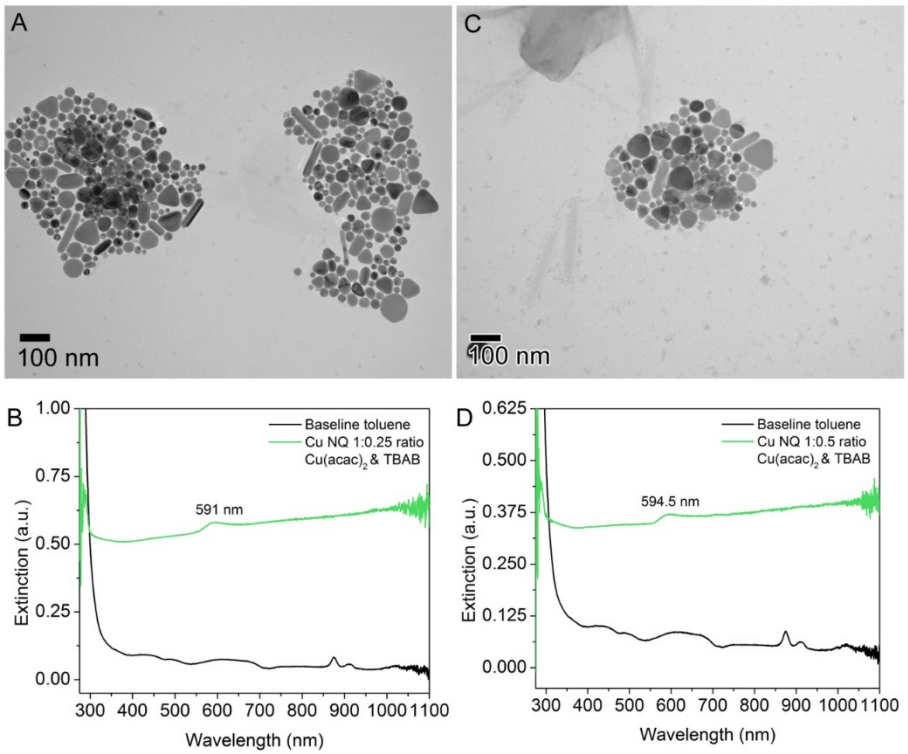

Figure S13. TEM (top row) and UV-vis (bottom row) characterization of synthesis set 6 at different ratios of $Cu(acac)_2$ to TBAB: (A, B) 1:0.25; and (C, D) 1:0.5.

Synthesis set 6: additional characterization of 1:0.5 ratio synthesis.

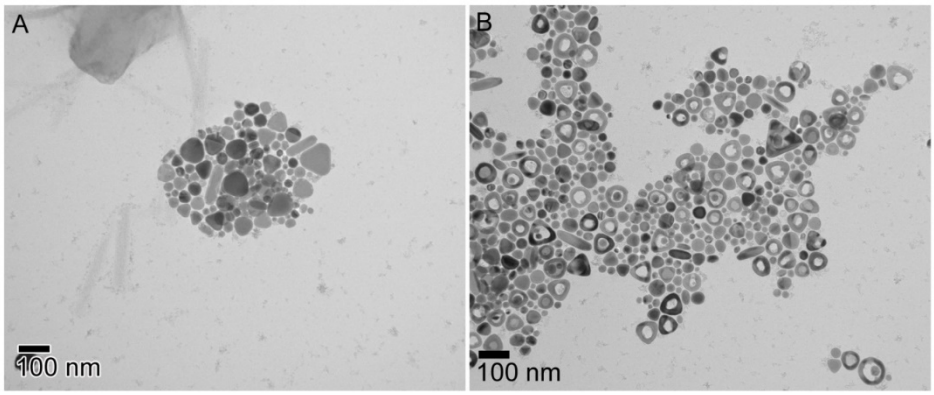

Figure S14. TEM characterization of the synthesis at a 1:0.5 ratio of $Cu(acac)_2$.

Synthesis set 5 and 6: detailed characterization of $Cu(acac)_2$ & CTAB and $Cu(acac)_2$ & TBAB at a ratio of 1:0.25.

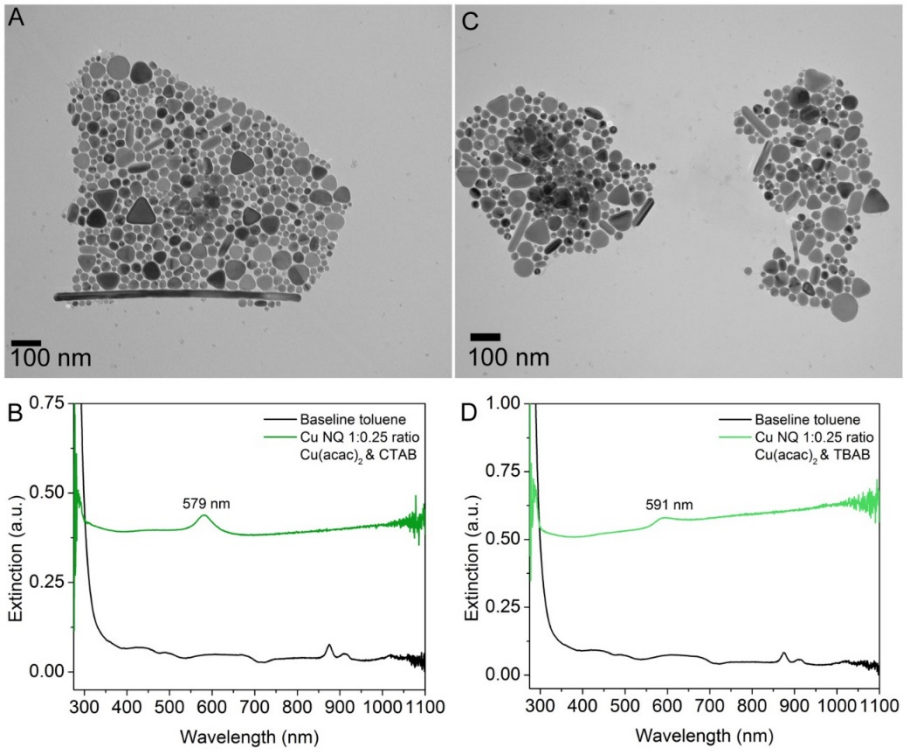

Figure S15. TEM (top row) and UV-vis (bottom row) characterization of synthesis at a 1:0.25 ratio of $Cu(acac)_2$ to different halides: (A,B) CTAB; and (C,D) TBAB.

Synthesis set 7: detailed characterization of $Cu(acac)_2$ & TBAI at various ratios.

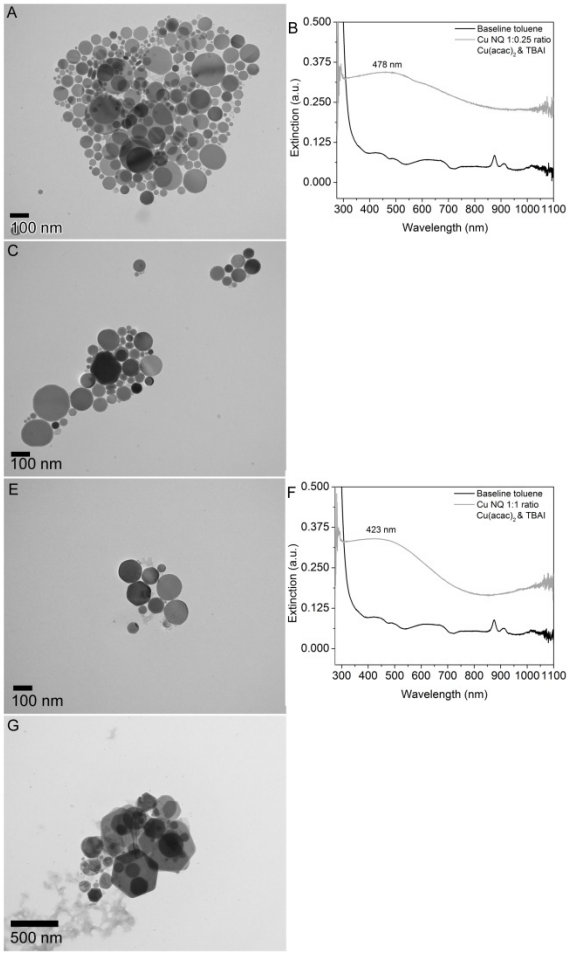

Figure S16. TEM (left) and UV-vis (right) characterization of synthesis set 7 at different ratios of $Cu(acac)_2$ to TBAI: (A,B) 1:0.25; (C,D) 1:0.5; (E,F) 1:1; and (G,H) 1:1.5.

Synthesis set 10: detailed characterization of $Cu(ac)_2$ and $CuCl_2$ at different ratios.

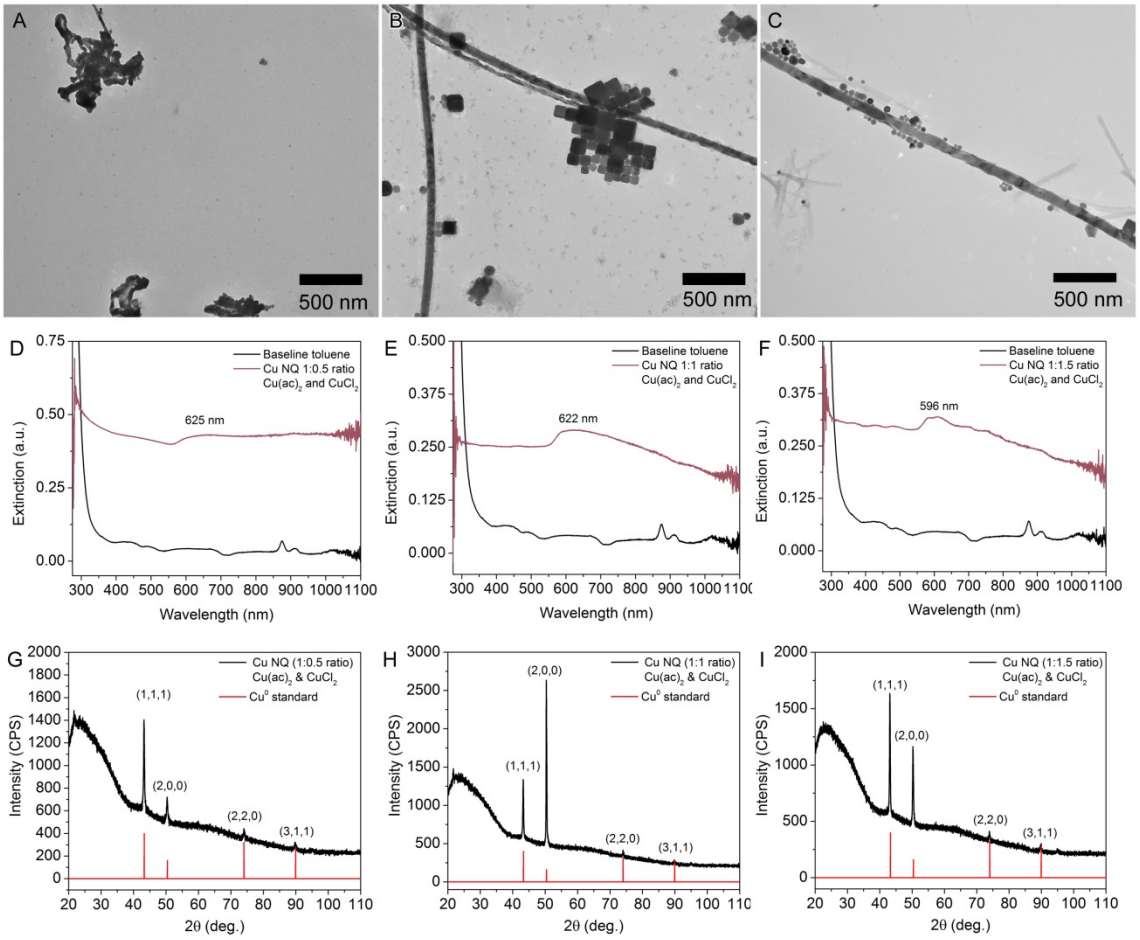

Figure S17. TEM (top row), UV-vis (middle row), and XRD (bottom row) characterization of synthesis set 10 at different ratios of $Cu(ac)_2$ to $CuCl_2$: (A,D,G) 1:0.5; (B,E,H) 1:1; and (C,F,I) 1:1.5.

Synthesis set 11: detailed characterization of $Cu(ac)_2$ and CTAC synthesis at different ratios.

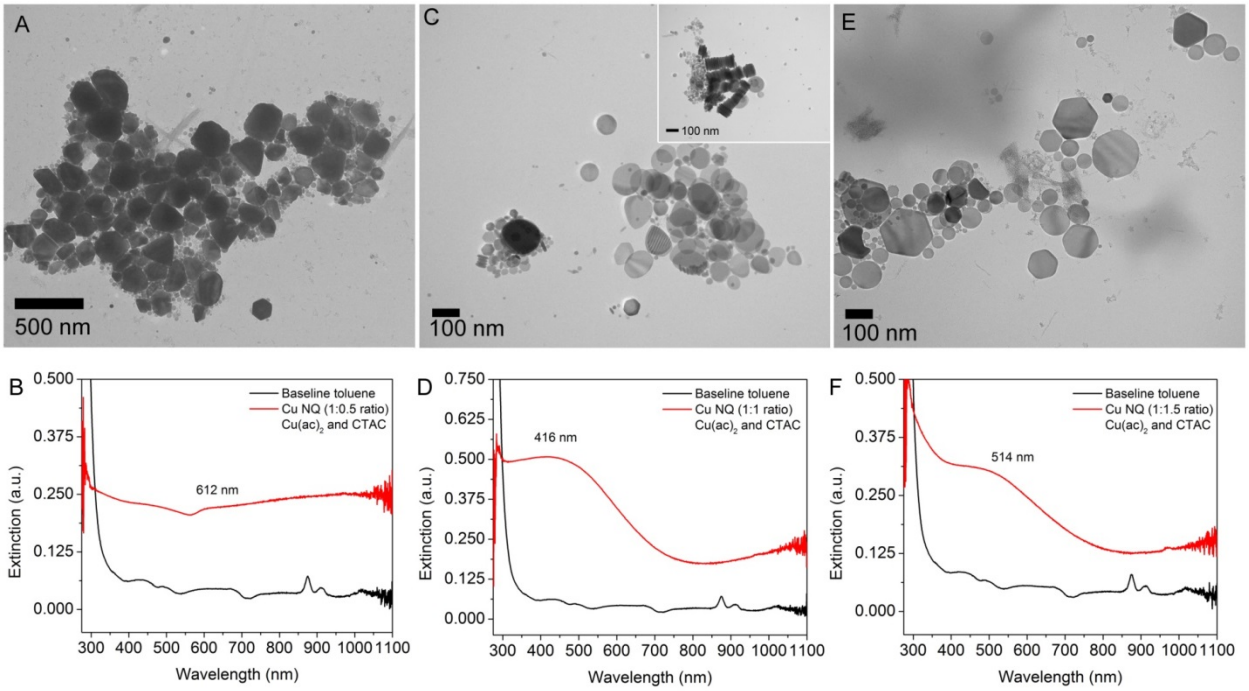

Figure S18. TEM (top row) and UV-vis (bottom row) characterization of synthesis set 11 at different ratios of $Cu(ac)_2$ to CTAC: (A,B) 1:0.5; (C,D) 1:1; and (E,F) 1:1.5.

Synthesis set 11: detailed characterization of $Cu(ac)_2$ and CTAC at a ratio of 1:0.25

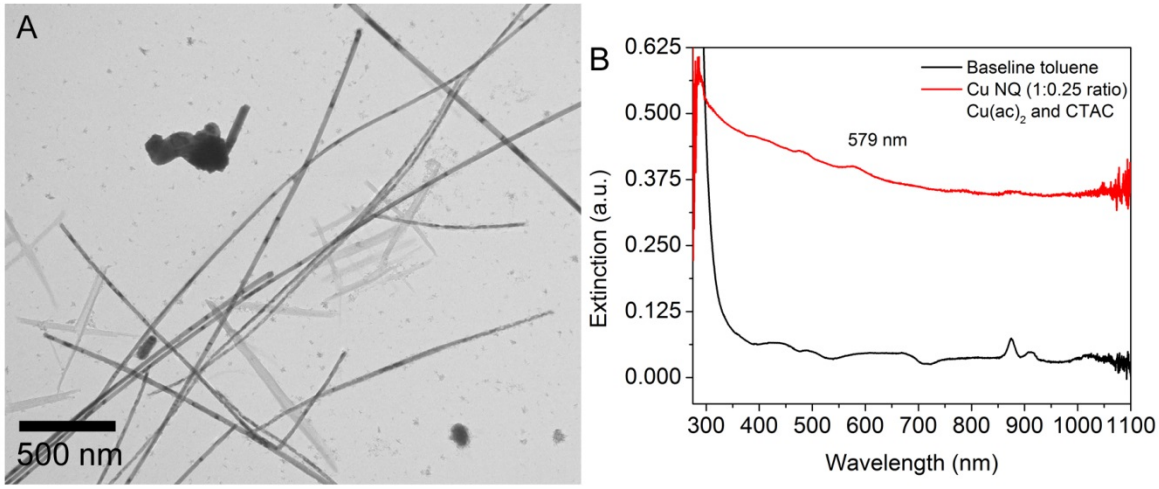

Figure S19. Characterization of synthesis at a 1:0.25 ratio of $Cu(ac)_2$ and CTAC: (A) TEM image; and (B) UV-Vis spectrum.

Synthesis set 13: Detailed characterization of $Cu(ac)_2$ and $CuBr_2$ synthesis at different ratios

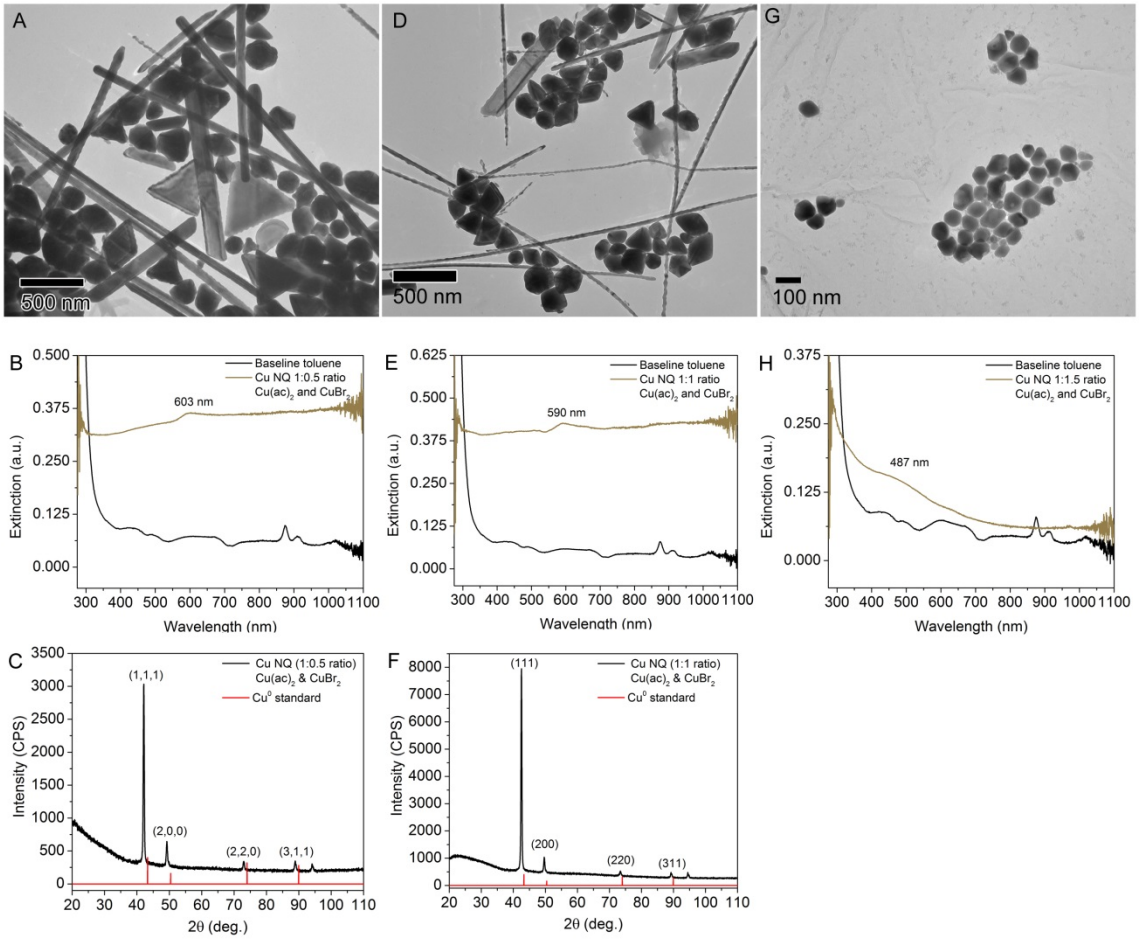

Figure S20. TEM (top row), UV-vis (middle row), and XRD (bottom row) characterization of synthesis set 12 at different ratios of $Cu(ac)_2$ to $CuBr_2$: (A-C) 1:0.5; (D-F) 1:1; and (G-I) 1:1.5.

Synthesis set 14: detailed characterization of $Cu(ac)_2$ and CTAB synthesis at different ratios.

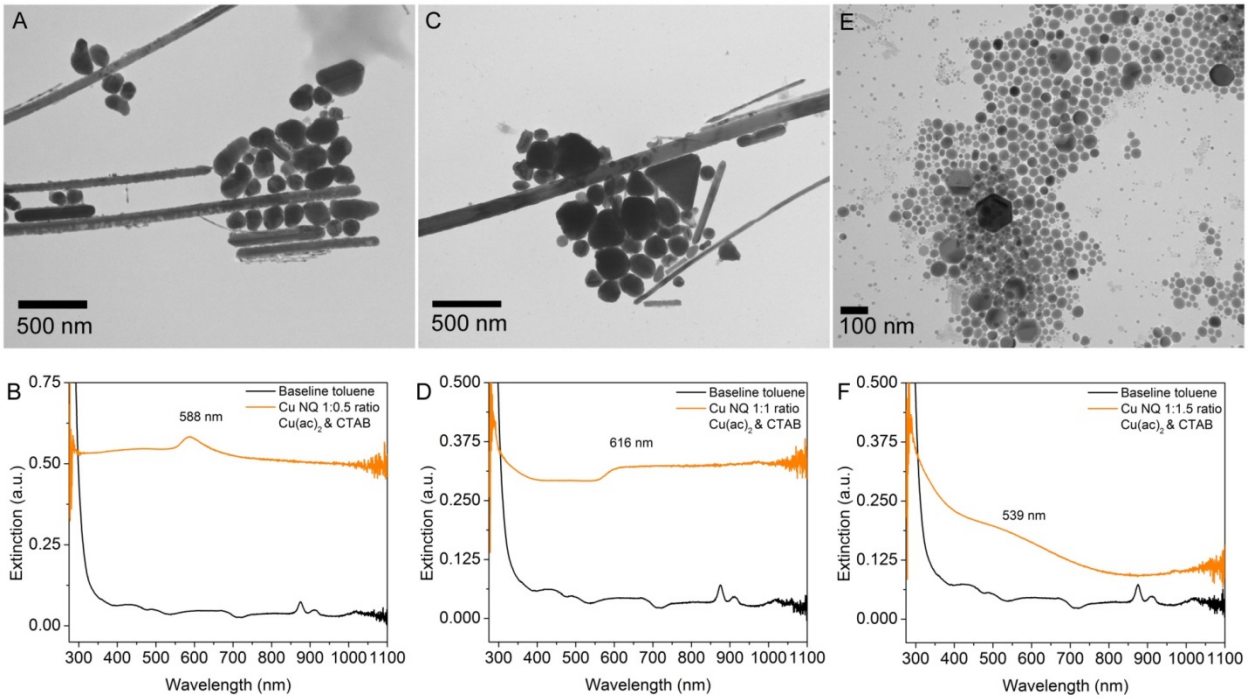

Figure S21. TEM (top row) and UV-vis (bottom row) characterization of synthesis set 13 at different ratios of $Cu(ac)_2$ to CTAB: (A,B) 1:0.5; (C,D) 1:1; and (E,F) 1:1.5.

Synthesis set 14: detailed characterization of $Cu(ac)_2$ and CTAB at a ratio of 1:0.25.

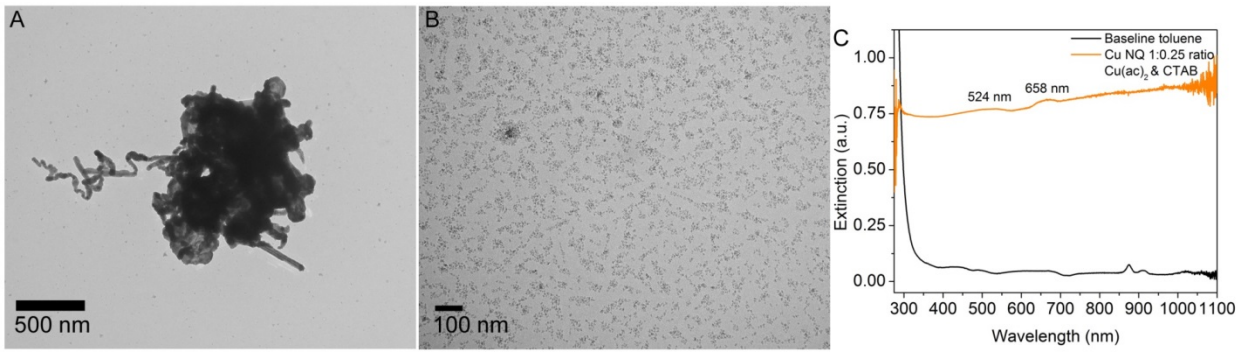

Figure S22. Characterization of synthesis at a 1:0.25 ratio of $Cu(ac)_2$ and CTAB: (A,B) TEM image; and (C) UV-Vis spectrum.

2.9. Appendix B: Supplemental information Reduction Kinetics/ITC Study

2.9.1. Abstract

This part focuses on studying the growth mechanism of the Cu NM through the heat of solvation and the reduction kinetics experiments. These experiments will determine the heat of

solvation when the amine ligand binds to the Cu precursor, forming the copper-amine complex prior to nucleation. From these results the change in molar enthalpy can be determined, which correlates to the change in entropy and the stability of the Cu precursor. The reduction kinetics as the Cu precursor is reduced by the amine ligand and nucleates. The amine ligands and the copper precursors were chosen based on their purpose in the Cu NM syntheses. The elucidation of the formation of the copper-amine complex and the reduction kinetics could provide useful information pertaining to the nucleation event, formation of copper nanoparticles, and ultimately the growth into a specified morphology.

2.9.2 Appendix B: Experimental Methods

2.9.2.1 ITC:

This research was to study the formation of the copper-amine complex that is formed prior to the copper reduction and formation of copper nanocrystals. The thermodynamic studies will focus on the heat of solvation of the amine-copper complex, which will provide the change in enthalpy of the copper-amine complex formation. The results can be related to the bond energy of the copper-amine complex, which correlates bond energy and the reduction kinetics of copper precursors to various amine ligands. The calorimetric studies were completed with an isothermal calorimeter; the results were used to obtain the change in enthalpy that occurred as a result of the amine ligand binding to the copper precursor.

The basic set up for the ITC system can be seen in **Figure SI1**. The experimental set up for the calorimetry experiments was specifically designed to obtain the heat produced as the amine ligand binds to one of the two possible binding sites on the copper precursors. Figure 3 also demonstrates the proposed reactions that occur when the copper precursor and respective amine capping ligand are combined in the ITC. In each of these reactions, the specific amine

capping ligand will replace one of the ethanols attached to the copper precursor in the axial position, forming the copper-amine complex. The copper precursors that were chosen for this experiment were $Cu(ac)_2$ and $CuCl_2$, and the two amine ligands chosen were OLA and DDA. The amine ligands were not only chosen due to their use in the Cu NW synthesis, but also due to their difference in chain length. The two copper precursors were chosen due to their use in the copper nanoparticle synthesis, as well as the number of binding sites present on the central copper atom. Additionally, the amines and the copper precursors were chosen due to their facile solubility in ethanol.

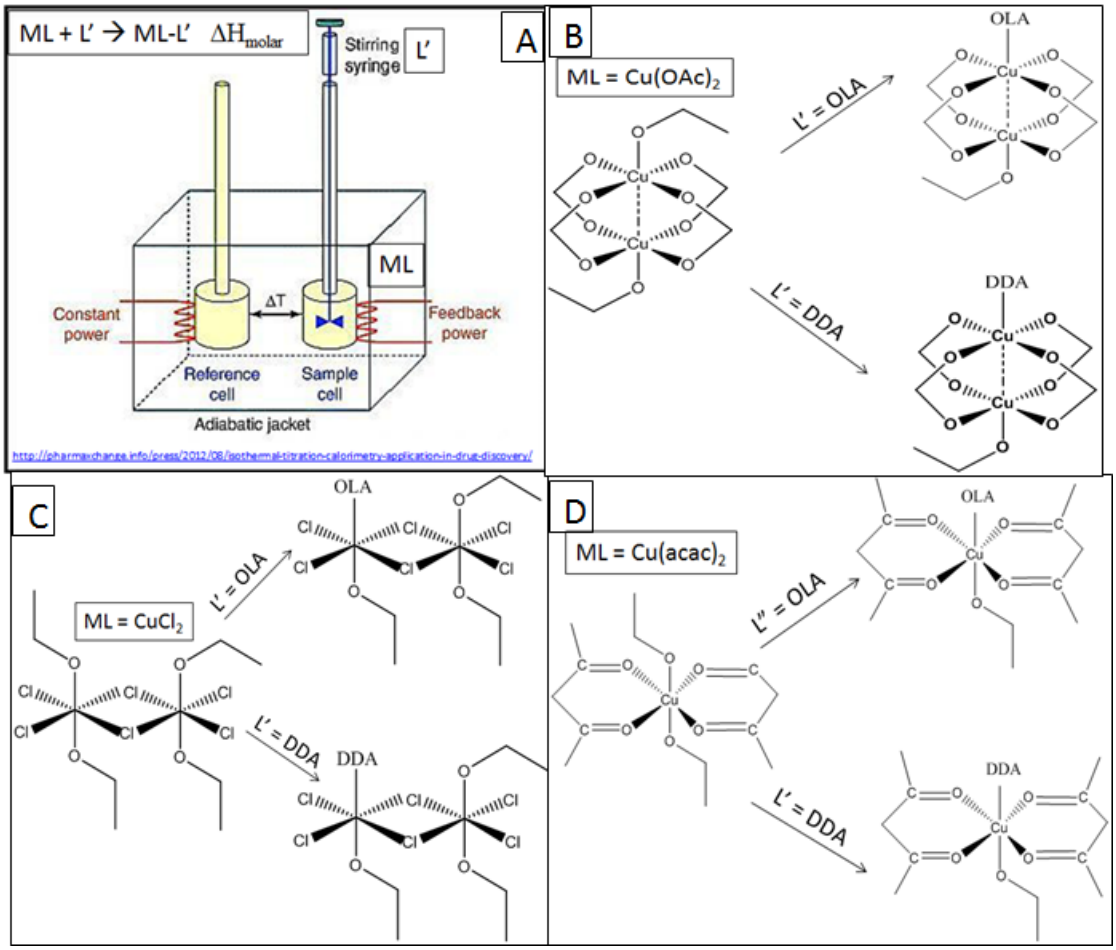

Figure SI. 1. Schematic illustration of ITC set up (A) and the three ITC experiments that will be studied (B-D).

The calorimetry experiments were broken into four main experiments, each experiment was run in triplicate to ensure reproducibility of the experiment, and these results can be found in the experimental section. The first type of experiments compared amines binding to $Cu(OAc)_2$, specifically the binding of OLA to $Cu(OAc)_2$ and the binding of DDA to $Cu(OAc)_2$. In the first experiment, $Cu(OAc)_2$ was dispersed in EtOH and OLA was dispersed in EtOH. The second experiment studied the binding of DDA in EtOH to $Cu(OAc)_2$ in EtOH. The second set of experiments compared the binding of various amines to $CuCl_2$. The third experiment studied the binding of OLA in EtOH to $CuCl_2$ in EtOH and the fourth experiment observed the binding of DDA in EtOH to $CuCl_2$ in EtOH. Each of the reaction types had the following experimental parameters: the ITC cell, with a total volume of 1.3mL, was filled with the specified copper precursor dispersed in an organic solvent, and a 100μL syringe was filled with the amine ligand dispersed the same organic solvent, and placed into the cell as shown in Figure 14. The surrounding temperature of the ITC cell was regulated using a water bath set to 18˚C. After the ITC was assembled, and allowed to equilibrate, this allowed for the solution temperature inside the cell to reach zero prior to experimental run. Once the solution had equilibrated, the reaction parameters were set to inject the amine ligand in 6μL increments 10 times. After 5 injections a 1:1 molar ratio was reached between the copper precursor and the amine ligand. After the reaction was complete the change in enthalpy (ΔH), binding constant (K), and the change in entropy (ΔS) were determined.

2.9.2.2 <u>Reduction Kinetics Study:</u>

The reduction kinetics experiments will focus on elucidating the reduction of copper (II) precursors to neutral valent copper in the presence of various amine capping ligands that are commonly utilized in the syntheses protocols of copper nanomaterials formulated by the Chen

group. With these experiments the reduction kinetics, supersaturation of Cu^0, and Cu NP nucleation can be monitored. These experiments will determine if the reduction kinetics of Cu^{2+} to Cu^0 and the nucleation event of copper nanoparticles are altered by either a change in copper (II) precursors or a change in amine capping ligands. These experiments will be correlated to the heat of solvation experiments, and ultimately determine if there is an effect on the resultant copper nanomaterial structure. The information procured from these reduction kinetics experiments will be utilized in the galvanic replacement to form platinum copper nanomaterials and will be discussed in greater detail in specific aim 3. The reduction kinetics experiments will be broken into multiple experiments total experiments. The first two experiments will study copper (II) acetylacetonate dispersed in either oleylamine or dodecylamine. The second two experiments will study copper (II) chloride dispersed in either OLA or DDA. The final reduction kinetics experiment will study the reduction of copper (II) acetate with OLA, to provide additional information for Cu^{2+} reduction kinetics. These chemicals were chosen due to their use in the formation of copper nanospheres and copper nanowires. In general, the copper precursor is dispersed into the amine capping ligand, degassed, and gradually heated in increasing increments of 25 ºC until 150 ºC has been reached. During this initial increase in temperature the reaction solution color will change from light blue to darker blue to dark green at ~150 ºC. At which point the reduction kinetics experiment will continue under a time course study. This means that the sample taken at 150 ºC corresponds to 0mins, a subsequent sample was taken at the following time intervals: 2, 5, 10, 15, 20, and 30 minutes. During this 30 minute period, the reaction solution will undergo a color change from green to yellow to orange to reddish orange and finally to dark red, which corresponds to the color of copper nanoparticles. At each sampling point (25 ºC, 50 ºC, 75 ºC, 100 ºC, 125 ºC, 150 ºC/0mins, 175 ºC /2mins, 5mins, 10mins,

15mins, 20mins, 30mins) an aliquot of reaction solution is removed and immediately quenched with toluene. By studying the initial heating of the reaction solution as well as a 30 minute period after 150 ºC, a full set of data can be obtained that include both the reduction of Cu^{2+} to Cu^{0} as well as the nucleation of copper nanoparticles. Each reaction solution sample is studied by UV-Vis spectroscopy.

2.9.3 Appendix B: Results and Discussion

2.9.3.1 ITC studies

The results from the heat of solvation experiments can provide insight to the stability of the different copper precursors, and the binding affinity of different amines to the precursors, which would have implications for the reduction of the metal precursors and the growth process of the copper nanomaterials. The major data obtained from the heat of solvation experiments included the change in heat produced by the reaction over time. This data could be utilized to obtain the change in enthalpy, change in molar enthalpy, and the corresponding binding curve and binding constant for the formation of the copper-amine complex. The heat of solvation results for $Cu(Ac)_2$ can be found in Figure 4. This figure provides an example spectrum of the heat of solvation over time during the formation of the copper-amine complex, as well as the corresponding binding curve. Spectrum A and graph B provide the heat of solvation results of the binding between $Cu(Ac)_2$ and OLA, while Spectrum C and graph D providing the heat of solvation results for the formation of the $Cu(Ac)_2$ and DDA complex. Since this data focuses on the formation of the copper-amine complex using $Cu(Ac)_2$ as the metal precursor, the only conclusions can be developed focus on the different amines. The heat of solvation studies show no major difference between the amines, which suggests that different chain length amines have no significant effect on the complexation. The second set of experiments studies the

complexation between different amines to copper chloride, the results of which can be found in Figure 5. In order to obtain these results, a reduction in the concentration of the amines and copper precursors was necessary. Spectrum A and graph B provide the heat of solvation over time and the corresponding binding curve of the $CuCl_2$ with OLA. Spectrum C and graph D provide the heat of solvation and binding curve information for DDA binding to $CuCl_2$. These results support the previous results that variations in the amine capping ligand did not significantly affect the change in heat or molar enthalpy of the copper-amine complex. When comparing the binding between the copper precursors a significance differences is observed. The $CuCl_2$ precursor obtained a much higher change in heat over time compared to the $Cu(ac)_2$, and this was further supported by the necessary reduction in $CuCl_2$ concentration to perform the experiment. From the heat of solvation results it can be determined that the $CuCl_2$ precursor is more stable precursor than the $Cu(ac)_{2,}$ due to the molar enthalpy.

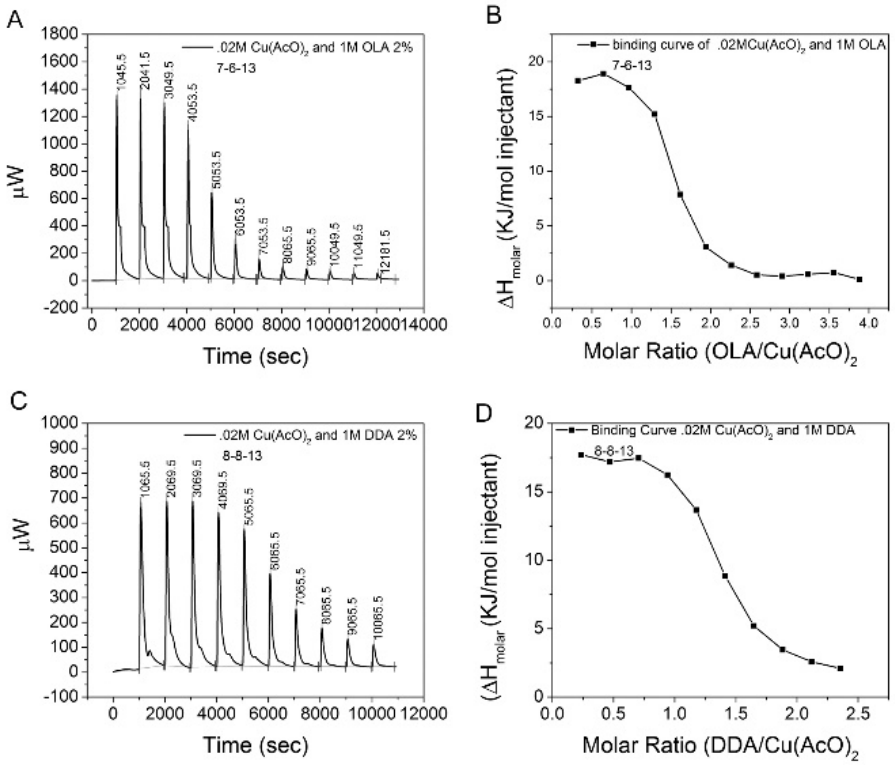

Figure SI 2. ITC measurement of the heat of solvation and the corresponding binding curve for $Cu(ac)_2$ and different amine ligands: (A,B) OLA; and (C,D) DDA.

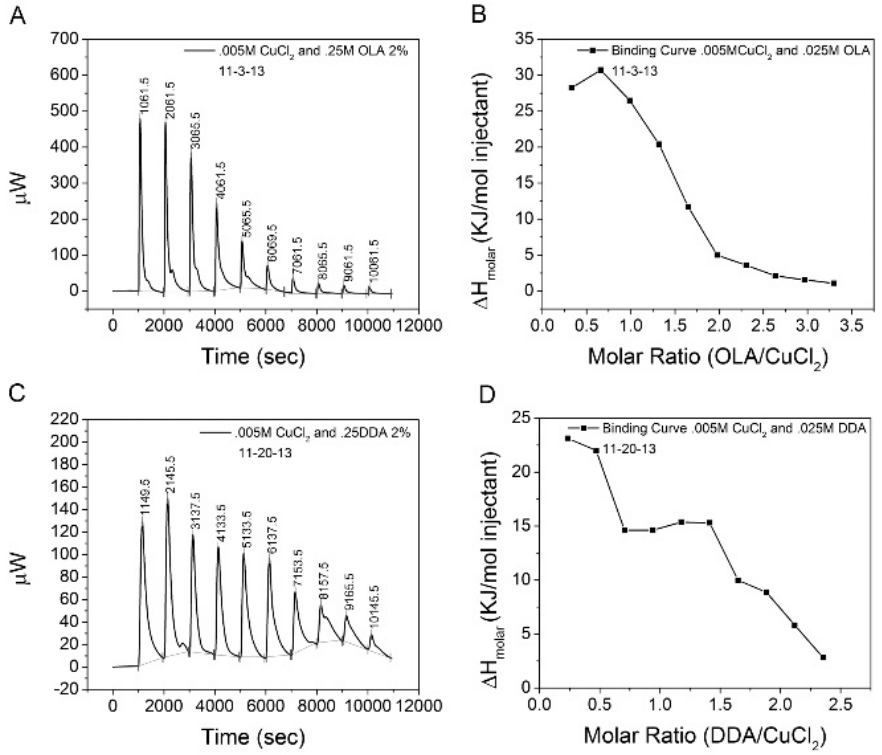

Figure SI 3. ITC measurement of the heat of solvation and the corresponding binding curve for $CuCl_2$ and different amine ligands: (A,B) OLA; and (C,D) DDA.

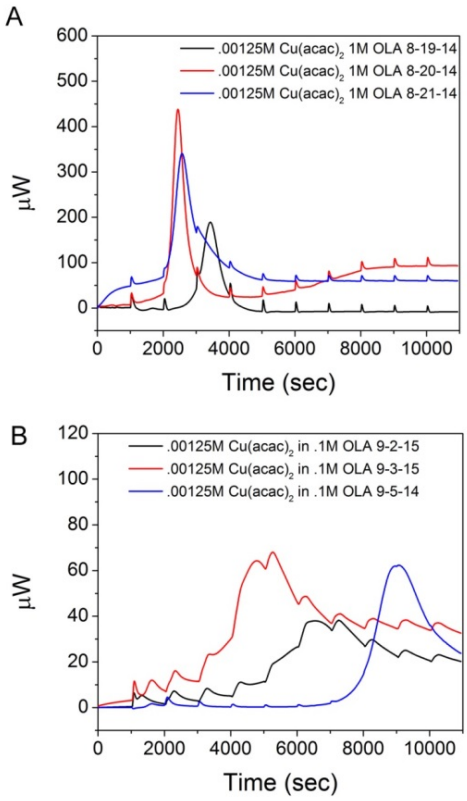

Figure SI 4: ITC measurement of the heat of solvation and the corresponding binding curve for $Cu(acac)_2$ and OLA.

2.9.3.2 Reduction Kinetics Studies

The reduction of the copper precursor was observed visually through a color change, and was monitored over time through UV-Vis spectroscopy. The copper reduction wavelengths are at 300nm and 580nm. The copper reduction is observed by the peak at 300nm, which denotes the presence and reduction of the Cu-N bond, and copper nucleation and nanoparticle growth is observed by the increase of a peak around 580nm. The reduction kinetics of $Cu(acac)_2$ with OLA and DDA were studied first and the results can be found in Figure 6. Spectra A & B and image C provide the reduction kinetics results for $Cu(acac)_2$ with OLA. Spectra D &E and image F correspond to the reduction kinetics of $Cu(acac)_2$ and DDA. The decrease in the 300nm peak, Cu-N bond can be seen in spectrum A (& D), and spectrum B (& E) provides a magnified wavelength range, from 500nm to 1000nm (300nm to 700nm), allowing for observation of the

580nm peak denoting the presence of the copper nanoparticles. The color change observed in image C and F correspond to the formation of the copper-amine complex, reduction, and nucleation of copper nanoparticles. The blue reaction solution corresponds to the formation of the complex, the alteration of the color from blue to yellow denotes the reduction of the copper precursor, and the change from yellow to red signifies the formation of copper nanoparticles.

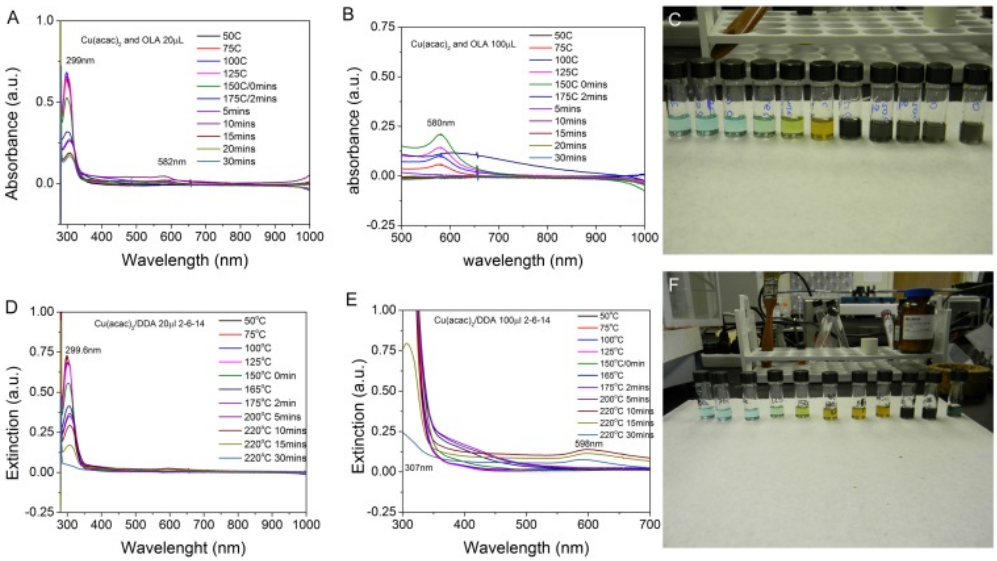

Figure SI 5. Reduction kinetics study by UV-vis and photograph of the reactions containing $Cu(acac)_2$ in different amines: (A-C) OLA; and (D-F) DDA.

The reduction kinetics of $CuCl_2$ and $Cu(Ac)_2$ with OLA were also studied, the results of which can be found in Figure 7. Spectra A & B provide the reduction kinetics results at 300nm for $CuCl_2$ and $Cu(ac)_2$, respectively. Neither spectra developed a peak around 580nm, which suggests that the copper precursors did not reduce or nucleate into copper nanoparticles. These results suggest that $CuCl_2$ and $Cu(ac)_2$ will reduce at a higher temperature and over a longer amount of time than $Cu(acac)_2$ in OLA.

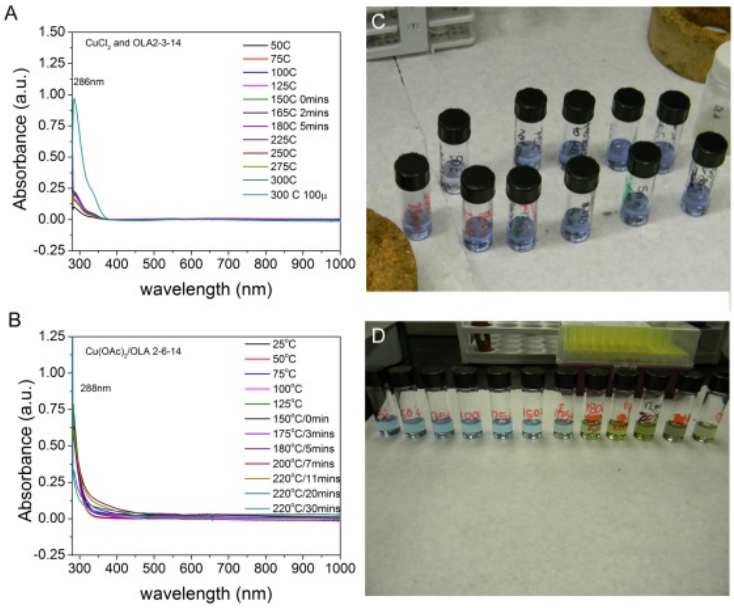

Figure SI 6. Reduction kinetics study by UV-vis and photograph of the reaction containing OLA with different Cu precursors: (A) $CuCl_2$; and (B) $Cu(acac)_2$.

2.9.4 Appendix B: Conclusion:

These experiments provide insight into the reduction and nucleation process of the synthetic routes outlined in this research, which would provide mechanistic information for Cu NM growth. The ITC results determine the strength of the various copper precursors, while the reduction kinetics provide information towards the growth process of Cu NM. The ITC results determined that variations in the amine capping ligand, between OLA and DDA, did not affect the change in heat or molar enthalpy of the copper-amine complex. A significant difference in change in heat and molar enthalpy was observed for the different copper precursors. The $CuCl_2$ precursor demonstrated a higher change in heat over time and corresponding molar enthalpy, compared to the $Cu(ac)_2$. This was further supported by the necessary reduction in $CuCl_2$ concentration to perform the experiment. From the heat of solvation results, the $CuCl_2$ precursor is more stable precursor than the $Cu(ac)_2$, which would have implications in the reduction of the copper precursors. The copper precursor that was more stable the longer it would take to form the copper-amine complex, resulting in a slower reduction of the precursor. ITC studies over

$Cu(acac)_2$ were not successful, even when amine concentration was varied. The challenges with $Cu(acac)_2$ ITC study correspond to the binding strength of the acetylacetonate ligand, which is a bidentate lignd. Additional studies need to be completed at a lower concentration of $Cu(acac)_2$, a different concentration of OLA, and repeated with DDA. This work could be expanded to include an ITC study and reduction kinetics study for copper (II) bromide.

From the reduction kinetics results, it can be determined that $CuCl_2$ and $Cu(ac)_2$ have more stable structures that will not reduce and nucleate as readily as $Cu(acac)_2$. These results correlate with the heat of solvation data for $CuCl_2$. Due to its high molar enthalpy, it can be determined that the change in entropy would be lower, forming a more stable amine copper complex. These results would have implications for the cu NM growth mechanism, from synthesis set 1. These results suggest that $Cu(acac)_2$ will reduce prior to $CuCl_2$ and the $Cu(acac)_2$ will form seeds. During this process, $CuCl_2$ will act as a secondary source of Cu^0 atoms to continue growth of the copper nanowires. A similar mechanism may be occurring in the Cu NPL synthesis, where $CuCl_2$ is in excess. The differences in reduction rate of $Cu(acac)_2$ and $CuCl_2$ may influence the Cu NPL synthesis. In this synthesis $CuCl_2$ is in excess and may cause a kinetically limited synthesis. In order to elucidate the competitive process between $Cu(acac)_2$ and $CuCl_2$ and the corresponding growth mechanism, additional studies would be required.

2.10 References:

1. (a) Darugar, Q.; Qian, W.; El-Sayed, M. A.; Pileni, M.-P., Size-Dependent Ultrafast Electronic Energy Relaxation and Enhanced Fluorescence of Copper Nanoparticles. *The Journal of Physical Chemistry B* **2005,** *110* (1), 143-149; (b) Xia, Y.; Xiong, Y.; Lim, B.; Skrabalak, S. E., Shape-Controlled Synthesis of Metal Nanocrystals: Simple Chemistry Meets Complex Physics? *Angewandte Chemie International Edition* **2009,** *48* (1), 60-103.

2. Lignier, P.; Bellabarba, R.; Tooze, R. P., Scalable strategies for the synthesis of well-defined copper metal and oxide nanocrystals. *Chemical Society Reviews* **2012,** *41* (5), 1708-1720.

3. Lu, X.; Yavuz, M. S.; Tuan, H.-Y.; Korgel, B. A.; Xia, Y., Ultrathin Gold Nanowires Can Be Obtained by Reducing Polymeric Strands of Oleylamine−AuCl Complexes Formed via Aurophilic Interaction. *Journal of the American Chemical Society* **2008,** *130* (28), 8900-8901.

4. Lohse, S. E.; Burrows, N. D.; Scarabelli, L.; Liz-Marzán, L. M.; Murphy, C. J., Anisotropic Noble Metal Nanocrystal Growth: The Role of Halides. *Chemistry of Materials* **2014,** *26* (1), 34-43.

5. Langille, M. R.; Personick, M. L.; Zhang, J.; Mirkin, C. A., Defining Rules for the Shape Evolution of Gold Nanoparticles. *Journal of the American Chemical Society* **2012,** *134* (35), 14542-14554.

6. Personick, M. L.; Langille, M. R.; Zhang, J.; Harris, N.; Schatz, G. C.; Mirkin, C. A., Synthesis and Isolation of {110}-Faceted Gold Bipyramids and Rhombic Dodecahedra. *Journal of the American Chemical Society* **2011,** *133* (16), 6170-6173.

7. (a) Zhang, J.; Langille, M. R.; Personick, M. L.; Zhang, K.; Li, S.; Mirkin, C. A., Concave Cubic Gold Nanocrystals with High-Index Facets. *Journal of the American Chemical Society* **2010,** *132* (40), 14012-14014; (b) Zeng, J.; Zheng, Y.; Rycenga, M.; Tao, J.; Li, Z.-Y.; Zhang, Q.; Zhu, Y.; Xia, Y., Controlling the Shapes of Silver Nanocrystals with Different Capping Agents. *Journal of the American Chemical Society* **2010,** *132* (25), 8552-8553.

8. (a) Xiong, Y.; McLellan, J. M.; Chen, J.; Yin, Y.; Li, Z.-Y.; Xia, Y., Kinetically Controlled Synthesis of Triangular and Hexagonal Nanoplates of Palladium and Their SPR/SERS Properties. *Journal of the American Chemical Society* **2005,** *127* (48), 17118-17127; (b) Wiley, B.; Sun, Y.; Xia, Y., Synthesis of Silver Nanostructures with Controlled Shapes and Properties. *Accounts of Chemical Research* **2007,** *40* (10), 1067-1076; (c) Chen, L.; Ji, F.; Xu, Y.; He, L.; Mi, Y.; Bao, F.; Sun, B.; Zhang, X.; Zhang, Q., High-Yield Seedless Synthesis of Triangular Gold Nanoplates through Oxidative Etching. *Nano Letters* **2014,** *14* (12), 7201-7206; (d) Zhang, Q.; Yang, Y.; Li, J.; Iurilli, R.; Xie, S.; Qin, D., Citrate-Free Synthesis of Silver Nanoplates and the Mechanistic Study. *ACS Applied Materials & Interfaces* **2013,** *5* (13), 6333-6345.

9. Bower, M. M.; DeSantis, C. J.; Skrabalak, S. E., A Quantitative Analysis of Anions and pH on the Growth of Bimetallic Nanostructures. *The Journal of Physical Chemistry C* **2014,** *118* (32), 18762-18770.

10. Mott, D.; Galkowski, J.; Wang, L.; Luo, J.; Zhong, C. J., Synthesis of size-controlled and shaped copper nanoparticles. *Langmuir : the ACS journal of surfaces and colloids* **2007,** *23* (10), 5740-5745.

11. (a) Yang, H.-J.; He, S.-Y.; Chen, H.-L.; Tuan, H.-Y., Monodisperse Copper Nanocubes: Synthesis, Self-Assembly, and Large-Area Dense-Packed Films. *Chemistry of Materials* **2014,** *26* (5), 1785-1793; (b) Kuo, C.-H.; Huang, M. H., Fabrication of Truncated Rhombic Dodecahedral Cu2O Nanocages and Nanoframes by Particle Aggregation and Acidic Etching. *Journal of the American Chemical Society* **2008,** *130* (38), 12815-12820.

12. (a) Hua, Q.; Chen, K.; Chang, S.; Ma, Y.; Huang, W., Crystal Plane-Dependent Compositional and Structural Evolution of Uniform Cu2O Nanocrystals in Aqueous Ammonia Solutions. *The Journal of Physical Chemistry C* **2011,** *115* (42), 20618-20627; (b) Hua, Q.; Shang, D.; Zhang, W.; Chen, K.; Chang, S.; Ma, Y.; Jiang, Z.; Yang, J.; Huang, W., Morphological Evolution of Cu2O Nanocrystals in an Acid Solution: Stability of Different Crystal Planes. *Langmuir* **2010,** *27* (2), 665-671; (c) Salzemann, C.; Lisiecki, I.; Urban, J.; Pileni, M. P., Anisotropic Copper Nanocrystals Synthesized in a Supersaturated Medium: Nanocrystal Growth. *Langmuir* **2004,** *20* (26), 11772-11777.

13. (a) Siegfried, M. J.; Choi, K.-S., Elucidating the Effect of Additives on the Growth and Stability of Cu2O Surfaces via Shape Transformation of Pre-Grown Crystals. *Journal of the American Chemical Society* **2006,** *128* (32), 10356-10357; (b) Hung, L.-I.; Tsung, C.-K.; Huang, W.; Yang, P., Room-Temperature Formation of Hollow Cu2O Nanoparticles. *Advanced Materials* **2010,** *22* (17), 1910-1914.

14. Filankembo, A.; Giorgio, S.; Lisiecki, I.; Pileni, M. P., Is the Anion the Major Parameter in the Shape Control of Nanocrystals? *The Journal of Physical Chemistry B* **2003,** *107* (30), 7492-7500.

15. Salzemann, C.; Urban, J.; Lisiecki, I.; Pileni, M. P., Characterization and Growth Process of Copper Nanodisks. *Advanced Functional Materials* **2005,** *15* (8), 1277-1284.

16. Pileni, M. P., Control of the Size and Shape of Inorganic Nanocrystals at Various Scales from Nano to Macrodomains. *The Journal of Physical Chemistry C* **2007,** *111* (26), 9019-9038.

17. Li, X.; Shen, H.; Niu, J.; Li, S.; Zhang, Y.; Wang, H.; Li, L. S., Columnar Self-Assembly of Cu2S Hexagonal Nanoplates Induced by Tin(IV)−X Complex as Inorganic Surface Ligand. *Journal of the American Chemical Society* **2010,** *132* (37), 12778-12779.

18. Garg, N.; Scholl, C.; Mohanty, A.; Jin, R., The Role of Bromide Ions in Seeding Growth of Au Nanorods. *Langmuir* **2010,** *26* (12), 10271-10276.

19. (a) Chen, S.; Carroll, D. L., Silver Nanoplates: Size Control in Two Dimensions and Formation Mechanisms. *The Journal of Physical Chemistry B* **2004,** *108* (18), 5500-5506; (b) Chen, S.; Carroll, D. L., Synthesis and Characterization of Truncated Triangular Silver Nanoplates. *Nano Letters* **2002,** *2* (9), 1003-1007.

20. (a) Chen, J.; McLellan, J. M.; Siekkinen, A.; Xiong, Y.; Li, Z.-Y.; Xia, Y., Facile Synthesis of Gold−Silver Nanocages with Controllable Pores on the Surface. *Journal of the American Chemical Society* **2006,** *128* (46), 14776-14777; (b) Zhang, Q.; Cobley, C.; Au, L.; McKiernan, M.; Schwartz, A.; Wen, L.-P.; Chen, J.; Xia, Y., Production of Ag Nanocubes on a Scale of 0.1 g per Batch by Protecting the NaHS-Mediated Polyol Synthesis with Argon. *ACS Applied Materials & Interfaces* **2009,** *1* (9), 2044-2048; (c) Siekkinen, A. R.; McLellan, J. M.; Chen, J.; Xia, Y., Rapid synthesis of small silver nanocubes by mediating polyol reduction with a trace amount of sodium sulfide or sodium hydrosulfide. *Chemical Physics Letters* **2006,** *432* (4–6), 491-496.

21. Zhuang, Z.; Peng, Q.; Zhang, B.; Li, Y., Controllable Synthesis of Cu2S Nanocrystals and Their Assembly into a Superlattice. *Journal of the American Chemical Society* **2008,** *130* (32), 10482-10483.

Chapter III. Synthesis of Branched Core-Frame and Frame Copper-Platinum-Ruthenium Rhombic Dodecahedra and Their Electrocatalytic Properties for Methanol Oxidation

Synthesis of Branched Core-Frame and Frame Copper-Platinum-Ruthenium Rhombic Dodecahedra and Their Electrocatalytic Properties for Methanol Oxidation

Leanne E. Mathurin,[†] Jing Tao,[‡] Huolin Xin,[§] Jun Li,[‡] Yimei Zhu,[‡] Jingyi Chen[†,*]

[†]Department of Chemistry and Biochemistry, University of Arkansas, Fayetteville, AR 72701

[‡]Condensed Matter Physics and Materials Science Department, Brookhaven National Laboratory, Upton, NY 11973

[§]Center for Functional Nanomaterials, Brookhaven National Laboratory, Upton, NY 11973

[*]Corresponding author: Jingyi Chen, chenj@uark.edu (+1 479-575-6203)

3. Chapter III: Synthesis of Branched Core-Frame and Frame Copper-Platinum-Ruthenium Rhombic Dodecahedra and Their Electrocatalytic Properties for Methanol Oxidation

3.1 Abstract:

The morphology of multimetallic nanostructures can be synthetically tailored to enhance catalytic properties, in addition to composition and size. This research reports novel binary and ternary branched core-frame and frame nanostructures that are composed of Cu, Pt, and Ru for enhanced electrocatalysis of methanol oxidation (MOR). These nanostructures were synthesized by selectively depositing, Pt and Ru, onto the edges and vertices of the Cu cores to generate CuPt and CuPtRu branched core-frame nanostructures. The core-frame nanostructures underwent an acetic acid etching process, resulting in the alloyed CuPt and CuPtRu frame structures. The CO stripping studies demonstrate that the branched frame structures double electrochemically active surface areas compared to the branched core-frame structures. Compared to the CuPt binary catalysts, the ternary catalysts lower the onset potential by 0.2 V vs RHE and completely suppress the peak current in the reverse scan. This result suggests that the presence of Ru is important to improve the CO oxidation, and thus reduces CO poisoning on Pt-based nanocatalysts. The entire frame nanostructure is comprised alloy throughout the entire structure, while the core-frame nanostructures only possess alloying along the edges and vertices., The alloyed frame nanostructures are more stable than the core-framenanostructures, because the Cu cores dissolve in the acidic environment and the alloying can prevent the dissolution of active metals. The presence of Cu in the trimetallic alloyed frame structures can improve the sustainability of the catalysts during MOR under the acidic conditions, resulting in an enhanced

electrocatalyst than the PtRu standard. Further fine tuning the composition of the novel ternary branched frame structures can lead to more efficient catalysts at a lower cost for MOR.

3.2 Introduction

Multimetallic nanostructures have emerged as one of the materials research frontiers, because morphology can be tailored to improve catalytic properties in addition to composition and size.[1] It has been reported that different nanomaterial structures have improved activity for electrochemical reactions. [1] Among various morphologies, frame nanostructures have shown promise as an effective catalyst for chemical and electrochemical reactions, based on the increased surface area of the structure.[2] These nanostructures possess very thin skeletons, with asurface structure less than a few nanometers; in a confined large framework, with a typical magnitude of tens of nanometers. The enhanced catalytic and electrocatalytic reactivity is due to the extremely thin skeleton structures that increase the quantity of surface atoms available for catalytic reaction, while the confined framework retains the stability of the ultrafine structure.[3] Similarly to the nanoframe structures, nanodendrites also exhibit high catalytic activity in various chemical and electrochemical reactions due to the ultrafine branches confined within the relatively-large assemblies.[4] This research developed a facile synthesis to generate multimetallic branched core-frame and frame structures that integrate the merits of both the frame and ultrafine branch structures for their enhanced electrocatalytic properties.

Methanol oxidation reaction (MOR) is an anodic reaction in the direct methanol fuel cell (DMFC). Methanol is an ideal fuel due to its high energy density and transportation stability,for the use of powering portable electronics.[5] The reaction kinetics of MOR is slow limiting the efficiency, which requires a high loading of noble metal catalysts to activate the reaction.[6] Thusdeveloping an efficient electrocatalysts for DMFC thatovercomes the kinetic issue of

MOR and lower noble metal loading, proves to be a challenging task.[7] Pt is the best known mono-metal catalyst for the activation of methanol, but the efficiency is limited by poisoning of the Pt catalysts. [8]. Pt is the leading catalyst for MOR, however carbon monoxide adsorbs onto the surface of the Pt electrocatalyst, which reduces the number of reactive sites along the surface leading to the rapid loss of catalytic activity. [8] Based on the bifunctional mechanism, alloying Pt with Ru or another oxophillic metal, can weaken the adsorbed CO bond and activate adsorbed OH. The adsorbed species are effectively removed from the Pt surface. Previous studies have determined that the PtRu alloy is the most active binary catalyst for MOR, however, Ru is a noble metal with its abundance even less than Pt.[9, 10] To lower the cost of electrocatalysts , it is important to replace Ru with an economical element in the binary catalysts or to find ternary catalysts with less use of noble metals for MOR.[7, 9, 11]

Cu has been identified as a promising replacement for Ru by density functional theory (DFT) prediction and the atomic arrangement of Pt and Cu in the alloy is thought to be important for optimizing the catalytic activity.[10] Experimentally, a number of research groups including our effort studied the effect of geometry and shape on the catalytic activity of PtCu alloy for MOR, including e.g., nanocubes,[12] nanocages,[3b, c, 13] hexapod concave structures,[14] and nanodendrites. [4d, 15]. These PtCu binary nanostructures exhibit higher electrocatalytic activity compared to their corresponding nanoparticles, due to the presence of more active sites. Despite this improvement, the onset potential of PtCu binary catalysts remains high (more positive), and the current density at a potential less than 0.6 V vs. RHE is essentially zero, which would not improve for DMFC.

A ternary catalyst could overcome these limitations. For example, PtRuCu has been identified to be more active than PtRu for MOR through a combinatorial approach.[16] More recently, PtRu coated Cu nanowires have been found to lower the onset potential of MOR

compared to PtRu nanotubes.[17] To further explore the effects of morphology on the electrocatalytic properties, this work synthesizes a series of novel nanostructures that integrate the morphological features of frames and dendrites into the branched core-frame and frame CuPtRu nanostructures as electrocatalysts for MOR. Initially, branched core-frame CuPtRu nanostructures (i.e. CuPtRu coreframe) were formed, which possesses a Cu core and a branched PtRu-rich frame with a rhombic dodecahedral shape. The CuPtRu branched frame nanostructures (i.e. CuPtRu frame) are then formed from the core-frame structures through an acetic acid etching process. (). CuPt bimetallic branched core-frame and frame nanostructures were developed without Ru for an electrochemical comparison. The electrochemically active surface area, electrocatalytic reactivity, and stability for MOR were evaluated for these bimetallic and trimetallic branched core-frame and frame nanostructures, and the results were compared to the PtRu black. Comparing the different electrocatalysts developed in thisresearch, the binary and ternary branched frame structures exhibited improved electrocatalytic activity and stability. The chemical and electronic properties of these novel structures before and after the electrochemical measurements were also studied, to unveil the effects of composition and morphology on electrocatalytic properties, which provide insights for the design of next generation nanocatalysts.

3.3 Experimental Methods

3.3.1 **Chemicals.**

Copper 2,4-pentanedionate ($Cu(acac)_2$, 98%), copper chloride ($CuCl_2$, anhydrous, 98% min.), dodecylamine (DDA, 98%), platinum 2,4-pentanedionate ($Pt(acac)_2$, Pt 48% min.), ruthenium chloride trihydrate ($RuCl_3 \cdot 3H_2O$, Ru 35-40%), butylamine (BTA, 99%), and glacial acetic acid (99.7%), were purchased from Alfa Aesar. Oleylamine (OLA, 70%) and

poly(vinylpyrolidone) (PVP, M.W.=55,000) was purchased from Sigma-Aldrich. Ultrapure gases, Ar (99.999%), N_2 (99.999 %), and CO (99.9%), were purchased from Airgas. All chemicals were used as received unless specified otherwise. Ultrapure deionized water (18 MΩ) was used in the experiments unless specified otherwise.

3.3.2 **Synthesis of CuPtRu and CuPt Branched Core-frame Nanostructures.**

The Cu rhombic dodecahedra were synthesized by reducing Cu precursors in aliphatic primary amine. In a typical synthesis, DDA (5 g), $Cu(acac)_2$ (0.2 mmol, 52.5 mg), and $CuCl_2$ (0.1 mmol, 13.4 mg) were combined in a 25 mL three-neck round bottom flask equipped with a stir bar. The solid mixture was degassed with Ar for 15 min to remove O_2, and then heated to 220 °C within 10 min. The solid mixture started to melt at 27 ^oC, and was liquidat 45 ^oC. While the mixture was melting, the stir rate was gradually increased to speed setting of 5.5. During the temperature increase, the color of reaction solution changed from light blue to teal (25-45 ºC), dark green (120 ºC), yellow (160 ºC), orange (180 ºC), black (200 ºC), and greenish black (220 ºC). After 5 min at 220 ^oC, the reaction changes to metallic reddish black, and the reaction was held at 220 ºC for 50 min to allow the formation of Cu nanoparticles as templates. After 50 min, the noble metal precursors were quickly injected into the reaction solution: $Pt(acac)_2$ (0.076 mmol, 30.0 mg) in 1 mL of OLA and $RuCl_3 \cdot 3H_2O$ (0.076 mmol, 15.0 mg) in 1 mL of OLA for the CuPtRu nanostructure synthesis, or $Pt(acac)_2$ (0.076 mmol, 30.0 mg) in 1 mL of OLA for the CuPt nanostructure synthesis. The reaction was held at 220 ºC for 90 min before the reaction was quenched by removing the reaction flask from the heating mantel. As reaction temperature was cooled to 180 ºC, the solution was removed from the reaction flask and placed into a 15 mL centrifuge tube containing 2 ml of ethanol. The tube was filled to 15 mL with ethanol, and

centrifuged at 6,000 rpm for 6 min. The precipitate was purified by toluene/ethanol (2:14 v/v) mixture twice, and the nanostructures were redispersed in 2 mL of toluene for characterization.

3.3.3 Synthesis of CuPtRu and CuPt Branched Frame Nanostructures.

The branched frame nanostructures were synthesized by removing Cu from the branched core-frame nanostructures through acetic acid etching process. Typically, the branched core-frame nanostructure suspension (0.75 mL) was added to the mixture containing 1 mL of 2 mg/ mL PVP aqueous solution, 2 mL of glacial acetic acid, and 2 mL of H_2O in a 2 dr vial. PVP is used as stabilizer to prevent the aggregation of the nanostructures during the etching process. The reaction solution was heated to 60 ºC for 48 h, with a stir rate set at 5 using a silicone oil bath and Corning stirring plate. After the reaction, the vial was filled with H_2O and the nanoparticle mixture was collected by centrifuge at 6,000 rpm for 6 min, and the supernatant was removed.. The pellet was purified twice by redispersing in 2 mL of H_2O and centrifuging at 6,000 rpm for 6 min. The product was redispersed in 2 mL of H_2O for characterization and electrochemical study.

3.3.4 Electrocatalyst Preparation.

To prepare the core-frame nanostructures for electrochemical characterization, the nanostructures were treated with BTA/H_2O (50% v/v) solution at 25 ºC overnight to replace DDA/OLA with BTA, and thus allow for the core-frame nanostructures to be dispersed in aqueous phase. After the ligand exchange, the core-frame nanostructures were purified with ethanol, ethanol/H_2O (75% v/v), ethanol/H_2O (50% v/v) twice, ethanol/H_2O (25% v/v) twice and H_2O twice. The nanostructures were collected by centrifuging at 6,500 rpm for 6 min. The final product was suspended in 2 ml of H_2O for characterization and electrochemical study.

The catalyst suspension was prepared by mixing 1:1 volume of 0.8 mg_{Pt}/mL nanostructures suspension with 0.05 wt.% Nafion, followed by sonicating for 5 min. A 5 μL aliquot of the suspension was dropcasted onto the glassy carbon working electrode, yielding a Pt loading of 2 μg or 28 $\mu g/cm^2$. The dropcasted electrocatalysts was dried at room temperature for 14 h.

3.3.5 **Electrochemical Measurement.**

The electrocatalytic activity of core-frame, frame, and the commercially available catalysts PtRu black (Pt 50 wt.%, Ru wt.50%) were characterized by CO stripping, cyclic voltammetry (CV) and chronoamperometry (CA) on a CHI760 electrochemical workstation at room temperature. The measurements were performed using a three-electrode cell with a Ag/AgCl/1.0 M KCl (E^o = -0.294 V vs. RHE) and Pt wire as reference and counter electrode, respectively. Glassy carbon disk (0.070 cm^2) was polished to a mirror finish before each experiment, and was used as dropcasting substrate for the working electrode. For each electrochemical measurement, the electrolyte solution was 0.1 M $HClO_4$ and the analyte solution contained 1.0 M CH_3OH and 0.1 M $HClO_4$.

The electrochemically active surface area (ECSA) was determined from the CO stripping voltammetry. For each electrocatalyst, a background scan, a control scan, and a CO stripping scan were obtained at the following conditions,see details are provided in supporting information. The background scan was obtained at a scan rate of 20 mV/s with the potential range from 0 to 1.2 V vs. RHE in 0.1 M $HClO_4$ solution. The control scan was obtained at a scan rate of 20 mV/s with the potential range from 0 to 1.2 V vs. RHE in 0.1 M $HClO_4$ solution after the potential was held at 0.1 V for 13 min with Ar purging. The CO stripping scan was obtained at a scan rate of 20 mV/s with the potential range from 0 to 1.2 V vs. RHE in 0.1 M $HClO_4$ solution after the potential was held at 0.1 V vs RHE for 3 min with CO purging and 10 min with

Ar purge. The net CO stripping charge was obtained by integrating the charge between the CO stripping scan and the control scan from the double layer region at ~ 0.5 V vs. RHE up to the potential that the two scans merged at ~1.0 V vs. RHE. The ECSA was calculated from eq. 1, the net CO stripping charge (Q_{CO}) divided by the charge for a monolayer of adsorbed CO (420 $\mu C \cdot cm^{-2}$) on PtRu surfaces.

$$ECSA = \frac{Q_{CO}}{420 \mu C \cdot cm^{-2}} \qquad (1)$$

Electrochemical evaluation of the catalysts was detailed in the supporting information, and a brief description is included as follows. Prior to methanol oxidation reaction (MOR), the CV profiles were obtained at a scan rate of 50 mV/s with the potential range from 0 to 1.2 V vs. RHE in 0.1 M $HClO_4$ solution. The MOR was carried out in a solution containing 1.0 M CH_3OH and 0.1 M $HClO_4$ at a scan rate of 50 mV/s. The CA was recorded at 0.6 V vs. RHE in a solution containing 1.0 M CH_3OH and 0.1 M $HClO_4$. The stability test was carried out by the following procedure, initial CV curves were obtained at a scan rate of 50 mV/s with the potential range from 0 to 1.2 V vs. RHE in 0.1 M $HClO_4$ solution or a solution containing 1.0 M CH_3OH and 0.1 M $HClO_4$. Continuous cycling was completed at 100mV/s for a certain number of cycles (e.g., 300 and 600 cycles), with Ar flow. the final CV profile was recorded at a scan rate of 50 mV/s over the same potential range, followed by the MOR scan. After the stability test, the electrocatalyst was sonicated off the working electrode with 0.5 mL ethanol, concentrated to 10 μL, and then deposited onto a Ni grid for further characterization.

3.3.6 Characterization Methods

Transmission electron microscopy (TEM) images were captured using a JEOL JEM-1011 microscope with an accelerating voltage of 100 kV. High angle annular dark field scanning

transmission electron microscopy (HAADF-STEM) images, high-resolution TEM (HRTEM) images, and energy-dispersive X-ray (EDX) mapping were obtained using a JEOL ARM microscope with an acceleration voltage of 200 kV. The mass concentrations of Pt, Ru and Cu were determined using a Thermo Scientific iCAP Q inductively coupled plasma mass spectrometry (ICP-MS). X-ray photoelectron spectroscopy (XPS) study was performed using PHI VersaProbe station. The XPS spectra was analyzed and deconvoluted using MultiPak Data Reduction Software.

3.4 Results and Discussion

The branched core-frame rhombic dodecahedra (RDH) were synthesized by first forming Cu cores through the reduction of Cu precursors in the presence of DDA, which functioned as the reducing agent, capping ligand, and solvent. After Cu cores were formed, metal precursors (Pt and Ru) were simultaneously injected into the reaction solution. Theseselectively reduced onto the edges and vertices of RDH Cu cores, forming CuPtRu core-frame nanostructures. **Figure 1** shows the TEM characterization of the resultant trimetallic RDHs, which were synthesized by co-reducing Pt and Ru precursors on the Cu cores. The trimetallic RDHs resembled as a “snowflake” structure containing a RDH Cu core and alloyed edges with overgrowth of branched structure from the vertices (**Fig. 1A**), providing a ultrafine branched structure. The HRTEM of an individual nanoparticle demonstrates the RDH structure viewed from [110] zone with an edge length of ~10 nm and 1-nm thick edge frames and branches at the vertices (**Fig. 1B**).

The trimetallic RHD structure was further validated by electron tomography, which records a three-dimensional (3-D) view of an individual particle. **Figure 1, C-E**, shows still-frames of the movie with directional views from (C) [100], (D) [110], and (E) [111] zones of a RHD structure, respectively. The HAADF-STEM image displays the contrast associated with the element’s Z

number, suggesting that edges and vertices contain elements heavier than those in the core (**Fig. 1F**). The elemental composition of an individual CuPtRu core-frame nanostructure was analyzed by EDX mapping as shown in **Figure 1, G-J**, for element Cu, Pt, Ru, and their overlay, respectively. The results are in agreement with HRTEM and HAADF-STEM analysis, which suggests the core is comprised of Cu while the edges and branches at the vertices possess a trimetallic composition of Cu, Pt and Ru. The selective deposition could result from higher surface energy of the edges and vertices, which contain a larger number of active sites compared to the faces.[3d, 3g] For the same reason, the overgrowth from the vertices results in the branched core-frame structures.[18] The spectral analysis of the EDX map indicated that the molar composition of the corresponding core-frame rhombic dodecahedron was composed of 60.89±2.35%, 25.30±1.84%, and 13.81±1.09% for Cu, Pt, and Ru, respectively. The ICP-MS analysis on the bulk sample revealed a molar composition of 71.96%, 18.79%, and 9.25% for Cu, Pt, and Ru, respectively. The composition discrepancy between the individual particle and the bulk measurement was due to the inhomogeneity of Pt and Ru deposition on different cores.

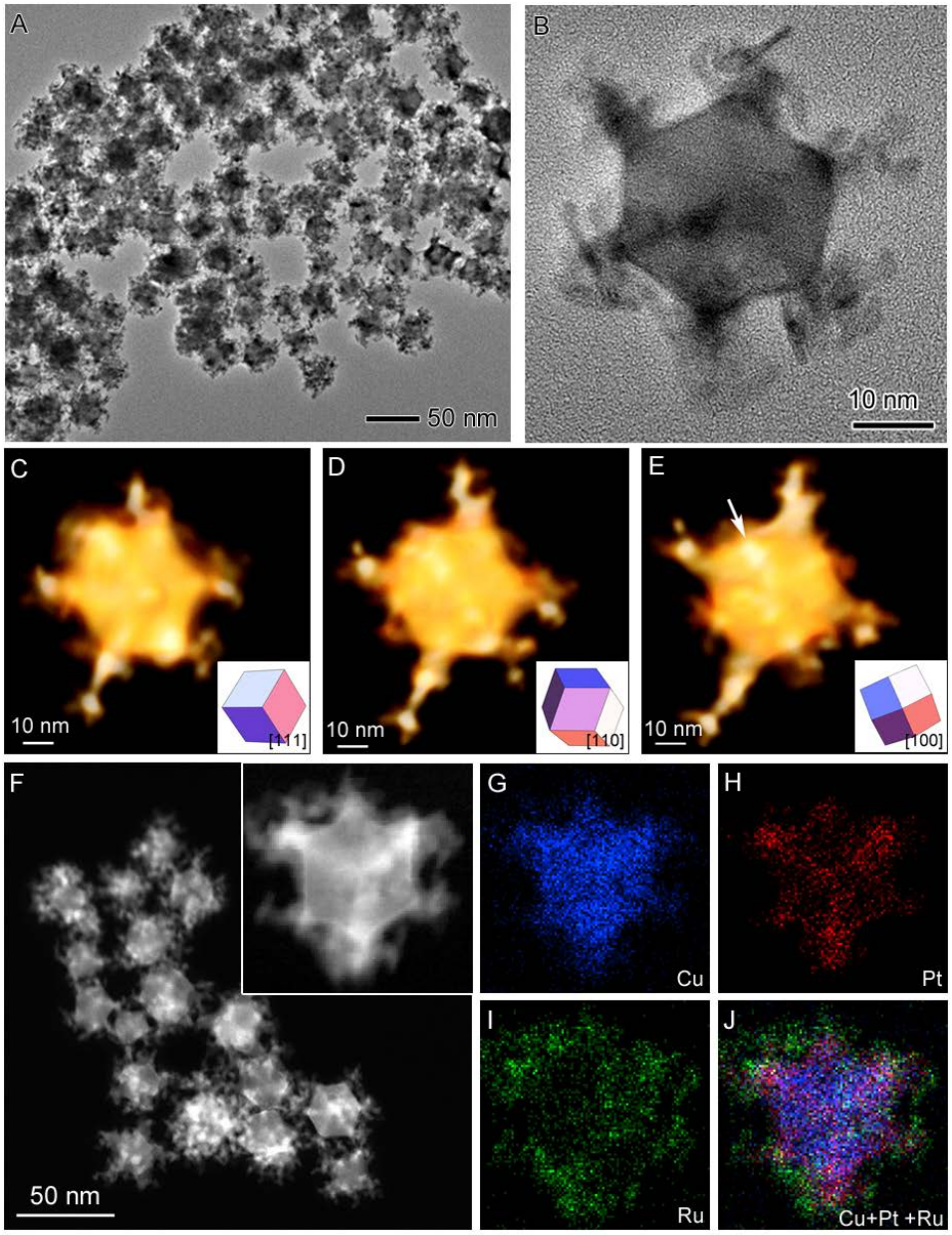

Figure 1. (A) TEM image of the CuPtRu branched core-frame rhombic dodecahedra. (B) HRTEM image of an individual branched core-frame nanostructure compromised of a rhombic dodecahedral core with edge length of ~10 nm and a 1-nm-thick frame with ~2 nm branches grown on the vertices. (C-E) TEM tomography of an individual trimetallic branched core-frame rhombic dodecahedron viewed from its [111] zone (C), [110] zone (D), and [100] zone (E) selected from the shots in Movie S1. (F) HAADF-STEM image of branched core-frame rhombic dodecahedra. The inset is an enlarged HAADF-STEM image of an individual branched core-frame rhombic dodecahedron viewed from its [111] zone. (G-J) EDX elemental mapping of the branched core-frame rhombic dodecahedron shown in the inset of (F): Cu in blue (G), Pt in red (H), Ru in green (I), and the overlay of Cu, Pt, and Ru (J).

To elucidate the crystal growth during the synthesis, intermediate aliquots were collected from the two-step reaction at different times and characterized by TEM. The first step involves the reduction of Cu precursors, $Cu(acac)_2$ and $CuCl_2$, by DDA at 220 ^oC for 50 min to form Cu cores (**Figure S1A**). It is speculated that the presence of Cl^- ions stabilizes the {110} facets of Cu, thus facilitating the formation of RDH shape. As a result, the core adopts a rhombic dodecahedron structure, which is enclosed by 12 {110} facets. Immediately after 50 min at 220 ^oC, $Pt(acac)_2$ and $RuCl_3 \cdot 3H_2O$ in OLA were simultaneously injected to reaction mixture. The Pt and Ru precursors reduced and deposited on the Cu cores. It was found that Pt and Ru preferentially deposited onto the edge of RDH cores, and 5 minutes after injecting the precursors overgrowth continued along the vertices of the cores. (**Figure S1B**). As the reaction proceeded, the trimetallic coreframe nanostructure growth branched out from the vertices and gradually evolved into ultrafine branched nanostructures or "snowflakes" (**Figure S1, C and D**). The schematic of this growth process is demonstrated in **Figure S3.**

The CuPtRu core-frame nanostructures can be hollowed out by dissolving the Cu core using glacial acetic acid to generate CuPtRu frame nanostructures. After etching in acetic acid at 60 ^oC for 48 h, the nanostructures were purified with aqueous solution to remove the excess reagents and Cu ions for characterization. **Figure 2A** demonstrates an overview of the CuPtRu frame nanostructures, indicating that nanostructures become hollow and maintain the rhombic dodecahedral shape with ultrafine branches along the vertices. An individual trimetallic frame nanostructure was magnified in the HRTEM image (**Fig. 2B**), showing the rhombic dodecahedral frame with edge length of ~10 nm and thickness of ~2 nm with branches of ~2 nm formed on the vertices. The frame nanostructures were further confirmed by the distinct difference in HAADF-STEM image contrast (**Fig. 2C**). The elemental EDX mapping of the individual frame

exhibits a trimetallic composition of CuPtRu. I Cu and Pt alloys at the edges and branches at the nanoframe vertices, while Ru is located mainly at the tips of the branches and along the surface of the edges. The spectral analysis of the EDX map indicated that the molar composition of the corresponding nanoframe was composed of 19.83±3.19% Cu, 47.85±4.45% Pt, and 32.31±3.40% Ru. The ICP-MS analysis on frame nanostructure prior to electrochemical characterization revealed a molar composition of 34.93% Cu, 58.82% Pt, and 6.25% Ru. The composition discrepancy between the individual particle and the bulk measurement was due to the inhomogeneity of the compositional changes during the etching process. After etching, the Cu content was reduced by ~60% (EDX analysis) to ~40% (ICP-MS analysis). The dissolution mechanism could be attributed to the combination of oxidation of pure Cu, followed by the etching of Cu oxides with acetic acid.[19] The alloyed Cu resists dissolution during acetic acid etching process, thereby remaining in the frame structure.

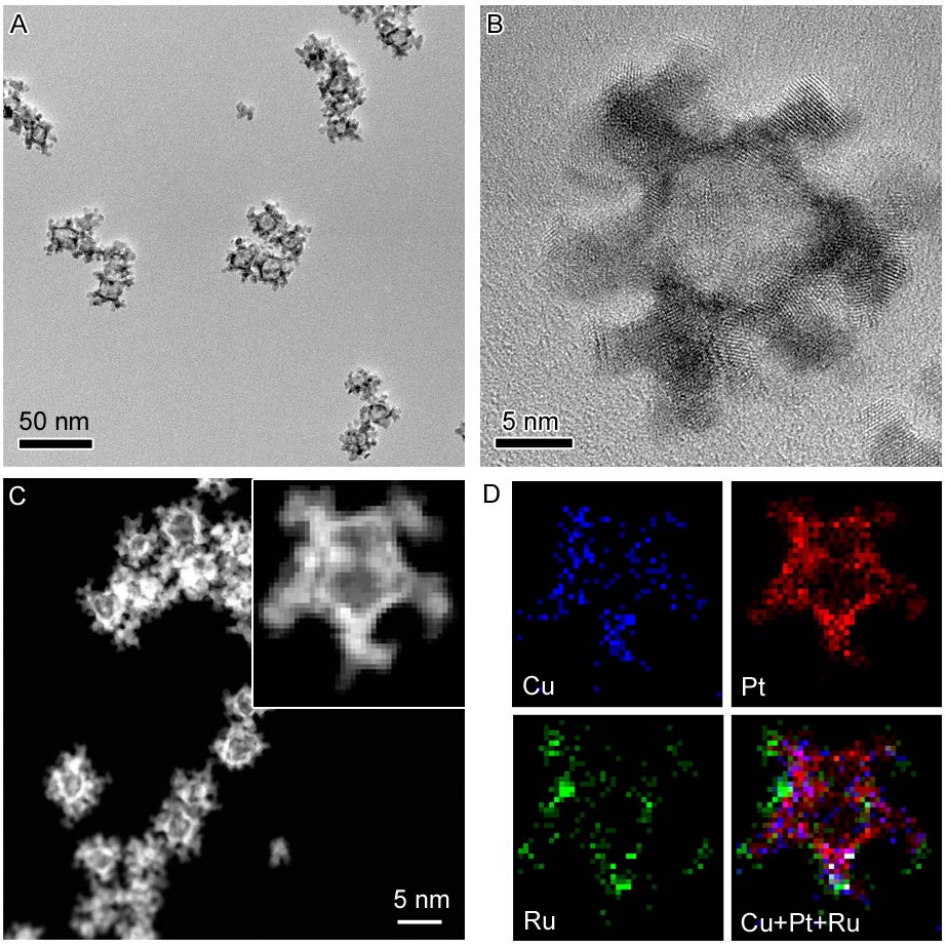

Figure 2. (A) TEM image of the CuPtRu trimetallic branched frame rhombic dodecahedra. (B) HRTEM image of an individual branched frame nanostructure compromised of a rhombic dodecahedral frame with edge length of ~10 nm and thickness of ~2 nm with branches of ~2 nm grown on the vertices. (C) HAADF-STEM image of branched frame rhombic dodecahedra. The inset is an enlarged HAADF-STEM image of an individual branched frame rhombic dodecahedron. (D) EDX elemental mapping of the branched frame rhombic dodecahedron shown in the inset of (C): Cu in blue, Pt in red, Ru in green (I), and the overlay of Cu, Pt, and Ru (J).

Bimetallic CuPt core-frame nanostructures were synthesized in a similar procedure as the trimetallic branched core-frame nanostructures. After the Cu cores were formed only the Pt precursor was subsequently injected into the reaction mixture. . The edge- and vertex-selective deposition was also observed in the CuPt system, resulting in the formation of CuPt bimetallic core-frame nanostructure. **Figure 3A** shows an overview of the bimetallic CuPt core-frame

nanostructures, exhibiting the overgrowth at the vertexes of the RDH cores. HRTEM was obtained on an individual rhombic dodecahedron from its [111] zone, clearly displaying a hexagonal shape with overgrowth at the vertices in its two-dimensional view (**Fig. 3B**). Additionally, fast frontier transform (FFT) of the HRTEM indicated a single crystal pattern of face-centered cubic structure viewed from [111] zoom axis (**Fig. 3C**). The lattice spacing of the core is 0.128 nm corresponding to {220} planes of Cu, indicating a pure Cu core. HAADF-STEM overview of CuPt core-frame nanostructures demonstrates a difference in contrast between the cores and edges/corners indicative of different metallic compositions (**Fig. 3D**). The EDX mapping of a representative CuPt RDH in **Fig. 3E** confirmed the composition of Cu core and Pt-rich edges and branches at the vertices (**Fig. 3F**). The spectral analysis of the EDX map indicated that the molar composition of the corresponding core-frame rhombic dodecahedron was composed of 85.91±9.52% and 14.09±4.95% for Cu and Pt, respectively. The ICP-MS analysis determined that the molar composition was 80.58% Cu and 19.42% Pt. The composition discrepancy between the individual particle and the bulk measurement was due to the inhomogeneity of Pt deposition on different nanoparticles with the variance at ~5%. The time course study on the CuPt branched core-frame nanostructures synthesis showed similar structure evolution process as that of the trimetallic core-frame nanostructures (**Fig. S2**).

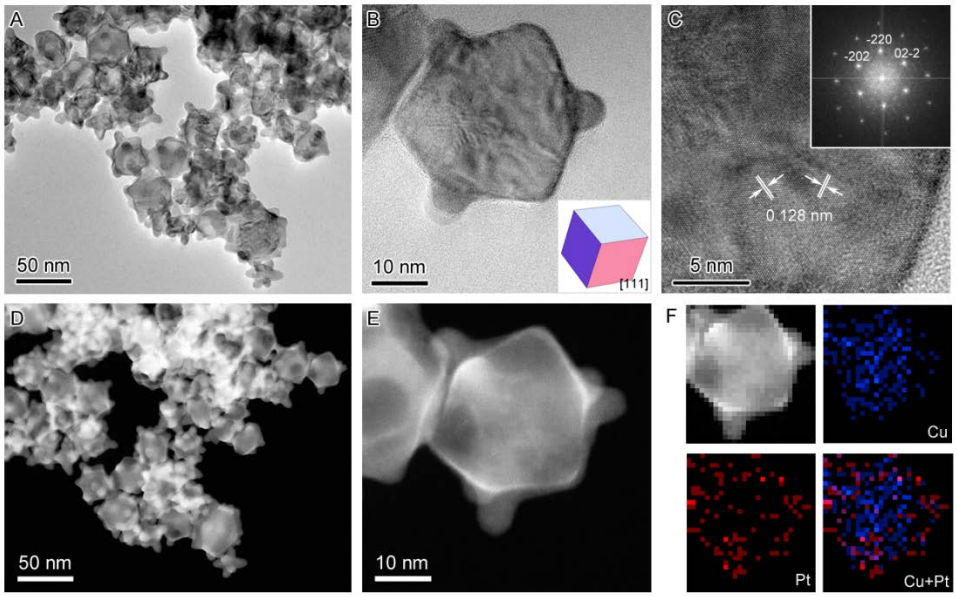

Figure 3. TEM characterization of CuPt bimetallic branched core-frame rhombic dodecahedra: (A) TEM overview; (B) HRTEM of an individual rhombic dodecahedron viewed from its [111] zone; (C) Zoom-in HRTEM of (B) with the lattice spacing corresponding to {220} planes of Cu. The inset is the fast Frontier transform (FFT) of (C) which is indexed as [111] face-centered-cubic single crystal pattern. (D-E) HAADF-STEM overview of the sample in (A) and close-up of an individual particle; and (F) EDX mapping of an individual particle for elemental Cu (blue), Pt (red) and the overlay of the two elements.

The acetic acid etching process was also applied on the CuPt core-frame nanostructures to form the binary frame nanostructures. After the etching process, the Cu cores were removed leaving the CuPt frame nanostructures, as demonstrated in **Figure 4A**. The HRTEM in **Figure 4B** shows that the individual frame nanostructure is a rhombic dodecahedral frame with edge length of ~10 nm and thickness of ~2 nm with overgrowth on the vertices. The HAADF-STEM image in **Figure 4C** confirmed the hollow frame structures, based on image contrast. The EDX mapping in **Figure 4D** revealed the distribution of the element Cu and Pt, indicating most of pure Cu was removed, and the frame structure was comprised of a CuPt alloy. The spectral analysis of the EDX mapping indicated that the molar composition of the corresponding core-frame rhombic dodecahedron was composed of 68.90±1.48% Cu and 31.10±1.27% Pt. The ICP-

MS analysis determined the molar composition was 47.99% Cu and 52.01% Pt. The compositional difference between the individual CuPt frame nanostructure and the bulk measurement was due to the inhomogeneity of the compositional changes during the etching process. After etching, the Cu content was reduced by ~20% (EDX analysis) to ~40% (ICP-MS analysis).

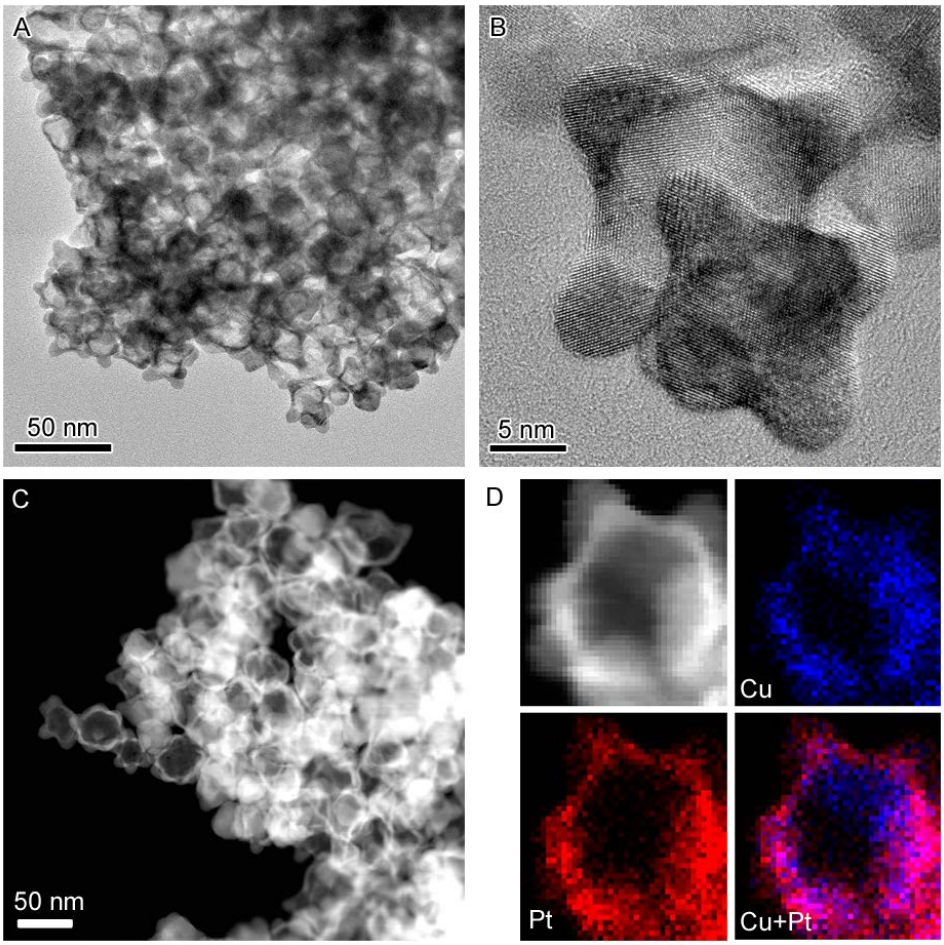

Figure 4. TEM characterization of the CuPt bimetallic frame rhombic dodecahedra: (A) TEM overview; (B) HRTEM image of an individual branched frame nanostructure compromised of a rhombic dodecahedral frame with edge length of ~10 nm and thickness of ~2 nm with overgrowth on the vertices. (C) HAADF-STEM image of branched frame rhombic dodecahedra. The inset is an enlarged HAADF-STEM image of an individual branched frame rhombic dodecahedron. (D) EDX elemental mapping of the branched frame rhombic dodecahedron viewed from its [111] zone as shown in upper left corner for elemental Cu (blue), Pt (red) and the overlay of the two elements.

The electrochemically active surface area (ECSA) was analyzed using CO stripping voltammetry. Due to the weak binding interaction between ruthenium and hydrogen, the electrocatalytic surface area of nanomaterials with ruthenium present cannot be accurately estimated by hydrogen underpotential deposition (H_{upd}).[17, 20] Each nanostructure was deposited on GC electrode (geometric surface area, A_{geo} = 0.071 cm^2) at a concentration of 0.28 $\mu g/cm^2$, and obtained voltammograms at a scan rate of 20 mV/s in 0.1 M $HClO_4$ electrolyte. Each panel in **Figure 5** and **Figure S4** shows the background voltammogram (dotted line), control voltammogram (dashed line),and CO stripping voltammogram (solid line) for each corresponding nanostructures (**Figure 5)** and the standard PtRu catalyst (**Figure S4)**. The background and control voltammograms remain similar, indicating that initial CV scans and holding the potential at 0.1 V vs RHE with Ar purge does not change the electrocatalytic activity of the nanostructures. Following methods in literature, the control voltammogram was utilized as the baseline for the CO stripping voltammogram to determine the ECSA of each nanostructure.[21]

Based on the CO stripping voltammograms, the ECSA was calculated to 0.06, 0.25, 0.54, 0.52, and 1.41 cm^2, for CuPt core-frame, CuPt frame, CuPtRu core-frame, CuPtRu frame structures, and the standard PtRu catalyst, respectively. In the case of CuPt nanostructures, the calculated ECSA of the frame structure was higher than that of the core-frame structure, because etching the Cu core exposed more surface area from the Pt-rich edges for electrochemical reactions. A slight difference in ECSA values were observed between the branched core-frame and frame structures for CuPtRu. Although the ternary CuPtRu nanostructured catalysts achieved ECSA values 8 times larger than that of the working electrode geometry, their ECSA was only about 40% of that of the PtRu catalyst, possibly due to aggregation of the nanostructures during

drying. The onset potential/peak potential of the ternary catalysts are lower than that of the binary catalysts, indicating that the ternary catalysts exhibit enhanced resistance towards CO poisoning. the value of onset potential/peak potential for frame structures shifts to a higher potential than those of the core-frame structures when the two different structures were compared. This suggests that the structure reconstruction from core-frame to frame slightly decreases the resistance towards CO poisoning of the catalysts.

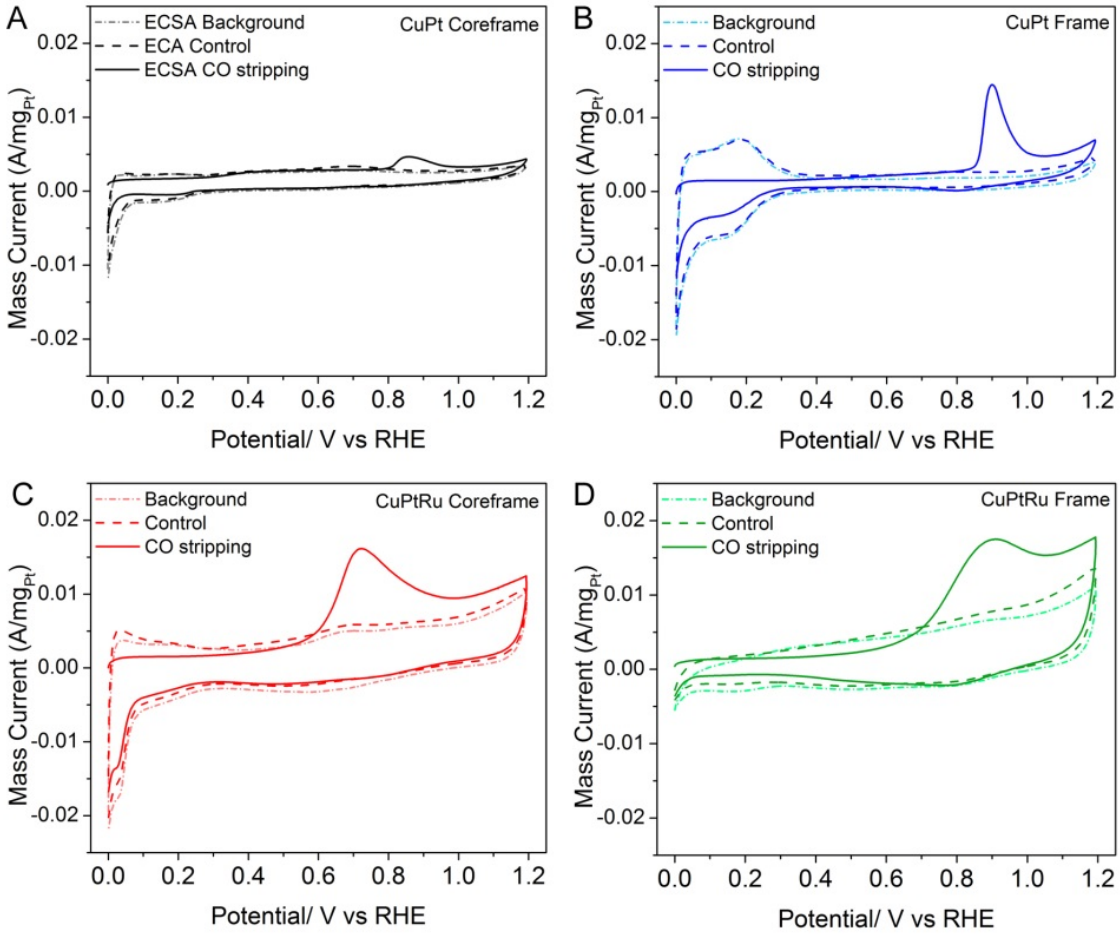

Figure 5. Comparison of the CO stripping voltammetry study on different nanostructures as electrocatalysts: (A) CuPt core-frame; (B) CuPt frame; (C) CuPtRu core-frame; and (D) CuPtRu frame. The CO stripping voltammograms (solid lines) were obtained at a scan rate of 20 mV/s after monolayer of CO was adsorbed on the electrocatalysts. The CV control baselines (dashed lines) were recorded after the potential was held at 0.1 V vs. RHE under argon flow while the CV background baselines (dot lines) were taken after the electrolyte solutions were degassed with argon.

The electrochemical activity of core-frame nanostructures for MOR was examined in acidic conditions. **Figure 6A** compares the CV curves for the CuPt and CuPtRu core-frame structures and the standard PtRu/C catalysts at a scan rate of 50 mV/s in 0.1 M $HClO_4$ electrolyte solution. Compared to the CuPt core-frame, the presence of Ru in CuPtRu core-frame and PtRu causes the significant increase of the charging double layer capacitance region (0.4-0.6 V vs RHE), and reduces the H_{upd} region.. The electrocatalytic activity of the core-frame structures for methanol oxidation was evaluated by the CV at a rate of 50 mV/s in 0.1 M $HClO_4$ solution containing 1 M of methanol, as shown in **Figure 6B**. The onset potential of methanol oxidation for the CuPt core-frame structures was 0.646 V vs RHE, and the overpotential was reduced to 0.459 V vs RHE for the CuPtRu core-frame structures. These results were comparable to the determined onset potential for the standard PtRu at 0.426 vs RHE. The ratio of forward peak current and backward peak current (I_f/I_b) is ~1.5 for the CuPt core-frame structures, which resists CO poisoning more effectively than the standard Pt/C (0.87), and is comparable to the CuPt nanodendrites (1.67) in our previous study[4d]. By incorporating Ru, the CuPtRu core-frame structure completely suppresses the oxidation peak in the reserve sweep. This suggests that the Ru incorporated core-frame structures improve the resistance towards CO poisoning, which is similar in performance to the PtRu standard.

The frame nanostructures were electrochemical activity for MOR was evaluated under the same conditions, as the core-frame structures. Compared to the CuPt frame, Ru in CuPtRu frame significantly increased thecharging double layer capacitance region, leading to the poorly defined H_{upd} region in the voltammogram (**Fig. 6D**). The frames nanostructures were characterized for methanol oxidation, as demonstrated in **Figure 6E**. The onset potentials for MOR occur at 0.605 V vs RHE and 0.507 V vs RHE, for CuPt and CuPtRu frame structures, respectively. Similarly to

the core-frame structures, the presence of Ru in the frame nanostructures significantly lowers the onset potential; however, removing the Cu core does not influence on the onset potential for MOR. The CuPt frame nanostructure exhibits a similar ratio of I_f/I_b (~1.5) as the CuPt core-frame nanostructure; however, the CuPt frame nanostructure possesses a higher peak mass current for MOR (~1.69 times) due to its larger ECSA than the core-frame nanostructure. Alloying Ru into the frame structure completely decreased the peak in the reverse sweep in the voltammogram for MOR, indicative of the suppression of CO poisoning. The CuPtRu frame structures have slightly higher mass current for MOR, 1.22 times of peak mass current of the core-frame equivalent. Since the CuPtRu frame and coreframe nanostructures exhibits a similar ECSA values, the higher MOR mass current of the frame structure indicates a higher catalytic activity..

CA curves were obtained by holding the voltage at 0.6 V vs RHE in 0.1 M $HClO_4$ solution containing 1 M methanol for the CuPt frame structure, the CuPtRu frame structure, and the PtRu standard (**Fig. S5**). The amperograms demonstrated the MOR stability of CuPtRu frame structure was comparable to that of the PtRu standard at 0.6 V vs. RHE maintaining a mass current of ~20 mA/mg_{Pt}, whereas the CuPt frame structure demonstrated noelectrocatalytic activity at this low onset potential.

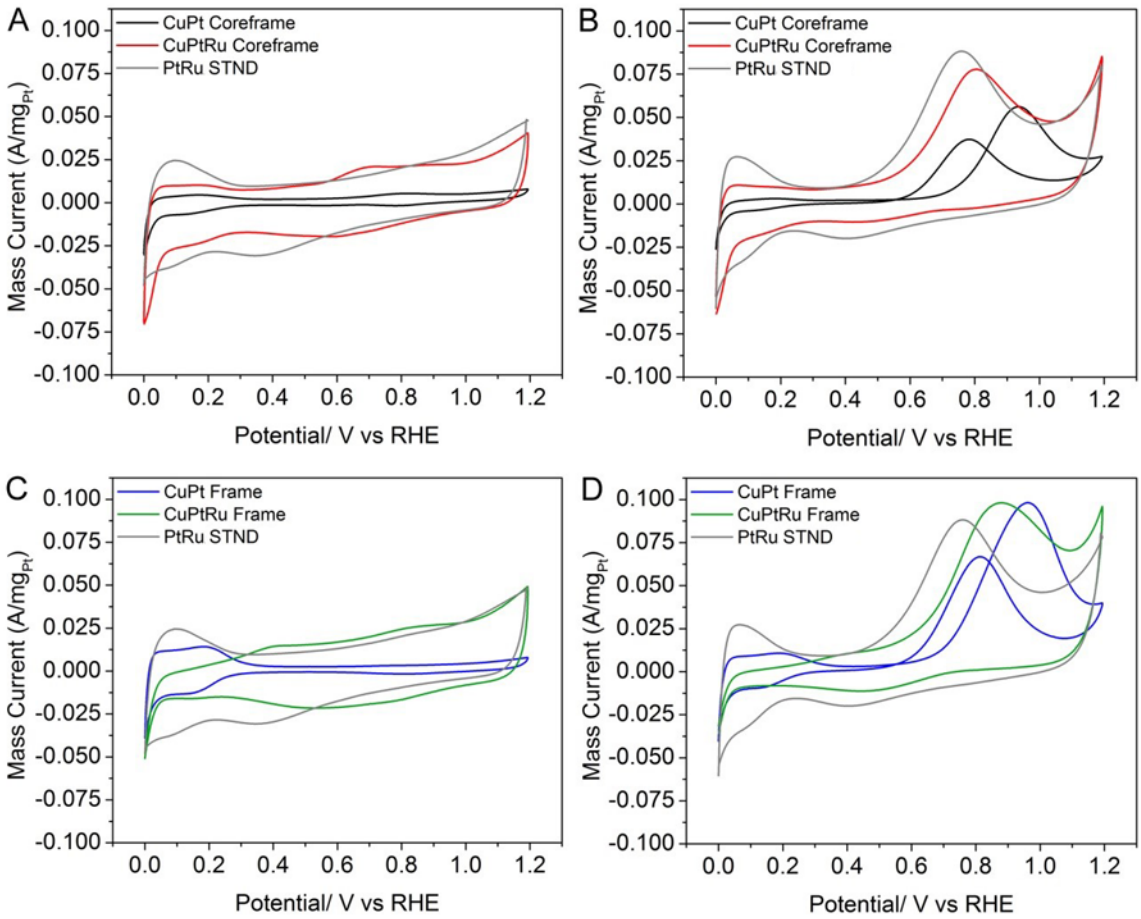

Figure 6. (A,B) Cyclic voltammetry profiles of CuPtRu (red) and CuPt (black) core-frame nanostructures in 0.1 M $HClO_4$ solution (A) and 0.1 M $HClO_4$ solution containing 1 M methanol (B) at a scan rate of 50 mV/s. (C & D) Cyclic voltammetry profiles of CuPtRu (green) and CuPt (blue) frame nanostructures in electrolyte (C) and analyte (D) at a scan rate of 50 mV/s. The PtRu standard was labeled in grey in all panels.

XPS was used to analyze the binding energy (BEs) of the core electrons in thefollowing elements Pt, Ru, and Cu, for the core-frame and frame nanostructures and the PtRu standard. This study was completed to elucidate chemical and electronic effects on the electrocatalytic activity for MOR. For the Pt $4f_{7/2}$ photoelectrons, the BEs were 71.0, 71.3, 70.4, 70.4, and 71.1 eV for the CuPt core-frame, CuPtRu core-frame, CuPt frame, CuPtRu frame structures, and PtRu standard, respectively (**Fig. 7A**). These Pt 4f photoelectron spectra were deconvoluted based on the BEs of the common Pt chemical states,, 71.0, 72.4, and 74.9, for Pt metal, Pt^{2+}, and Pt^{4+},

respectively. The splitting of Pt $4f_{7/2}$ and Pt $4f_{5/2}$ was determined to be 3.33 eV (**Fig. S6**). The BE of Pt 4f electrons in the core-frame structures and PtRu standard are slightly upshifted from bulk Pt^0, while the BE in the frame structures downshifted indicating that the Pt in the frame structure was electron rich or more metallic, and may be due to the formation of an alloy in the frame nanostructures. The BEs of Ru $3p_{3/2}$ were 462.0, 461.0, and 461.8 eV for CuPtRu core-frame, CuPtRu frame structure, and PtRu standard (**Fig. 7B**). These Ru $3p_{3/2}$ photoelectron spectra were deconvoluted based on the common Ru chemical states Ru^0, anhydrous RuO_2, and hydrated RuO_2, at Bes of, 461.2, 462.5/465.4(sat.), and 462.7/465.6(sat.) eV, respectively, as shown in **Figure S7**. The deconvoluted spectra for all three catalysts contained oxidized Ru. The BE of Ru $3p_{3/2}$ in the CuPtRu core-frame structure was almost the same at that in the PtRu standard. The BE of Ru $3p_{3/2}$ in the CuPtRu frame structure was downshifted suggesting that the Ru in the frame structure was electron rich or more metallic, due to the alloying with Cu and Pt forming a more stable electrocatalyst. The BE of Cu $2p_{3/2}$ photoelectrons of both the binary and ternary frame structures were downshifted by 0.75 eV compared to the corresponding core-frame structures (**Fig. S8**).The Cu 2p peak deconvolution demonstrated oxidized Cu in the core-frame structures than in the frame structures, due to the absence of Cu faces on the frame nanostructures and the presence of Cu core in the core-frame nanostructures.

The capping ligands on the surface of the frame and coreframe nanostructures could donate electrons to the catalyst surface, causing multiple three elements appear more metallic or electron-rich in the frame structures.

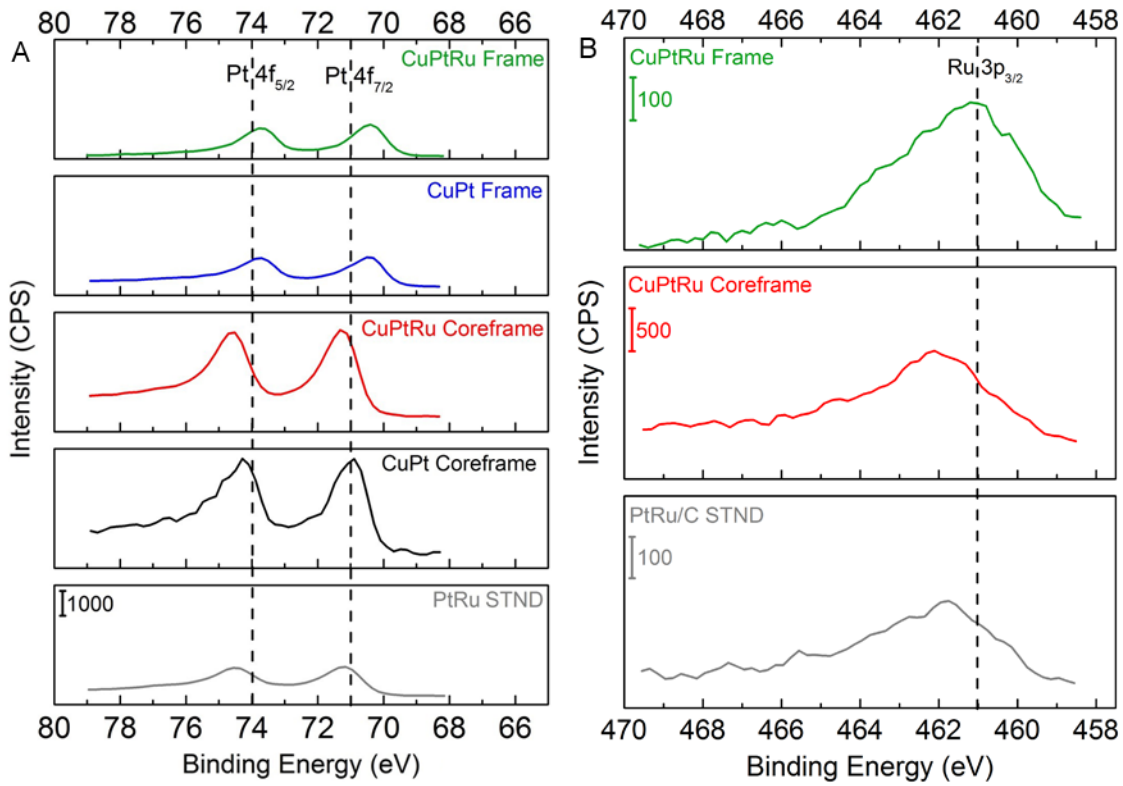

Figure 7. XPS spectra of Pt 4f (A) and Ru $3p_{3/2}$ (B) for CuPtRu frame (green lines), CuPt frame (blue lines), CuPtRu core-frame (red lines), CuPt core-frame (black lines), and PtRu black (grey lines).

Stability studies were carried out in both electrolyte and analyte solutions on the core-frame, frame nanostructures, and the PtRu standard. CV profiles in electrolyte solution exhibit four different regions that could be identified in their voltammograms binary frame and coreframe nanostructures including the hydrogen adsorption/desorption region below 0.25 V vs RHE, the charging double layer capacitance region in 0.4-0.6 V vs RHE, and the metal oxide region in 0.6-1.2 V vs RHE in electrolyte, the MOR region in 0.6 – 1.0 V vs RHE in analyte.[22] For the core-frame structures, CuPt in **Fig. S12A** and CuPtRu in **Fig. S12B**, the current density decreased in both hydrogen adsorption/desorption and Pt oxidation/Pt-O reduction regions after 300 scans in 0.1 M $HClO_4$ electrolyte solution. After 300 cycles, the peak mass current of MOR decreased by 82% and 63% of their original values for CuPt and CuPtRu core-frame structures,

respectively (**Fig. S12, A and B**). This loss of catalytic activity could be attributed to the dissolution of the pure Cu cores under the acidic condition, leading to the loss of Pt or Pt/Ru from theelectrocatalyst , or the presence of highly-active Pt or Pt/Ru with low coordinate numbers[23].

In contrast, the frame nanostructures are more stable during continuous cycling in electrolyte. After 300 cycles, the CuPt frame nanostructure lost about one third of ECSA based on H_{upd} and had a slight increase of mass current in the metal oxide region, due to CO adsorption during the preliminary MOR CV (**Fig. 8A**). Interestingly, the binary frame nanostructure enhanced activity for methanol oxidation after 300 cycles as indicated by the increase of peak mass current by 88%; however, the CO resistance decreases showed by the decreased of I_f/I_b ratio from 1.7 to 1.1 (**Fig. 8B**). The results suggest that the CuPt catalysts may undergo reconstruction at the surfacce during the stability study. This could form a Pt-rich skin on the alloyed frame structures due to the acidic condition, and thus increase available Pt for methanol oxidation while decreasing the CuPt pair sites for CO tolerance. In the case of CuPtRu frame structure, after 300 cycles the hydrogen adsorption/desorption region slightly increased, while the oxidation region slightly decreased (**Fig. 8D**). The MOR peak mass current dramatically increased by 5 times of the original value, while the peak current in the reverse sweep changed from complete suppression to I_f/I_b of 2.2 (**Fig. 8D**). Similarly to the CuPt frame, the CuPtRu frame surface may be reconstructed under the acidic condition during the electrolyte stability study, to expose more Pt on the surface while reducing the number of Cu-Pt or Ru-Pt pair sites.

Comparing the initial electrocatalytic activity, the CuPtRu ternary catalysts were more active than the binary counterparts, indicating that the presence of Ru in the catalysts are critically important to enhance MOR activity , which agreed with the previous reports. Among the forms

of Ru species, the contribution for MOR enhancement follows the order of hydration RuO_2 ($RuO_2 \cdot xH_2O$ or RuO_xH_y) > Ru metal >> anhydrous RuO_2.[24] The dissolution or irreversible oxidation of hydrated RuO_2 or Ru metal is not favorable for MOR. Since it is challenging to separate the contribution of Pt and Ru oxidation in the 0.6-1.2 V region, the region of 0.25-0.6 V are used to compare the behavior of Ru in different catalysts. In the forward sweep, the mass current of the CuPtRu core-frame structure decreased rapidly (**Fig. S8C**), followed by PtRu standard whose mass current in 0.25-0.6 V region also decreased after 300 cycles (**Fig. S7A**). The mass current of the CuPtRu frame nanostructure demonstrated no change (**Fig. 8C**). In the reverse sweep, after 300 cycles both the CuPtRu core-frame structure and PtRu catalyst exhibited significant decrease of Pt-O reduction, however, the CuPtRu frame structure maintained similar level of Pt-O reduction. These observations suggested that alloyed Cu, not pure Cu, could reduce the dissolution or irreversible oxidation of Ru thus stabilizing the active Ru species in the catalyst.

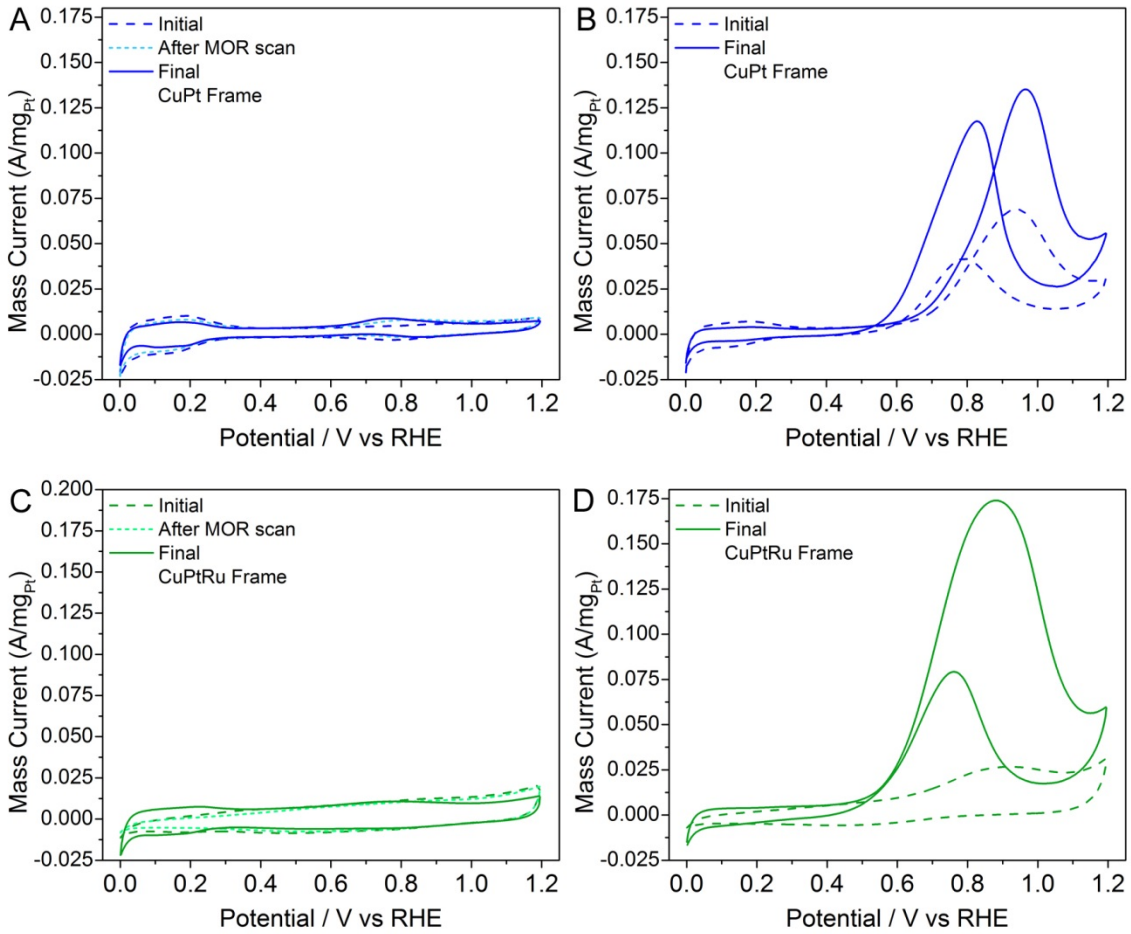

Figure 8. CV profiles of the frame nanostructures performed in 0.1 M $HClO_4$ solution (dashed lines), after initial MOR (dotted lines), and after 300 scans (solid lines) with a potential range from 0 to 1.2 V vs RHE at a scan rate of 100 mV/s: (A) CuPt core-frame structures; (B) CuPtRu core-frame structures; (C) CuPt frame structures; and (D) CuPtRu core-frame structures.

Vigorous analyte stability tests were conducted in 0.1 M $HClO_4$ solution containing 1 M methanol to obtain the CV profiles after several hundred cycles, with a potential range from 0 to 1.2 V vs. RHE at a scan rate of 50 mV/s. After 300 cycles, the core-frame structures lost ~90% of their ECSA based on the H_{upd} and ~85% of their electrocatalytic activities for MOR as shown in **Figure S13**; the loss is more severe than the corresponding core-frame structures in the electrolyte stability study (0.1 M $HClO_4$ solution). (**Fig. S10 & S12**). Compared to the core-frame structures, the frame structures are more stable during the analyte stability study. **Figure**

9A demonstrates the voltammograms of CuPt binary frame structure in 0.1 M $HClO_4$ solution before and after analyte stability cycles for 300 and 600 cycles.The H_{upd} region decreased by about one third after 300 cycles in methanol solution, and then remained the same after another 300 cycles in analyte solution. This indicates the ECSA of H_{upd} does not alter after the initial decay in the first 300 cycles. The increase in mass current at 0.75 V vs RHE in the forward sweep , and different behavior of Pt-O reduction region, in the CV profile, after 600 cycles in analyte solution, suggests an irreversible change on catalyst surface. This could due to poisoning of Pt by the CO intermediate from the MOR. These observations support the previous findings of nanoframe surface reconstruction in electrolyte solution under the acidic reaction. In which the surface is reconfigured from an alloyed surface to a Pt-rich surface, resulting in a more pronounced MOR mass current in presence of the reactant methanol. **Figure 9B** shows the methanol oxidation of CuPt binary frame structure before and after 300 and 600 cycles in analyte solution. As more Pt was exposed on the surface, the mass current increased from the 50 to 75 and 110 mA/mg_{Pt} after initial cycling, then 300 cycles and 600 cycles, respectively. The CO tolerance reduced as indicated by the decrease of I_f/I_b ratio initially at1.75 to 1.61 after 300 cycles and 1.33 after 600 cycles.

The CuPtRu nanoframe structure exhibited enhanced CO tolerance than CuPt frame, by completely suppressing the peak current in the initial reverse sweep. During analyte stability studies, the results suggest a similar surface reconstruction to with a Pt-rich surface. The CuPtRu frame structure maintained resistance towards CO poisoning during the analyte stability study. **Figure 9C** shows the CV profiles of CuPtRu frame nanostructure in 0.1 M $HClO_4$ solution before and after 300 and 600 cycles in analyte solution. The H_{upd} region became more predominant with the signature of hydrogen adsorption and desorption, and a decrease of mass

current was seen in the charging double layer region, which indicates a Pt-rich surface and less Pt-Ru pair sites after theanalyte stability study.. The poisoning of the Pt-rich surface wasobserved after 600 cycles in analyte solution, by the increase of mass current at 0.75 V vs RHE in the forward scan, and the Pt-O reduction region was altered. This observation is consistent with the changes in the methanol oxidation after the stability studies in analyte solution for coreframe nanostructures. **Figure 9D** shows the methanol oxidation of CuPtRu ternary frame structure initially, after 300 cycles, and 600 cycles in methanol solution. As more Pt was exposed on the surface, the mass current increased from the initial 60 to 90 and 110 mA/mg_{Pt} after 300 and 600 cycles, respectively.The CO tolerance decreased as indicated by the change in peak current, in the reverse sweep, from complete suppression of to an I_f/I_b ratio of 2.6 after 300 cycles, and 2.4 after 600 cycles. Compared to CuPt frame structure, the CuPtRu frame structure demonstrated the same peak mass current for MOR, with an improvement for CO resistance of 1.8 times, after 600 cycles in analyte solution.

For comparison, the stability test were performed on PtRu standard with cycling in analyte solution. **Figure 9E** shows the CV curves of PtRu standard in 0.1 M $HClO_4$ solution initially, after 300, and after 600 cycles in analyte solution. The H_{upd} region mass current decreased by two thirds of the original value, which indicated the rapid loss of ECSA. Compared to CuPtRu frame structure, a larger decrease in mass current was observed in the charging double layer capacitance region, as well as an increase of mass current at 0.75 V vs RHE in the forward sweep. Additionally, changes in Pt-O reduction region were observed. These observations suggested that the surface reconstruction was more pronounced for the PtRu standard. Initial cycling in analyte resulted in a more pronounced loss of electrocatalytic activity and CO tolerance. Similar trends were also observed for CV in analyte, during the stability tests. **Figure**

9F shows the methanol oxidation of PtRu standard frame structure initially, after 300, and after 600 cycles in analyte solution. The mass current decreased from the initial at 130 mA/mg_{Pt}, to 125 mA/mg_{Pt} after 300 cycles, and 60 mA/mg_{Pt} after 600 cycles. The CO tolerance was reduced from complete suppression of reverse sweep peak current to an I_f/I_b ratio of 1.5 and 1.9, after 300 and 600 cycles, respectively. Compared to PtRu standard, the CuPtRu frame structure exhibited double the peak mass current for MOR and 1.2 times enhanced CO tolerance, after 600 cycles in methanol solution.

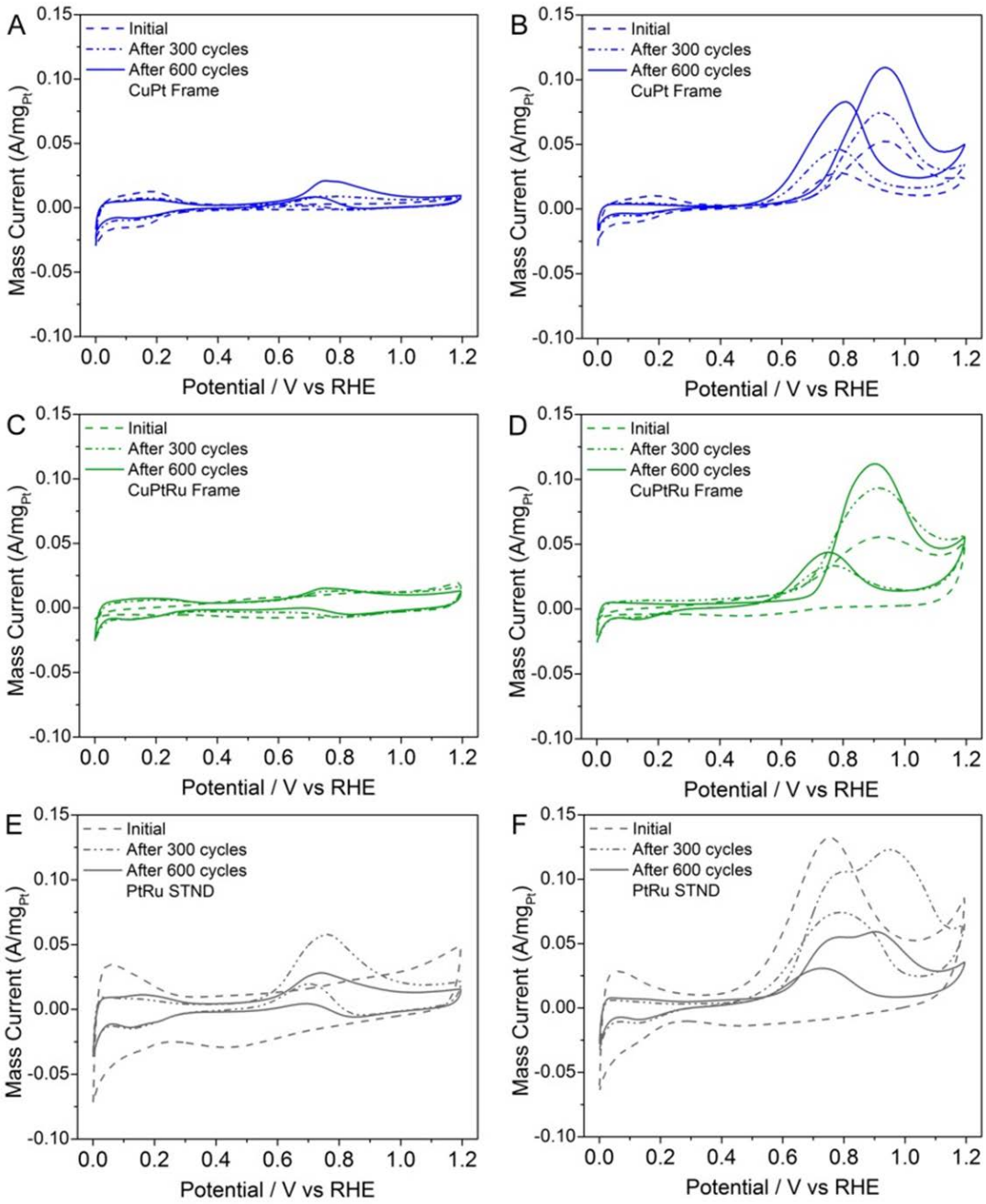

Figure 9. Stability studies of the frame nanostructures performed in 0.1 M $HClO_4$ solution containing 1 M methanol before (dotted lines) and after 300 scans (solid lines) with a potential range from 0 to 1.2 V vs RHE at a scan rate of 100 mV/s: (A) CV profiles of the CuPt frame structure in 0.1 M $HClO_4$; (B) CV profiles of the CuPt frame structure in 0.1 M $HClO_4$ solution containing 1 M methanol; (C) CV profiles of the CuPtRu frame structure in 0.1 M $HClO_4$; (D) CV profiles of the CuPtRu frame structure in 0.1 M $HClO_4$ solution containing 1 M methanol; (E) CV profiles of the PtRu standard in 0.1 M $HClO_4$; and (D) CV profiles of the PtRu standard in 0.1 M $HClO_4$ solution containing 1 M methanol.

After the durability study, the electrocatalyst samples were collected from the working electrode and the morphology was characterized. **Figures S14** characterizes coreframe (A and C) and frame nanotsuctures (B and D) by TEM. After the electrolyte stability study, the exterior morphology at the vertices of the coreframe structure was maintained, however, the interior was porous. The frame nanostructures maintained their surface structure and morphology during the electrolyte stability studies. **Figure S15** characterizes the morphology of the coreframe (A and C) and frame (B and D) nanostructures after the analyte stability study. Based on the TEM images (A and C), the coreframe nanostructures became porous and the surface structure was slightly altered, while the morphology of the frame nanostructures was not altered during the analyte stability study. These TEM images also demonstrate the presence of organic spheres, based on the TEM contrast. This result could be attributed to the presence of either nafion or unbound capping ligand from the electrocatalysts.

The frame nanostructures maintained their surface structure and morphology during both the electrolyte and analyst stability study. Since the frame nanostructure's morphology was not altered during the stabilty studies, an alteration in morphology can be omitted as the rationale behind the increased mass current exhibited by the frame nanostructures. This suggests that alterations to either the composition or alloy in the crystal structure of the frame nanostructures may cause the increased electrochemical activity.

After the analyte stability study (300 cycles), the frame nanostructured catalysts were sonicated off the working electrode, and collected characterization. **Figure 10** shows the TEM bright-field, HRTEM, and HAADF-STEM images, as well as the elemental mapping by EDX to reveal the morphologies and compositions of the frame nanostructures catalysts after analyte stability study. Both of the CuPt binary and CuPtRu ternary frame structures were maintained

their morphology and surface integrities with a thin frame of 2 nm thickness branched from the vertices of the structure. For CuPt, the EDX mapping shows, to some degree, Pt-rich regions, which could be the result of surface reconstruction (**Fig. 10D**). The composition of the CuPt frame nanostructure is 34.64±3.48% and 65.36±5.40% for Cu and Pt, respectively. Compared to the initial composition, the atomic percentage of Cu was decreased by 50%, due to its leach during MOR in acidic environment. This result agreed with the observations in the electrochemical measurements of CuPt that the loss of Cu mainly on the surface, resulting in the formation of Pt-rich surface for an enhancement of mass current but a reduction of CO tolerance.[25] In the case of CuPtRu frame nanostructure, the quantification of the EDX mapping exhibits a composition of 34.29±3.62%, 33.80±3.63%, and 31.91±2.77% for Cu, Pt, Ru, respectively. Compared to the initial values, the atomic percentage of Cu increased almost double, but the atomic percentage of Pt decreased by 7% and the Ru% remained unchanged. The EDX mapping results (**Fig. 10H**) reveal that the Cu and Pt overlaid well with each other on the frame surface, while the Ru was mainly distributed on the branches along the vertices. These results suggest that the dissolution of Cu in the ternary frame structures increased the loss of Pt and caused a phase segregation of Ru, however, the remaining Pt and the Pt-M (M = Cu, Ru) pair sites rearranged to improve the MOR mass current and maintain relatively-strong CO resistance.[26] Compared to the PtRu standard catalyst, the CuPtRu frame nanostructure enhances stability due to the presence of Cu in the alloyed nanostructure and high surface area.

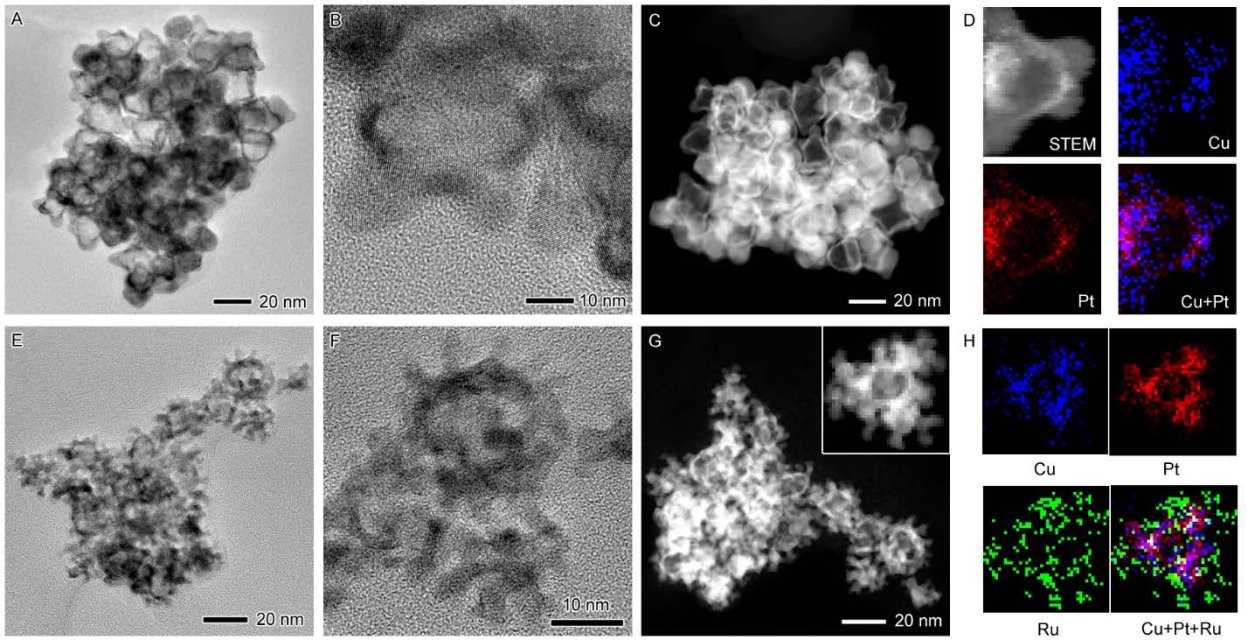

Figure 10. (A-D) TEM characterization of CuPt frame nanostructures after the stability test for 300 scans: (A) low-magnification image; (B) HRTEM; (C) HAADF-STEM; and (D) EDX elemental mapping of Cu (blue), Pt (red), and their overlaid. (E-H) TEM characterization of CuPtRu frame nanostructures after the stability test for 300 scans: € low-magnification image; (F) HRTEM; (G) HAADF-STEM; and (H) EDX elemental mapping of Cu (blue), Pt (red), and Ru (green), and their overlaid.

3.5 Conclusion

This research has successfully synthesized the multimetallic branched core-frame and frame nanostructures containing binary (CuPt) and ternary (CuPtRu) compositions. These nanostructured catalysts provided a platform to study the effects of composition, surface structure, and morphology on electrocatalytic activity. The novel nanostructures with high surface area and improved alloying enhanced the energy-related reaction MOR. It was found that the ternary catalysts was more active than the binary ones indicating that the presence of Ru is crucial for the enhancement of the CO tolerance and thus reduce the poisoning of Pt-based catalysts. The frame alloyed nanostructures aremore stable than the core-frame nanostructures, suggesting the alloy can prevent the dissolution of active metals in the harsh acidic environment. It was determined that the enhancement of electrochemical activity was not based on

morphological or overall compositional alterations to the binary and ternary frame nanostructures during the stability studies. It was found that during the stability tests, the binary frame nanostructures surface is reconstructed into Pt-rich surfaces, while the ternary frame nanostructure possesss Pt-rich surface with phase segregated region that was Ru-rich. The presence of Cu in ternary alloyed frame nanostructures can improve the sustainability of the catalysts during MOR under the acidic condition, forming an enhanced electrocatalysts than the PtRu standard. By optimizing the composition and refining the morphology, it is possible to develop more efficient catalysts for MOR that utilize less of noble metals, and thus create a more economically viable electrocatalyst and enable the commercialization of the DMFCs in the near future.

3.5.1 SUPPORTING INFORMATION

TEM characterization of the time course study of the CuPtRu nanostructures; TEM characterization of the time course study of the CuPt nanostructures; the CO stripping voltammetry study of the standard PtRu catalyst; Methanol oxidation of the catalysts performed in 0.1 M $HClO_4$ solution before and after 300 scans; XPS spectra of Pt $4f_{7/2}$ and Pt $4f_{5/2}$; XPS spectra of Ru $3p_{3/2}$; XPS spectra of Cu $3p_{3/2}$; Stability studies of the core-frame nanostructures performed in 0.1 M $HClO_4$ solution containing 1 M methanol before and after 300 scans.

3.5.2 ACKNOWLEDGEMENT

This work was supported in part by the grant NSF EPSCoR IIA 1457888 and the startup fund from the University of Arkansas. Park of the work done at Brookhaven National Laboratory (BNL) is sponsored by the U.S. DOE BES, by the Materials Sciences and Engineering Division, and Early Career Research Program under Contract DE-SC0012704. We thank the Center for Functional Nanomaterials at the BNL for the support of the electron microscopy. We would like

to thank Mourad Benamara for his help with XPS data analysis at the Arkansas Nano & Bio Materials Characterization Facility. We would like to thank E. Pollock for his help with the ICP-MS analysis at the Trace Element and Radiogenic Isotopic Laboratory, which was supported by the Arkansas Biosciences Institute.

3.6 Appendix A: Supporting Information Experimental Methods

3.6.1 Electrochemical Measurement.

The electrocatalytic activity of core-frame, frame, and the commercially available catalysts PtRu black (Pt 50 wt.%, Ru wt.50%) were characterized by CO stripping, cyclic voltammetry (CV) and chronoamperometry (CA) on a CHI760 electrochemical workstation at room temperature. The measurements were performed using a three-electrode cell with a Ag/AgCl/1.0 M KCl (E^o = -0.294 V vs. RHE) and Pt wire as reference and counter electrode, respectively. Glassy carbon disk (0.070 cm^2) was polished to a mirror finish before each experiment, and was used as substrate for the working electrode. For each electrochemical measurement, the electrolyte solution was 0.1 M $HClO_4$ and the analyte solution contained 1.0 M CH_3OH and 0.1 M $HClO_4$.

The electrochemically active surface area (ECSA) was determined from the CO stripping voltammetry. For each electrocatalyst, a background scan, a control scan, and a CO stripping scan were obtained at the following conditions. The set of background CVs were obtained by purging the electrolyte solution with Ar, and completing preliminary CV scans 1.5 cycles, at a scan rate of 20 mV/s for the potential range from 0 to 1.2 V vs. RHE, followed by 15 cycles at a scan rate of 100 mV/s, to remove excess capping ligand. The background scan was obtained at a scan rate of 20 mV/s with the potential range from 0 to 1.2 V vs. RHE in electrolyte, to determine the activity in electrolyte. The control scan was obtained at a scan rate of 20 mV/s

with the potential range from 0 to 1.2 V vs. RHE in electrolyte after the potential was held at 0.1 V vs RHE, using chronoamperometry (CA), for 13 min with Ar purging. This is completed to determine if the nanomaterial's activity is affected by holding the potential with Ar purging. The CO stripping voltammograms were obtained after first, purging the electrolyte with CO, while holding the potential at 0.1 V vs RHE for 3 min, using CA. After 3 min, the purging gas was changed to Ar and the potential was held at 0.1 V vs RHE for 10 min. The CO stripping CV scan was obtained at a scan rate of 20 mV/s with the potential range from 0 to 1.2 V vs. RHE in electrolyte. The net CO stripping charge (integrated area in Fig. S3B divided by scan rate 0.02 V/s) was obtained by integrating the charge between the CO stripping scan and the control scan from the double layer region at ~ 0.5 V vs. RHE up to the potential that the two scans merged at ~1.0 V vs. RHE. The ECSA was calculated from eq. 1, the net CO stripping charge (integrated area/scan rate) divided by the charge for a monolayer of adsorbed CO (420 $\mu C \cdot cm^{-2}$) on PtRu surfaces.

$$ECSA = \frac{Q_{CO}}{420 \mu C \cdot cm^{-2}} \qquad (1)$$

The electrochemical activity of the core-frame and frame nanostructures were evaluated by CV profiles in both electrolyte and analyte solutions, as well as CA study in anlyte solution. The CV profiles were obtained at a scan rate of 50 mV/s with the potential range from 0 to 1.2 V vs. RHE in electrolyte solution after purging with Ar for 10 min. The CV profiles was also carried out in analyte solution to evaluate the MOR activity. The CA evaluation was completed by holding the potential at 0.3 V vs. RHE in analyte solution for 5000 s.

Durability experiments were carried out on each electrocatalyst in electrolyte and analyte solutions. For the electrolyte stability studies, preliminary CV were obtained by completing 1.5 cycles at 50 mV/s, 15 cycles at 100 mV/s, 1.5 cycles at 50 mV/s from a potential range from 0 to

1.2 V vs RHE, in electrolyte. The stability scans were completed by continuous cycling in electrolyte solution, for 300 cycles at 100 mV/s. Then final CV curves were obtained by cycling for 3 sweeps at 50 mV/s in electrolyte and analyte solutions. The electrolyte stability studies were performed with preliminary CV scans in analyte solution prior to continuous cycling in electrolyte solution. The preliminary scans in electrolyte solution were obtained, CV scans in analyte solution were obtained by 1.5 cycles at 50 mV/s. The three electrode cell solution was changed to the electrolyte and continuous cycling was completed. The final CV scans (1.5 cycles at 50 mV/s) in electrolyte and analyte solutions were obtained.

The electrolyte stability study was repeated, and preliminary CV scans were obtained in analyte. After purging with Ar, preliminary CV were obtained by completing 1.5 cycles at 50 mV/s, 15 cycles at 100 mV/s, 1.5 cycles at 50mV/s from a potential range from 0 to 1.2 V vs RHE, in electrolyte. CV scans were completed in analyte at a scan rate of 50mV/s at the normal potential range. The stability scans were completed by continuous cycling in electrolyte, for 300 cycles at 100 mV/s. Then final CV curves were obtained by cycling for 3 sweeps at 50 mV/s in electrolyte and analyte solutions.

The durability study completed in analyte solution was completed by obtaining preliminary CV scans (1.5 cycle at 50 mV/s) in electrolyte and analyte solution. Continuous cycling in analyte was completed at 100mV/s for 300 cycles. The final CV scans were obtained in analyte and then electrolyte (1.5 cycles at 50mV/s). After both the electrolyte and analyte durability study, the nanomaterial electrocatalysts were sonicated off the working electrode with 0.5 mL ethanol. After which, the particles were centrifuged at 7,000 rpm for 6 min, and redispersed in 20 μL of ethanol, and then deposited onto a Ni grid for further characterization.

3.7 Appendix B Supporting Information: Results and Discussion

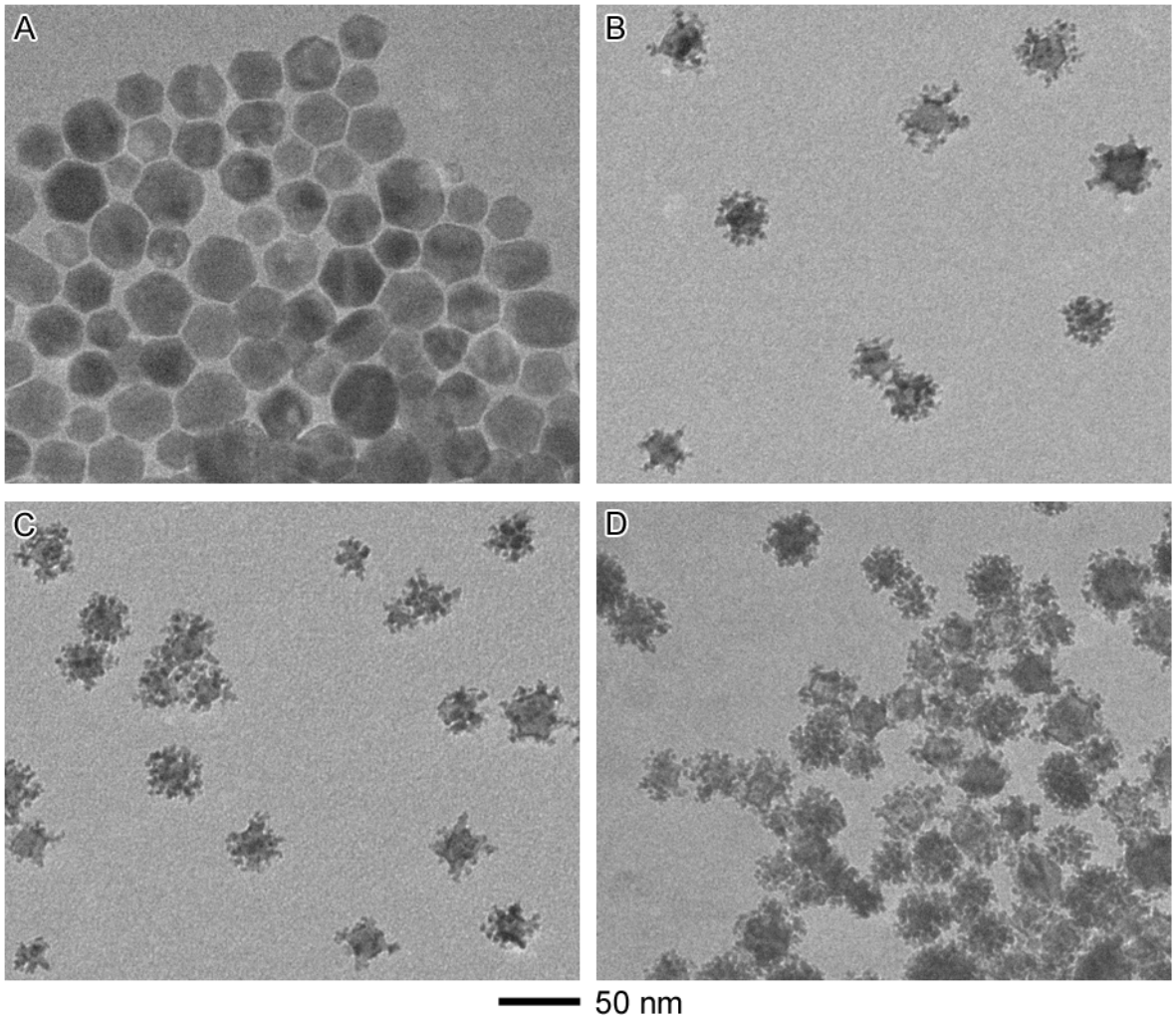

Figure S1. TEM characterization of the aliquot samples taken from the reaction when the temperature reaches 220 ^{o}C prior to the addition of Pt and Ru precursors (A) and after the addition of Pt and Ru at different periods of time: (B) 5 min; (C) 30 min; and (D) 60 min.

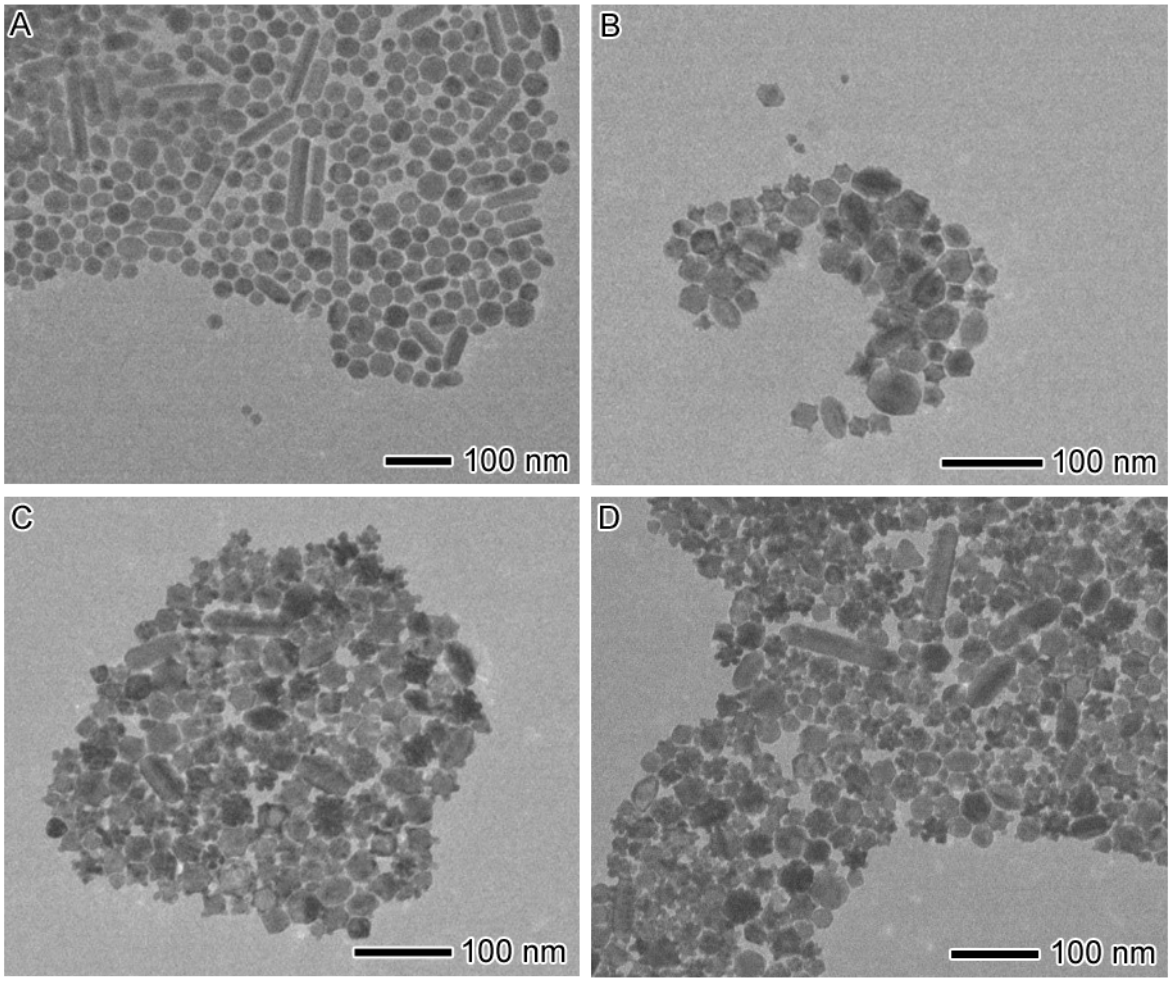

Figure S2. TEM characterization of the aliquot samples taken from the reaction when the temperature reaches 220 ^{o}C prior to the addition of Pt precursors (A) and after the addition of Pt and Ru at different periods of time: (B) 5 min; (C) 30 min; and (D) 60 min.

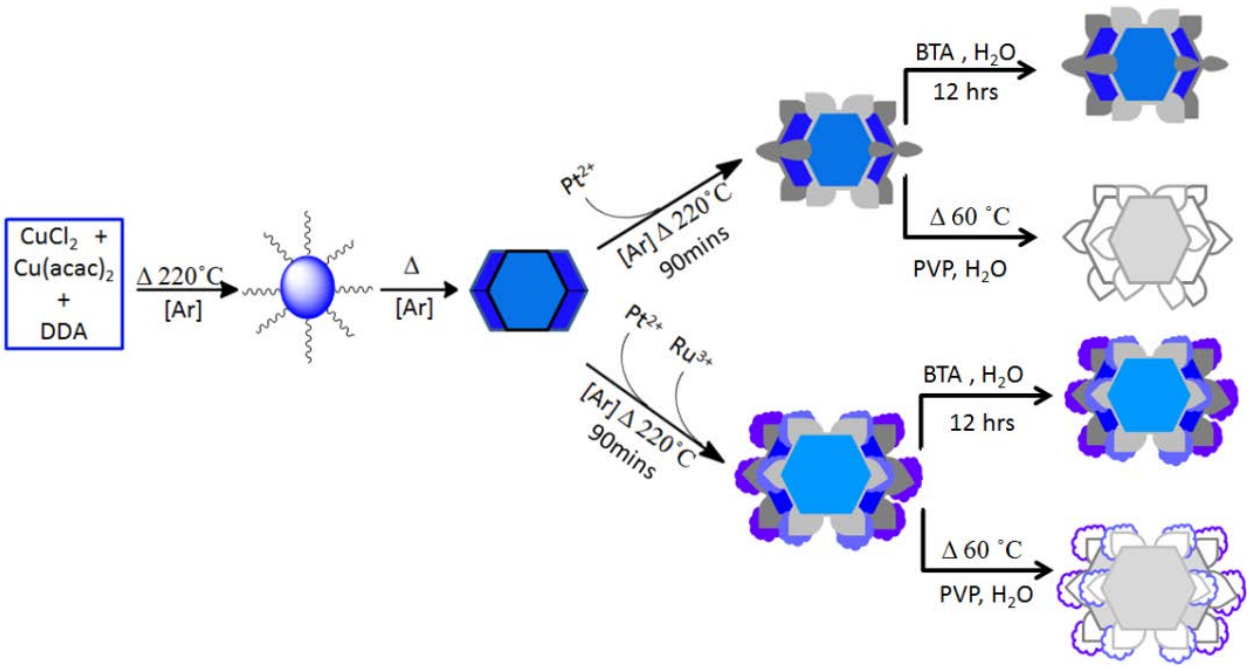

Figure S3: Schematic of the bimetallic and trimetallic coreframe nanostructures. The coreframe nanostructures are then phase transferred to aqueous phase for electrochemical characterization, or treated with acetic acid to form Frame nanostructures.

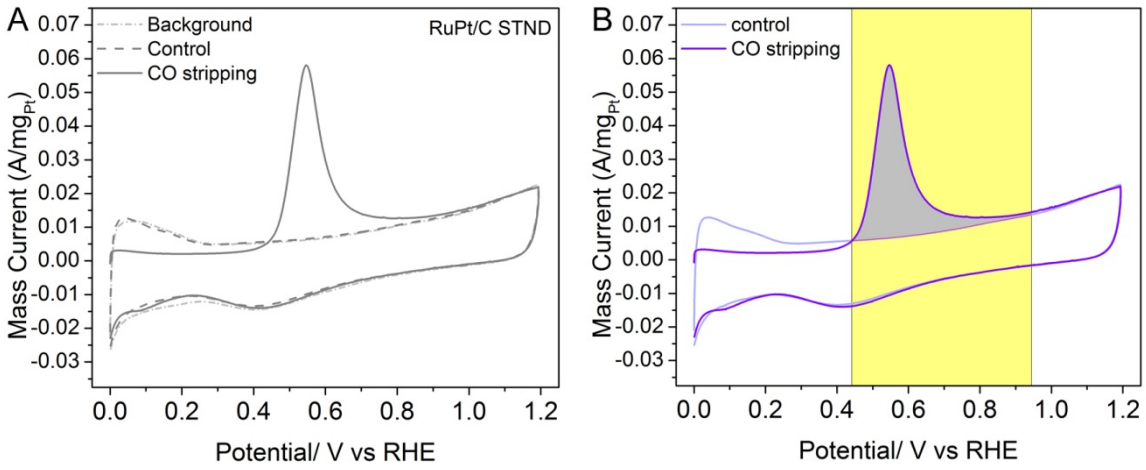

Figure S4. (A) The CO stripping voltammetry study of the standard PtRu catalyst. The CO stripping voltammograms (solid lines) were obtained at a scan rate of 20 mV/s after monolayer of CO was adsorbed on the electrocatalysts. The CV control baselines (dashed lines) were recorded after the potential was held at 0.1 V vs. RHE under argon flow while the CV background baselines (dot lines) were taken after the electrolyte solutions were degassed with argon. (B) Demonstration of the integrated area for the calculation of the net charge CO stripping charge.

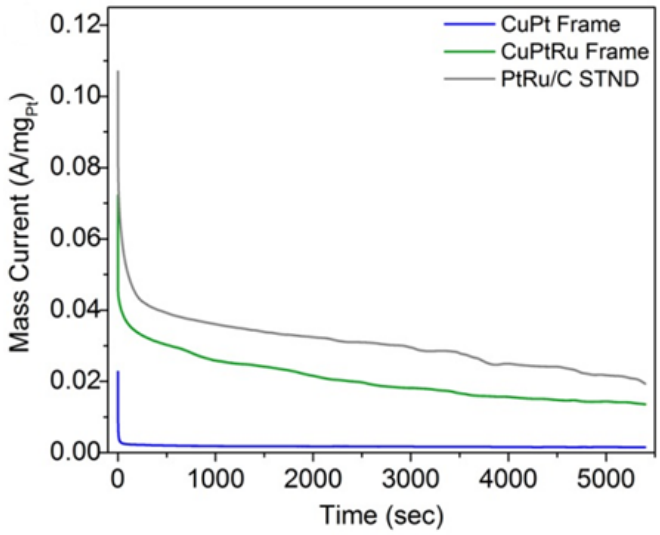

Figure S5. Chronoamperometry (CA) curves of CuPt frame (blue), CuPtRu frame (green), and PtRu standard (grey) obtained by holding the voltage at 0.6 V vs RHE in 0.1 M $HClO_4$ solution containing 1 M methanol.

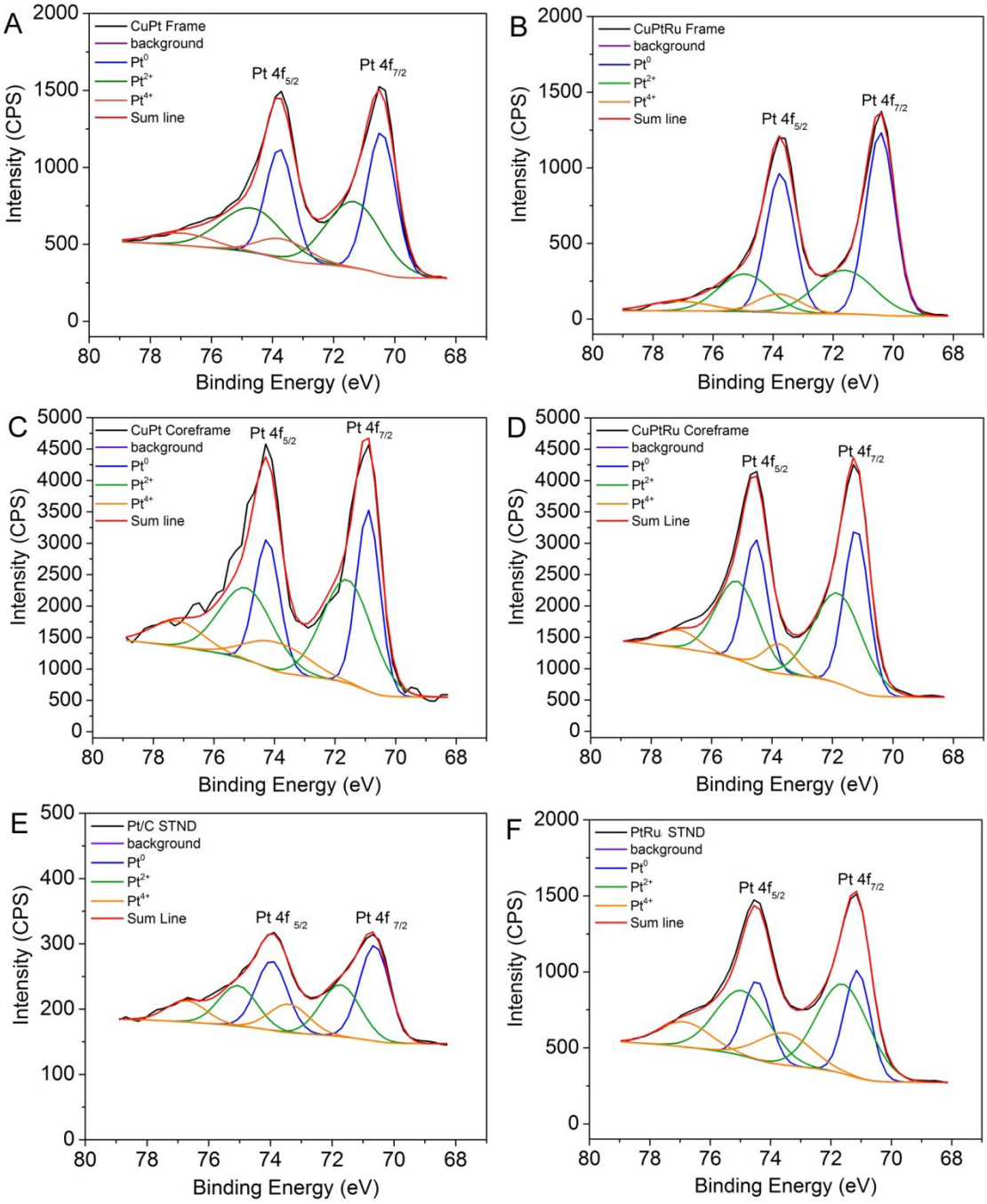

Figure S6. XPS spectra of Pt $4f_{7/2}$ and Pt $4f_{5/2}$ (black lines) which were deconvoluted and fitted with Multipak software as indicated by the smooth color curves: Pt^0 (blue lines), Pt^{2+} (green lines), Pt^{4+} (yellow lines), and the sum of these three oxidation states (red lines). As references (https://srdata.nist.gov/xps/), the binding energies of Pt $4f_{7/2}$ are 71.1, 72.7, 74.0, and 74.9 eV for Pt^0, $Pt(OH)_2$, PtO, and PtO_2, respectively. The Pt $4f_{7/2}$ and Pt $4f_{5/2}$ is splitted by 3.33 eV.

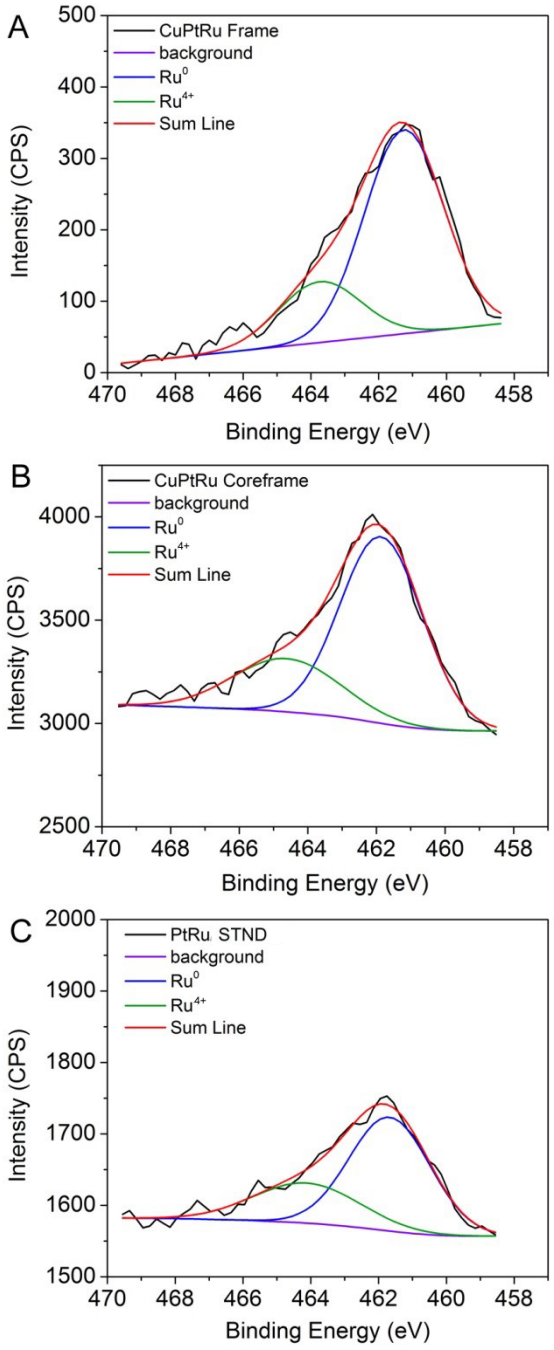

Figure S7. XPS spectra of Ru $3p_{3/2}$ (black lines) which were deconvoluted and fitted with Multipak software as indicated by the smooth color curves: Ru^0 (blue lines), Ru^{4+} (green lines), and the sum of these two oxidation states (red lines). As references (https://srdata.nist.gov/xps/), the binding energies of Ru $3p_{3/2}$ are 461.2, 462.5/465.4(sat.), and 462.7/465.6(sat.) eV for Ru^0, anhydrous RuO_2, and hydrated RuO_2, respectively.

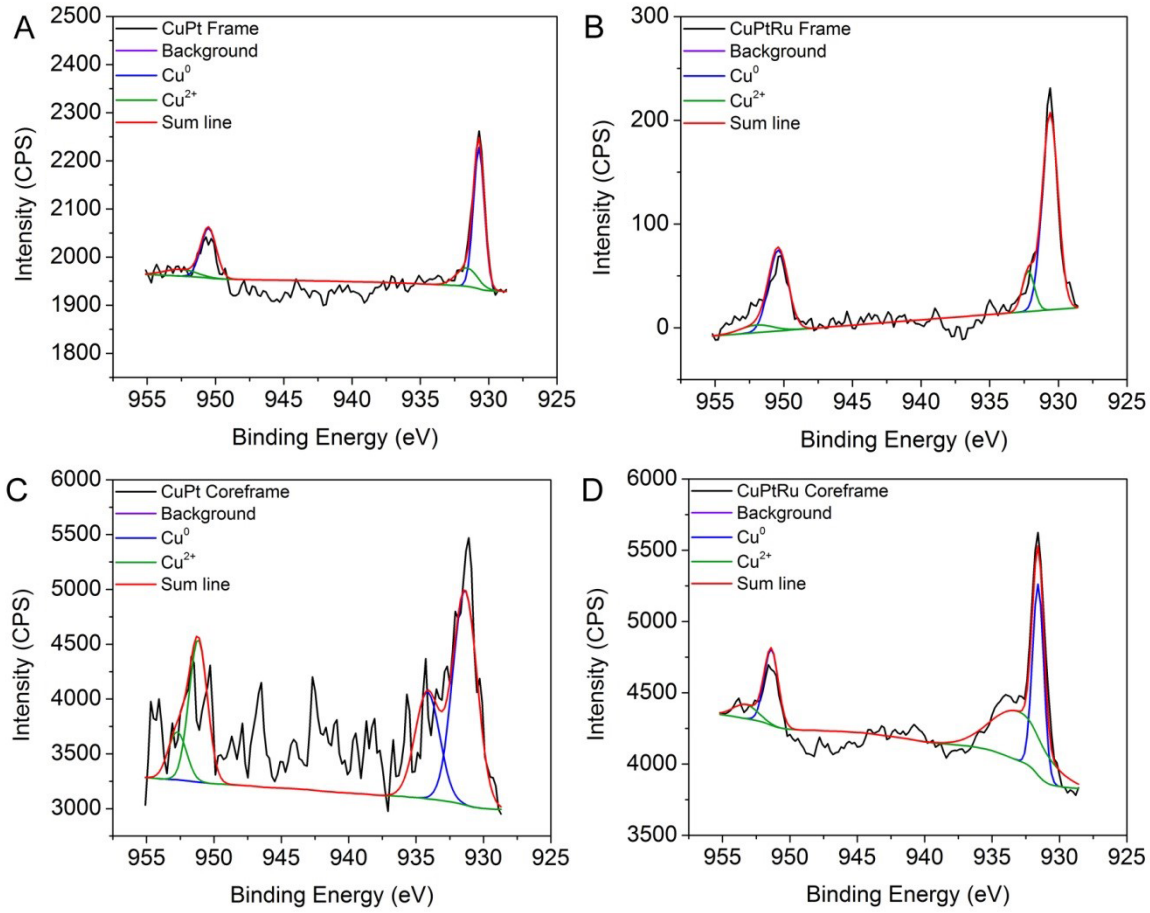

Figure S8. XPS spectra of Cu $2p_{3/2}$ (black lines) which were deconvoluted and fitted with Multipak software as indicated by the smooth color curves: Cu^0 (blue lines), Cu^{2+} (green lines), and the sum of these two oxidation states (red lines). As references (https://srdata.nist.gov/xps/), the binding energies of Cu $2p_{3/2}$ are 932.6, 933.8, and 934.7 eV for Cu^0/Cu_2O, CuO, and $Cu(OH)_2$, respectively.

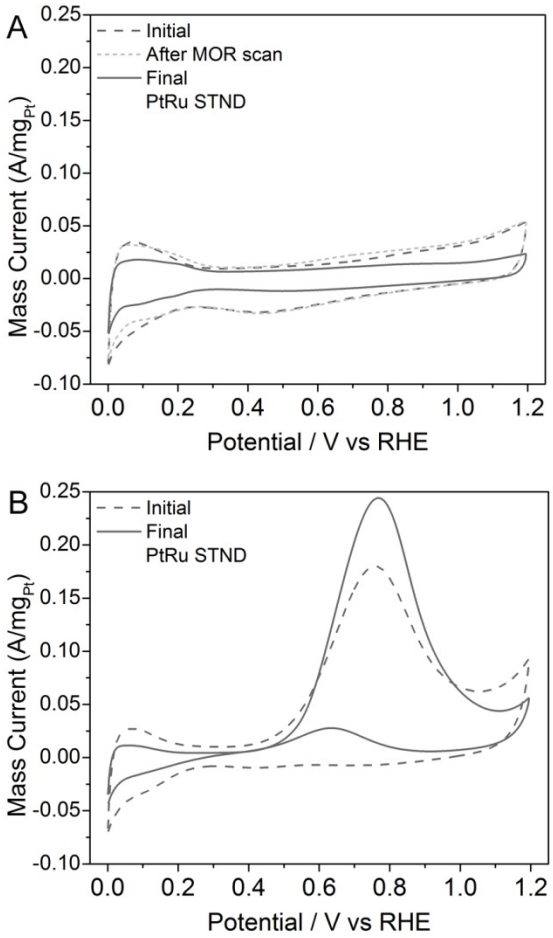

Figure S9: Electrolyte stability study with initial MOR CV of PtRu STND frame. Voltammogram A were obtained in electrolyte, and voltammogram B in analyte. The preliminary CV scans were denoted by dashed lines while the final CV scans were shown by the solid lines.

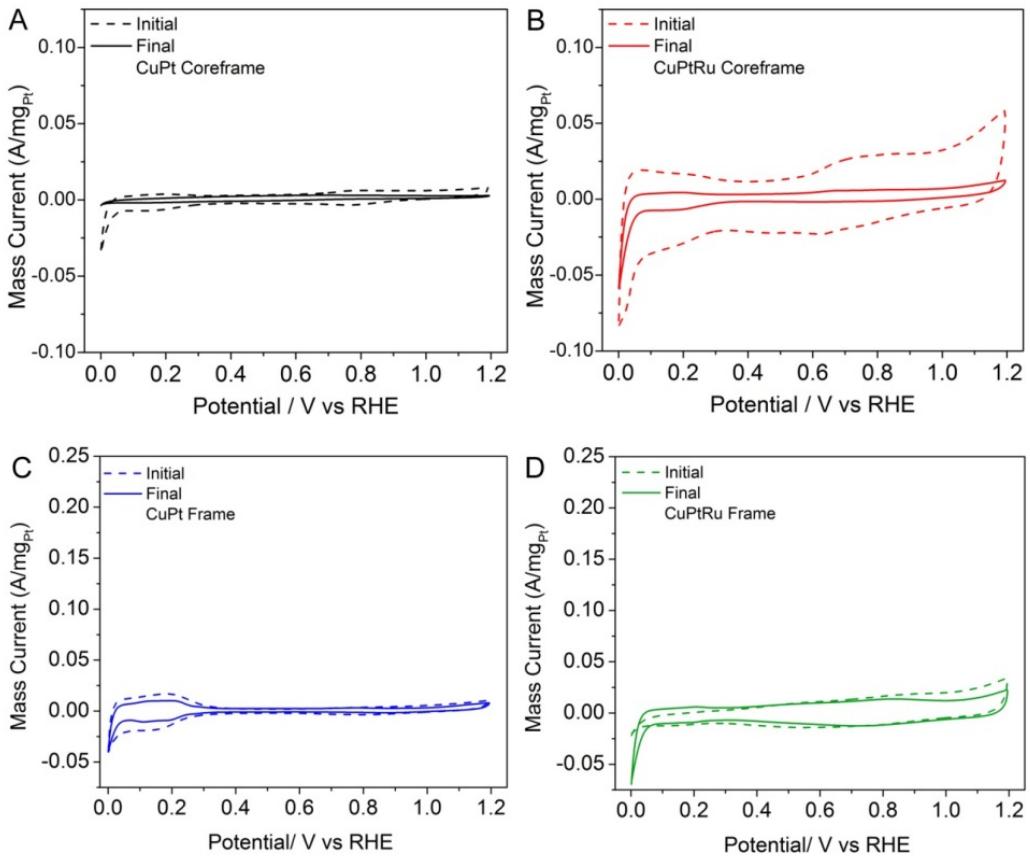

Figure S10: Electrolyte stability study of core-frame (A and B) and frame (C and D) nanostructures. Voltammogram A - D were obtained in electrolyte. The preliminary CV scans were denoted by dashed lines while the final CV scans were shown by the solid lines.

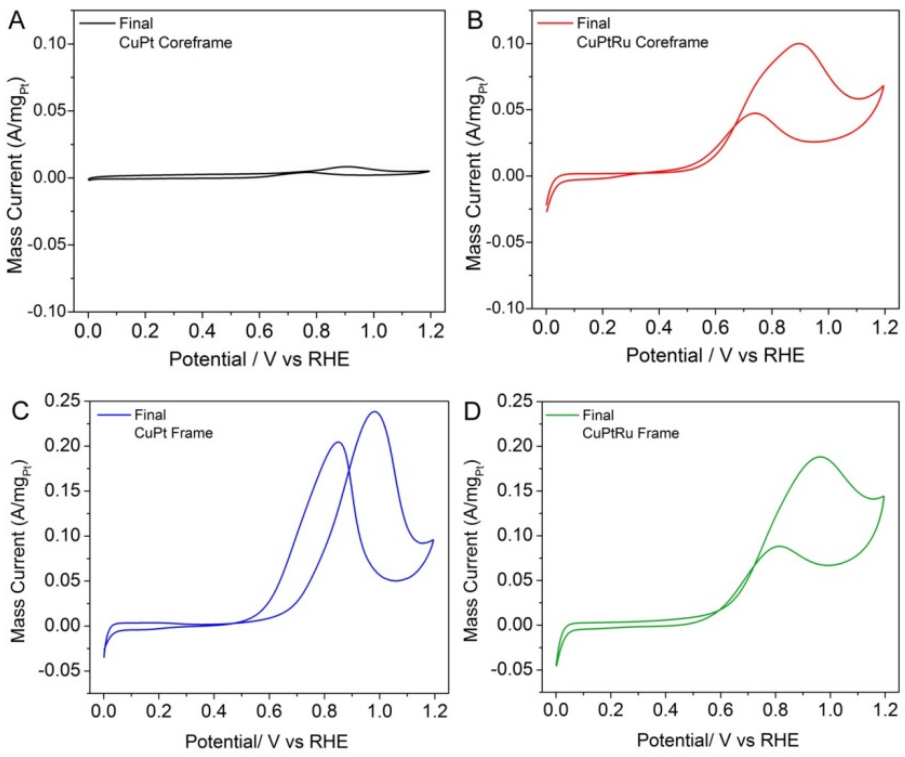

Figure S11: Corresponding MOR CV to the electrolyte stability study in **Figure S9** of core-frame (A and B) and frame (C and D) nanostructures. Voltammogram A - D were obtained in analyte. The preliminary CV scans were denoted by dashed lines while the final CV scans were shown by the solid lines.

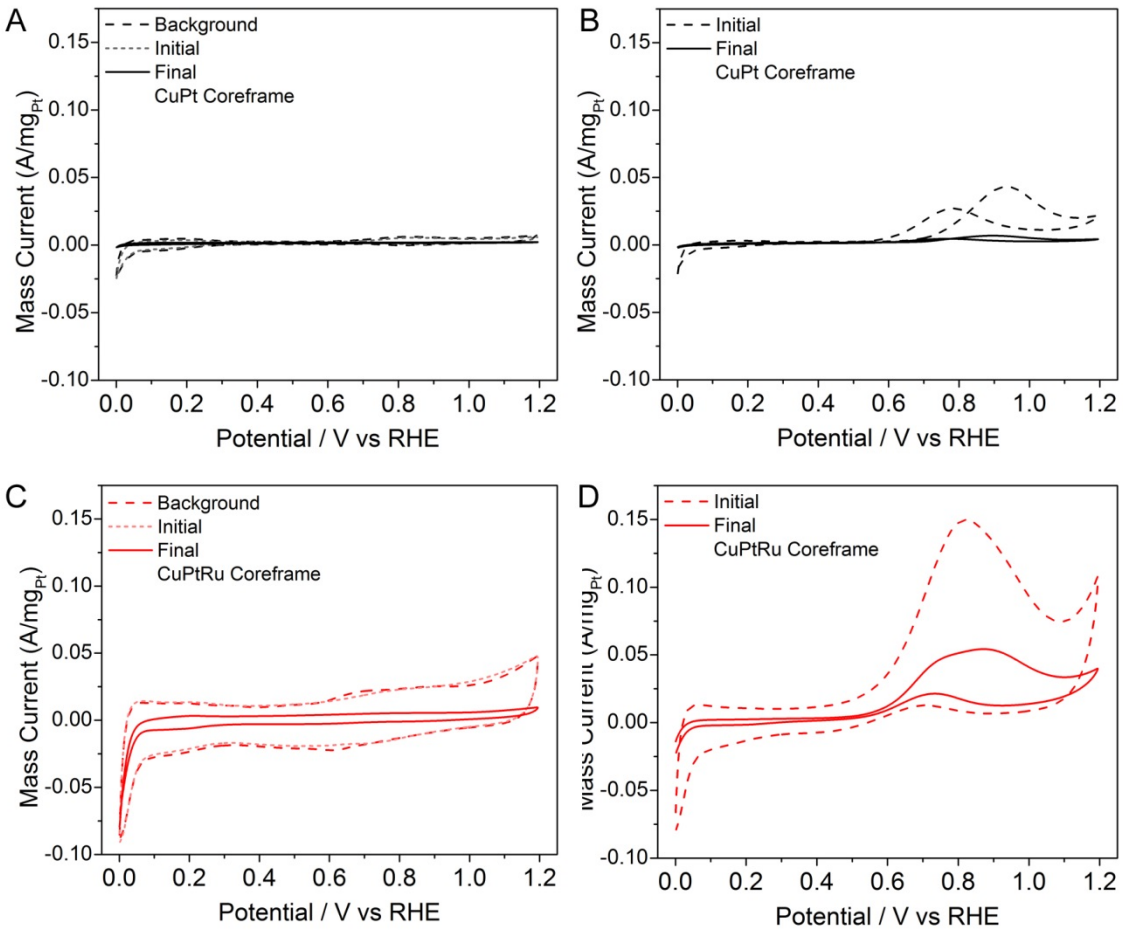

Figure S12. Electrolyte stability study with initial MOR CV, for the coreframe nanostructures, voltammograms performed in 0.1 M $HClO_4$ solution initial (dotted lines) and final 300 cycles (solid lines) with a potential range from 0 to 1.2 V vs RHE at a scan rate of 50 mV/s: (A and B) CuPt core-frame structures; (C and D) CuPtRu core-frame structures.

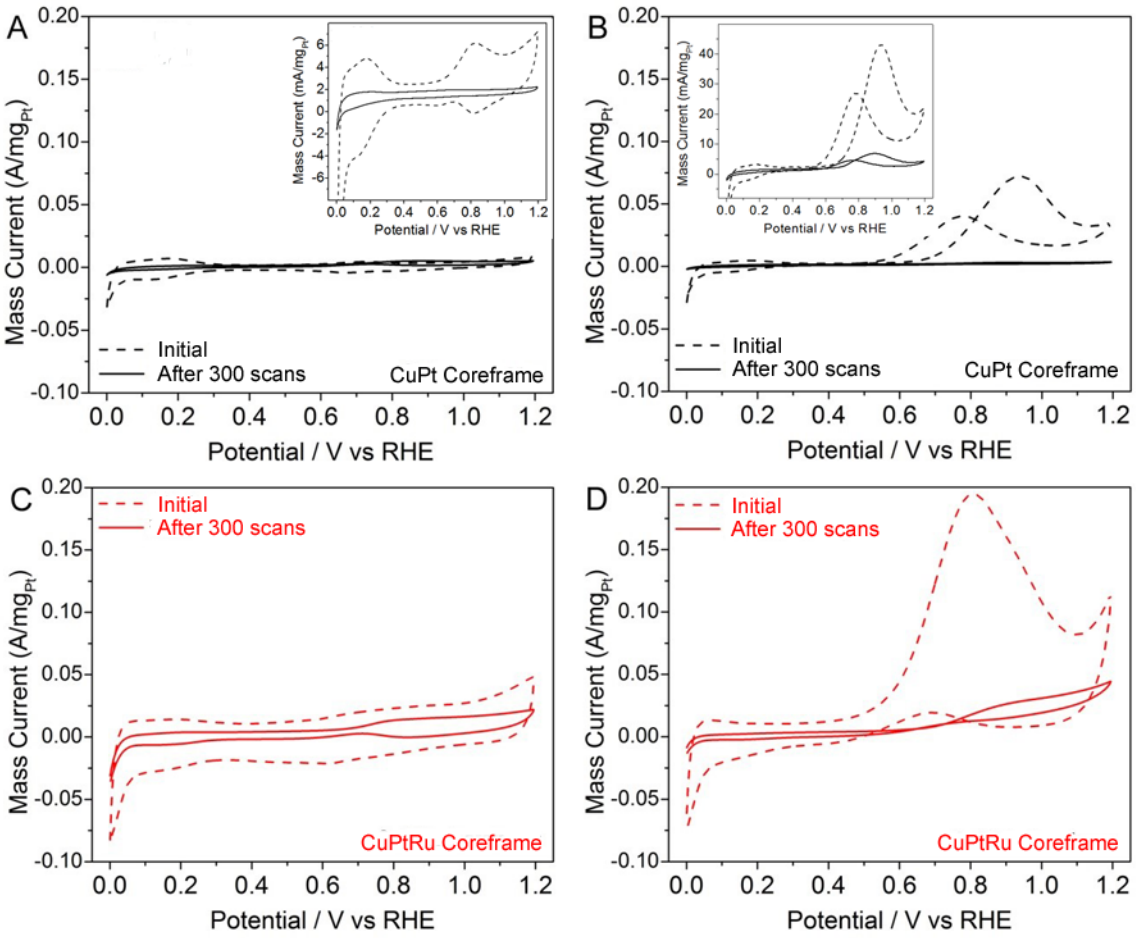

Figure S13. Stability studies of the core-frame nanostructures performed in 0.1 M $HClO_4$ solution containing 1 M methanol before (dotted lines) and after 300 scans (solid lines) with a potential range from 0 to 1.2 V vs RHE at a scan rate of 100 mV/s: (A) CV profiles of CuPt core-frame structures in 0.1 M $HClO_4$; (B) CV profiles of CuPt core-frame structures in 0.1 M $HClO_4$ solution containing 1 M methanol; (C) CV profiles of CuPtRu core-frame structures in 0.1 M $HClO_4$; and (D) CV profiles of CuPtRu core-frame structures in 0.1 M $HClO_4$ solution containing 1 M methanol.

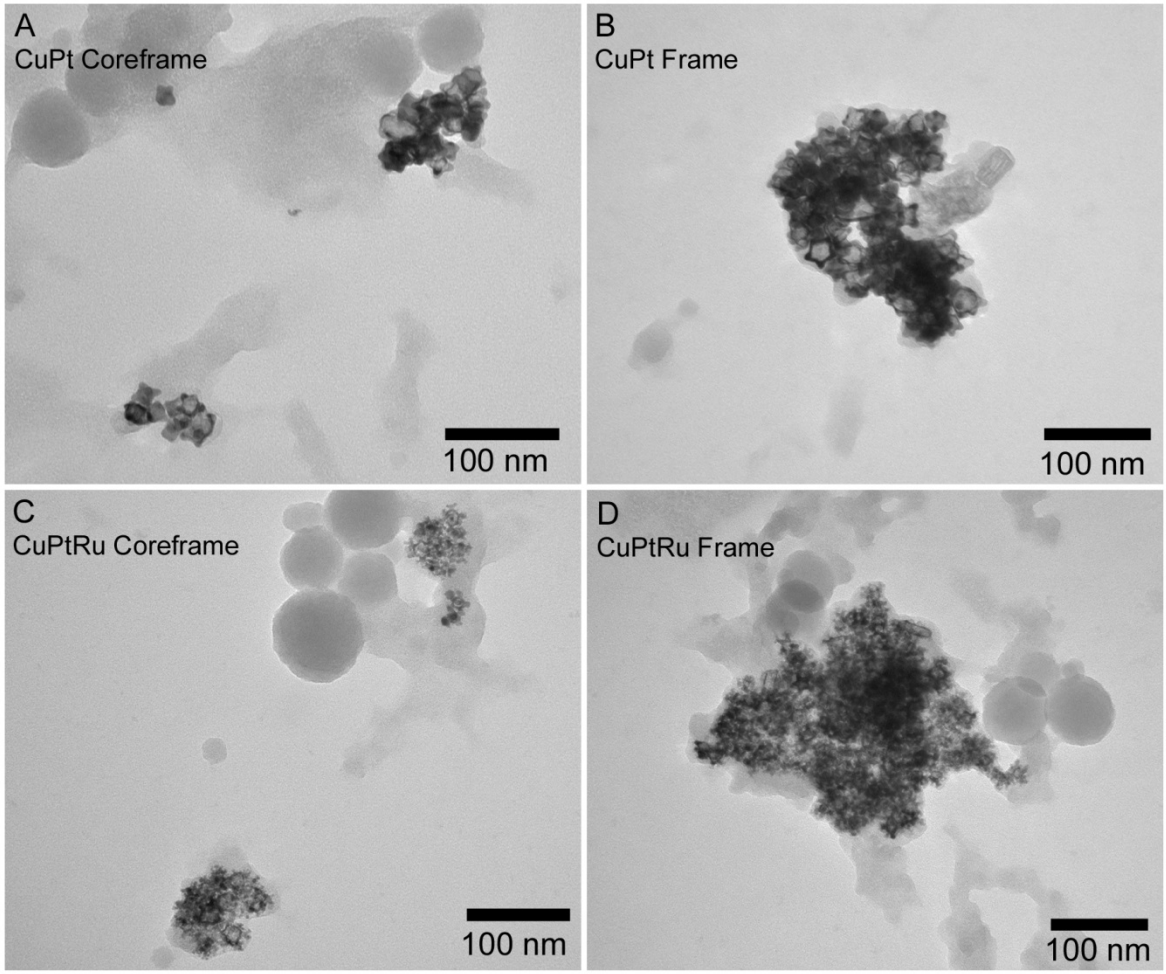

Figure S14. TEM images of coreframe and frame nanostructures collected from the working electrode after electrolyte stability studies. TEM images A & B demonstrate the morphological durability of CuPt coreframe (A) & frame (B) nanostructures, while TEM images C & D determine the durability of the CuPtRu coreframe (C) & frame (D) structure.

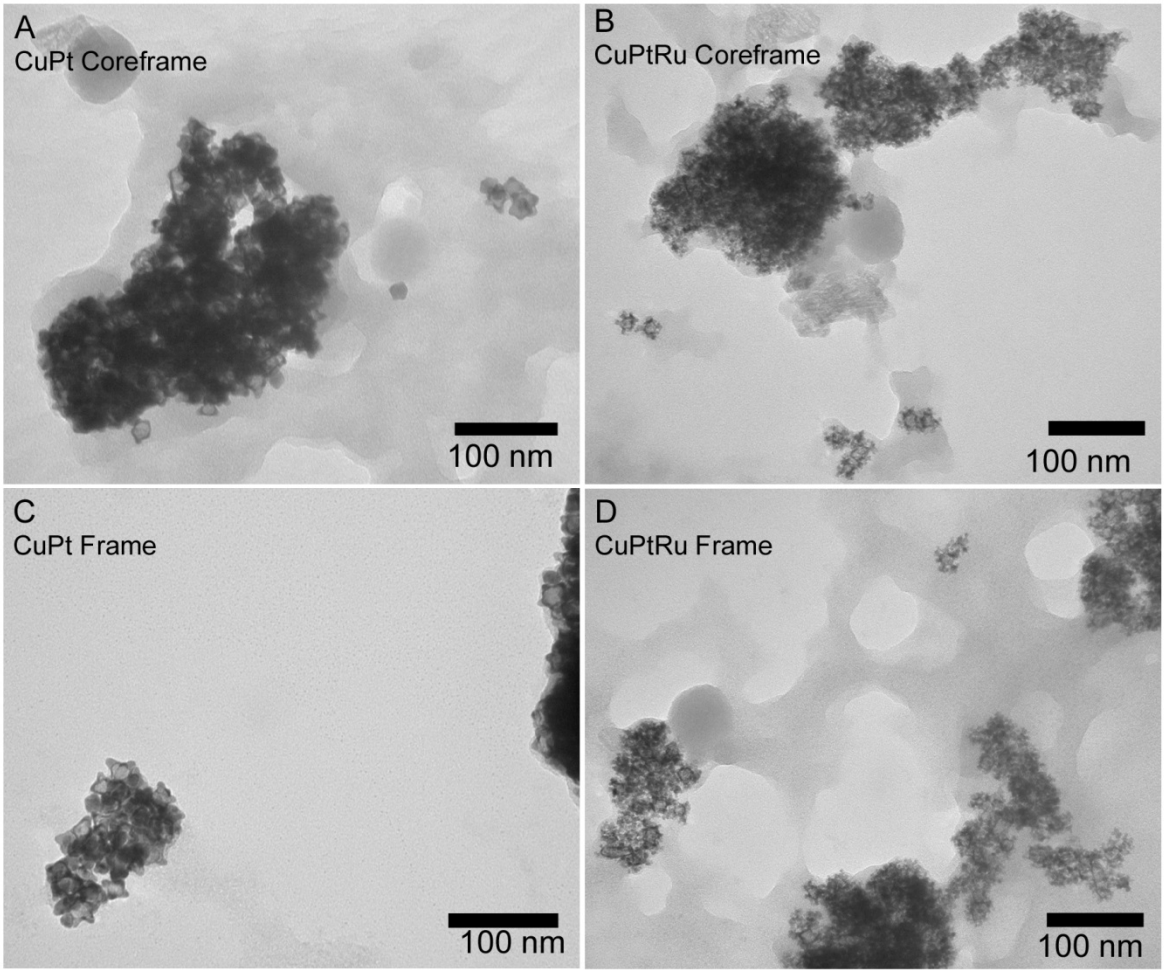

Figure S15. TEM images of coreframe and frame nanostructures collected from the working electrode after analyte stability studies. TEM images A & B demonstrate the morphological durability of CuPt coreframe (A) & frame (B) nanostructures, while TEM images C & D determine the durability of the CuPtRu coreframe (C) & frame (D) structure.

3.8 Appendix C: Supplemental Information, Experimental Methods:

3.8.1 *Ligand exchange methods & Preparation for Electrochemcial Characterization:*

3.8.1.1 Overview

The influence of phase transfer method on nanotube morphology and composition was studied on the CuPt coreframe and CuPtRu coreframe. The coreframe nanostructures were phase transferred using three different methods: the butylamine method, the acetic acid method, and the amine-peg method. The nanotubes from each phase transfer method were characterized and their

electrocatalytic properties were studied. The electrocatalytic properties of each phase transfer method's nanotubes were compared, and the most efficient was choosen for reproducibility studies.

3.8.1.2 Butylamine Method:

The coreframe nanostructures were prepared for electrochemical characterization by first exchanging surface ligands to allow for the synthesized nanotubes to be dispersed in aqueous phase. The ligand exchange process occurred by combining as-synthesized nanotubes with 2 mL of butylamine/water (50% v/v) solution at 25 ºC. The solution was stirred for 14 hr at 25 ^{o}C in a glass vial (1 dr) equipped with a magnetic stir bar. After the ligand exchange, the nanotubes were rinsed by dispersing in ethanol and centrifuging at 6,500 rpm for 6 min. The this process continued by rinsing the NP in a 50% v/v ethanol/water solution twice, then rinsing the NP in a 25% v/v ethanol/water solution twice, and finally rinsing in 18 MΩ H_2O twice. The electrocatalysts were suspended in 2 ml of 18 MΩ H_2O for morphological, and composition characterization by ICP-MS (or AA) and TEM.

3.8.1.3 Acetic Acid Method:

The CuPt corefame & CuPtRu coreframe nanostructures were phase transferred by ligand exchange using the acetic acid method. The electrocatalysts were prepared by combining 2 ml of 18 MΩ H_2O, 2 ml of acetic acid, and 0.75 ml of electrocatalyst in a 2 dr vial. The reaction solution was spun at 60 ˚C for 4 hours. After which the sample was purified by removing to a 15 ml centrifuge tube, adding 10 ml of ethanol, and separating by centrifuge at 6,000 rpm for 6 minutes. After rinsing the nanoparticles, the nanotube solution was redispersed into 2 ml of 18MΩ H_2O. The nanotubes's surface structure, morphology, and composition were studied.

3.8.1.4 Amine-PEG Method:

The coreframe nanostructures were phase transferred, and prepared for electrochemical characterization by weighing 0.0159 g of amine peg (full name), and dispersing in 15 ml of chloroform. The reaction solution was cooled to 5 ˚C in an ice bath, while degassing for 15 minutes. The electrocatalysts were then injected into the cooled reaction solution. The nanotube solution was spun overnight at a stir rate of 5.5. The nanotubes were purified by the following method. The nanotubes were purified by combining with 45 ml of hexanes, and the nanotubes were separated by centrifuge for 10 minutes at 9,000 rpms (rcf). The particles were redispersed in 15 mL of ethanol, and separated again by centrifuging at 6,000 for 6 minutes, this step was repeated twice. The nanotubes were redispersed in 2 ml of 18MΩ H_2O. The nanotubes were then prepared by electrochemical characterized by the protocol outlined below.

3.8.2 Determination of reproducibility studies

Four individual synthesis batches of PtCu bNS and RuPtCu bNS were synthesized, phase transferred, and their electrochemical properties were also studied. The syntheses and the individual electrochemical studies were completed by the previously outlined procedures. The electrochemical properties of PtCu bNS and RuPtCu bNS were also investigated in a different electrolyte, sulfuric acid. In this study, the other electrochemical parameters were held constant.

3.9 Appendix D: Supplemental Information, Results and Discussion:

3.9.1 *Choosing the phase transfer method, and characterization of coreframe nanostructures after ligand exchange process*

The various phase transfer methods and resulting electrochemical properties of each coreframe phase transferred by the different methods were compared. Phase transfer method that

resulted in the coreframe nanostructures having the highest produced current, lowest overpotential, and increased resistance to CO poisoning was chosen for reproducibility studies. Prior to the electrochemical characterization the coreframe nanostructures underwent the butylamine phase transfer. After phase transferring the morphology of each type of nanotube was characterized by TEM to determine if the morphology was maintained during the phase transfer. The results of which can be found in Figure #. The PtCu bNS after the ligand exchange is shown in TEM image A, and the RuPtCu bNS results can be found in image B. The TEM images demonstrate that the nanotube morphology and surface structure is not altered during the phase transfer process. The images also possess light grey non uniform structures, which can be attributed to remaining butylamine from the ligand exchange method.

Morphological characterization of coreframe nanostructures after the various phase transfer methods.

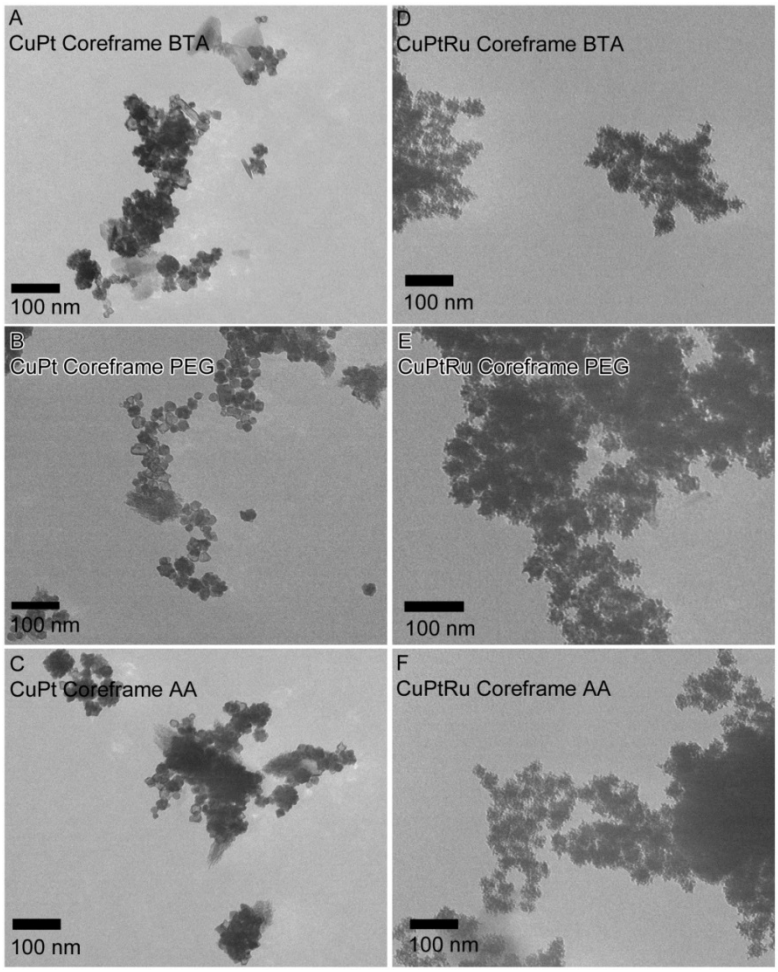

Figure SI 1: contains the various phase transfer methods that were tried for the coreframe nanostructures.

Electrochemical characterization of the coreframe nanostructures after the various phase transfer methods

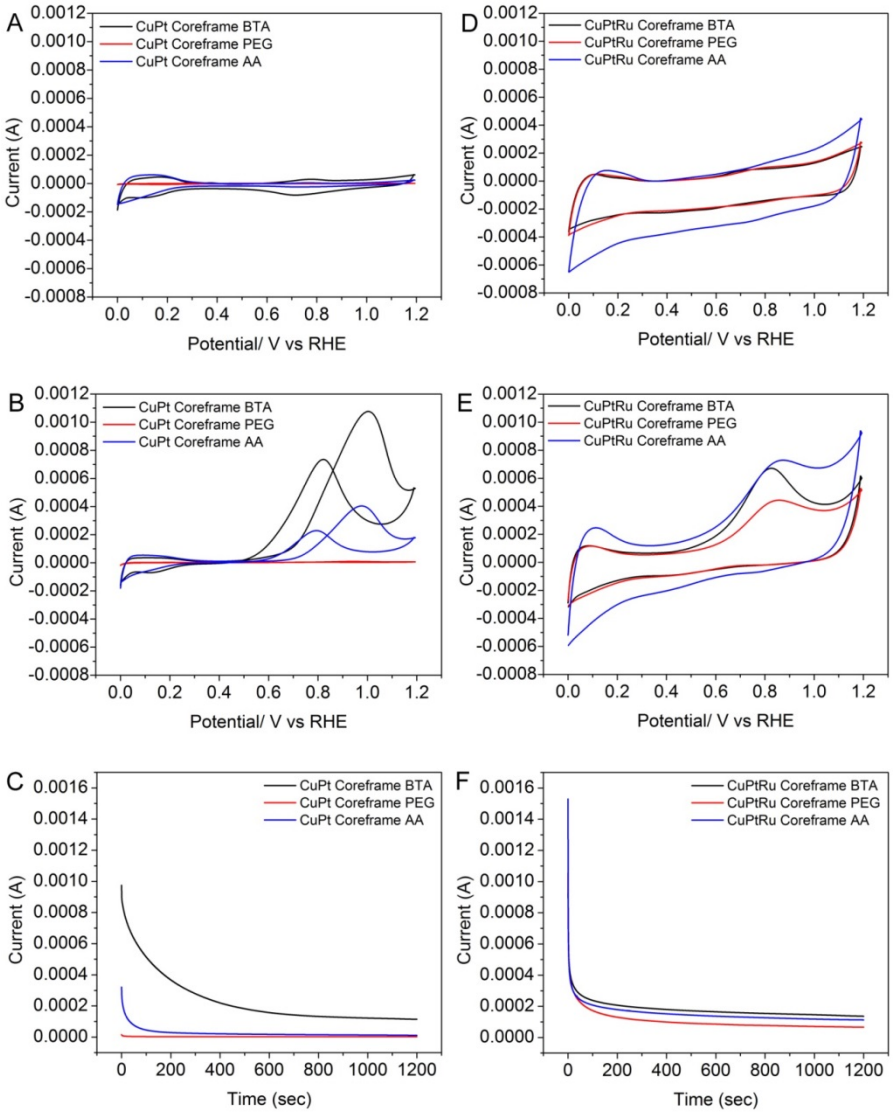

Figure SI 2: electrochemical characterization of various phase transfer methods.

Coreframe Reproducibility Studies:

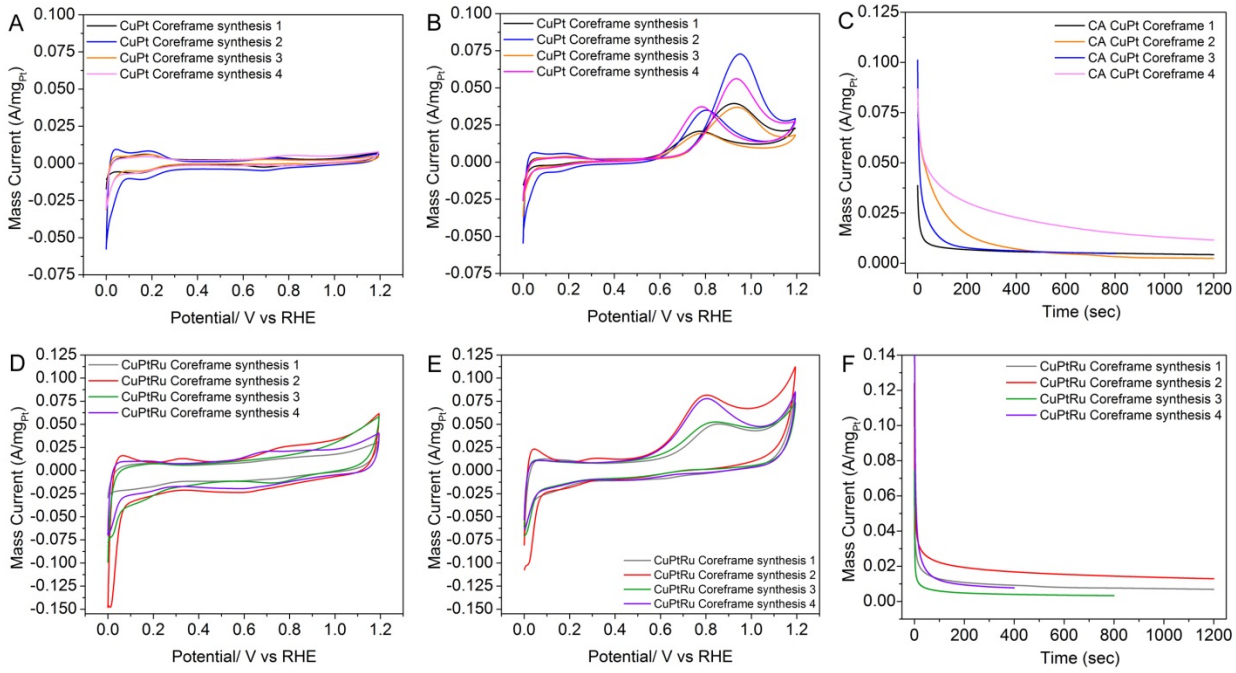

Figure SI 3: provides preliminary electrochemical characterization of CuPt coreframe (A-C) and CuPtRu coreframe (D – F) nanostructure for three synthetic batches. CV in electrolyte (A&D), CV in analyte (B & E), CA in analyte (C&F).

Frame Reproducibility Studies

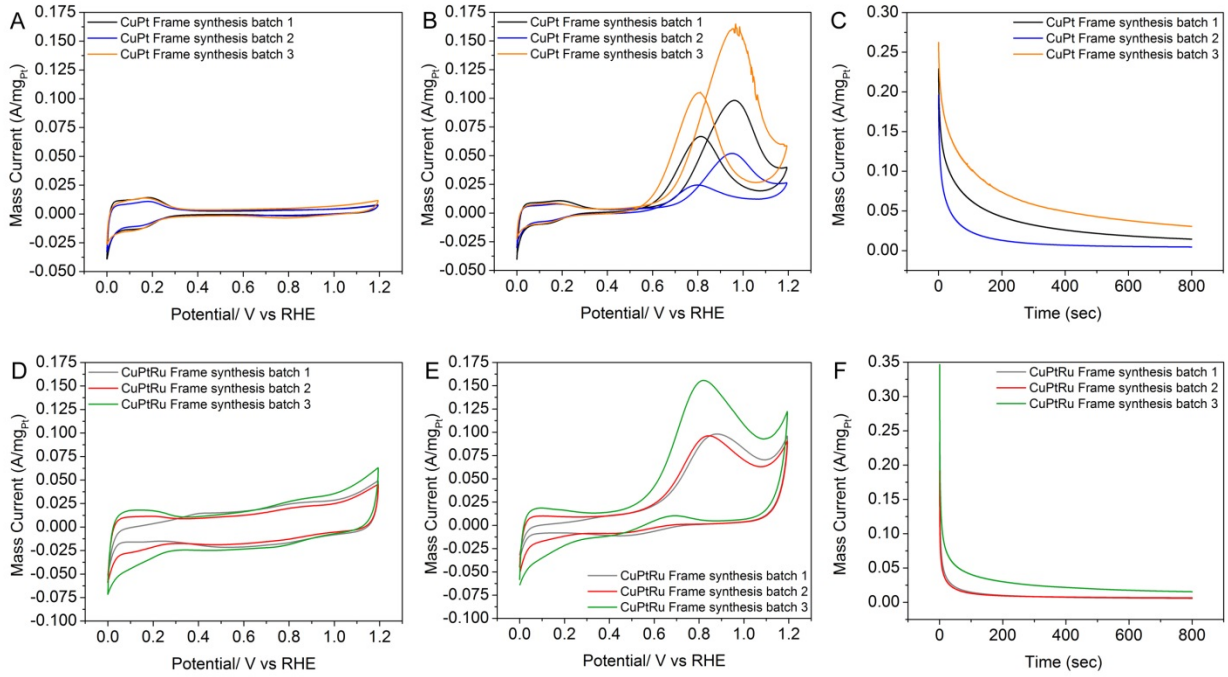

Figure SI 4: provides preliminary electrochemical characterization of CuPt frame (A-C) and CuPtRu frame (D – F) nanostructure for three synthetic batches. CV in electrolyte (A&D), CV in analyte (B & E), CA in analyte (C&F).

The composition of the electrocatalysts after stability experiments was studied by ICP-MS. The deposited electrocatalysts were collected after the stability studies, and prepared for ICP-MS analysis. The electrocatalyst composition was determined, and the results can be found in chart 1. This chart possess ICP-MS results for the composition of PtCu bNS, RuPtCu bNS, and PtCu bNS after acetic acid etching (PtCu bNS Cu →) collected after the stability studies in electrolyte and analyte. These results show the prescence of Ru, Pt, Cu in each electrocatalyst. Due to the difference in electrocatalyst composition before and after the durability studies, the electrolyte and analyte stolutions were studied to determine the composition. The solution from the stability studies were collected, and studied by ICP-MS to determine if metals were leaching from the electrocatalyst during the stabiltiy studies. Chart 2 contains ICP-MS results for each electrocatalyst, which demonstrates the change in ruthenium, platinum, and copper concentration

for each electrolyte and analyte stability studies. These results suggest that only trace amounts of each metal was being removed from the deposited electrocatalysts during the stability studies. This suggests that the RuPtCu Coreframe, PtCu Coreframe, RuPtCu Frame, and PtCu Frame nanostructures are durable electrocatalysts for MOR.

Chart 1: chart demonstrating the concentration change after stability studies for PtCu & RuPtCu coreframe nanostructures.

stability samples	Cu conc (mg/ml)	Ru conc (mg/ml)	Pt conc (mg/ml)
CuPtRu Coreframe electrolyte stability	0.000966633	0.006332934	0.007200036
CuPtRu Coreframe analyte stability	0.00131945	0.007827369	0.00398277
CuPt Coreframe electrolyte stability	0.009108432	0.00046284	0.015142193
PtCu bNs analyte stability	0.005106276	0.00046122	0.007968548
PtCu frame electrolyte stability	0.001648	-1.96476E-05	0.00352069
PtCu frame analyte stability	0.0025	-1.97257E-05	0.0090297

Chart 2: Chart demonstrating the change in copper content after stability studies.

sample Cu 63	counts	ppb	ppm	mg/ml
CuPtRu coreframe electrolyte	2728554	293.3939	0.293394	0.000293
CuPtRu coreframe analyte	89303.06	9.487453	0.009487	9.49E-06
CuPt coreframe electrolyte	2800014	301.0809	0.301081	0.000301
CuPt coreframe analyte	187259.7	20.02473	0.020025	2E-05
CuPt coreframe electrolyte soak	3071318	330.2653	0.330265	0.00033
CuPt coreframe analyte soak	3589307	385.9858	0.385986	0.000386

Chart 3: Chart demonstrating the change in ruthenium content after stability studies.

sample	counts	ppb	ppm	mg/ml
RuPtCu bNS electrolyte	539998.7	41.61233	0.041612	4.16E-05
RuPtCu bNS analyte	23045.05	1.791526	0.001792	1.79E-06

Chart 4: Chart demonstrating the change in platinum content after stability studies.

sample	counts	Conc (ppb)	Conc. (ppm)	Conc. (mg/ml)
CuPtRu Coreframe electrolyte stability	5257623	324.088	0.324088	0.000324
CuPtRu Coreframe analyte stability	26411.99	1.770622	0.001771	1.77E-06
CuPt Coreframe electrolyte stability	4158293	256.3536	0.256354	0.000256
CuPt Coreframe	31790.5	2.102015	0.002102	2.1E-06
CuPt Coreframe electrolyte soak	5561.278	0.48592	0.000486	4.86E-07
CuPt Coreframe analyte soak	5495.225	0.48185	0.000482	4.82E-07

3.10 Appendix E: Supplemental Information, Conclusion

In conclusion the electrochemical studies were expanded to include an experimental method to determine the charging double layer capacitance value, which corresponds to the electrochemically active surface area. The durability of each electrocatalyst was also studied in electrolyte as well as analyte. These results demonstrated that the electrocatalysts are more active after durability scans in electrolyte compared to the analyte solution. After continuous cycling, the final CV scans possess a shorter peak on the reverse sweep, which suggests that both electrocatalysts maintain resistance towards intermediate species poisoning. The morphology and composition of PtCu bNS and RuPtCu bNS were characterized through TEM and ICP-MS. These results suggest that the morphology was maintained after 500 cycles; however, there was a change in composition during the stability studies. The electrocatalytic studies as well as the morphological and compositional characterization suggest that our electrocatalysts does begin to breakdown during the study; therefore, the durability of these electrocatalysts needs to be

improved. Preliminary electrochemical studies were also completed on the influence of the pair site in the PtCu bNS nanomaterial. The preliminary characterization results suggest that the core copper was removed from the electrocatalyst, and the resulting structure was electrochemically active. However, additional studies need to be completed to determine if the electrochemical activity is related to the increased surface area of the nanomaterials or the increased number of pair sites between platinum and copper.

3.11 References

1. (a) Wang, D.; Li, Y., Bimetallic nanocrystals: liquid-phase synthesis and catalytic applications. *Advanced Materials* **2011,** *23* (9), 1044-1060; (b) Zhang, H.; Jin, M.; Xia, Y., Enhancing the catalytic and electrocatalytic properties of Pt-based catalysts by forming bimetallic nanocrystals with Pd. *Chemical Society Reviews* **2012,** *41* (24), 8035-8049; (c) Wu, J.; Yang, H., Platinum-based oxygen reduction electrocatalysts. *Accounts of chemical research* **2013,** *46* (8), 1848-1857; (d) Weiner, R. G.; Kunz, M. R.; Skrabalak, S. E., Seeding a new kind of garden: synthesis of architecturally defined multimetallic nanostructures by seed-mediated co-reduction. *Accounts of chemical research* **2015,** *48* (10), 2688-2695; (e) Gilroy, K. D.; Ruditskiy, A.; Peng, H.-C.; Qin, D.; Xia, Y., Bimetallic nanocrystals: syntheses, properties, and applications. *Chemical Reviews* **2016,** *116* (18), 10414-10472.

2. Fang, Z.; Wang, Y.; Liu, C.; Chen, S.; Sang, W.; Wang, C.; Zeng, J., Rational design of metal nanoframes for catalysis and plasmonics. *Small* **2015,** *11* (22), 2593-2605.

3. (a) Zeng, J.; Zhang, Q.; Chen, J.; Xia, Y., A comparison study of the catalytic properties of Au-based nanocages, nanoboxes, and nanoparticles. *Nano letters* **2009,** *10* (1), 30-35; (b) Xia, B. Y.; Wu, H. B.; Wang, X.; Lou, X. W., One-pot synthesis of cubic PtCu3 nanocages with enhanced electrocatalytic activity for the methanol oxidation reaction. *Journal of the American chemical Society* **2012,** *134* (34), 13934-13937; (c) Nosheen, F.; Zhang, Z.-c.; Zhuang, J.; Wang, X., One-pot fabrication of single-crystalline octahedral Pt–Cu nanoframes and their enhanced electrocatalytic activity. *Nanoscale* **2013,** *5* (9), 3660-3663; (d) Chen, C.; Kang, Y.; Huo, Z.; Zhu, Z.; Huang, W.; Xin, H. L.; Snyder, J. D.; Li, D.; Herron, J. A.; Mavrikakis, M., Highly crystalline multimetallic nanoframes with three-dimensional electrocatalytic surfaces. *Science* **2014,** *343* (6177), 1339-1343; (e) Li, J.; Sun, X.; Qin, D., Ag-Enriched Ag-Pd Bimetallic Nanoframes and Their Catalytic Properties. *ChemNanoMat* **2016,** *2* (6), 494-499; (f) Luo, S.; Shen, P. K., Concave Platinum–Copper Octopod Nanoframes Bounded with Multiple High-Index Facets for Efficient Electrooxidation Catalysis. *ACS Nano* **2016**; (g) Becknell, N.; Zheng, C.; Chen, C.; Yu, Y.; Yang, P., Synthesis of PtCo3 polyhedral nanoparticles and evolution to Pt3Co nanoframes. *Surface Science* **2016,** *648*, 328-332.

4. (a) Lim, B.; Jiang, M.; Camargo, P. H.; Cho, E. C.; Tao, J.; Lu, X.; Zhu, Y.; Xia, Y., Pd-Pt bimetallic nanodendrites with high activity for oxygen reduction. *Science* **2009,** *324* (5932),

1302-1305; (b) Wang, L.; Nemoto, Y.; Yamauchi, Y., Direct synthesis of spatially-controlled Pt-on-Pd bimetallic nanodendrites with superior electrocatalytic activity. *Journal of the American Chemical Society* **2011,** *133* (25), 9674-9677; (c) Wang, W.; Wang, D.; Liu, X.; Peng, Q.; Li, Y., Pt–Ni nanodendrites with high hydrogenation activity. *Chemical Communications* **2013,** *49* (28), 2903-2905; (d) Taylor, E.; Chen, S.; Tao, J.; Wu, L.; Zhu, Y.; Chen, J., Synthesis of Pt–Cu Nanodendrites through Controlled Reduction Kinetics for Enhanced Methanol Electro-Oxidation. *ChemSusChem* **2013,** *6* (10), 1863-1867.

5. Winter, M.; Brodd, R. J., What are batteries, fuel cells, and supercapacitors? ACS Publications: 2004.

6. Rabis, A.; Rodriguez, P.; Schmidt, T. J., Electrocatalysis for Polymer Electrolyte Fuel Cells: Recent Achievements and Future Challenges. *Acs Catalysis* **2012,** *2* (5), 864-890.

7. Steele, B. C.; Heinzel, A., Materials for fuel-cell technologies. *Nature* **2001,** *414* (6861), 345-352.

8. Wasmus, S.; Küver, A., Methanol oxidation and direct methanol fuel cells: a selective review. *Journal of Electroanalytical Chemistry* **1999,** *461* (1), 14-31.

9. Liu, H.; Song, C.; Zhang, L.; Zhang, J.; Wang, H.; Wilkinson, D. P., A review of anode catalysis in the direct methanol fuel cell. *Journal of Power Sources* **2006,** *155* (2), 95-110.

10. (a) Rossmeisl, J.; Ferrin, P.; Tritsaris, G. A.; Nilekar, A. U.; Koh, S.; Bae, S. E.; Brankovic, S. R.; Strasser, P.; Mavrikakis, M., Bifunctional anode catalysts for direct methanol fuel cells. *Energy & Environmental Science* **2012,** *5* (8), 8335-8342; (b) Tritsaris, G. A.; Rossmeisl, J., Methanol Oxidation on Model Elemental and Bimetallic Transition Metal Surfaces. *The Journal of Physical Chemistry C* **2012,** *116* (22), 11980-11986.

11. Antolini, E., Evaluation of the optimum composition of low-temperature fuel cell electrocatalysts for methanol oxidation by combinatorial screening. *ACS Combinatorial Science* **2016**.

12. (a) Xu, D.; Liu, Z.; Yang, H.; Liu, Q.; Zhang, J.; Fang, J.; Zou, S.; Sun, K., Solution-Based Evolution and Enhanced Methanol Oxidation Activity of Monodisperse Platinum–Copper Nanocubes. *Angewandte Chemie International Edition* **2009,** *48* (23), 4217-4221; (b) Yin, A. X.; Min, X. Q.; Zhu, W.; Liu, W. C.; Zhang, Y. W.; Yan, C. H., Pt □ Cu and Pt□ P Nanocubes with High-Index Facets and Superior Electrocatalytic Activity. *Chemistry–A European Journal* **2012,** *18* (3), 777-782; (c) Qi, Y.; Bian, T.; Choi, S.-I.; Jiang, Y.; Jin, C.; Fu, M.; Zhang, H.; Yang, D., Kinetically controlled synthesis of Pt–Cu alloy concave nanocubes with high-index facets for methanol electro-oxidation. *Chemical Communications* **2014,** *50* (5), 560-562.

13. Zhang, Z.; Luo, Z.; Chen, B.; Wei, C.; Zhao, J.; Chen, J.; Zhang, X.; Lai, Z.; Fan, Z.; Tan, C., One-Pot Synthesis of Highly Anisotropic Five-Fold-Twinned PtCu Nanoframes Used as

a Bifunctional Electrocatalyst for Oxygen Reduction and Methanol Oxidation. *Advanced Materials* **2016,** *28* (39), 8712-8717.

14. (a) Liu, X.; Wang, W.; Li, H.; Li, L.; Zhou, G.; Yu, R.; Wang, D.; Li, Y., One-pot protocol for bimetallic Pt/Cu hexapod concave nanocrystals with enhanced electrocatalytic activity. *Scientific reports* **2013,** *3*; (b) Xiong, Y.; Ma, Y.; Lin, Z.; Xu, Q.; Yan, Y.; Zhang, H.; Wu, J.; Yang, D., Facile synthesis of PtCu 3 alloy hexapods and hollow nanoframes as highly active electrocatalysts for methanol oxidation. *CrystEngComm* **2016,** *18* (40), 7823-7830.

15. Cao, Y.; Yang, Y.; Shan, Y.; Huang, Z., One-Pot and Facile Fabrication of Hierarchical Branched Pt–Cu Nanoparticles as Excellent Electrocatalysts for Direct Methanol Fuel Cells. *ACS applied materials & interfaces* **2016,** *8* (9), 5998-6003.

16. Jeon, M. K.; Cooper, J. S.; McGinn, P. J., Methanol electro-oxidation by a ternary Pt–Ru–Cu catalyst identified by a combinatorial approach. *Journal of Power Sources* **2008,** *185* (2), 913-916.

17. Zheng, J.; Cullen, D. A.; Forest, R. V.; Wittkopf, J. A.; Zhuang, Z.; Sheng, W.; Chen, J. G.; Yan, Y., Platinum–Ruthenium Nanotubes and Platinum–Ruthenium Coated Copper Nanowires As Efficient Catalysts for Electro-Oxidation of Methanol. *ACS Catalysis* **2015,** *5* (3), 1468-1474.

18. (a) Chen, J.; Herricks, T.; Xia, Y., Polyol synthesis of platinum nanostructures: control of morphology through the manipulation of reduction kinetics. *Angewandte Chemie* **2005,** *117* (17), 2645-2648; (b) Chen, J.; Lim, B.; Lee, E. P.; Xia, Y., Shape-controlled synthesis of platinum nanocrystals for catalytic and electrocatalytic applications. *Nano Today* **2009,** *4* (1), 81-95.

19. Chavez, K.; Hess, D., A novel method of etching copper oxide using acetic acid. *Journal of The Electrochemical Society* **2001,** *148* (11), G640-G643.

20. (a) Kinoshita, K.; Ross, P., Oxide stability and chemisorption properties of supported ruthenium electrocatalysts. *Journal of Electroanalytical Chemistry and Interfacial Electrochemistry* **1977,** *78* (2), 313-318; (b) Trasatti, S.; Petrii, O., Real surface area measurements in electrochemistry. *Pure and applied chemistry* **1991,** *63* (5), 711-734.

21. (a) Schmidt, T. J.; Noeske, M.; Gasteiger, H. A.; Behm, R. J.; Britz, P.; Brijoux, W.; Bönnemann, H., Electrocatalytic Activity of PtRu Alloy Colloids for CO and CO/H2 Electrooxidation: Stripping Voltammetry and Rotating Disk Measurements. *Langmuir* **1997,** *13* (10), 2591-2595; (b) Binninger, T.; Fabbri, E.; Kötz, R.; Schmidt, T. J., Determination of the Electrochemically Active Surface Area of Metal-Oxide Supported Platinum Catalyst. *Journal of The Electrochemical Society* **2014,** *161* (3), H121-H128.

22. (a) Hamann, C. H.; Hamnett, A.; Wielstich, W., *Electrochemistry*. Wiley-VCH: Weinheim, 2007; (b) Attard, G. A.; Brew, A.; Hunter, K.; Sharman, J.; Wright, E., Specific adsorption of perchlorate anions on Pt {hkl} single crystal electrodes. *Physical Chemistry Chemical Physics* **2014,** *16* (27), 13689-13698.

23. Topalov, A. A.; Cherevko, S.; Zeradjanin, A. R.; Meier, J. C.; Katsounaros, I.; Mayrhofer, K. J., Towards a comprehensive understanding of platinum dissolution in acidic media. *Chemical Science* **2014,** *5* (2), 631-638.

24. (a) Long, J. W.; Stroud, R. M.; Swider-Lyons, K. E.; Rolison, D. R., How to make electrocatalysts more active for direct methanol oxidation avoid PtRu bimetallic alloys! *The Journal of Physical Chemistry B* **2000,** *104* (42), 9772-9776; (b) Jeon, M. K.; Won, J. Y.; Woo, S. I., Improved performance of direct methanol fuel cells by anodic treatment. *Electrochemical and solid-state letters* **2007,** *10* (1), B23-B25; (c) Kennedy, B. J.; Smith, A. W., Reactivity of RuO2 as a promoter for methanol oxidation. *Journal of Electroanalytical Chemistry and Interfacial Electrochemistry* **1990,** *293* (1-2), 103-110.

25. (a) Oezaslan, M.; Hasché, F.; Strasser, P., PtCu3, PtCu and Pt3Cu alloy nanoparticle electrocatalysts for oxygen reduction reaction in alkaline and acidic media. *Journal of The Electrochemical Society* **2012,** *159* (4), B444-B454; (b) Mani, P.; Srivastava, R.; Strasser, P., Dealloyed binary PtM 3 (M= Cu, Co, Ni) and ternary PtNi 3 M (M= Cu, Co, Fe, Cr) electrocatalysts for the oxygen reduction reaction: performance in polymer electrolyte membrane fuel cells. *Journal of Power Sources* **2011,** *196* (2), 666-673.

26. Tremiliosi-Filho, G.; Kim, H.; Chrzanowski, W.; Wieckowski, A.; Grzybowska, B.; Kulesza, P., Reactivity and activation parameters in methanol oxidation on platinum single crystal electrodes ‘decorated’by ruthenium adlayers. *Journal of Electroanalytical Chemistry* **1999,** *467* (1), 143-156.

4. Chapter IV. Tailoring the Surface Morphology and Composition of Copper-Platinum-Ruthenium multimetallic nanotubes, and their electrocatalytic properties for MOR.

4.1 Abstract

The anode efficiency of direct methanol fuel cell is limited by slow kinetics, overpotential, and CO adsorption on the electrocatalyst surface for methanol oxidation reaction (MOR). This research overcomes the limitations of methanol oxidation by developing CuPt or CuPtRu multimetallic nanotubes with synthetically tunable surface morphology and composition. Platinum-copper nanotubes with smooth and rough surface morphologies were synthesized through the in situ separation of the galvanic replacement reaction and the co-reduction mechanism during the alloying process with Cu nanowires. The electrocatalytic activity of the CuPt nanotubes was studied to determine the influence of surface morphology and composition on the electrocatalytic activity of the nanotubes. The preliminary electrochemical characterization of multimetallic nanotubes with rough surface morphology demonstrated an improvement of electrocatalytic activity including the onset potential for MOR. The electrocatalytic activity for methanol oxidation is further improved for CuPt with rough surface and increased atomic ratio of Pt.In order to overcome CO poisoning and achieve even lower onset potential for MOR, Ru was incorporated into the CuPt nanotubes with different surface morphologies. CuPtRu with nanotubes with rough surface were formed through the combination of both the galvanic replacement reaction and the co-reduction mechanisms; while the CuPtRu nanotubes with smooth surface were formed through solely the galvanic replacement reaction. The electrochemical results suggest that both the composition and the surface roughness of the nanotube are important for optimization of their electrocatalytic activities. The incorporation of

Ru into the rough nanotubes resulted in an increase in electrocatalytic activity, a lower overpotential, and a decrease in CO adsorption to the surface for MOR.

4.2 **Introduction**

Nanomaterials with high index facets on the surface have shown to improve electrocatalytic activity for many reactions.[1, 2, 3, 4, 5] One-dimensional (1-D) nanomaterials can improve stability of the nanostructures against sintering/aggregation effects during the electrochemical reactions in addition to the improved electrocatalytic activity. For example, Yan et al. reported nanotubes improved MOR activity due to the high surface area of the hollow nanotube morphology, and deposition of additional noble metals overgrown on the tube surface with high index facets.[2b] On the other hand, 1-D structures can be synthetically tailored, through the galvanic replacement reaction, to possess different degrees of porosity on the surface.[6] This can increase the electrocatalytic surface area and improve MOR activity, as shown by Feng et al.[6] This work develops an oil-based solution to synthesize CuPt and CuPtRu with systematically tuned composition and surface roughness for the study of their electrocatalytic activity for MOR.

While Pt is the most efficient single component electrocatalyst for MOR, efficiency is limited by CO poisoning. The oxidation of methanol in acidic media forms 6 different intermediates, including CO.[7] Once formed CO will strong onto Pt, which reduces the number of active sites for MOR thereby lowering the MOR efficiency. Previous research has shown that alloying Pt with an oxophillic metal such as Ru, Sn, and Cu can reduce CO poisoning through the bifunctional mechanism.[8] Alloying Pt with these oxophillic metals could alter the electronic structure of Pt and thus weaken the bound CO on the Pt surface.[3b, 8-9] As a result, CO could further oxidize to CO_2 preventing the re-adsorption of CO on the Pt surface.[10] It has been shown that alloys of Pt and Ru or Pt and Cu lead to the greatest resistance towards CO poisoning,

forming a more efficient electrocatalyst.[11] Additional studies have been carried out over altering the composition of nanomaterials for improved electrocatalytic activity.[12] has been determined that electrocatalytic activity can be influenced by composition, as well as atomic ratio within the nanomaterial.[13] The composition at the surface of the nanomaterial can influence the methanol oxidation pathway, resulting in a volcano plot of the composition versus electrocatalytic activity.[13c] Other studies suggested that a trimetallic nanomaterial can improve the electrocatalytic activity.[14]

In this work, an oil-based solution method was developed to synthesize bimetallic CuPt and trimetallic CuPtRu nanotubes with tunable surface morphology and Pt content by manipulating the reaction kinetics of galvanic replacement and co-reduction on the preformed Cu NW. CuPt nanotubes with smooth surface (CuPt sNT10%) were formed through the galvanic replacement reaction while CuPt nanotubes with rough surface (CuPt rNT 10%) were synthesized through both the galvanic replacement reaction and the co-reduction mechanisms. Ru was further incorporated into these smooth and rough nanotubes during synthesis by adding the Ru precursor into the reaction mixture. CuPtRu nanotubes with smooth surface (CuPtRu sNT 10%) were formed through the galvanic replacement reaction, while CuPtRu nanotubes with rough surface (CuPtRu rNT 10%) were formed through both reaction mechanisms. The atomic ratio of Pt in the rough nanotubes was also tailored by varying the precursor concentration and reaction time to increase to 20% Pt, forming CuPt rNT 20% and CuPtRu rNT 20%. The electrocatalytic properties of these nanotubes with different composition and surface morphologies were then investigated for MOR. The electronic and chemical properties of these nanotubes for the enhancement of MOR activity were also discussed to provide evidence to

correlate the structure and composition variations of these multimetallic nanotubes with the electrocatalytic activity for MOR.

4.3 **Experimental Methods**

4.3.1 Chemicals.

Copper 2,4-pentanedionate ($Cu(acac)_2$, 98%), copper chloride ($CuCl_2$), dodecylamine (DDA, 98%), platinum 2,4-pentanedionate ($Pt(acac)_2$), ruthenium chloride trihydrate ($RuCl_3 \cdot 3H_2O$), and butylamine were purchased from Alfa Aesar. Oleylamine (OLA, 70%) was purchased from Sigma-Aldrich. All chemicals were used as received unless specified otherwise.

4.3.2 Instrumentation

Transmission electron microscopy (TEM) images were captured using a JEOL 100cx microscope with an accelerating voltage of 100 kV. High angle annular dark field scanning transmission electron microscopy (HAADF-STEM) images, high-resolution TEM (HRTEM) images, and energy-dispersive X-ray (EDX) mapping were obtained using a JEOL ARM microscope with an acceleration voltage of 200 kV. The mass concentrations of Pt, Ru and Cu were determined using a GBC 932 atomic absorption (AA) spectrometer or Thermo Scientific iCAP Q inductively coupled plasma mass spectrometry (ICP-MS).

4.3.3 Synthetic Methods for bimetallic nanotubes:

4.3.3.1 Copper-platinum nanotubes with smooth surface morphology (PtCu sNT 10%):

Copper-platinum nanotubes with smooth surface morphology (CuPt sNT 10%) are synthesized by the following method. Cu NW were formed by synthetic procedure outlined in chapter 1. After 50 minutes, the reaction temperature was reduced to 190 ºC, and then the platinum precursor was injected into the solution. The platinum precursor comprised of 0.0763 mmol (30 mg) of $Pt(acac)_2$ dissolved in 1 ml OLA, by vortexing and heating. The reaction

solution's temperature was held at 190 ºC for 5 hours, which allowed for the alloying of platinum along the Cu NW outer surface and interior. The solution was quenched by combining with ethanol in a 15 mL centrifuge tube. The reaction solution was purified by centrifugation at 6,000 rpm for 4 min. The precipitate was purified by ethanol/toluene (2:13 v/v) mixture twice, and the CuPt sNT 10% were redispersed in 2 ml of toluene. The purification steps were necessary in order to remove excess surfactant and unreacted metal precursors that would influence the nanomaterial's morphology & composition after the synthesis.. The CuPt sNT 10% morphology and composition were characterized by TEM, SEM, XRD, and EDX line scan. The nanotubes also underwent electrochemical characterization

4.3.3.2 Copper-platinum nanotubes with rough surface morphology (CuPt rNT ~ 10%):

CuPt nanotubes with rough surface (CuPt rNT 10%) are synthesized following the protocol in 4.3.3.1 except that $Pt(acac)_2$ (0.05 mmol, 20 mg) in 1 ml OLA was injected at 220 ºC and the reaction time was held for 60 min. The nanotubes were purified and characterized by the previously outlined protocol.

4.3.3.3 Platinum copper nanotubes with rough surface morphology (CuPt rNT ~20%)

CuPt rough nanotubes with 20% platinum (CuPt rNT 20%) were synthesized by the protocol in 4.3.3.1, however, 0.0763 mmol of $Pt(acac)_2$ (30 mg) dissolved in 1 ml OLA was injected at 220 ˚C and held at this temperature for 90 minutes. After which the nanotubes were purified and characterized by the previously outlined procedure.

4.3.3.4 In Situ synthetic separation of separation of platinum copper nanotubes with rough and smooth surface morphology.

Synthetic tuning of the surface structure of platinum-copper nanotubes was based on the in situ separation of the two alloying mechanisms, galvanic replacement reaction and the coreduction process. This separation was completed synthetically by varying the reaction temperature and time, while maintaining the initial platinum precursor concentration during the alloying step. In the first synthetic trial, the reaction temperature was set to the following temperatuers are as follows: 220 ˚C, 200 ˚C, 195 ˚C, and 190 ˚C, and then the Pt precursor was injected. For each temperature point, the reaction solution was held for two different intervals, 90 min and 5 hours, to determine the amount of time necessary to produce the highest percentage of platinum alloyed with the Cu NW, without altering the surface morphology. Characterization of the resulting nanotubes can be found in **SI Figures 3 - 5.** After the determination of reaction parameters necessary to separate the smooth and rough surface morphologies, the composition of the nanotubes was synthetically tuned to contain the same Pt percent composition. Protocols for the synthetic optimization of the copper platinum nanotubes with rough surface structure can be found in the **SI experimental section.** Characterization of these nanotubes can be found in **SI figure 3 - 5.**

4.3.4 Synthetic methods for trimetallic nanotubes

4.3.4.1 Separation of dual growth mechanisms & optimization of ruthenium platinum copper nanotubes with smooth nanotubes: development of CuPtRu sNT 10%

The synthesis of copper platinum ruthenium smooth nanotubes (CuPtRu sNT 10%) was similar to the CuPt sNT 10% protocol; with the inclusion of ruthenium during the alloying step. CuPtRu sNT 10% were synthesized by the following protocol: Cu NW were synthesized as normal, after 50 minutes the reaction temperature was reduced to 190 ºC. The platinum

precursor, at a concentration of 0.076 mmol $Pt(acac)_2$ (0.0300 g dissolved in 1 mL OLA), was quickly injected into the solution. After 1 hour, the ruthenium precursor, at a concentration of 0.075 mmol $RuCl_3$ (0.015 g dissolved in 1 mL OLA), was injected into the reaction solution. The reaction temperature was held at 190 ºC for 4 additional hours. The reaction solution was quenched, purified, and characterized according to previously outlined protocol.

4.3.4.2 Copper platinum rutheniums nanotubes with rough surface morphology (CuPtRu rNT 10%) synthetic protocol:

Copper-platinum-ruthenium nanotubes with rough surface structure(CuPtRn rNT 10%) were synthesized similarily to the protocol in 4.3.4.1. The precursors, $Pt(acac)_2$ (0.05 mmol, 20 mg) dissolved in 1 ml OLA and $RuCl_3$ (0.0150 mg, 0.075 mmol) dissolved in 1 ml OLA, and the ruthenium and platinum precursors are simultaneously injected into the reaction solution at 220 ºC. The reaction solution is held at 220 ºC for 60 minutes, after which the reaction is quenched, and purified by normal protocol.

4.3.4.3 Copper platinum ruthenium nanotubes (CuPtRu rNT 20%) Synthetic protocol:

Copper-platinum-ruthenium nanotubes with rough surface structure (CuPtRu rNT 20%) were synthesized by the same method as 4.3.4.2. The synthetic difference is 0.0763 mmol (30 mg) of $Pt(acac)_2$ dispersed in 1 ml OLA and 0.075mmol (15mg) $RuCl_3$ in 1 ml OLA were simultaneously injected into the reaction solution at 220 ºC for 90 minutes. The CuPtRu rNT 20% were then quenched, purified, and characterized by the previously outlined procedure.

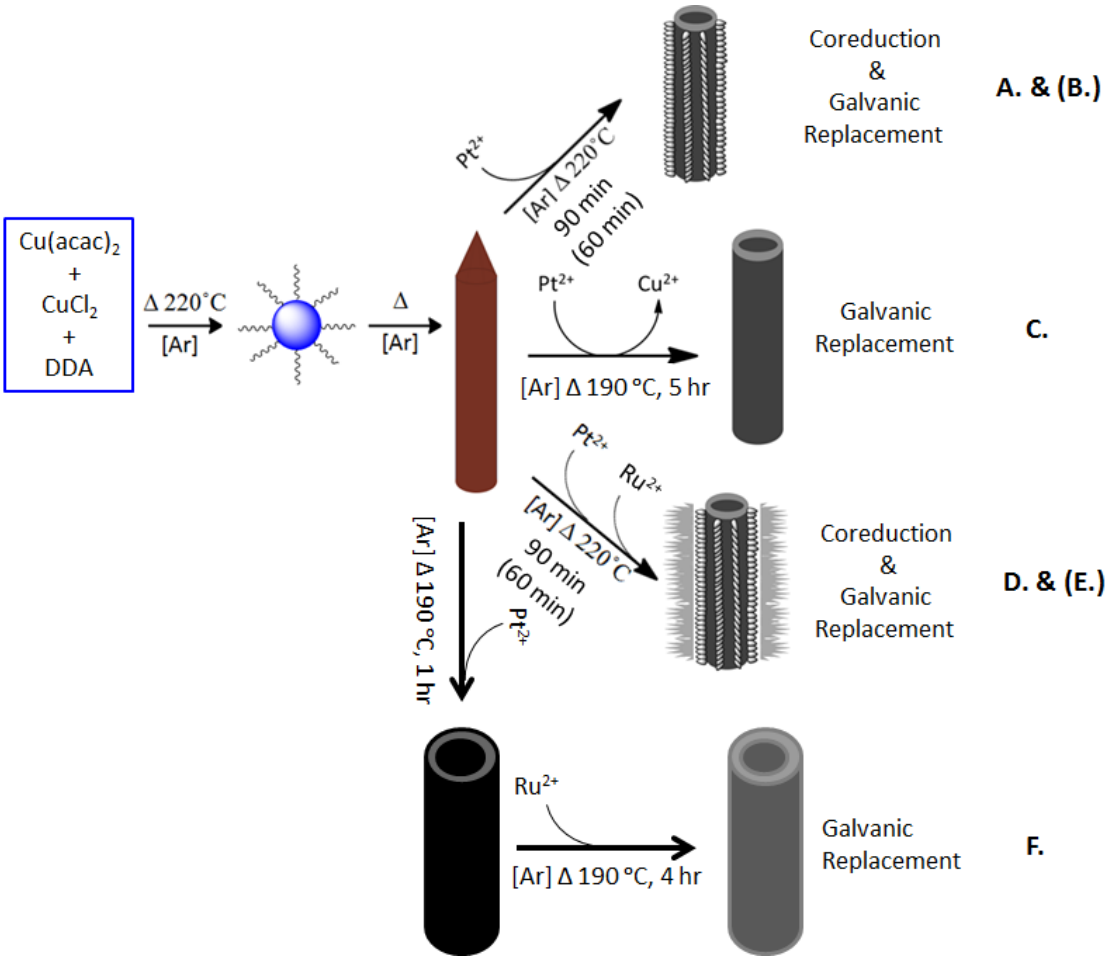

Schematic 1: demonstrates the growth mechanism of multimetallic nanotubes with varying surface morphology and composition. Schematics A, B, & C demonstrate the synthetic separation of the two mechanisms responsible for platinum copper nanotubes with smooth and rough surface morphology. Illustrations A & B highlight the synthetic differences between copper platinum rough nanotubes with varying platinum amount, specifically for CuPt rNT 20% (A) and CuPt rNT 10% (B). Schematics D, E, & F demonstrates the growth mechanism of copper-platinum-ruthenium nanotubes with smooth and rough surface morphology. Illustrations D & E demonstrate the synthetic differences between copper-platinum-ruthenium rough nanotubes with varying atomic percentages of platinum, specifically CuPtRu rNT 20% (D) and CuPtRu rNT 10% (E).

4.3.4.4 Optimization of trimetallic nanotubes of varying surface structure

The composition and morphology of the copper platinum ruthenium nanotubes were synthetically tailored by varying the reaction parameters during the alloying step. Reaction time, temperature, and precursor injection order were altered to develop trimetallic nanotubes, and the resulting effects of variations in the reaction parameters were studied. Protocols for the in situ

separation of the two growth mechanisms responsible for trimetallic nanotubes with smooth and rough surface structures can be found in **SI experimental section.** The corresponding compositional and morphological characterization of these experiments can be found in **SI Figures 4 - 6.** The synthetic protocols for each ruthenium incorporated nanotube were optimized to contain a specific atomic ratio of platinum. The protocols utilized for these experiments are outlined in **SI experimental section,** and the characterization of morphology and composition are found in **SI figure 4 - 6.**

4.3.5 Characterization methods by XPS

XPS study was completed on CuPt sNT 10%, CuPtRu sNT 10%, CuPt rNT 10%, CuPtRu rNT 10%, CuPt rNT 20%, and CuPtRu rNT 20%. Each nanotube sample was normalized to a platinum concentration of 0.8 mg/ml_{Pt} prior to electrochemical characterization (without nafion). The normalized solution was studied through XPS, by dropcasting approximately 40 µl onto carbon tape and allowing the samples to dry for two days prior to XPS investigation. Survey scans were completed to determine the metals present in the nanotube samples. After which, focused scans were obtained of the following energy levels: Pt $4f_{5/2\ \&\ 7/2}$, Cu $2p_{1/2\&\ 3,2}$, Ru $3p_{1/2\&3/2}$, C 1s, an O 1s.

4.3.6 Ligand Exchange Method & Preparation for Electrochemcial Characterization

4.3.6.1 <u>Butylamine Method:</u>

The nanotubes were prepared for electrochemical characterization by first exchanging surface ligands to allow for the synthesized in oil phase nanotubes to be dispersed in aqueous phase. The ligand exchange process occurred by combining as-synthesized nanotubes with 2 mL of butylamine/water (50% v/v) solution at 25 ºC. The solution was stirred for 14 hr at 25 ^{o}C in a glass vial (1 dr) equipped with a stir bar. After the ligand exchange, the nanotubes were rinsed by

dispersing in ethanol and centrifuging at 6,500 rpm for 6 min. The this process continued by rinsing the nanotubes in a 50% v/v ethanol/water solution twice, then rinsing the nanotubes in a 25% v/v ethanol/water solution twice, and finally rinsing in 18 MΩ H_2O twice. The electrocatalysts were suspended in 2 ml of 18 MΩ H_2O for morphological, and composition characterization by ICP-MS (or AA) and TEM.

4.3.7 Electrochemical Preparation and Characterization:

4.3.7.1 Preliminary Characterization and CO stripping studies

The nanotubes were prepared for electrochemical characterization through the same method as chapter 3, found in section 3.3.4. The preliminary electrocatalytic activity of CuPt sNT 10%, CuPt rNT 10%, CuPt rNT 20%, CuPtRu sNT 10%, CuPtRu rNT 20%, and the commercial catalysts Ru:Pt (20 wt% Pt, 50 wt.% Ru) were characterized utilizing the same method as chapter 3, section 3.3.5. CO stripping studies were completed to determine the electroactive surface area of each electrocatalyst. The CO stripping study protocol and data analysis method can be found in chaper 3 section 3.3.5

4.3.8 Stability Studies

The stability studies were carried out for each electrocatalyst in both electrolyte and analyte solution. The durability of each electrocatalyst was monitored by continuous cyclic voltammetry over 300 cycles. For the electrolyte stability study, the electrolyte was degassed with nitrogen for 10 minutes. Initial CV scans in electrolyte were obtained at a scan rate of 50 mV/s at a potential range from 0 to 1.2 V vs RHE (-0.294 V to 0.9 V vs Ag/AgCl 1 M KCl) for 1.5 cycles, then 15 cycles, and finally 1.5 cycles. The continuous cycling was completed in electrolyte for 300 cycles at a scan rate of 100 mV/s over a potential range of 0 to 1.2 V vs RHE.

After 300 cycles, final voltammograms in both electrolyte and analyte were obtained at 50 mV/s over the potential range of 0 V to 1.2 V vs RHE.

For the analyte stability study, the three electrode cell was set up as previously outlined, and the analyte solution purged with nitrogen for 10 minutes. Initial CV scans were obtained in electrolyte over a potential range of 0 to 1.2 V vs RHE (-0.294 V to 0.9 V vs AgAgCl 1 M KCl) at a scan rate 50mV/S for 1.5 cycles, 15 cycles, and 1.5 cycles. Preliminary CV scans in analyte were also obtained at the same potential range, at 50 mV/s for 1.5 cycles. This allowed for characterization prior to continuous cycling. Then the electrocatalysts' durability was monitored by continuously for 300 cycles in analyte at a scan rate of 100mV/s over the same potential range. Final CV scans were obtained in analyte were obtained at 50 mV/s over the potential range of 0 V to 1.2 V vs RHE. The solution was exchanged for electrolyte, purged with nitrogen for 10 mins, and CV scan was obtained. After each stability study, the electrocatalyst was sonicated from the G.C. W.E. surface with 0.5 ml ethanol. The electrocatalysts were then concentrated to 10 µl of ethanol, and deposited onto a Ni grid for characterization by HRTEM, HAADF-STEM & EDX mapping.

4.4 **Results and Discussion**

4.4.1 Results: morphology and compositional characterization of nanotubes

4.4.1.1 Characterization of platinum copper nanotubes with smooth surface morphology

The smooth copper platinum nanotubes (CuPt sNT 10%) compositional and morphological characterization results can be found in **Figure 1**, and Schematic **1 C.** The CuPt sNT 10% were characterized by SEM, TEM, HRTEM-STEM, and EDX line scan. SEM image A (**Figure 1)** demonstrates the smooth surface structure, without overgrowth along the vertices and edges of the Cu NW, and hollow interior of the nanowire. This suggests alloying was due to the

galvanic replacement reaction, due to the exchange of copper atoms along the interior with platinum atoms. The SEM images determined the average length to be ~ 5 μm, with lengths ranging from 500 nm to 5 μm, which is a decrease in length compared to the original Cu NW, suggesting that the Cu NW were shorten during the alloying process. The TEM image B determined the average diameter to be 20 nm and demonstrated the smooth surface structure across multiple CuPt sNT 10%, and the presence of smaller nanoparticles. TEM image B inset provides HRTEM results provide a magnified image of a singular CuPt sNT 10%. This exhibits the smooth and porous nature of CuPt sNT 10%, and deformation in the surface structure, due to sample storage prior to preparation of the HRTEM grid. **Figure 1 C** demonstrates the porous surface of CuPt sNT 10% by HAADF-STEM image contrast. The EDX line scan shows that the nanotube possesses a higher intensity of Cu, around 150 CPS with some areas as high as 220 CPS, and a lower intensity of Pt around 20 CPS. These results are consistent with ICP-MS results in **Table S4** from which the atomic ratio of CuPt sNT 10% was determined to be 90% copper and 10% platinum. These results suggest that the nanotube is composed mostly of copper, while only the surface interior and exterior has been alloyed with platinum, and the separation of the two growth mechanisms was successful.

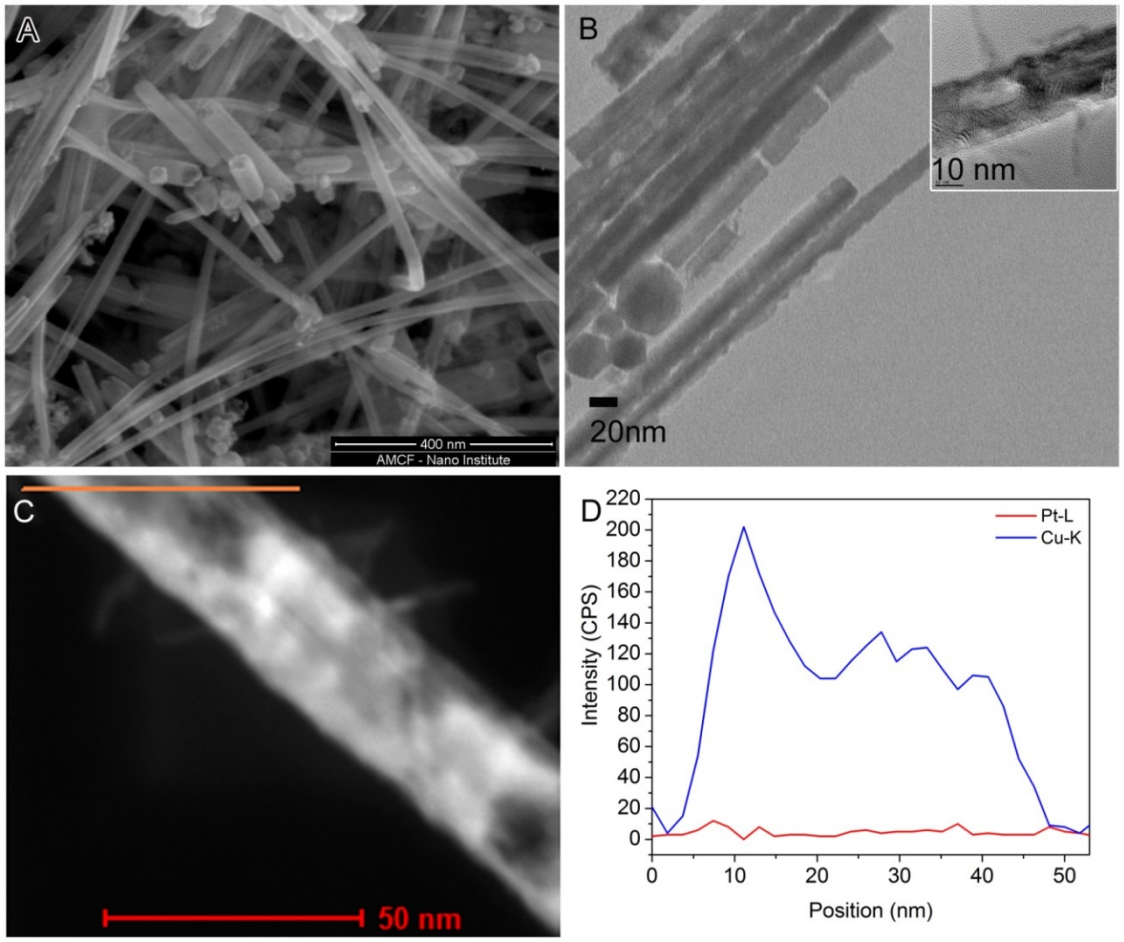

Figure 1: contains composition and morphology characterization results for CuPt sNT 10% . (A) SEM images demonstrate the smooth surface morphology and hollow interior at two magnifications. (B) TEM image demonstrating the morphology of multiple CuPt sNT 10%, (B inset) HRTEM image, demonstrating the porous, smooth surface morphology of a singular CuPt sNT 10%, and (C & D) HAADF-STEM image and EDX line scan across the diameter of CuPt sNT 10%, showing the nanotube composition.

4.4.1.2 Characterization of platinum copper nanotubes 10% with rough surface morphology

The copper platinum nanotubes with rough surface structure (CuPt rNT 10%) and an atomic ratio of 10% platinum correspond to **Schematic 1 B**, and were synthetically formed through both the galvanic replacement reaction and coreduction mechanism**.** Copper platinum nanotubes with rough surface structure (CuPt rNT 10%) were characterized in **Figure 2** by TEM (A), HRTEM (B & inset), HAADF-STEM (C), and EDX Mapping (D). TEM image A demonstrates that the length and diameter of the nanotubes were around ~ 5μm and 20 nm,

respectively. Additionally, CuPt rNT 10% exhibited overgrowth along the nanotube edges. HRTEM image B of CuPt rNT 10% magnifies the surface overgrowth along the nanotube edges. HAADF-STEM image C demonstrates two brighter areas along the nanotube, denoting the edge overgrowth, which could result from multiple metals depositing along the vertices. The EDX Mapping (D) results demonstrate portion of the CuPt rNT 10% that is copper (green) and the portion that contains platinum (yellow), which determined that the overgrowth along the edges of the nanotubes is comprised of platinum and copper. Overgrowth along the edges of the CuPt rNT 10% demonstrates the influence of both the coreduction mechanism in addition to the galvanic replacement reaction.

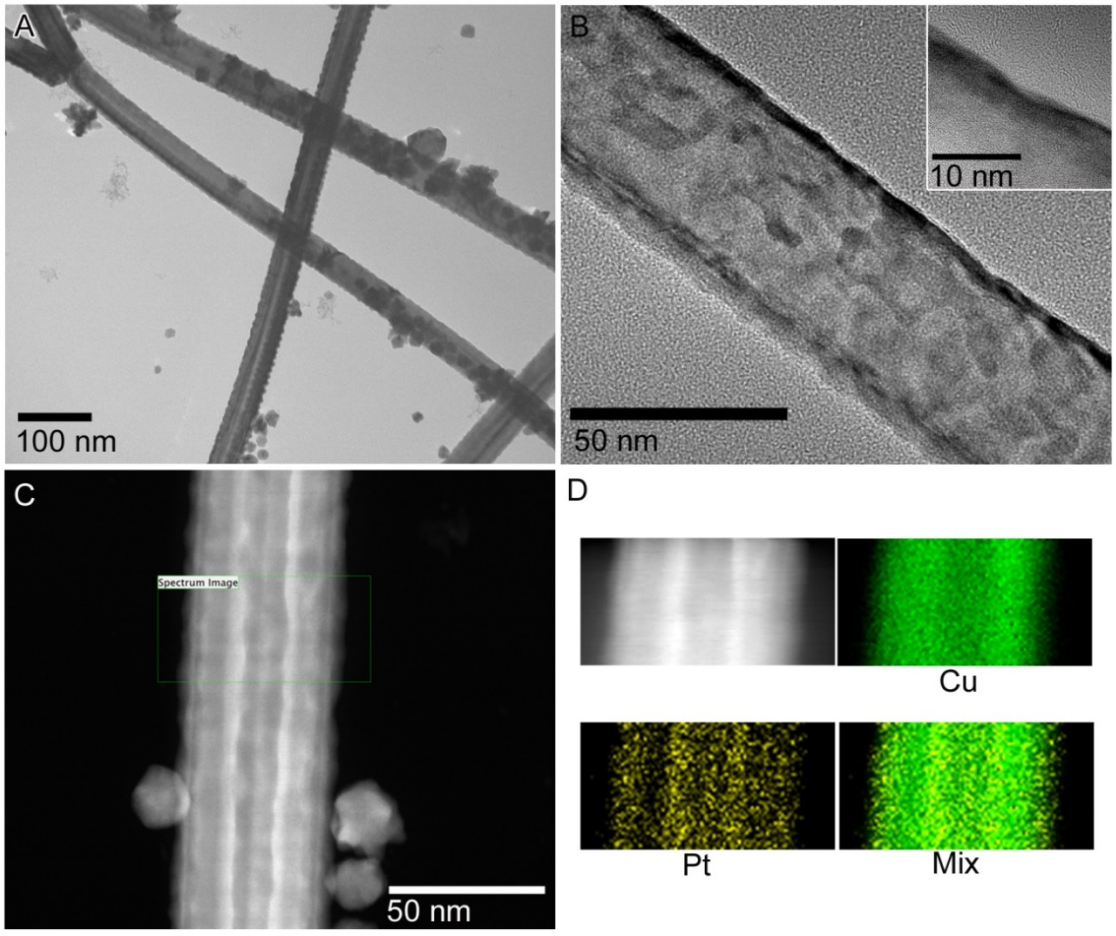

Figure 2: characterizes CuPt rNT 10% by TEM (A), HRTEM (B & inset), HAADF-STEM image (C), and EDX Mapping (D), in which green denotes copper and platinum is denoted by yellow.

4.4.1.3 Characterization of copper platinum nanotubes 20% with rough surface structure

Copper platinum nanotubes with rough surface structure and 20% Pt (CuPt rNT 20%) corresponds to **Schematic 1 A.** CuPt rNT 20% were characterized in **Figure 3** by SEM (A), TEM (B), HRTEM (B inset), HAADF-STEM (C & E), EDX line scan (D & F). SEM Image A contains results for CuPt rNT 20%. These nanotubes are hollow in nature, and possess an average length of 5 micrometers and an average diameter of 40 nm. The SEM image A determined CuPt rNT 20% possess uniform overgrowth, in specific increments, along the nanotube edge. Additionally, the circumference of the nanotube possesses 6 edges along which the overgrowth has formed. This overgrowth could form from high surface energy of the edges along the nanotube that Pt and Cu will deposit onto stabilizing the nanotube. **Figure 3** HRTEM image B inset characterizes the CuPt rNT 20% edge, which exhibits the semi-ellipsoid ovegrowth are approximately 10 nm – 12 nm in length and approximately 6 nm to 8 nm in diameter. **Figure S1** image A & B provides the HRTEM of CuPt rNT 20% and the corresponding electron diffraction pattern, focusing on the surface structure. The electron diffraction results demonstrate the single crystalline nature of the semi-ellipsoid overgrowth.

Figure 3 images C & E and spectra D & F determine the composition of the CuPt rNT 20%. HAADF-STEM image E & EDX line spectrum F scan characterize the diameter of the nanotube, which is comprised of Pt and Cu. The EDX line scan demonstrates a higher intensity of copper (100 CPS Cu), and a lower intensity of platinum (40 – 50 CPS Pt). HAADF-STEM image C, exhibits a brighter contrast on the right side of CuPt rNT 20%, which could be attributed to scanning multiple edges along the nanotube simultaneously. HAADF-STEM image G & EDX line scan spectrum H along the semi-ellipsoid overgrowth of CuPt rNT 20%. The nanotube was comprised of 70 CPS platinum and 140 CPS copper. The semi-ellipsoid

overgrowth contains approximately twice the intensity of copper than platinum. These results that both metals will coreduce and adsorb onto the 6 nanotube edges, however, copper will favorably coreduce onto the edges.

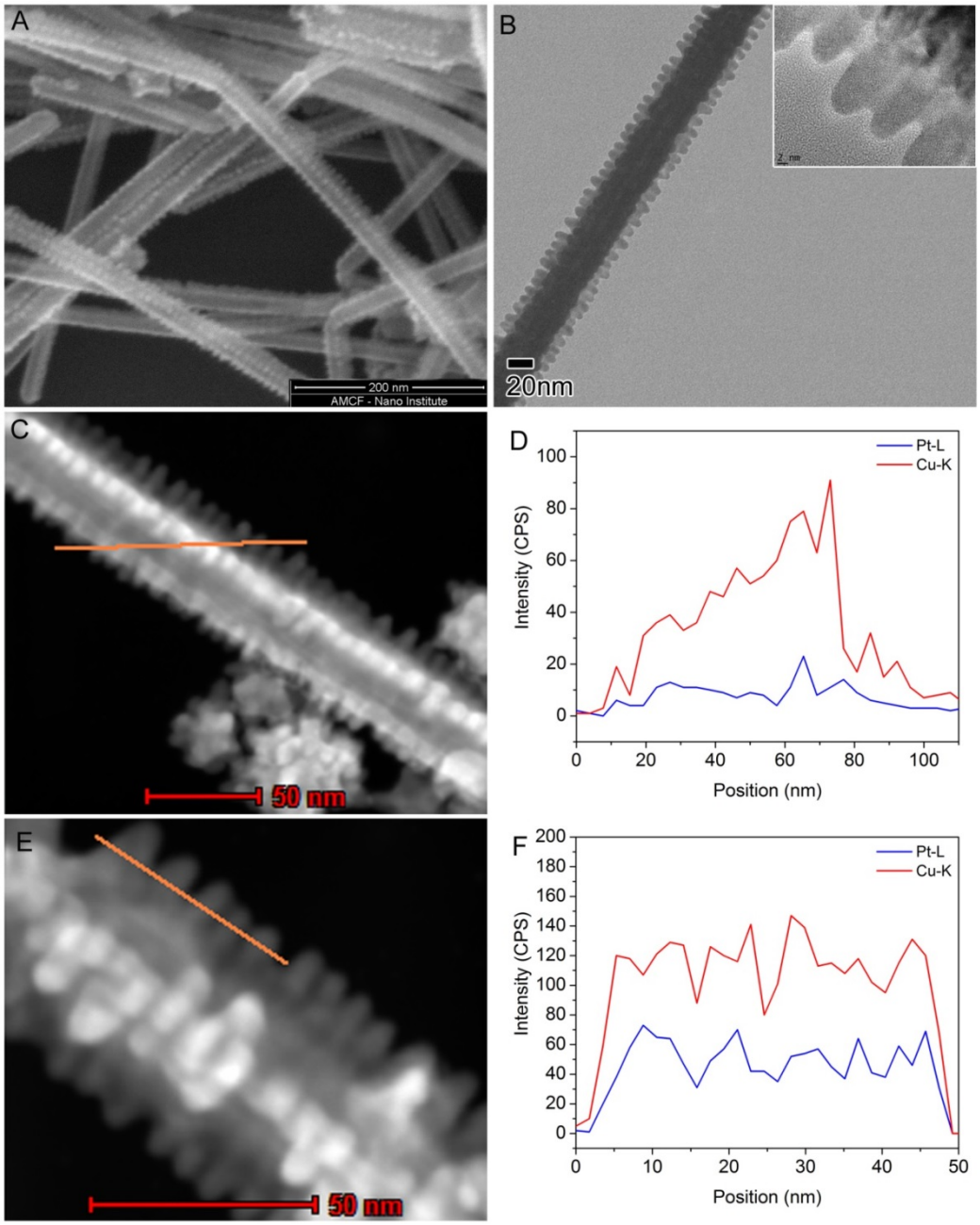

Figure 3: contains morphology and composition characterization results for CuPt rNT 20%. CuPt rNT 20% morphology was characterized by SEM (A) TEM (B), HRTEM (B inset). CuPt rNT 20% composition was characterized by HAADF-STEM image (C & E) & EDX line scan (D & F). The HAADF-STEM & EDX mapping results were obtained across the CuPt rNT 20% (C & D), as well as along the semi-ellipsoid overgrowth (E & F).

4.4.2 Supporting information: Optimization of platinum-copper nanotubes of rough surface morphology based on temperature, time, and starting precursor

The composition of the copper platinum nanotubes with rough surface morphology was synthetically tuned based on the reaction temperature and the starting platinum precursor concentration. **Figure S2 & S3** contains characterization results for the in situ optimization of the CuPt rNT surface morphology. This synthetic optimization was completed by varying the secondary precursor amount and maintaining other reaction parameters. The Pt precursor concentration are as follows: (A & B) 0.153 mmol, (C & D) 0.102 mmol, (E & F) 0.076 mmol, and 0.050 mmol of $Pt(acac)_2$ dispersed into 1ml OLA. TEM images (A, C, E, G) demonstrate the variations in surface morphology of each CuPt rNT produced through the synthetic variation, and XRD patterns (B, D, F, H) determined the degree of alloying on the nanotube. Based on the XRD results there was a linear tread between the percentage of alloying and the concentration of platinum precursor. Based on the TEM results, the synthesis with 0.15 mmol $Pt(acac)_2$ and .076 mmol $Pt(acac)_2$ produced the highest uniformity in surface morphology, while maintaining a high percentage of platinum.

The influence of reaction time on copper platinum nanotubes surface structure, uniformity, and composition was also studied. These synthetic studies are outlined in greater detail in the **SI experimental section**. **Figure S3** characterizes the resulting nanotube surface structures and compositions from the synthetic variations in reaction time after the injection of the platinum precursor, which optimized the CuPt rNT. The reaction time studied includes: 50 min (A & B), 90 min (C &D), and 120 min (E & F). TEM images (A, C, E) demonstrate the variations in surface morphology of the CuPt rNT produced through each synthetic variation, while XRD patterns (B, D, F) determined the composition. The percentage of alloying showed

no trend with increasing time, however, the increase in reaction time lead to more pronounced semi-ellipsoid overgrowth along the edges of the nanotubes.

4.4.3 Characterization of ruthenium platinum copper nanotubes

The development of copper platinum ruthenium nanotubes with smooth and rough surface structure, would allow for the influence of surface structure and composition on electrocatalytical activity to study. Copper platinum ruthenium nanotubes with rough surface morphology formed through the dual growth mechanisms, the galvanic replacement process and the seeded co-reduction mechanism, while the copper platinum ruthenium nanotubes with smooth surface structure were synthesized through solely the galvanic replacement reaction.

4.4.3.1 Characterization of ruthenium platinum copper nanotubes with smooth surface morphology

Copper platinum ruthenium nanotubes with smooth surface structure (CuPtRu sNT 10%) are depicted in **Schematic 1 F.** CuPtRu sNT 10% morphology, surface structure, and composition were characterized in **Figure 4. Figure 4** TEM image A & B determined the length of the CuPtRu sNT 10% to be 1 μm, and the diameter was approximately 45 nm. HRTEM image inset B, does not demonstrate overgrowth along the vertices or edges of CuPtRu sNT 10%., which suggests only the galvanic replacement reaction was responsible for alloying. CuPtRu sNT 10% HAADF-STEM C image exhibits the porous structure, based on image contrast. The EDX mapping results (D) determined the compoisition to be a Cu core, with some Pt and Ru co-deposited along the exterior surface of the nanotube.

RuPtCu rNT formed through the dual growth mechanisms, the galvanic replacement process and the seeded co-reduction mechanism. The CuPtRu sNT 10% were formed through solely the galvanic replacement reaction. Synthetic trials to separate the galvanic replacement

process with the seeded coreduction mechanism can be found in **Figure S6**, as well as the synthetic optimization.

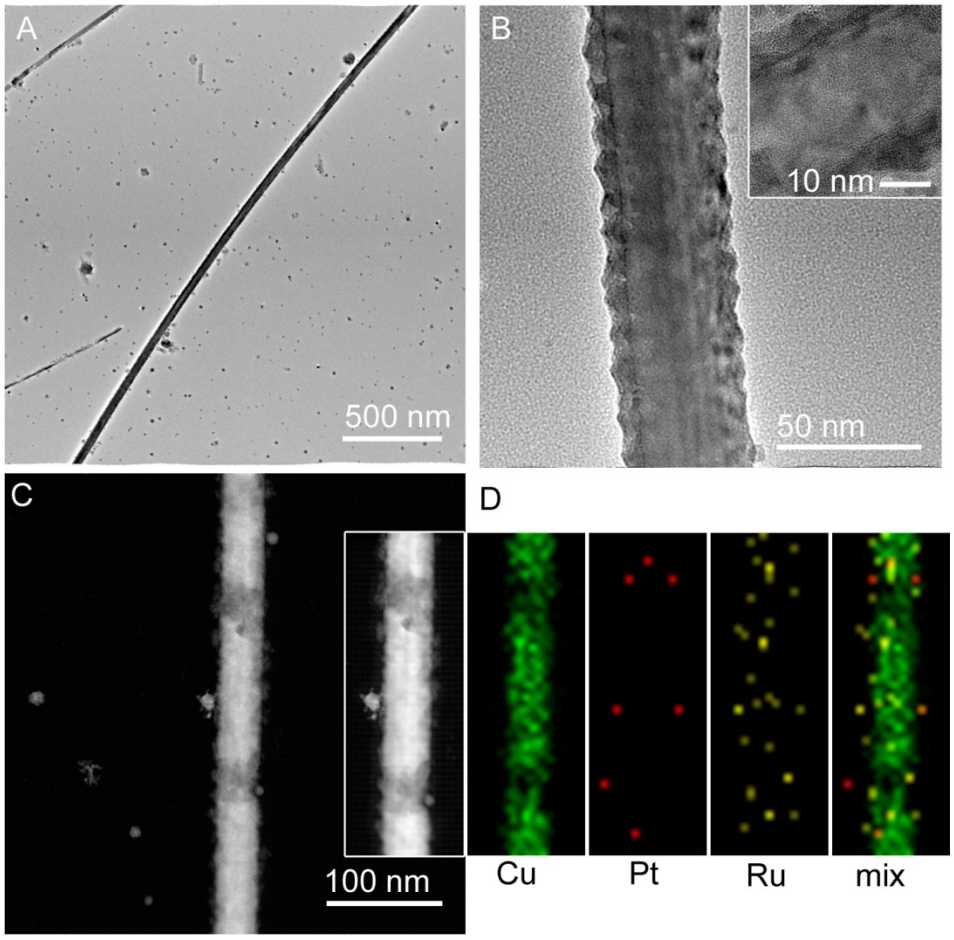

Figure 4 characterizes the morphology and composition of CuPtRu sNT 10% by TEM (A & B), HRTEM (B inset), HAADF-STEM (C & inset), and EDX mapping (D). The EDX mapping contain copper (green), platinum (red), ruthenium (yellow), and mix.

4.4.3.2 Characterization of CuPt rNT 10%

Ruthenium was incorporated into the CuPt rNT 10% synthesis to develop copper platinum ruthenium nanotubes with rough surface structure (CuPtRu rNT 10%), illustrated in **Schematic 1 E. Figure 5** TEM image A characterizes CuPtRu rNT 10% morphology, and highlights the length of the nanotubes that are ~ 5 μm in length. **Figure 5** HRTEM image B characterizes the surface structure of CuPtRu rNT 10%, which demonstrates the overgrowth along three edges of the nanotube. The inset provides a magnified image of the edge overgrowth,

and it was determined that the overgrowth is approximately 7 nm in length and porous in structure. HAADF-STEM image D demonstrates the non porous nature of CuPtRu rNT 10% with surface overgrowth based on image contrast. The EDX mapping results of the nanotubes, demonstrate a copper core for the nanotube, with the highest intensity of platinum and ruthenium on the exterior of the nanotube and the edge overgrowth. The alloying present in CuPtRu rNT 10% was formed through the same growth mechanisms as the CuPt rNT 10%.

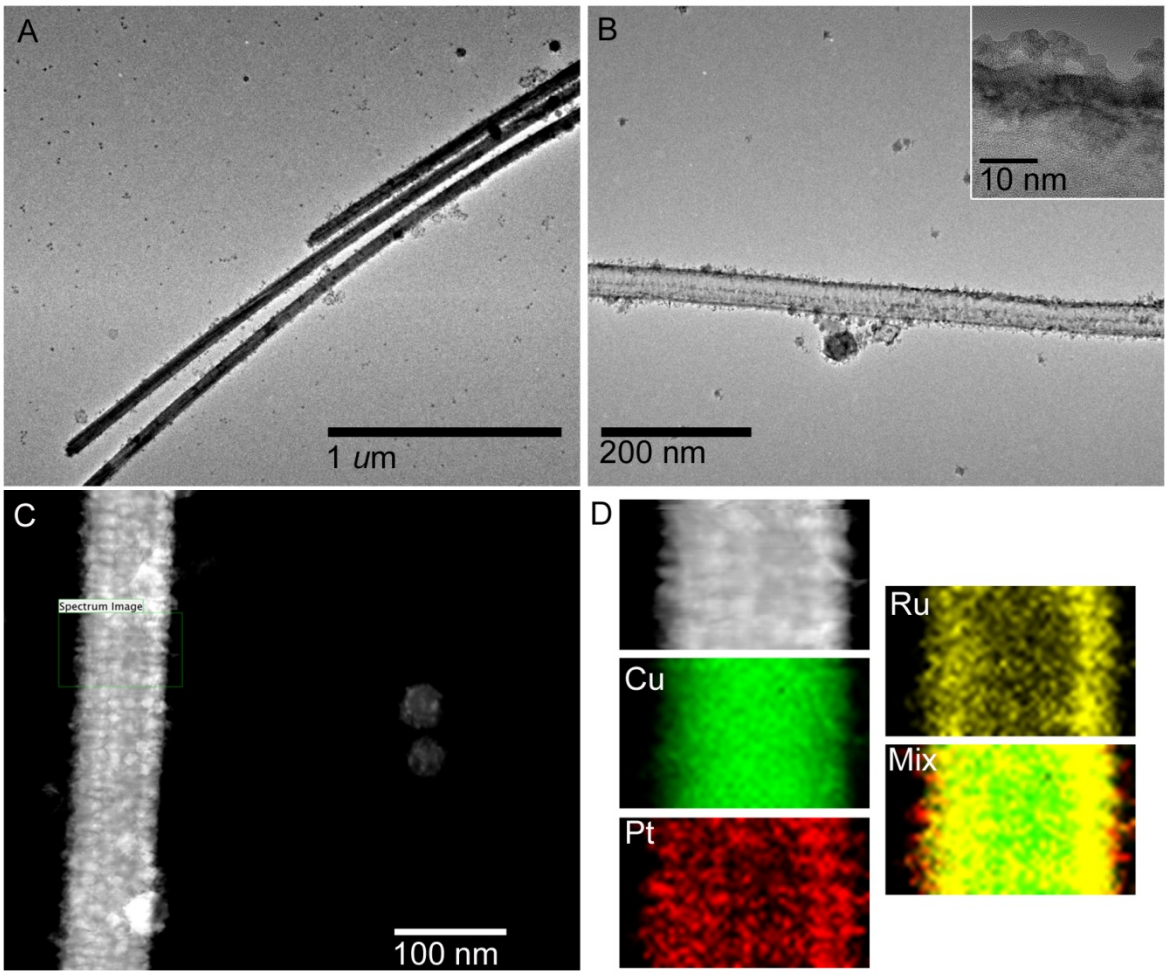

Figure 5: characterizes CuPtRu rNT 10% by TEM (A), HRTEM (B & inset), HAADF-STEM (C), and EDX mapping (D). EDX mapping results are denoted as follows: copper (green), platinum (red), ruthenium (yellow).

4.4.3.3 Characterization of ruthenium platinum copper nanotubes (20% Pt) with rough surface morphology

Copper platinum ruthenium nanotubes with rough surface morphology and 20% Pt (CuPtRu rNT 20%) were formed through the galvanic replacement process and co-reduction mechanism, outlined in **Schematic 1 D**. **Figure 6** TEM image (A) demonstrates the structure and overgrowth along the edges of multiple CuPtRu rNT 20%, which determined the nanotube dimension to be 5 μm in length and 25 nm in diameter. The surface morphology of the CuPtRu rNT 20% possesses uniform overgrowth in specific intervals along each edge of the nanotubes. Additionally, the overgrowth along CuPtRu rNT 20% is more pronounced than the overgrowth along CuPtRu rNT 10%. This can be attributed to the increased reaction time. HRTEM image (B) provides a magnified image of the CuPtRu rNT 20% surface overgrowth which formed a branched structure. The average size of the individual surface overgrowth is approximately 10 nm in length and 5 to 10 nm in width. The HAADF-STEM image C and corresponding EDX mapping D indicates the presence of Cu, Pt, and Ru in the CuPtRu rNT 20%. Copper and platinum are interdispersed throughout the width of the CuPtRu rNT 20%, while ruthenium alloyed along the exterior of the nanotube.

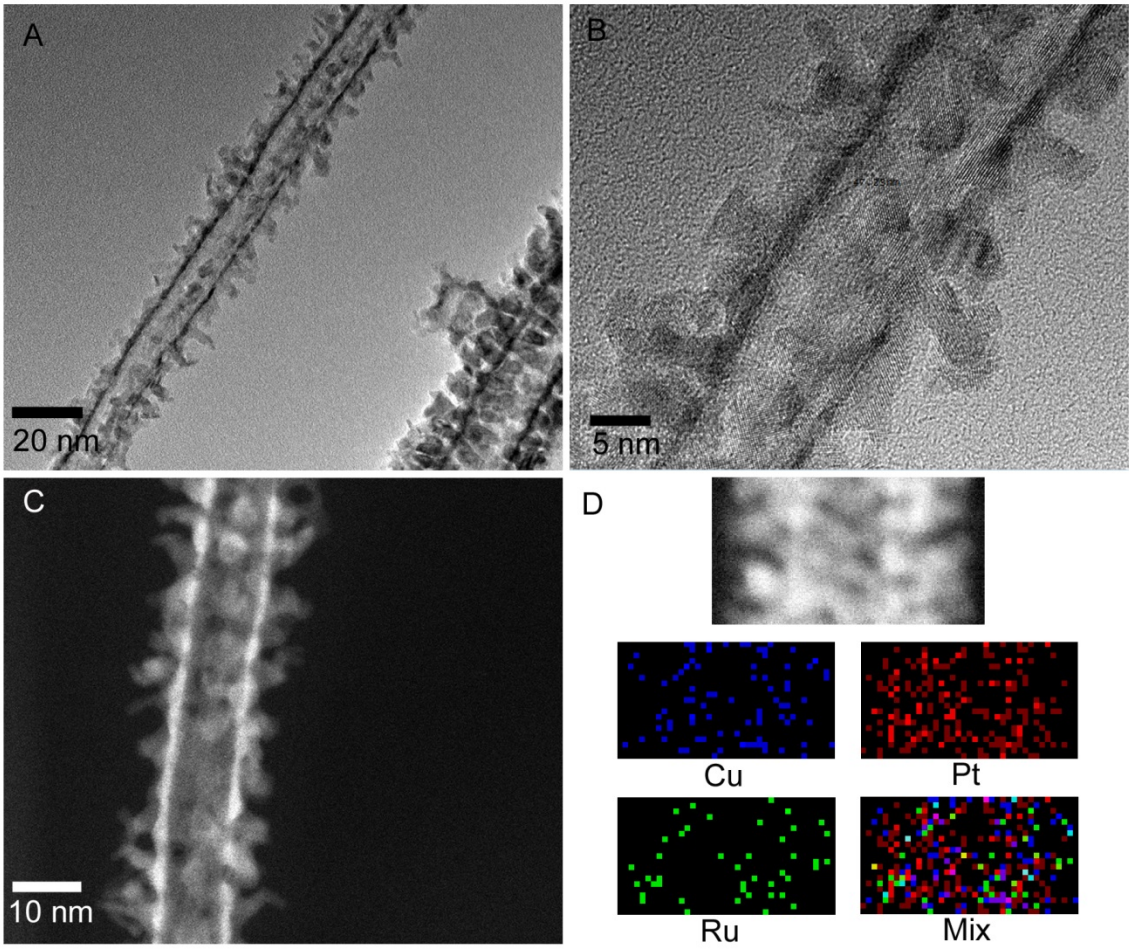

Figure 6 contains the characterization results for the composition and morphology of CuPtRu rNT 20%. CuPtRu rNT 20% were characterized by TEM (A), HRTEM (B), HAADF-STEM (C), and EDX mapping (D). The elemental composition in the EDX mapping results were denoted by: blue (copper), red (platinum), green (ruthenium), and mix.

4.4.4 Morphological characterization of nanotubes after butylamine phase transfer.

After the butylamine phase transfer, the morphology and surface structure of the nanotubes was assessed by TEM in **Figure 7.** Images A - C characterize the copper platinum nanotubes of smooth (A) and rough (B & C) surface structure, while TEM images D - F characterize the copper platinum ruthenium nanotubes of smooth (D) and rough (E & F) surface structure. The morphology and surface structure of the bimetallic and trimetallic nanotubes did not alter during the phase transfer process. The TEM images also demonstrated the presence of

surfactants and smaller nanoparticles, and the presence of residual surfactant from the phase transfer.

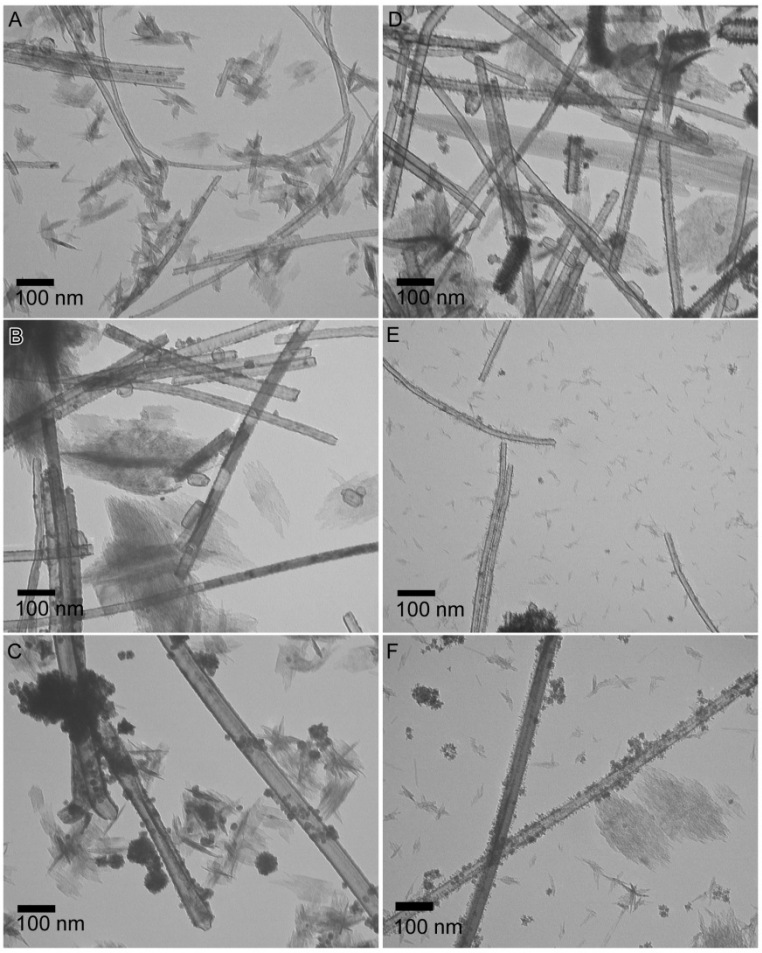

Figure 7: contains TEM images of each type of nanotubes after the butylamine phase transfer process prior to electrocatalytic characterization. TEM images A – C characterize copper platinum nanotubes after butylamine phase transfer; image A) CuPt sNT 10%, image B) CuPt rNT 10%, image C) CuPt rNT 20%. TEM images D-F characterize copper platinum ruthenium nanotubes after phase transfer; image (D) CuPtRu sNT 10%, image (E) CuPtRu rNT 10%, image (F) CuPtRu rNT 20%.

4.4.5 Electrochemical characterization of platinum-copper nanotubes with smooth and rough surface morphology: comparing surface structure influence on electrocatalytic activity

Figure 8 compares the preliminary electrochemical activity for methanol oxidation based on the nanotube surface structure with an atomic ratio of ~ 10% platinum. **Figure S7** provides the preliminary electrochemical results of the smooth nanotubes with enlarged CV profile.

Figure 8 A – C compares the activity of copper platinum nanotubes with smooth and rough surface structure in electrolyte (A), analyte (B), and chronoamperometry (C). Voltammogram A demonstrates the H-upd region (0.0 V to ~ 0.25 V vs RHE) as well as the metal-oxide layer (0.6 V vs 0.8 V vs RHE) that forms on the nanotube surface. CuPt rNT 10% demonstrates the presence of each region, while CuPt sNT 10% does not demonstrate peaks in the metal oxide regions. CuPt sNT 10% exhibit low mass current for MOR, while CuPt rNT 10% demonstrate an increase in MOR mass current, based on voltammogram B. This suggests that CuPt rNT 10% are more electrochemical active than both the smooth nanotubes and the standard. Additionally, the overpotential of the rough nanotubes is 0.63 V vs RHE, while the smooth copper platinum nanotubes overpotential is 0.64 V vs RHE. Chromatogram (C) demonstrates prolonged MOR current at a held potential (0.6 V vs RHE), which determined CuPt rNT 10% possesses the highest produced current for methanol oxidation. **Figure 8 D – F** compares the activity of copper platinum ruthenium nanotubes of smooth and rough surface morphology in electrolyte (D) and analyte (E and F). Voltammogram D demonstrates a suppressed H-UPD region (0.0 V to 0.3 V vs RHE) and metal-oxide region from 0.55 V to 0.85 V vs RHE. Voltammogram E determined CuPtRu rNT 10% possesses an increase in MOR mass current compared to CuPtRu sNT 10%. Additionally, the overpotential of the CuPtRu rNT 10% is 0.42 V vs RHE, which is lower than CuPtRu sNT 10% at 0.062 V vs RHE and comparable to the PtRu standard at 0.05 V vs RHE. This suggests that CuPtRu rNT 10% improves resistance towards CO poisoning compared to the other nanotubes.

The improved electrocatalytic activities of the rough nanostructures could result from the combination of a 1-D nanostructure with an increase in surface area due to the overgrowth along the edges. The nanotubes with ruthenium incorporated into the surface structures are more active

for MOR and possess lower onset potentials. Comparing the efficiency of the copper-platinum nanotubes and the copper-platinum-ruthenium nanotubes with varying surface structure, the nanotubes with rough surface structure are more active for methanol oxidation. The decrease in electrochemical activity can be related to the lower amount of platinum and ruthenium on the smooth nanotube surface.

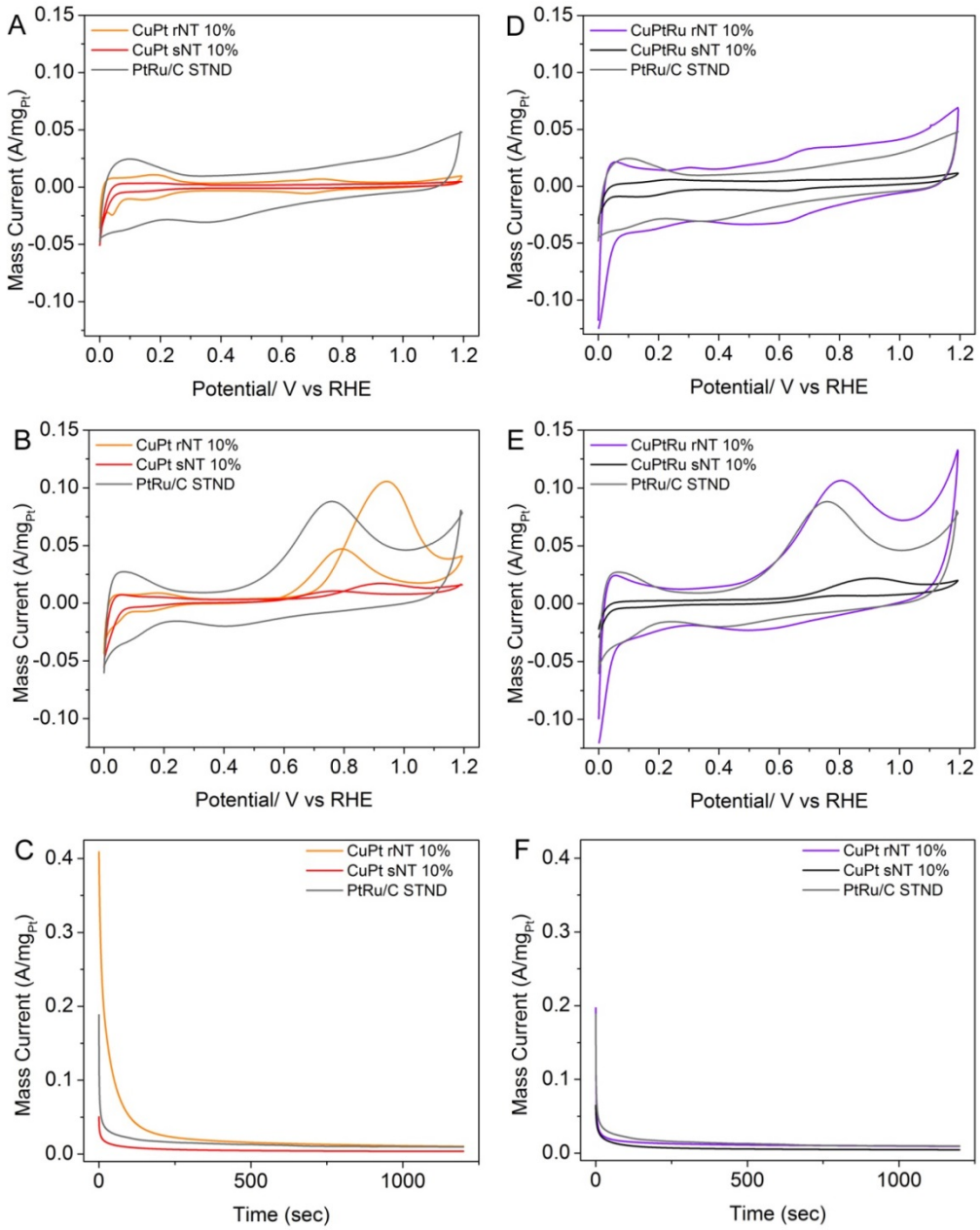

Figure 8 compares the electrochemical efficiency of the copper-platinum nanotubes with rough and smooth surface structure (A – C), and the copper-platinum-ruthenium nanotubes with rough

and smooth surface structure (D – F). These were studied by cyclic voltammetry in electrolyte (A & D) and analyte (B & E), as well as chronoamperometry (D & F). The nanotube sample is denoted by color, CuPt sNT 10% (red), CuPt rNT 10% (orange), CuPtRu sNT 10% (black), CuPtRu rNT 10% (purple), and the PtRu/C Standard (grey).

4.4.6 Electrochemical characterization of platinum-copper nanotubes & ruthenium platinum copper nanotubes with rough surface morphology: increasing the platinum content

The preliminary electrochemical activity of the CuPt rNT 20% and the CuPtRu rNT 20% was characterized by cyclic voltammetry (A & B) and chronoamperometry (C) in **Figure 9.** CV curve A, in electrolyte, determines the hydrogen adsorption and desorption region is pronounced in CuPt rNT 20% than CuPtRu rNT 20% due to the weak binding of hydrogen with ruthenium. Voltammogram B compares the MOR activity of CuPt rNT 20% and CuPtRu rNT 20%. CuPtRu rNT 20% possessed a lower MOR onset potential (0.428 V vs RHE) than CuPt rNT 20% (0.627 V vs RHE), the values of which can be found in **Table 1.** CuPtRu rNT 20% exhibited an increase in MOR mass current compared to the CuPt rNT 20% and the RuPt STND. Both CuPt rNT 20% & CuPtRu rNT 20% exhibited a decrease in produced current on the reverse sweep, which can be attributed to improved resistance towards CO poisoning on the electrocatalyst. These results are consistant with the rough nanotubes of 10%. The chronoamperometry results demonstrate the nanotube's MOR activity over a prolonged period at a potential of 0.6 V vs AgAgCl. While CuPt rNT 20% and CuPtRu rNT 20% were more active than the PtRu standard, both nanotubes demonstrated poor MOR activity over a prolonged period. **Figure S8** compares the electrochemical activity of the CuPt rNT & CuPtRu rNT with 10% and 20% of platinum in the nanotube. In both cases, the ternary rough nanotubes were more electrocatalytically active than the binary rough nanotubes. The enhancement of electrocatalytic activity of the ternary rough nanotubes could result from the branched surface morphology and the 1-D structure. These

results demonstrate that rough nanotubes with a higher content of platinum are more electrochemically active for MOR, and more resistant towards CO poisoning.

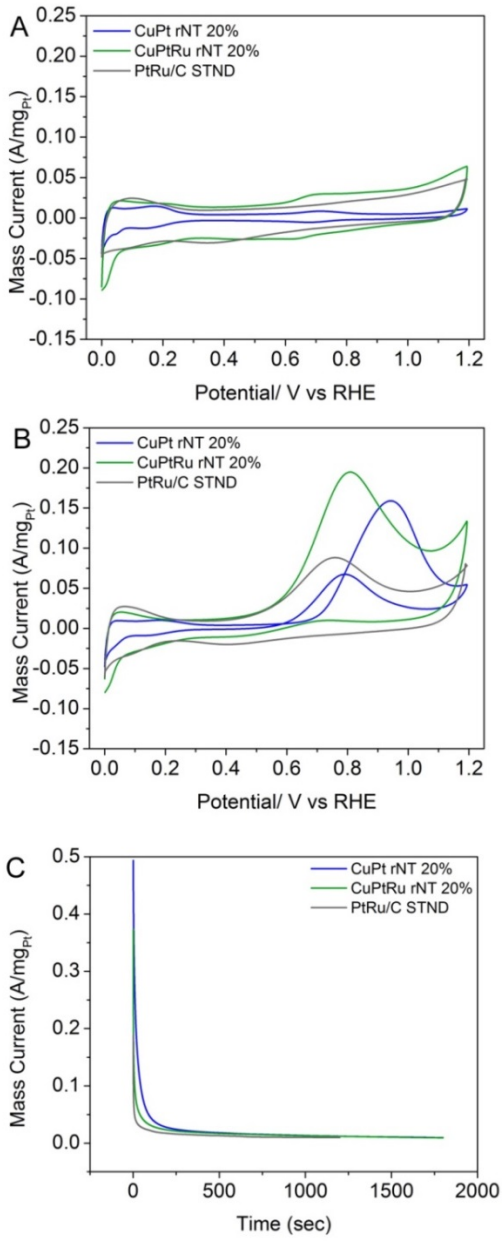

Figure 9: provides the preliminary electrochemical characterization of the CuPt rNT 20% (blue), and CuPtRu rNT 20% (green), and the RuPt/C STND. The rough nanotubes were characterized by cyclic voltammetry in electrolyte (A) and analyte (B), as well as chronoamperometry (C).

sample	overpotential (V vs RHE)
CuPtRu sNT 10%	0.623683626
CuPt sNT 10%	0.643756943
CuPtRu rNT 10%	0.427571651
CuPt rNT 10%	0.630037769
CuPtRu rNT 20%	0.428293713
CuPt rNT 20%	0.626860698

Table 1: provides the overpotential required for MOR, for each electrocatalysts in **Figure 8 & 9.**

If/Ib values			
Samples	If (mA/mgP_t)	Ib (mA/mg_{Pt})	If/Ib (mA/mg_{Pt})
CuPtRu sNT 10%	0.022056815	0.007006282	3.14814815
CuPt sNT 10%	0.017482928	0.010710189	1.632364192
CuPtRu rNT 10%	0.107409178	-0.01672016	-6.42393304
CuPt rNT 10%	0.10577711	0.04767823	2.218562015
CuPt rNT 20%	0.159293909	0.067857143	2.347489184
CuPtRu rNT 20%	0.194755531	0.009928981	19.61485555

Table 2: provides the If/Ir mass current, for each electrocatalyst in **Figure 8 & 9**

4.4.7 **CO stripping Studies of nanotubes with rough surface structure**

The electrochemically active area of a nanotube was determined through a CO stripping study. The electrochemical surface area can determined through the H-upd section, which 0.0 V to 0.3 V vs RHE, however, hydrogen does not favorably bind to ruthenium. Due to the unfavorable adsorption of hydrogen, the CO stripping study was needed to determine the surface area that can be electroactive. In this study, CO is deposited onto the nanotubes surface, and then oxidized during cyclic voltammetry. The area under the oxidation peak can be integrated and the current value can be converted into the electrochemical surface area value using formula 1:

$$ECSA = \frac{integrated\ area}{\left(420\frac{\mu C}{cm^2}\right)\left(0.02\frac{V}{s}\right)}$$

Figure 10 (A – D) contains the CO stripping studies completed on the nanotubes with rough surface structure. In these studies, the background voltammogram was shown by the lighter dashed line, the control voltammogram was shown by the darker dashed line, and the CO stripping voltammogram was shown by the darker solid line. Comparing CuPt rNT 20% (B) with CuPt rNT 10% (A), CuPt rNT 10% possesses a larger CO oxidation peak. This indicates that CuPt rNT 10% possesses a larger electrochemically active surface area than CuPt rNT 20%. The onset potential of the copper platinum rough nanotubes of varying composition is comparable, CuPt rNT 10% at 0.808 V vs RHE and CuPt rNT 20% at 0.810 V vs RHE.

Both CuPt rough nanotubes possess smaller electrochemical surface areas compared to the CuPtRu rough nanotubes of varying composition, which suggests that the CuPtRu rough nanotubes may be more electrocatalytically active MOR. Additionally, CuPtRu rough nanotubes possess lower onset potentials for the CO oxidation than their CuPt rough nanotube components. CuPtRu rNT 10% has an onset potential of 0.65 V vs RHE, while CuPtRu rNT 20% begins CO oxidation at 0.58 V vs RHE. This suggests both trimetallic nantoubes with rough surface structure enhance resistance to CO poisoning, which supports the preliminary electrochemical study completed on the rough and smooth nanotubes. In all cases ruthenium incorporated were more electrochemically active, possessed lower onset potentials.

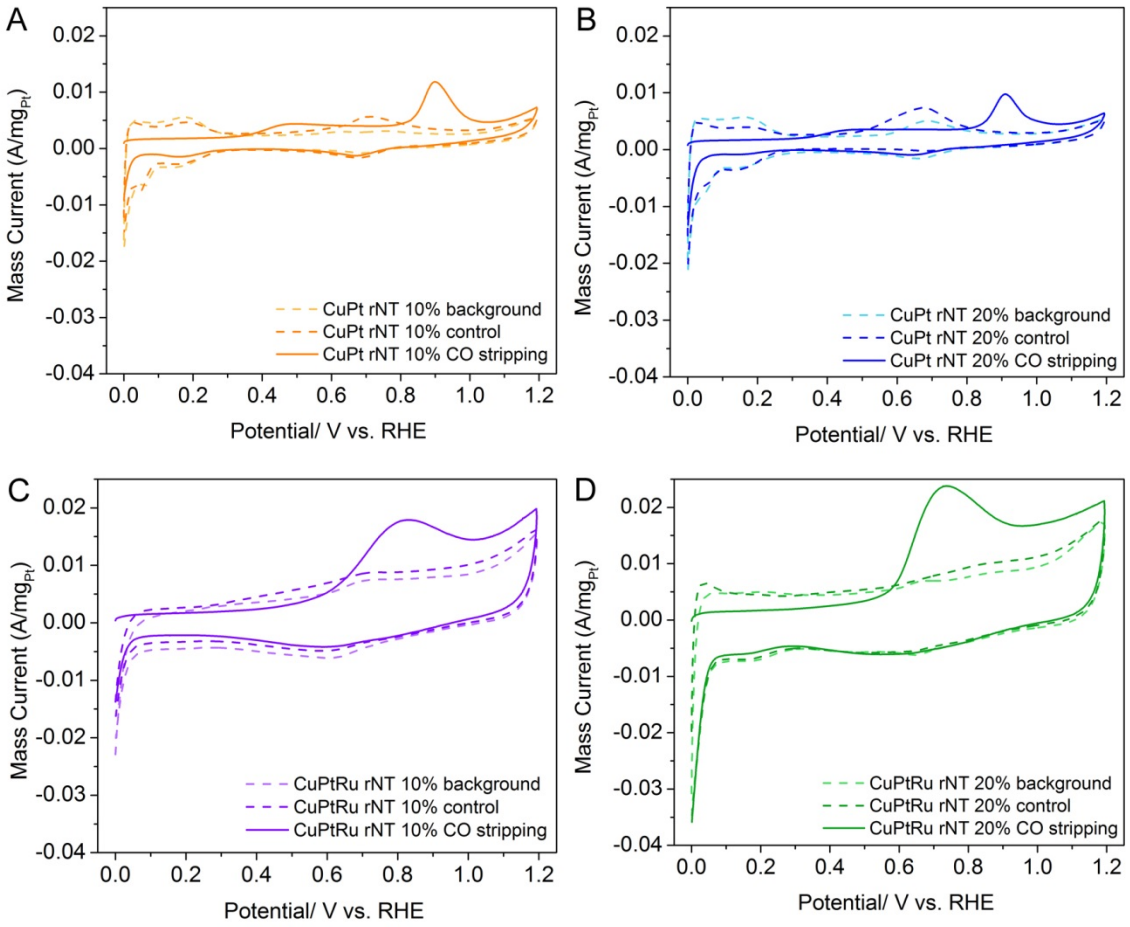

Figure 10: provides the CO stripping voltammograms completed on CuPt rNT 10% (A), CuPt rNT 20% (B), CuPtRu rNT 10% (C), CuPtRu rNT 20%. The background voltammogram is shown by the lighter dashed line. The control CV scan is demonstrated by the darker dashed line, and the CO stripping voltammogram is shown by the darker solid line.

sample	overpotential (V vs RHE)
CuPt rNT 10%	0.8080982
CuPt rNT 20%	0.810697623
CuPtRu rNT 10%	0.656754055
CuPtRu rNT 20%	0.586858476

Table 3: contains the overpotential values for the CO stripping, for copper-platinum rough nanotubes and the copper-platinum-ruthenium rough nanotubes.

nanotube sample	CO stripping area	ECSA correnting for mass normalization (A*V)= (C)
CuPt rNT 10%	1.40E-03	0.333333333
CuPtRu rNT 10%	4.85E-03	1.154761905
CuPt rNT 20%	6.49E-04	0.154507619
CuPtRu rNT 20%	3.59E-03	0.854761905

Table 4: provides the CO stripping integration area, and the calculated ECSA values for the rough nanotubes of various platinum content

4.4.8 Electrolyte stability studies:

The electrolyte stability studies were completed on CuPt rNT 10% sample as well as the CuPtRu rNT 10%, the results of which can be found in **Figure 11**. The electrolyte stability studies for CuPt rNT 10% are found in voltammogram A & B, and C & D provide the results for CuPtRu rNT 10%. Voltammogram A demonstrates the activity of the copper platinum rough nanotube, before and after continuous cycling in electrolyte for 300 cycles. The nanotube efficiency in electrolyte does decrease after the continuous cycling. Voltammogram B provides the nanotube's efficiency for methanol oxidation and resistance towards CO poisoning, after cycling. While CuPt rNT 10% are not as active as the preliminary electrochemical study, the voltammogram demonstrates a methanol oxidation peak at 0.9 V vs RHE. Additionally, CuPt rNT 10% also demonstrates resistance towards CO poisoning, due the oxidation peak in the reverse sweep (0.75 V vs RHE) that is not as active as the oxidation peak attributed to MOR.

Voltammogram C and D provide the electrolyte stability study for CuPtRu rNT 10% with CV scans obtained in electrolyte (C) and in analyte (D). The preliminary CuPtRu rNT 10% voltammograms obtained in electrolyte do no show the presence of an H-UPD region (0.0 V vs 0.25 V vs RHE), which can be explained by the poor hydrogen adsorption onto the ruthenium

incorporated into the nanotube with rough surface morphology. This voltammogram also contains oxidation and reduction peaks in the region of 0.4 V to 0.85 V vs RHE. The final voltammogram obtained in analyte demonstrates that CuPtRu rNT 10% are still active for methanol oxidation, however resistance towards CO poisoning is reduced after continuous cycling. As shown by the preliminary electrochemical characterization of CuPtRu rNT 10%, the second oxidation peak present in the CV scan is completely suppressed. Voltammogram D demonstrates the presence of a small oxidation peak in the reverse scan (0.8 V vs RHE), which suggests the CuPtRu rNT 10% losses some of its resistance towards CO poisoning. Comparing CuPt rNT 10% and CuPtRu rNT 10% activity for MOR and resistance towards CO poisoning, CuPtRu rNT 10% possesses a lower onset potential for MOR (0.5 V vs RHE), and has a higher mass current after continuous cycling. The morphology of CuPt rNT 10% and CuPtRu rNT 10% were studied after the electrochemical characterization and TEM images can be found in **Figure S16**.

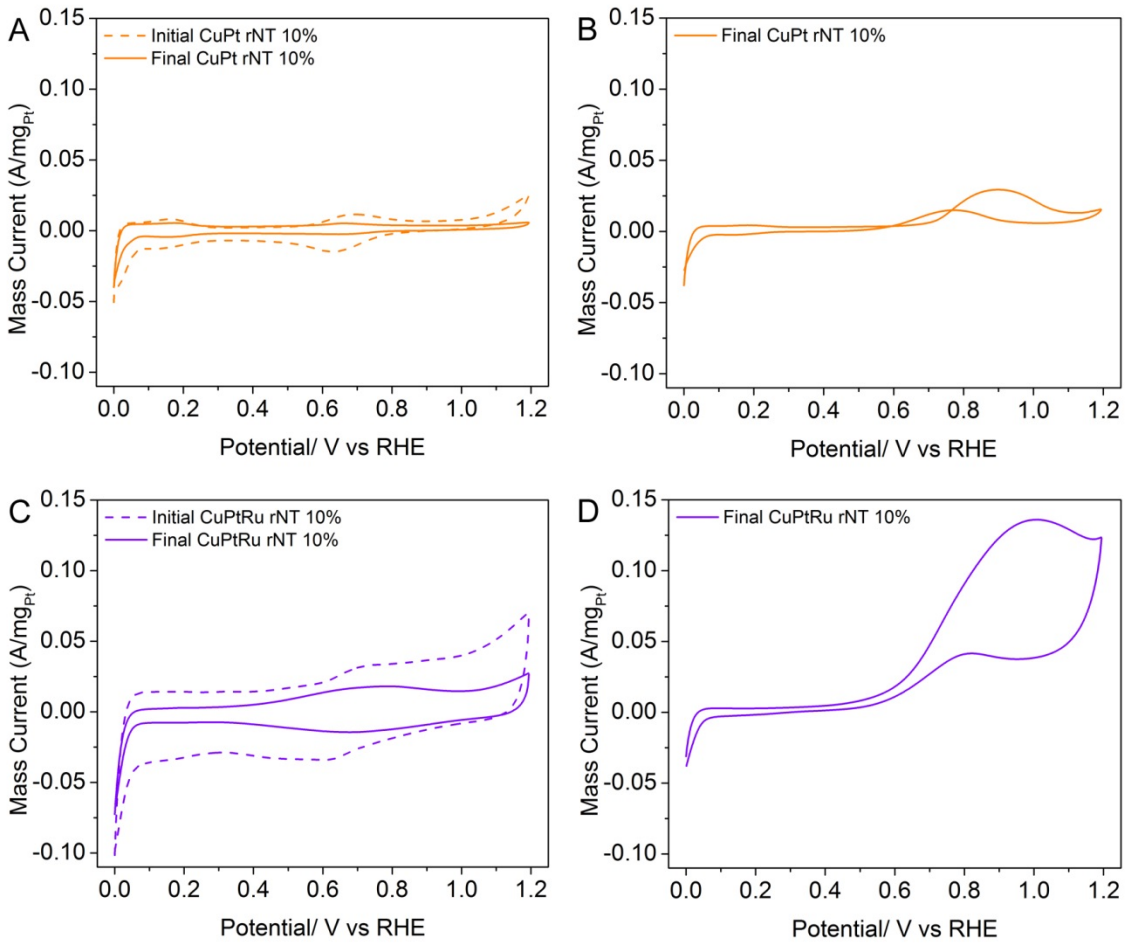

Figure 11: electrolyte stability studies of CuPt rNT 10% (A & B) and CuPtRu rNT 10% (C & D). CV scans completed in electrolyte can be found in (A & C), while CV scans in analyte can be found in (B & D). Initial CVs were denoted by dashed lines, while final CVs were denoted by solid lines.

Electrolyte stability studies were repeated on CuPt rNT 20% (A & B) and CuPtRu rNT 20% (C & D), **Figure 12**. Voltammograms were obtained in electrolyte (A & C) and analyte (B & D), preliminary CVs are denoted by the dashed line and solid lines denote the final CV. **Table 5 & 6** provides the overpotential and If/Ib current values for the rough nanotubes with 20% platinum. CuPt rNT 20% electrochemical activity in electrolyte. Comparing the preliminary and final voltammograms, there was a decrease in activity in both the hydrogen adsorption and desorption region and the metal oxide region (0.45 V vs 0.8 V vs RHE). Voltammogram B demonstrates that CuPt rNT 20% can still oxidize methanol shown by the oxidation peak at 0.9

V vs RHE, and the overpotential for MOR is 0.633 V vs RHE. The positive peak at 0.8 V vs RHE, can be related to the oxidation of adsorbed CO on the surface of CuPt rNT 20%. This suggests that CuPt rNT 20% is partially resistant towards intermediate poisoning.

Voltammogram C & D demonstrate the initial and final electrochemical activity for CuPtRu rNT 20% during the electrolyte stability study. The initial voltammogram in **Figure 12** C demonstrates a suppression of H-UPD due to hydrogen's weak binding affinity to ruthenium. The presence of metal oxide peaks is also shown by the oxidation and reduction peaks in the region of 0.6 V to 0.8 V vs RHE. Comparing the initial and final voltammogram for CuPtRu rNT 20% in electrolyte, there is a reduction in produced current. CuPtRu rNT 20% efficiency for methanol oxidation after continuous cycling in electrolyte is demonstrated by the forward sweep in voltammogram D at 0.9 V vs RHE. The onset potential for MOR is 0.484 V vs RHE. The efficiency after the electrolyte stability study is comparable to the preliminary electrochemical characterization, however, there is a loss of resistance towards CO poisoning. This is shown by the oxidation peak in the reverse sweep in voltammogram D. CuPtRu rNT 20% demonstrated a higher activity for MOR and resistance towards CO poisoning, after the electrolyte stability when compared to CuPt rNT 20%. Based on the electrolyte stability study, altering the atomic ratio of platinum present (10% vs 20%) in the nanotube with rough surface morphology does not influence the activity for MOR or the resistance towards CO poisoning. The incorporation of ruthenium into the nanotube with rough surface morphology has a larger impact on MOR efficiency and resistance towards CO poisoning after the electrolyte stability study.

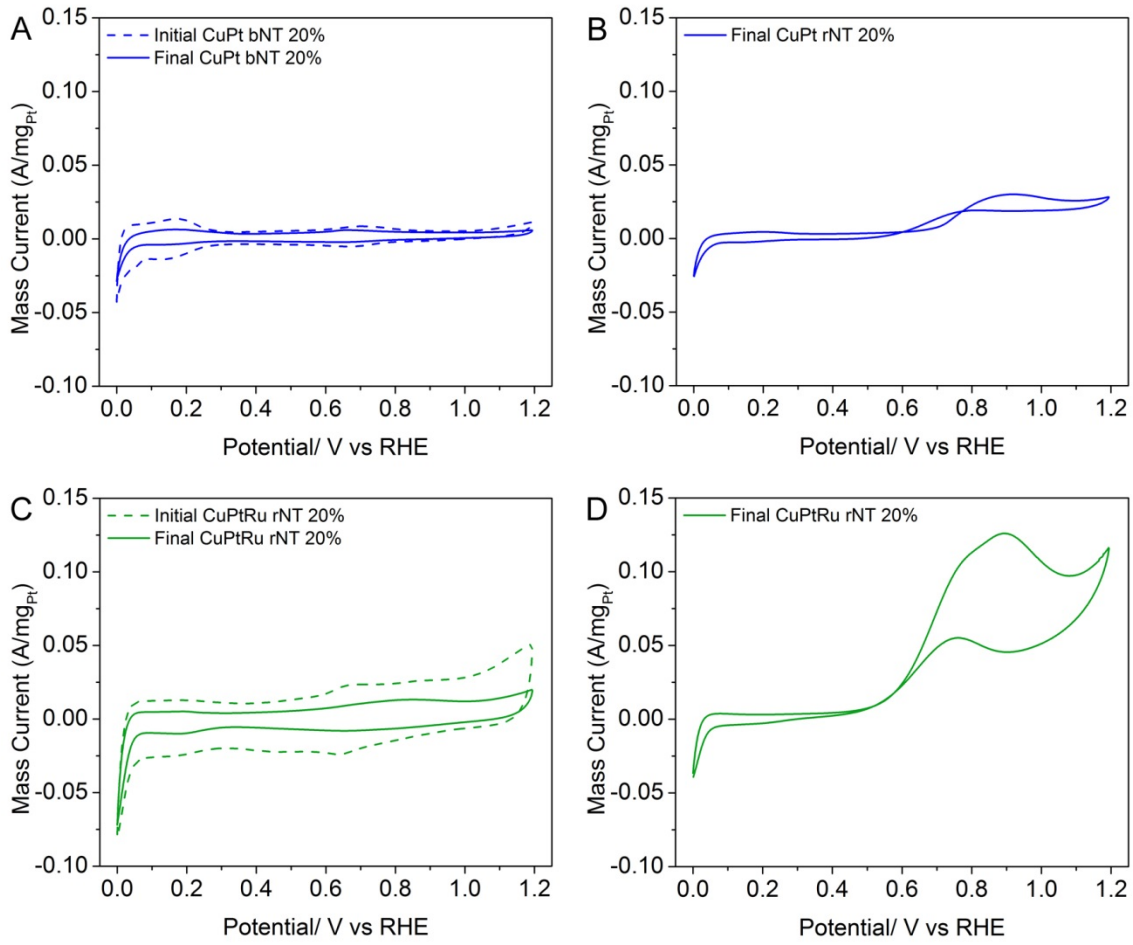

Figure 12: electrolyte stability study of CuPt rNT 20% (A & B) and CuPtRu rNT 20% (C & D). voltammograms were completed in electrolyte (A & C) and analyte (B & D). The initial voltammograms were shown by the dashed lines, while the final voltammograms were denoted by the solid lines.

sample	overpotential (V vs RHE)
CuPt rNT 10%	0.633648078
CuPtRu rNT 10%	0.454287936
CuPt rNT 20%	0.594223506
CuPtRu rNT 20%	0.484181129

Table 5: contains the MOR overpotential for the rough nanotubes with varying atomic ratio of platinum. These data correspond to the electrolyte stability study contained in **Figure 11 & 12.**

If/Ib values			
Samples	If (y)	Ib (Y)	If/Ib
CuPt rNT 10%	0.029582081	0.01506419	1.963735269
CuPtRu rNT 10%	0.136151325	0.04172357	3.263175128
CuPt rNT 20%	0.038527725	0.02529364	1.523218145
CuPtRu rNT 20%	0.126536465	0.05570882	2.27139004

Table 6: contains If/Ir values for methanol oxidation of the rough nanotubes with varying atomic ratio of platinum. These data correspond to the electrolyte stability study contained in **Figure 11 & 12.**

4.4.9 Analyte Stability studies for rough nanotubes ~10% &~ 20%

The results from the analyte stability study are shown in **Figure 13** for CuPt rNT 10% (A & B) and CuPtRu rNT 10% (C & D). To study the analyte stability study, cyclic voltammograms were obtained in both electrolyte (A & C) and analyte (B & D), initial voltammograms are shown by dashed lines and final voltammograms are shown by solid lines. **Table 7 & 8** provides the overpotential values and If/Ib current for the rough nanotubes during the analyte stability study. CuPt rNT 10% results in electrolyte are shown by voltammogram A, in which the initial voltammogram demonstrates the expected regions for H-UPD and metal oxide. The initial and final voltammograms demonstrate a slight decrease in activity after continuous cycling. Voltammogram B demonstrates the alteration in MOR activity, onset potential, and CO poisoning for CuPt rNT 10%. CuPt rNT 10% does maintain some activity for MOR; however, there is a significant reduction in activity after continuous cycling. The initial CV demonstrates an onset potential of 0.65 V vs RHE, and the final voltammogram demonstrates an onset potential of 0.75 V vs RHE. Although the MOR activity was reduced, the resistance for CO poisoning was maintained, as shown by the partially suppressed oxidation peak in the reverse scan.

Voltammograms C & D provide the results for CuPtRu rNT 10%, and comparing the initial and final voltammograms demonstrates the alteration in activity resulting from the stability study. The initial scan in voltammogram C does not demonstrate the H-UPD region, which is expected from an electrocatalyst with ruthenium present in the structure. Additionally, the shape of the CV curve denotes the presence of a metal-oxide layer, in the region of 0.4 V to 0.9 V vs RHE. The final CV curve in **Figure 13** C, does show the CuPtRu rNT 10% are not as active after the stability study. Voltammogram D demonstrates the initial activity for MOR, shown by the oxidation peak in the forward sweep, the onset potential (0.43 V vs RHE initial and 0.66 V vs RHE). CuPtRu rNT 10% resistance towards CO poisoning is also denoted by the suppression of the positive peak in the reverse sweep attributed to methanol oxidation and CO poisoning. From the change in activity from the initial and final CV curves, the reduction in MOR activity by CuPtRu rNT 10% can be seen. Although CuPtRu rNT 10% loses its activity over the analyte stability study, the efficiency for CO poisoning is maintained. This is denoted by the lack of a positive peak in the reverse scan. Although CuPt rNT 10% and CuPtRu rNT 20 % the initial activity for MOR demonstrates that CuPtRu rNT 10% is more active, the final scans demonstrate that CuPt rNT 10% and CuPtRu rNT 10% are comparable in MOR efficiency after the stability study.

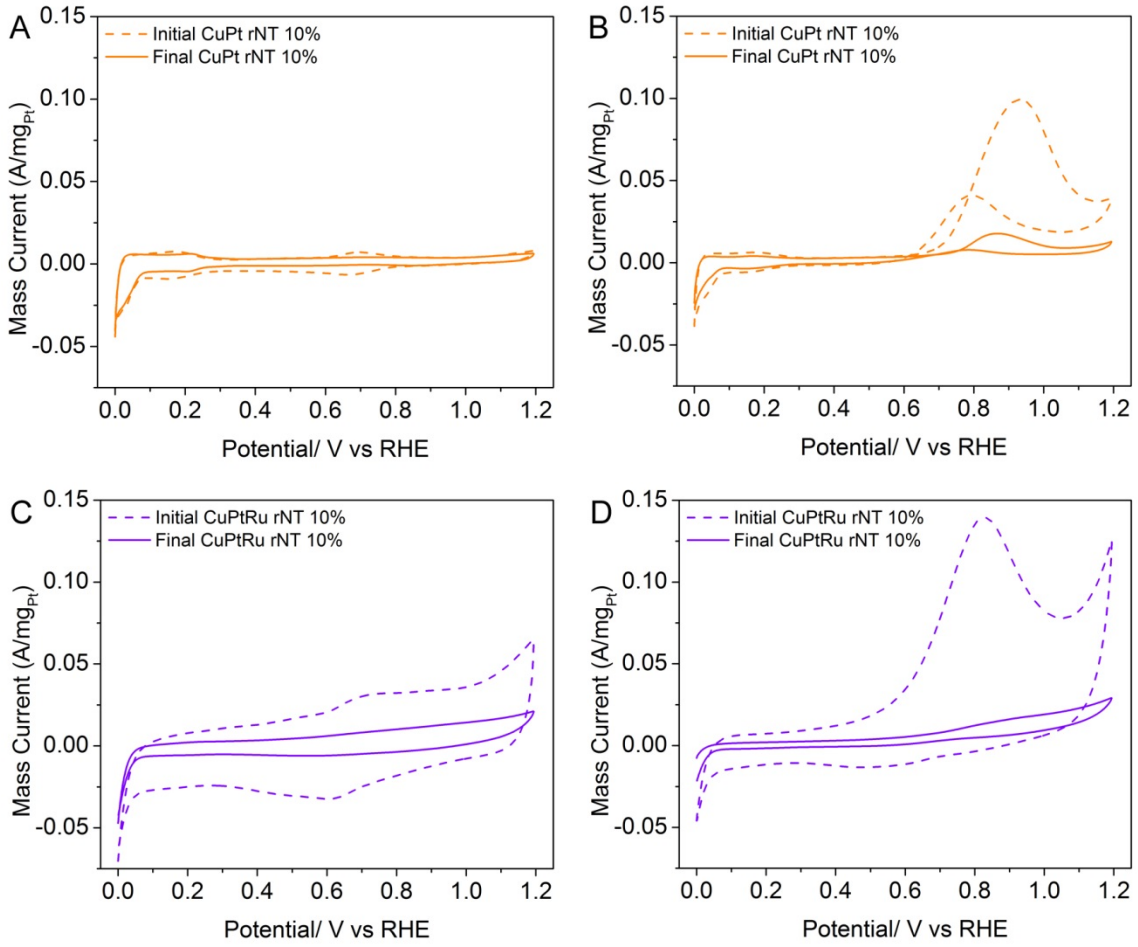

Figure 13: analyte stability studies for CuPt rNT 10% (A & B) and CuPtRu rNT 10% (C & D). Voltammograms completed in electrolyte are found in (A & C), while voltammograms completed in analyte are found in (B &D). Initial voltammograms are denoted by dashed lines and final voltammograms are denoted by solid lines.

4.4.10 Analyte stability studies of rough nanotubes 20%

The analyte stability study, shown by **Figure 14**, was repeated on CuPt rNT 20% (A & B) and CuPtRu rNT 20% (C & D). Initial and final voltammograms were obtained in electrolyte A & B and analyte C & D, which highlights the change in nanotube activity as a result of continuous cycling in analyte. The initial CV curve in voltammogram A demonstrates the presence of the H-UPD region (0 to 0.25 V vs RHE), and oxidation and reduction peaks present from 0.5 V to 0.8 V vs RHE. These peaks can be attributed to the formation of a metal oxide layer on the surface of the nanotubes. The final CV curve demonstrates that the H-UPD region

was maintained during the stability study. The voltammogram also contains two positive peaks, the first peak is in the forward sweep (0.8 V vs RHE), and the second peak is in the reverse sweep at 0.7 V vs RHE. These can be attributed to methanol oxidation and CO oxidation, which likely occurred to adsorbed CO on the electrocatalyst's surface after the analyte stability study. Voltammogram B demonstrates the activity for MOR, denoted by the positive peak in the forward scan at 0.9 V vs RHE, and the positive peak in the reverse scan at 0.8 V vs RHE. The lower mass current in the reverse scan demonstrates that the electrocatalyst is partially resistant towards CO poisoning, which is likely due to the Cu-Pt pair site on the surface of the nanotube. The final CV curve demonstrates a decrease in MOR mass current, and the resistance towards CO poisoning is maintained. Comparing the analyte stability results between CuPt rNT 10% and CuPt rNT 20%, while both CuPt rNT maintained their resistance towards CO poisoning, CuPt rNT 20% is more active for methanol oxidation. This suggests that the increase in platinum content for the rough nanotubes, is beneficial for the electrochemical stability of the electrocatalysts.

Voltammograms C & D provide the analyte stability results for CuPtRu rNT 20%. The initial and final CV curves in electrolyte are shown in **Figure 14** C. As expected the H-UPD region is not as pronounced as CuPt rNT 20%, due to the weak binding interaction between ruthenium and hydrogen. Additionally, the initial voltammogram demonstrates the presence of some metal-oxide peaks from 0.5 V vs 0.7 V vs RHE. The final CV curve demonstrates a decrease in CuPtRu rNT 20% activity. Also, there is a slight H-UPD region and the presence of two positive peaks in the following region: 0.6 V to 0.9 V vs RHE. Voltammogram D demonstrates the change in activity for MOR during the durability study by the peak at 0.8 V vs RHE. The final CV curve demonstrates a significant decrease in mass current for MOR. CuPtRu

rNT 10% with CuPtRu rNT 20% possess similar efficiencies at the beginning of the analyte stability study. When comparing the final CV of CuPtRu rNT 10% and CuPtRu rNT 20%, the increase in platinum content does contribute to the overall activity of the CuPtRu rNT 20% and maintaining the MOR efficiency, which is consistent with the CuPt rNT 20% results.

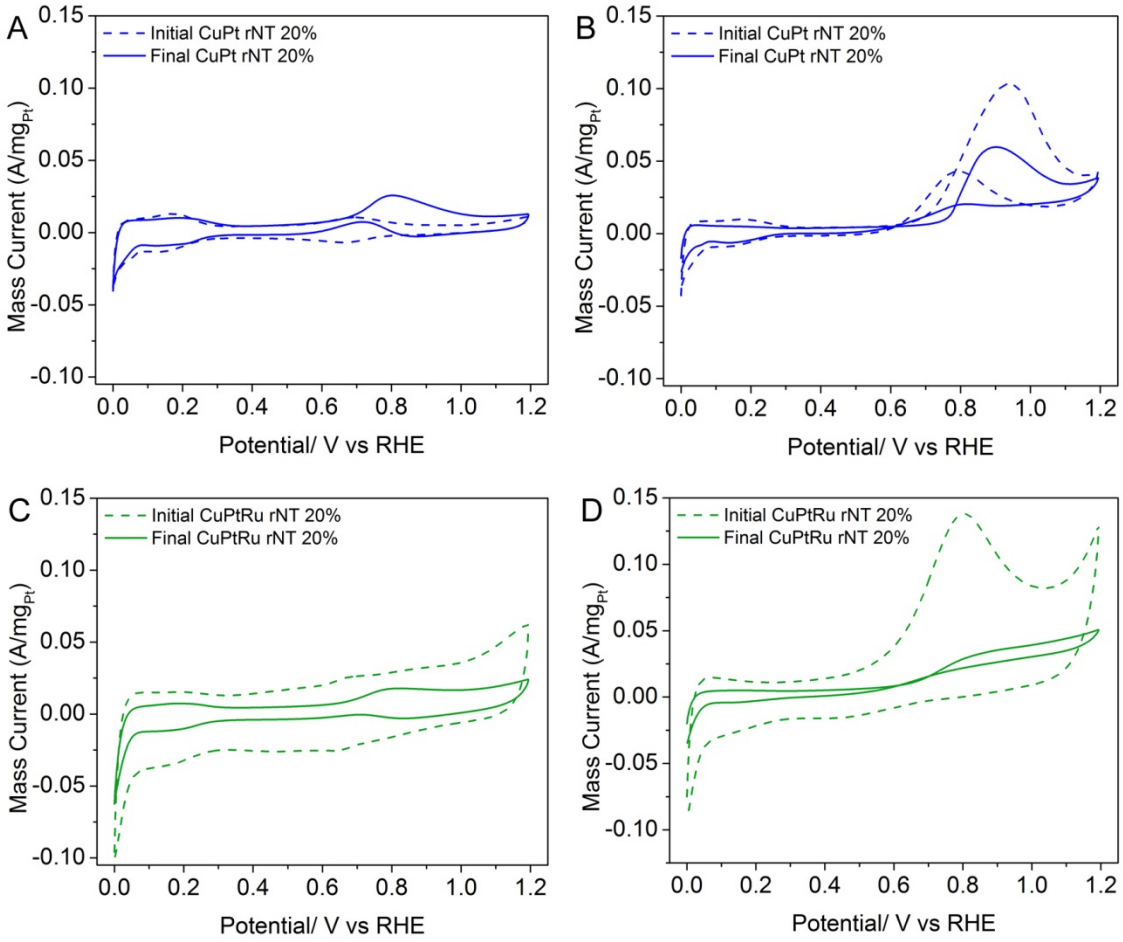

Figure 14: analyte stability studies for CuPt rNT 20% (A & B) and CuPtRu rNT 20% (C & D). Voltammograms completed in electrolyte are found in (A & C), while voltammograms completed in analyte are found in (B &D). Initial voltammograms are denoted by dashed lines and final voltammograms are denoted by solid lines.

sample	Initial or final	overpotential (V vs RHE)
CuPtRu rNT 10%	initial	0.429737836
CuPtRu rNT 10%	final	0.662386136
CuPt rNT 10%	initial	0.648522551
CuPt rNT 10%	final	0.750044435
CuPtRu rNT 20%	initial	0.444034659
CuPtRu rNT 20%	final	0.652710509
CuPt rNT 20%	initial	0.652710509
CuPt rNT 20%	final	0.750044435

Table 7: contains MOR overpotential values for rough nanotubes with varying contents of platinum. It provides the initial and final overpotential values for the analyte stability studies contained in **Figure 13 & 14.**

If/Ib values				
Samples	initial or final	If (mA/mg_{Pt})	Ib (mA/mg_{Pt})	If/Ib (mA/mg_{Pt})
CuPtRu rNT 10%	initial	0.139756897	-0.00626878	-22.294118
CuPtRu rNT 10%	final	0.016539197	0.004356733	3.7962382
CuPt rNT 10%	initial	0.100068287	0.041450423	2.414168
CuPt rNT 10%	final	0.018096149	0.008235455	2.1973466
CuPtRu rNT 20%	initial	0.138186288	-0.00350997	-39.36965
CuPtRu rNT 20%	final	0.032818902	0.020561322	1.5961475
CuPt rNT 20%	initial	0.10345534	0.04325321	2.3918535
CuPt rNT 20%	final	0.059860694	0.020936903	2.8590998

Table 8: contains MOR If/Ir values for rough nanotubes with varying contents of platinum. It provides the initial and final overpotential values for the analyte stability studies contained in **Figure 13 & 14.**

4.4.11 TEM Characterization of nanotubes after electrochemical characterization

The morphology of the nanotubes, surface structure, and composition was characterized in order to determine the durability of the nanotubes during the electrochemical studies. **Figure 15** characterizes each nanotube after the preliminary electrochemical characterization. TEM images of copper-platinum nanotubes with varying surface structure (A - C) and copper-platinum-ruthenium nanotubes of varying surface structure (D – F). TEM image A characterizes the morphology of the CuPt sNT 10%, which demonstrates that the smooth surface structure was maintained during the preliminary electrochemical characterization. The nanotubes morphology was slightly degraded as well as, the nanotubes were shortened from approximately 2 μm to approximately 300 nm in length. TEM image B characterizes the CuPt rNT 10%, which demonstrates the morphology was maintained, the length of the nanotube was not degraded during the study. The rough surface structure was also not altered during this study. This TEM image does demonstrate the presence of smaller particles along the surface of CuPt rNT 10%. These smaller particles were formed due to the initial copper nanowire synthesis, and were not removed during the purification process. TEM image C characterizes CuPt rNT 20%, which demonstrates the length and diameter was not altered during the electrochemical study. Additionally, the surface structure was maintained on multiple vertices along the nanotubes. The image also shows the presence of smaller nanoparticles, which remained from the synthesis and purification of the copper nanowires.

TEM image D characterizes the CuPtRu sNT 10%, which shows a mixture of nanotubes with smooth surface structure as well as rough surface structure. While the diameter of the nanotubes remained unaltered, the length of CuPtRu sNT 10% was shortened to approximately 300 nm. The image also demonstrates the presence of smaller particles, which may be present

from the original synthesis. CuPt rNT 10% is characterized by TEM image E, which demonstrates that the length and diameter of the nanotube remains unchanged after electrochemical characterization, and the surface roughness of CuPtRu rNT 10% is still present. CuPtRu rNT 20% is characterized in TEM image F. These nanotubes demonstrate that the original morphology was maintained, and the surface roughness was not altered, and can be seen on multiple vertices along the nanotubes. This TEM demonstrates the presence of some smaller nanoparticles, which are most likely due to the synthesis. Each TEM image also contains amorphous spheres, which based on the image contrast can be attributed to the presence of unremoved surfactant or the presence of nafion from the electrocatalytic study. CuPt sNT 10% and CuPtRu sNT 10% are altered the most during the electrochemical characterization, while the nanotubes with rough surface structure demonstrate less change after the characterization. Comparing the various types of nanotubes with rough surface morphology, the rNT 20% shows less alteration in the morphology. This suggests that the increase in platinum content could create a more durable nanomaterial for electrocatalysis.

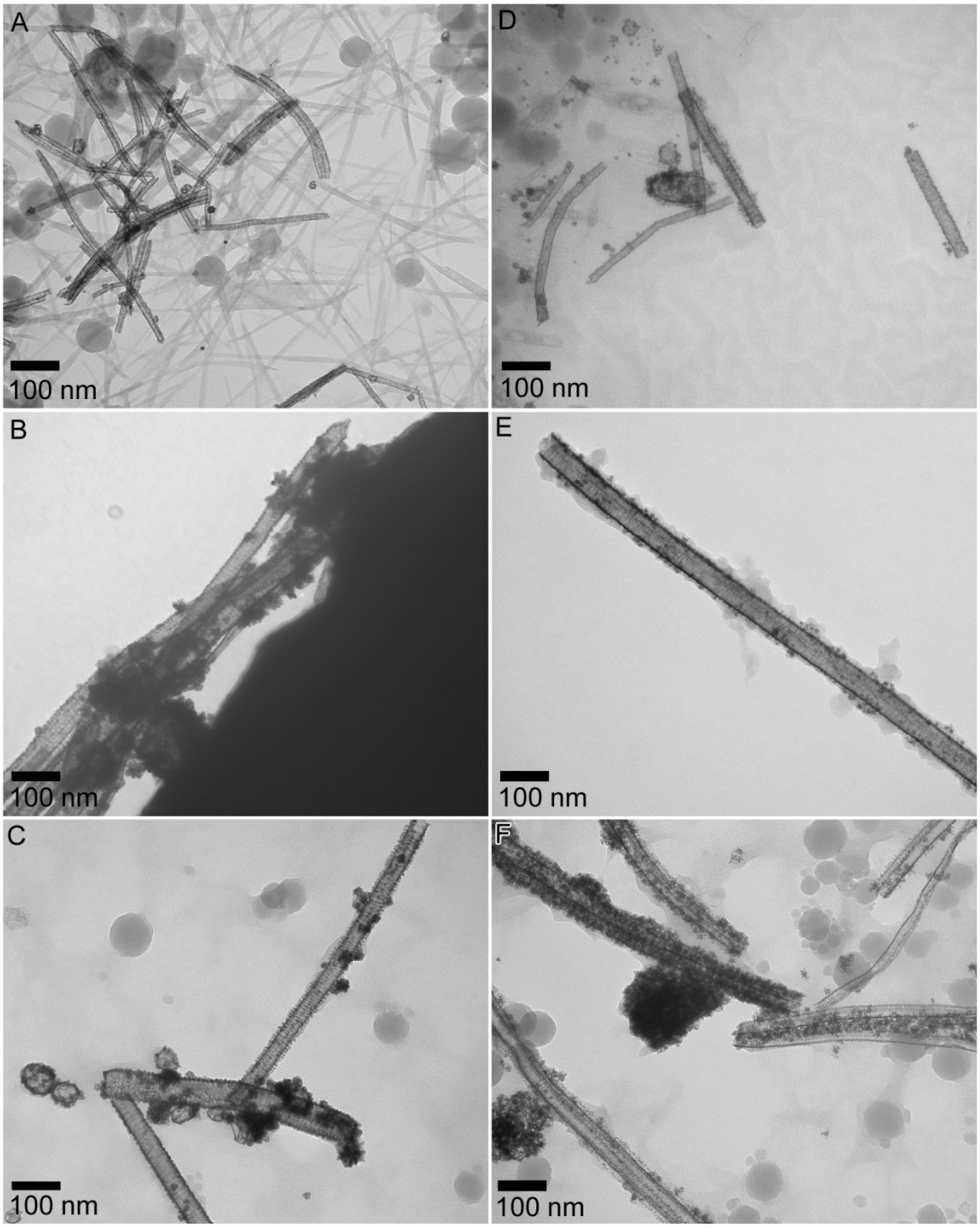

Figure 15: TEM images of the nanotubes after preliminary electrochemical characterization. TEM images are organized as follows: A) CuPt sNT 10%, B) CuPt rNT 10%, C) CuPt rNT 20%, D) CuPtRu sNT 10%, E) CuPtRu rNT 10%, and F) CuPtRu rNT 20%.

TEM images of the rough nanotubes were obtained after electrolyte stability studies. TEM images A & B characterize the rough nanotubes with 10% platinum, while TEM images C

& D provide results for rough nanotubes with 20% platinum. TEM image A characterizes CuPt rNT 10%, which demonstrates that the structure of the nanotube was altered during the study. The length of CuPt rNT 10% was shortened and the surface structure is not as pronounced. CuPtRu rNT 10% in TEM image B is not degraded as much as CuPt rNT 10%. The length of the nanotube was maintained, and the surface structure is still present. TEM image C characterizes CuPt rNT 20%, in which the nanotube original morphology and surface structure was maintained. CuPtRu rNT 20% is characterized by TEM image D, which also demonstrates that the surface shape and morphology of the nanotube was not changed during the electrochemical study. Each TEM image demonstrates the presence of smaller nanoparticles, which are remnants of the original synthesis and purification process. Based on the contrast of the TEM image, each nanotube sample contains amorphous structures. These can be contributed to the nafion from the electrocatalytic studies as well as the removal of capping ligands during the electrolyte stability study. Additional characterization, through EDX mapping, would be needed in order to determine the composition of amorphous substance. CuPt rNT 10% demonstrated the most morphological degradation during the electrolyte stability study, while CuPtRu rNT 10% maintained its shape, the surface structure did degrade during the stability study. This suggests that the incorporation of ruthenium into the nanotube can improve the durability of the electrocatalyst. Comparing the 10% rough nanotubes and 20% rough nanotubes, the 20% rough nanotubes were not only able to resist alteration on their length, they were also able to maintain their surface structure. This is consistent with the preliminary electrochemical result that increasing the platinum content can create a more durable nanomaterial electrocatalyst.

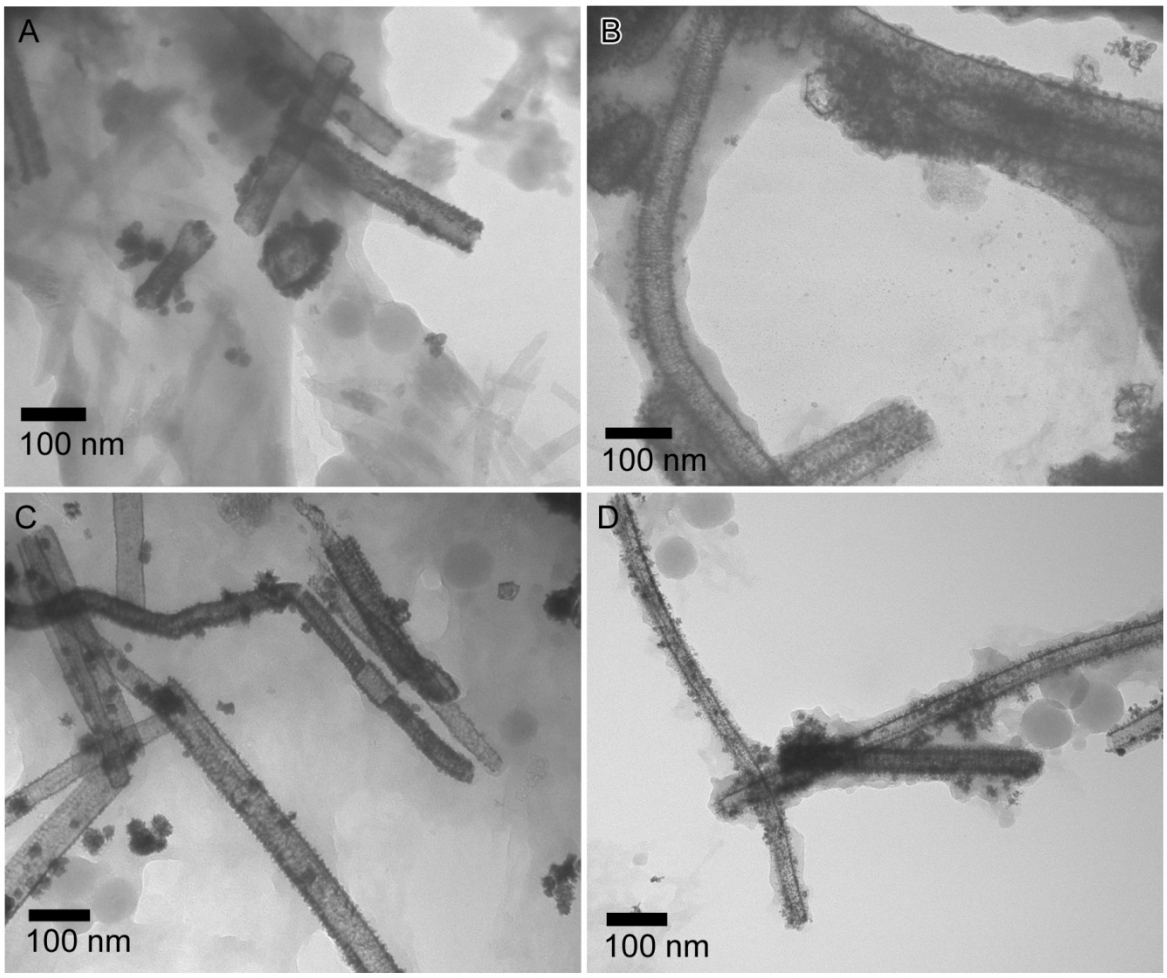

Figure 16: TEM images of the rough nanotubes after the electrolyte stability study. Image A CuPt rNT 10%, image B CuPtRu rNT 10%, image C CuPt rNT 20%, and image D CuPtRu rNT 20%.

The rough nanotubes stability in analyte was studied, and the morphology after electrochemical characterization was evaluated through TEM. CuPt rNT 10% morphology is characterized in TEM image A. The morphology of the nanotube is maintained during this study, and the surface structure was not altered during this study. This image also shows the presence of smaller particles, which were formed during the synthesis and were not effectively removed during the purficiation process. CuPtRu rNT 10% is characterized by TEM image B. This image demonstrates that the length of the nanotube was not altered. Additionally, the surface roughness is visible along the vertices, suggesting that the surface structure was maintained. This image

also demonstrates the presence of nanoparticles and aggregrated nanoparticles, from the synthetic process. These larger particles may possess some influence on the electrocatalytic properties.

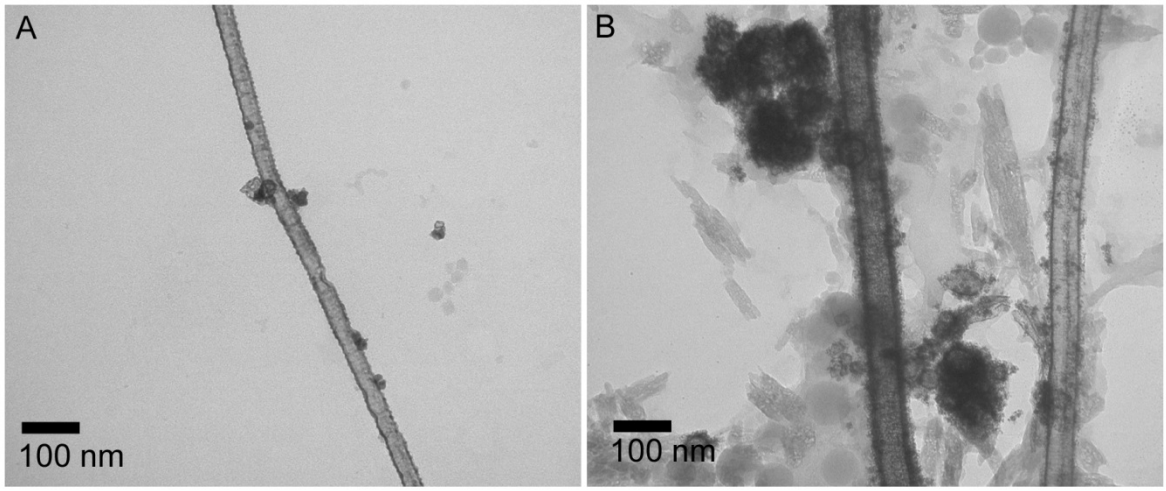

Figure 17: TEM images of the rough nanotubes after the analyte stability study. Image A CuPt rNT 10%, image B CuPtRu rNT 10%

4.4.12 Pt 4f XPS characterization of smooth and rough nanotubes with 10% platinum

Each nanotube was studied by XPS, in order to determine the type of alloying present in the nanotubes as well as the chemical surround of the nanotubes. For each nanotube a survey scan was collected to determine the composition of each nanotube. In addition to the survey scan, focused scans were collected in the binding energy range of each element present in the nanotubes. The photoelectron lines that were studied for each nanotube included Pt 4f 5/2 & 7/2, Ru 3p ½ & 3/2, and Cu 2p ½ & 3/2. **Figure 18 - 22** provide the XPS spectra for each photoelectron line and nanotube sample. **Figure 18** compares the Pt 4f orbital for each nanotube with 10% platinum, by atomic ratio. CuPt sNT 10% is shown in red, CuPtRu sNT 10% is shown by black, CuPt rNT 10% is shown in orange, and CuPtRu rNT 10% is shown in violet. The Pt^0 reference value for Pt $4f_{5/2\ \&\ 7/2}$ is denoted by the black dashed line. This highlights any shift in binding energy that the nanotubes may possess, due to alloying or oxidation of the nanotube. A

downward shift (lower in binding energy) can generally related to alloying, while an upward shift in binding can generally be linked to oxidation of the nanotube. The specific Pt 4f binding energy, for each nanotube with 10% platinum can be found in **Table 9,** which allows for a comparison of the alloying of the nanotubes. CuPt sNT 10% and CuPt rNT 10% possess a larger upward shift in binding energy, while CuPtRu sNT 10% and CuPtRu rNT 10% possess a larger downward shift in binding energy. Previous research has shown that a downward shift in binding energy can be linked to a difference in alloying, and has been correlated with an improvement in electrocatalytic activity. The peak deconvolutions of the Pt 4f photoelectron line of each nanotube can be found in **Figure S10,** and the binding energies and FWHM of each peak corresponding to Pt^0, Pt^{2+}, and Pt^{4+}. Coreframe and frame nanostructures deconvolutions also account for the Cu 3p photoelectron line in the XPS spectra of $4f_{7/2}$ & $4f_{5/2}$. Since the binding energy for the Cu 3p orbital overlaps with the Pt 4f orbital, an additional doublet is added to the deconvolution. This fourth doublet, denoted by the cyan line, is attributed to the Cu 3p ½ & 3/2 orbitals. This overlap could influence the platinum 4f spectrum by broadening the base of the doublet peak.

sample	Pt 4f 5/2 (eV)	Pt 4f 7/2 (eV)
CuPt sNT 10%	74.9411765	71.5823529
CuPtRu sNT 10%	74.8323529	71.3970588
CuPt rNT 10%	75.4470588	72.0470588
CuPtRu rNT 10%	74.9764706	71.5058824

Table 9: provides the binding energies at the max intensity for the Pt 4f photoelectric line. Binding energies for the following nanotubes: CuPt sNT 10%, CuPtRu sNT 10%/, CuPt rNT 10%, and CuPtRu rNT 10%.

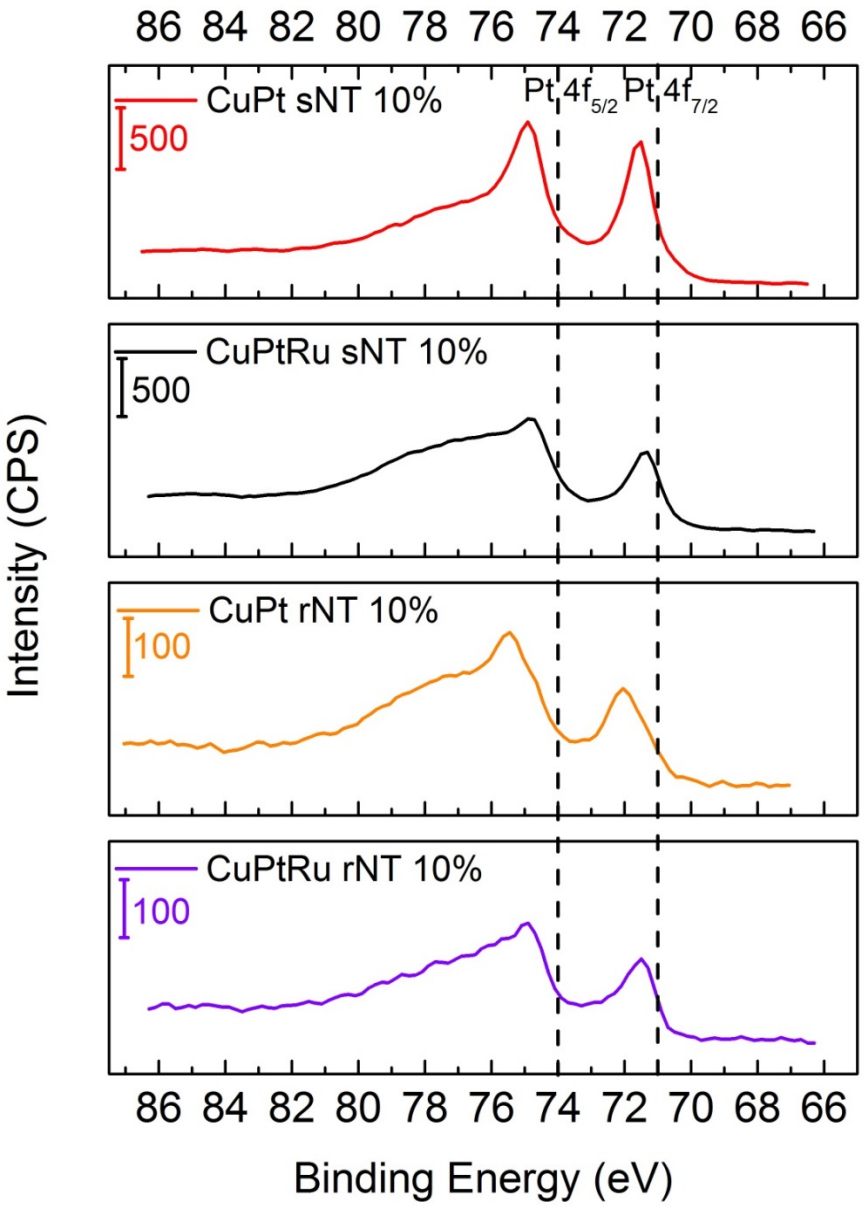

Figure 18: XPS Pt 4f orbital characterization of smooth and rough nanotubes at 10% of platinum, with a focus of the Pt 4f orbital. CuPt sNT 10% (red), CuPtRu sNT 10% (black), CuPt rNT 10% (orange), and CuPtRu rNT 10% (violet).

4.4.13 Pt 4f XPS characterization of rough nanotubes with varying platinum content

Figure 19: characterizes the Pt $4f_{5/2}$ and Pt $4f_{7/2}$ of the rough nanotubes with 10% and 20% platinum. CuPt rNT 10% is shown by orange, CuPtRu rNT 10% is shown by violet, CuPt rNT 20% is shown by blue, CuPtRu rNT 20% is shown by green. The Pt^0 literature value is

shown by the black dashed line, at 71 eV and 74 eV. The binding energy values for each nanotube can be found in **table 10,** and a comparison of the XPS spectra can be **Figure 19.** The type of alloying and oxidation that occurs on the nanotube surface can be determined by the nanotube's shift in Pt 4f binding energy. Based on the rough nanotubes' max intensity at the Pt 4f binding energies, the copper-platinum-ruthenium nanotubes have more of a downward shift in binding energy, compared to the copper-platinum nanotubes. Additionally, when the platinum content is increased from 10% to 20%, a downward shift (negative/lower binding energy) in the binding energy is seen in both CuPt rNT and CuPtRu rNT samples. This suggests that the increase in platinum could relate to the nanotube possessing a higher electron density, and has larger d-band vacancy (poh). Additionally, these results provide insight into which nanotube would function as the best electrocatalyst for methanol oxidation. The Pt 4f XPS results suggest that the CuPtRu rNT would function as better electrocatalysts, specifically CuPtRu rNT 20%.

sample	Pt 4f 5/2 (eV)	Pt 4f 7/2 (eV)
CuPt rNT 10%	75.4470588	72.0470588
CuPtRu rNT 10%	74.9764706	71.5058824
CuPt rNT 20%	74.7941176	71.4705882
CuPtRu rNT 20%	74.6852941	71.3264706

Table 10: compares the Pt 4f binding energies of the rough nanotubes with varying platinum content.

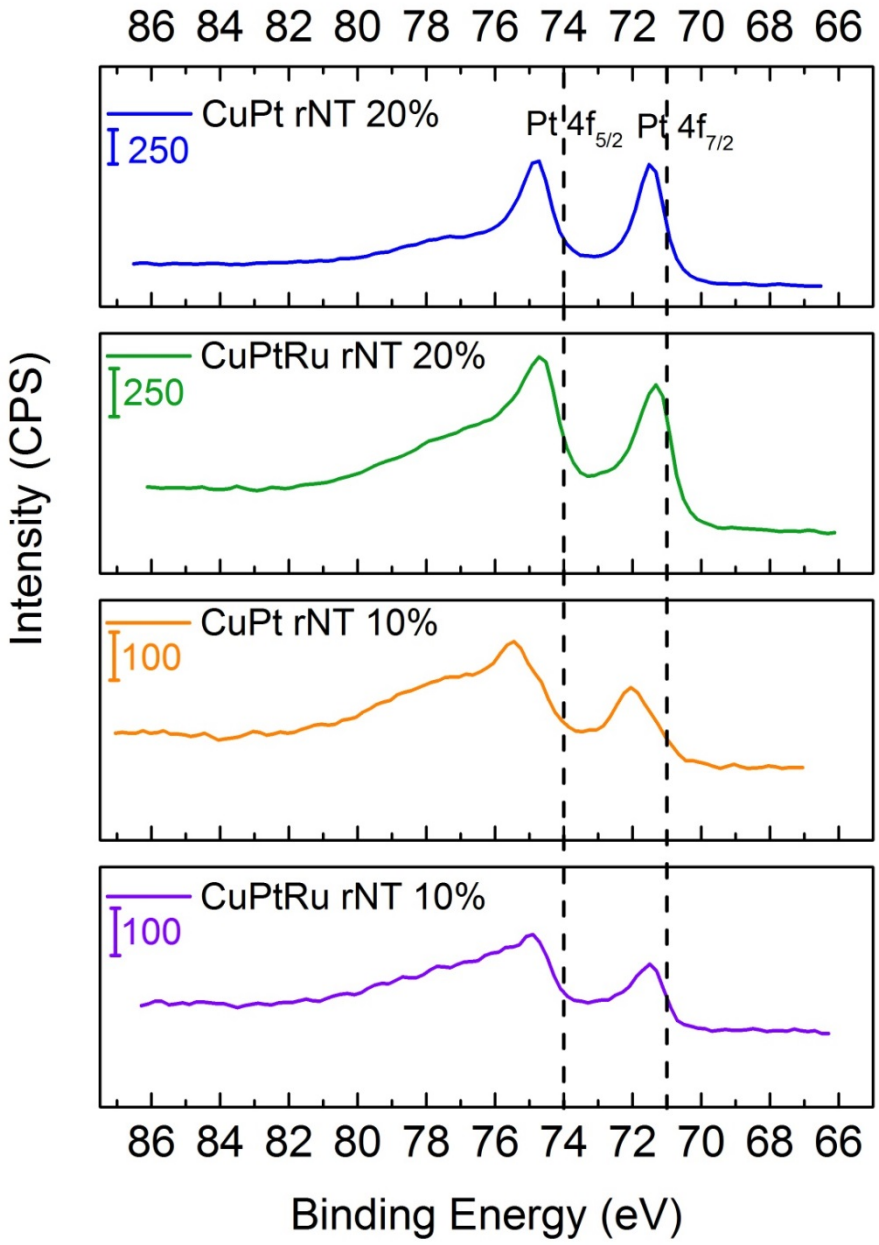

Figure 19: XPS characterization of smooth and rough nanotubes at 10% of platinum, with a focus of the Pt 4f orbital. CuPt rNT 20% (blue), CuPtRu sNT 20% (green), CuPt rNT 10% (orange), and CuPtRu rNT 10% (violet).

4.4.14 Cu 2p XPS characterization of smooth and rough nanotubes containing 10% platinum

The Cu 2p photoelectron line was also investigated for each nanotube, the results of which can be found in **Figure 19 & 20 and table 11. Figure 19** compares smooth and rough

nanotubes with 10% platinum, from these results a slight downward shift (lower binding energy) from the reference value for Cu^0. There is no distinct difference in Cu 2p binding energies for the smooth and rough nanotubes with 10% platinum. The Cu 2p binding energy of the nanotubes with rough surface structure and varying amounts of platinum is in **Figure 20**. There is a larger downward shift (lower binding energy) in both the CuPt rNT 20% and CuPtRu rNT 20% compared to their 10% platinum variants. The binding energies for Cu 2p orbtial from the nanotube spectra can be found in **Table S2**. Each of the Cu 2p peaks also shows the presence of Cu 2p scatter peaks.

sample	Cu 2p 1/2 (eV)	Cu 2p 3/2 (eV)
CuPt sNT 10%	952.094118	932.141176
CuPtRu sNT 10%	952.67451	932.627451
CuPt rNT 20%	951.803922	932.047059
CuPtRu rNT 20%	952	932.141176
CuPt rNT 10%	952.290196	932.431373
CuPtRu rNT 10%	952.094118	932.431373

Table 11: Cu 2p photoelectron line for the nanotubes.

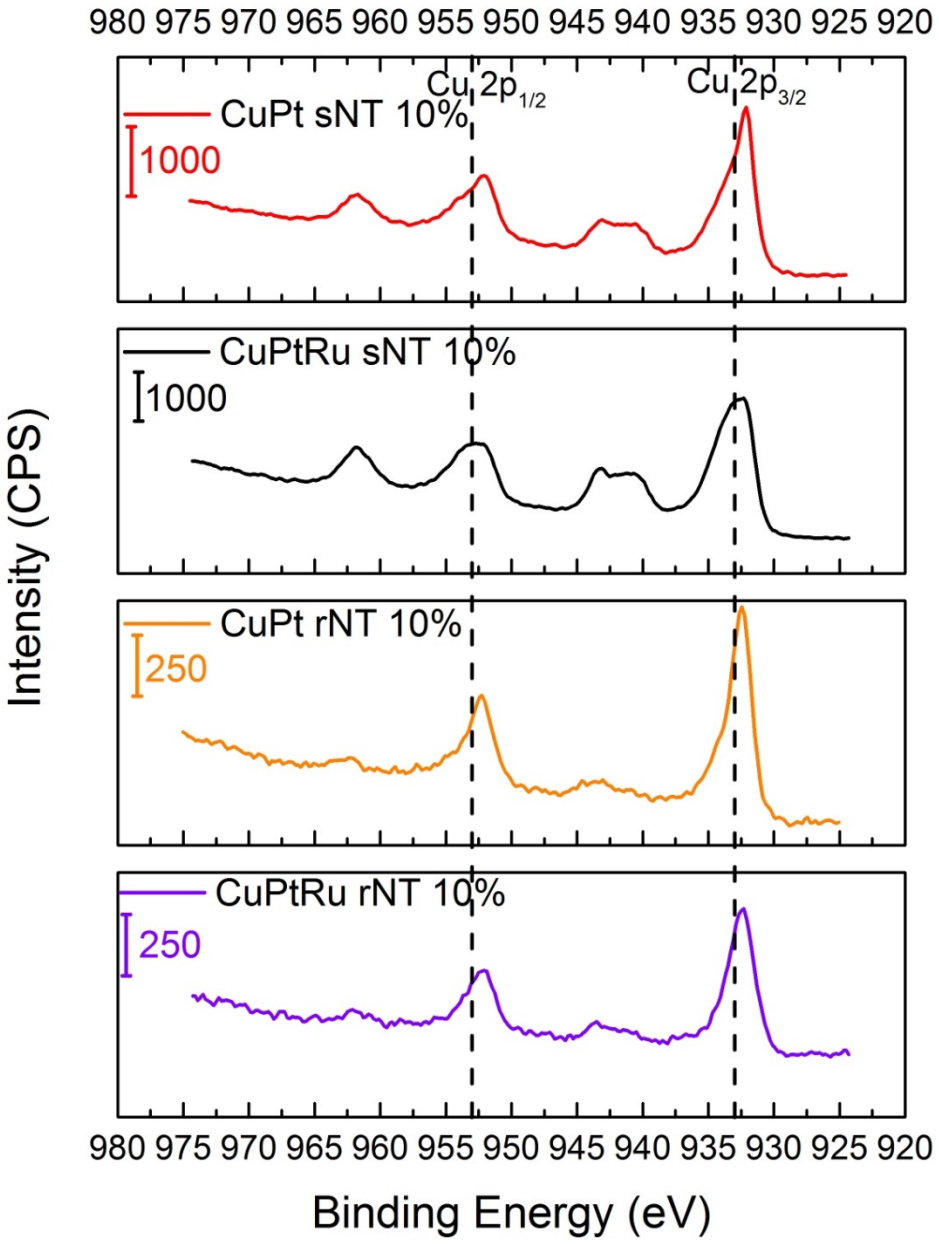

Figure 20: XPS spectra of Cu 2p orbital characterization for the smooth and rough nanotubes with 10% platinum. CuPt rNT 10% (orange), CuPtRu sNT 10% (red), CuPtRu rNT 10% (violet), and CuPtRu sNT 10% (orange).

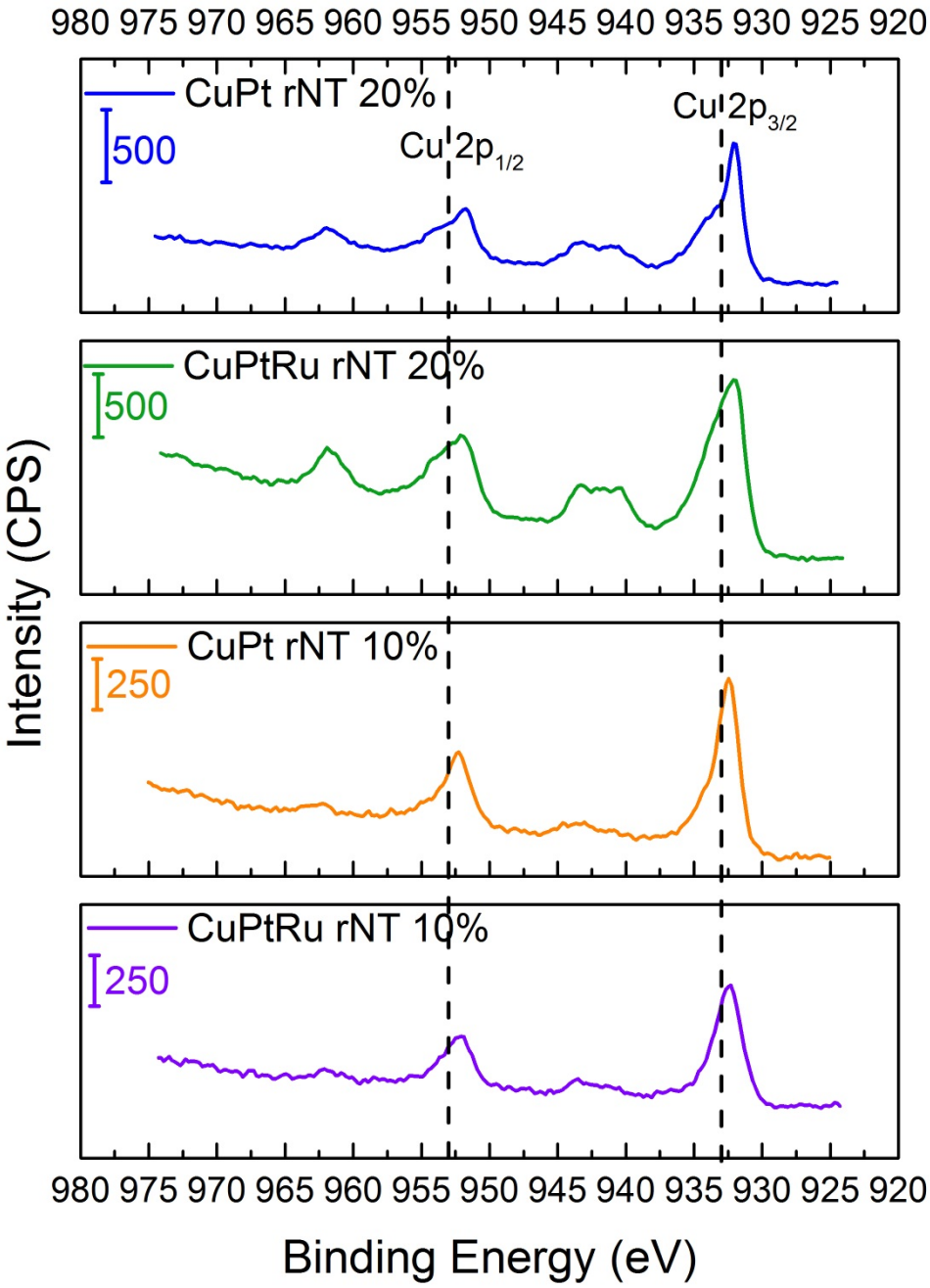

Figure 21: XPS characterization of smooth and rough nanotubes at 10% and 20 % of platinum, with a focus of the Cu 2p photoelectric line. CuPt rNT 20% (blue), CuPtRu sNT 20% (green), CuPt rNT 10% (orange), and CuPtRu rNT 10% (violet).

4.4.15 XPS characterization of Ru 3p photoelectron lines with ruthenium incorporated lines

CuPtRu sNT 10%, CuPtRu rNT 10%, and CuPtRu rNT 20% were characterized by XPS, and the results are in **Figure 22** the Ru 3p $_{½ \text{ \& } 3/2}$ and **Table 12** provides binding energy values for the max intensity for each nanotube. The binding energy for each nanotube does not demonstrate much of a deviation from the Ru 3p reference values, which suggests there is Ru^0 present in the sample. The intensity for each sample suggests that only a low amount of ruthenium is alloyed onto the surface of the nanotube. Additionally, these results do correspond to the ICP-MS atomic ratio of ruthenium in each nanotube. The ICP-MS results can be found in **Table S7**, which determined the atomic ratio of ruthenium to be ~5% for the rough nanotubes, and ~ 2% for the smooth nantubes. The XPS spectra with peak deconvolutions with for CuPtRu rNT 10%, CuPtRu rNT 20%, and CuPtRu sNT 10% can be found in **Figure S3.** The peak deconvolutions account for the presence of Ru^0 and Ru^{2+} present in each nanotube sample. The binding energy values for the deconvolution are located in **Table 12**.

sample	Ru 3p1/2 (eV)	Ru 3p 3/2 (eV)
CuPtRu sNT 10%	483.988235	462.958824
CuPtRu rNT 20%	483.988235	462.011765
CuPtRu rNT 10%	484.205882	462.158824

Table 12: binding energies of the Ru incorporated nanotubes, at the Ru 3p photoelectric line.

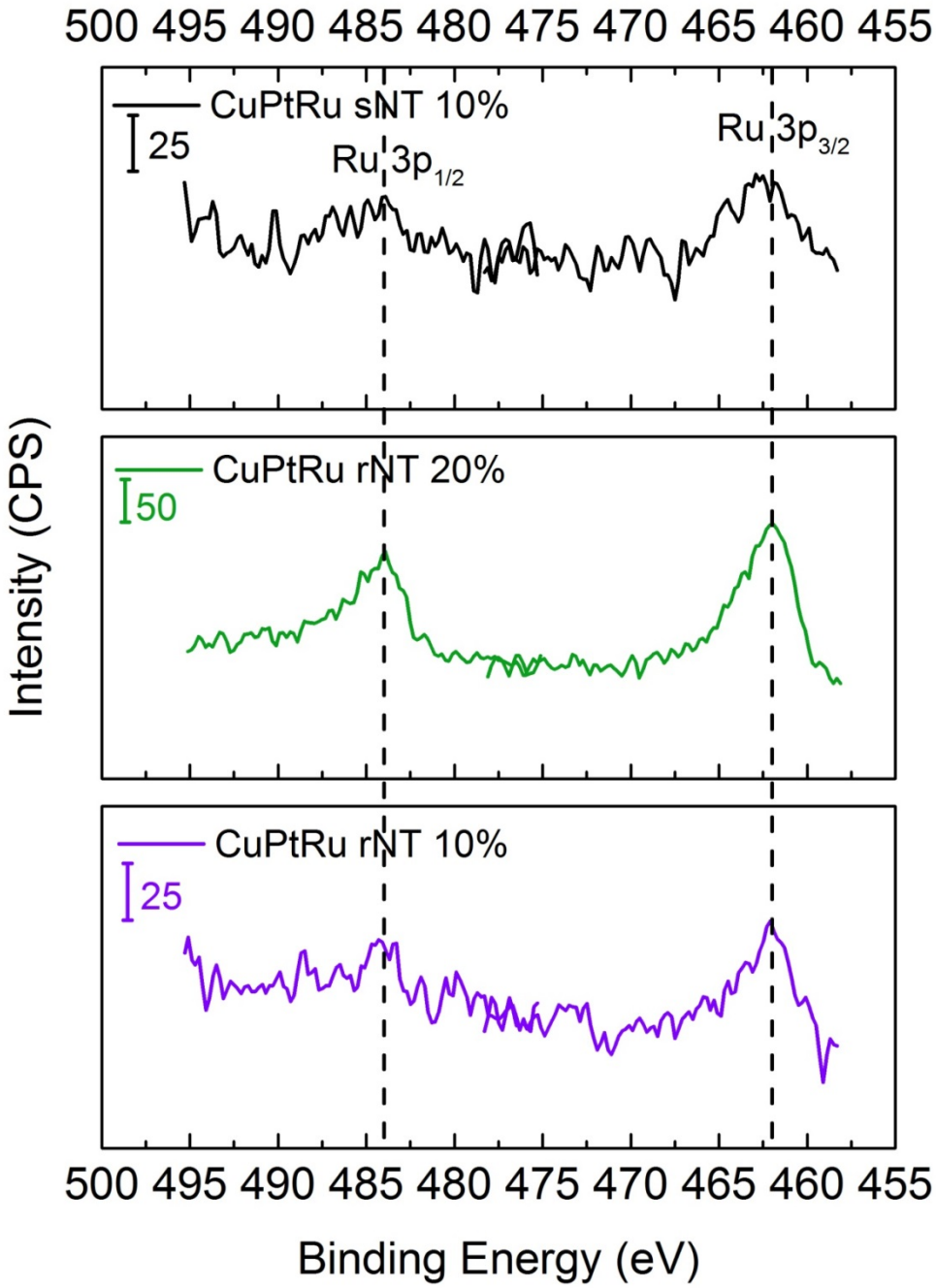

Figure 22: XPS characterization of Ru 3p ½ & Ru 3p 3/2 of the ruthenium incorporated nanotubes. CuPtRu sNT 10% is denoted by the black lines, CuPtRu rNT 20% is denoted by the green line, CuPtRu rNT 10% is denoted by the violet line. The dashed black lines provide the literature values for the Ru $3p_{1/2}$ & Ru $3p_{3/2}$ photoelectron lines.

4.5 **Conclusion**

This research developed multimetallic nanotubes with synthetically tunable composition and surface structure. Copper platinum nanotubes with rough and smooth surface structure were developed through the in situ separation of the growth mechanisms. The rough nanotubes were developed through both the coreduction mechanism and the galvanic replacement reaction, while the smooth nanotubes were developed with solely the galvanic replacement reaction. Ruthenium was incorporated into each nanotube to develop copper platinum ruthenium nanotubes with smooth and rough surface structure. The copper platinum ruthenium nanotubes with various surface structures were developed through the same growth mechanisms as copper platinum nanotubes. The electrocatalytic properties of the nanotubes were evaluated, and the influence of surface structure on MOR activity was determined. It was determined that the nanotubes with rough surface structure were more electrocatalytical active for MOR than the smooth nanotubes, when the atomic ratio of platinum remained constant. The rough nanotubes with ruthenium proved to be more electrocatalytically active for methanol oxidation, additionally the overpotential is comparable to the PtRu STND. The electrocatalytic activity of the rough nanotubes with an increase in atomic ratio of platinum was studied. It was determined that an increase in platinum content on the rough nanotubes resulted in a more active electrocatalyst for MOR, as well as a more durable electrocatalyst during the stability studies.

4.6 **Appendix A: Supporting Information, Experimental Methods**

4.6.1 **Tailoring the copper-platinum nanotubes with rough surface morphology to approximately 10% of platinum. synthetic control of composition**

The composition of copper platinum rough nanotubes was synthetically optimized to platinum content in order for the nanotubes to possess a similar composition to the platinum copper nanotubes with a smooth nanotube. Synthetic tuning of the composition will allow for a

comparison of electrocatalytic activity based on nanotube surface structure. The synthetic tailoring was completed by altering the ratio time as well as the platinum precursor concentration, while holding the reaction temperature constant. In the first set of syntheses the reaction time for platinum alloying was varied, and Cu NW were prepared by the previously outlined method. After which the platinum precursor, at a concentration of 0.076 mmol of $Pt(acac)_2$ dispersed in 1 ml OLA, and was injected into the reaction solution and held at 220 ºC for the following reaction times: 50 min, 90 min, and 120 min. The alloyed nanotubes were purified and characterized by the previously outlined protocol. The second set of syntheses altered the platinum precursor amount during the alloying step. Cu NW were prepared by the previous method, after 50 minutes the platinum precursor was injected at the following concentrations: 0.153 mmol, 0.102 mmol, (E & F) 0.076 mmol, and 0.050 mmol of $Pt(acac)_2$ dispersed into 1ml OLA. The reaction solution was held at 220 ºC for 90 mins, then was purified and characterized.

4.6.2 Ex situ attempts for synthetic separation of copper platinum nanotubes with rough and smooth surface morphology.

Synthetic separation of the two nanotube morphologies were also attempted through ex situ methods. These experiments were separated into two main steps. The first step synthetically prepared and purified the copper nanowires. In the second step, the Cu NW were redispersed with OLA at a lower temperature. The platinum precursor was then injected into the reaction solution, and the reaction temperature was held for 60 minutes. In this synthetic study, both tetrachloroplatinate and platinum acetylacetonate at 0.0765 mmol (30mg) were tried as the platinum precursor. These nanotubes were quenched, purified, and characterized.

4.6.3 **Separation of dual growth mechanisms & optimization of ruthenium platinum copper nanotubes with smooth nanotubes: separate injections of precursor**

The composition CuPtRu sNT 10% synthesis was optimized by altering the reaction time for the platinum and ruthenium alloying steps. Additional trial syntheses to develop copper-platinum-ruthenium smooth nanotubes focused on altering the precursor injection order. In the first trial of CuPtRu sNT 10%, Cu NW were synthesized and the reaction temperature as reduced to 190 ºC. The platinum precursor was prepared (0.076 mmol, 30 mg, of $Pt(acac)_2$ dissolved in 1 mL OLA), and injected into the reaction solution. The reaction solution was held for 3 hours, during which the ruthenium precursor was prepared (0.076 mmol, 15 mg, $RuCl_3$ dissolved in 1 mL OLA). The ruthenium precursor was injected into the reaction solution, and the reaction temperature was held for two additional hours, for a total of four hours for the alloying step. After which, the reaction solution was quenched, purified, and characterized according to the previous protocol.

The second trial reduced the platinum alloying time while maintaining the ruthenium alloying time. The protocol is as follows: Cu NW were synthesized and the reaction temperature as reduced to 190 ºC. The platinum precursor was prepared (0.076 mmol, 30 mg, of $Pt(acac)_2$ dissolved in 1 mL OLA), and injected into the reaction solution. The reaction solution was held for 2 hours, during which the ruthenium precursor was prepared (0.076 mmol, 15 mg, $RuCl_3$ dissolved in 1 mL OLA). The ruthenium precursor was injected into the reaction solution, and the reaction temperature was held for 2 hours, for a total of four hours for the alloying step. After which, the reaction solution was quenched, purified, and characterized according to the previous protocol.

The third synthetic trial varied the alloying time for ruthenium and platinum. Cu NW were synthesized, and the solution temperature was reduced to 190 ºC. The platinum precursor was prepared, 0.0765 mmol of $Pt(acac)_2$ (30mg) dissolved in 1 mL OLA, and injected into the reaction solution. The reaction time for the platinum alloying step was held for 3 hours at 190 ºC. The ruthenium precursor was prepared, 0.075 mmol (15 mg) dissolved in 1 mL OLA, and then injected into the solution. The reaction solution was held at 190 ºC for 1 additional hour to allow for ruthenium alloying. The reaction solution was then quenched and purified. These results were first characterized by TEM and ICP-MS to determine the morphology, surface structure, and composition. The samples that possessed smooth surface morphology by TEM, and the highest concentration of copper, platinum, and ruthenium by ICP-MS were then characterized by EDX mapping.

An additional study was completed on the third synthetic protocol, which increase the reaction times by half an hour. The platinum alloying time was altered first, by the following protocol. The Cu NW were synthesized, and the reaction temperature was reduced to 190 ºC. The platinum precursor, 0.076 mmol $Pt(acac)_2$ dissolved in 1 mL OLA, was injected into the Cu NW solution. The reaction time was held for 3.5 hrs, after which the ruthenium precursor, 0.075 mmol $RuCl_3$ dissolved in 1 mL OLA, was injected into the reaction solution. The reaction was held at 190 ºC for 1 hour, and the nanotube solution was quenched and purified.

The ruthenium alloying step was altered by the following method. The Cu NW were synthesized, the temperature of the reaction solution was reduced from 220 ºC to 190 ºC, after which the platinum precursor was injected. The reaction solution was held for 3 hours; during this time $RuCl_3$ dissolved in 1 mL OLA was prepared as the ruthenium precursor. The ruthenium precursor was injected into the reaction solution, and the temperature was held for 1.5 hours. The

reaction solution was then quenched and purified by the previously outlined procedure. The RuPtCu sNT were then characterized by TEM and ICP-MS, to determine if the surface structure remained smooth and the concentration of platinum and ruthenium in the nanotubes increased.

4.7 **Appendix B: Supporting Information, Results and Discussion**

4.7.1 ***Electron diffraction of CuPt rNT 20%***

SI Figure 1 characterizes the morphology of CuPt rNT 20% by TEM and HRTEM. HRTEM demonstrates the surface structure along a singular CuPt rNT 20%. HRTEM image B and inset provide a magnified image of the surface structure, and the corresponding electron diffraction, which demonstrates the crystalline nature of CuPt rNT 20%.

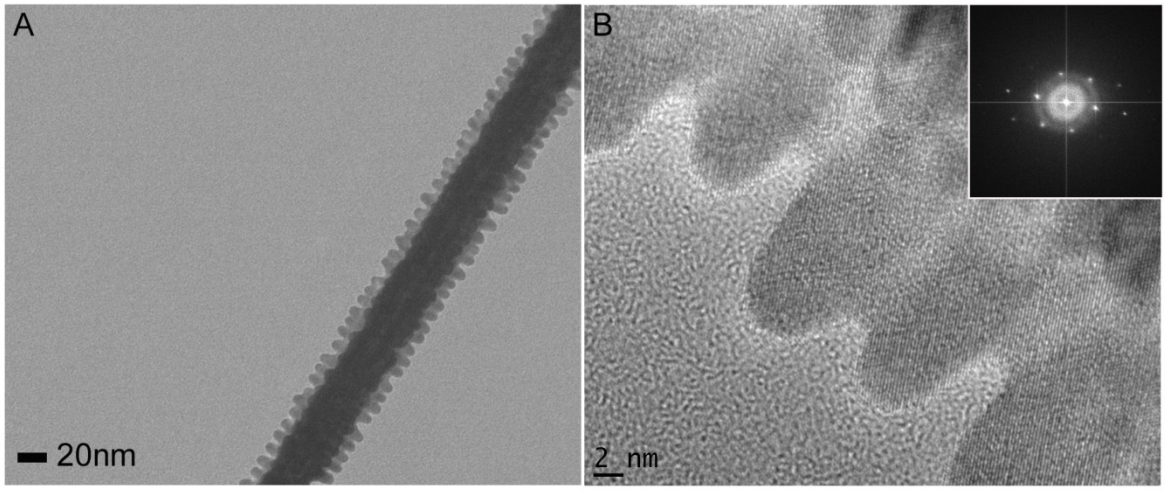

Figure S1: CuPt rNT 20% characterization of morphology by TEM (A), HRTEM (B), HRTEM electron diffraction (B inset),

4.7.2 ***Results from synthetic separation of alloying mechanisms for copper platinum nanotubes***

Copper platinum nanotubes utilize Cu NW as a template to alloy with platinum and ruthenium. Variations in the surface morphology of the platinum-copper nanotubes can be achieved by separating the two main mechanisms, present during the platinum alloying of the Cu NW. By separating the galvanic replacement reaction and coreduction mechanism platinum-

copper nanotubes with specific, uniform surface morphologies (CuPt sNT 10% or CuPt rNT 10%) can be synthesized. The two growth mechanisms influence the alloy of platinum with copper differently, which results the two structures of bimetallic nanotubes. The galvanic replacement reaction is responsible for the formation of hollow nanotubes with a surface composition of platinum and copper. This occurs through the replacement of copper atoms on the surface of Cu NW with reduced platinum atoms. PtCu sNT 10% is formed through the galvanic replacement reaction between platinum and copper. The co-reduction mechanism is responsible for the formation of semi-ellipsoid overgrowth along the vertices and edges of the copper platinum nanotubes. During the coreduction mechanism, platinum and copper co-reduced and adsorbed onto the edges and vertices of the Cu NW templates forming the CuPt rNT 10%. The galvanic replacement reaction alloys the surface with platinum and hollows the interior nanowire. Simultaneously, the seeded co-reduction mechanism causes reduced platinum and copper to adsorb onto the edges and vertices of the Cu NW templates.

The exact reaction parameters necessary to separate the two growth mechanisms were determined by TEM and XRD. **Figure S5** contains characterization results for in situ separation of the two mechanisms, galvanic replacement reaction and the coreduction process, which are responsible for the production of CuPt sNT 10% and CuPt rNT 10%. The in situ separation was completed synthetically by varying the reaction temperature, while maintaining the initial platinum precursor concentration and reaction time. The variations in reaction temperature after the injection of the platinum precursor are as follows: 190 ˚C (A & B), 195 ˚C (C & D), 200 ˚C (E & F), 220 ˚C (G & H). These mechanisms are synthetically separated by the temperature of the reaction, as shown by the TEM images (A, C, E, G) and the XRD spectra (B, D, F, H). The TEM images show the transition from nanotubes possessing smooth surface morphology at

synthetic temperatures of 190 ˚C (A) and 195 ˚C (C); to nanotubes possessing both smooth and rough surface morphology at reaction temperatures of 200 ˚C (E). With an additional increase in reaction temperature to 220 ˚C the surface morphology on the nanotubes transition to solely bumpy nanotubes (G). From the XRD spectra and Vegard's Law the percentage of alloying between platinum and copper based on the reaction temperature can be ascertained. With an increase in reaction time the percentage of platinum present in the nanotubes increased while the percentage of copper is reduced. The XRD results suggest that the CuPt sNT 10% will possess a lower percentage of platinum compared to the CuPt rNT 10%.

The final reaction parameters were determined to be the smooth platinum copper nanotubes (CuPt sNT 10%) synthesis is illustrated in **schematic 1 C**, and is formed through the galvanic replacement reaction. Initially, Cu NW are formed and the temperature is reduced to 190 ˚C in order to create a favorable reaction environment for the galvanic replacement reaction with platinum. The platinum precursor is combined with the reaction solution, and allowed to react with the Cu NW for 5 hours, which allows for the highest amount of platinum alloying without overgrowth occurring along the edges and vertices. The results from the optimization of the PtCu sNT can be found in **Figure S6.**

CuPt rNT 10% & CuPt rNT 20% are illustrated in **Schematic 1 A & B**, synthetic optimization results can be found in **Figure S2 – S4**. These structures are formed through both the galvanic replacement reaction and the co-reduction mechanism. CuPt rNT 20% was optimized to the following procedure; after the initial formation of Cu NW, the platinum precursor (0.076 mmol $Pt(acac)_2$ in 1 ml OLA) is injected into the reaction solution and the reaction temperature is held constant at 220 ºC for 90 minutes. **Figure S2** determined the ideal initial platinum precursor concentration for the CuPt rNT 10% synthesis, which was 0.076 mmol

or 0.05 mmol. The reaction parameters are favorable for the simultaneous exchange of surface copper atoms with platinum atoms as well as the nucleation of platinum and unreacted copper onto the vertices and edges of the Cu NW.

CuPt rNT 10% protocol was optimized to after the initial formation of Cu NW, the platinum precursor (0.05 mmol $Pt(acac)_2$ in 1 ml OLA) is injected into the reaction solution and the reaction temperature is held constant at 220 ºC for 60 minutes. The optimization of this synthesis was determined through **Figure S2** TEM image G & XRD spectrum H, which identified the necessary concentration of platinum precursor to be 0.05 mmol $Pt(acac)_2$ in 1 mL OLA. The reaction time of CuPt rNT 10%, 60 min, was determined through **Figure S3** TEM image A & XRD spectrum B.

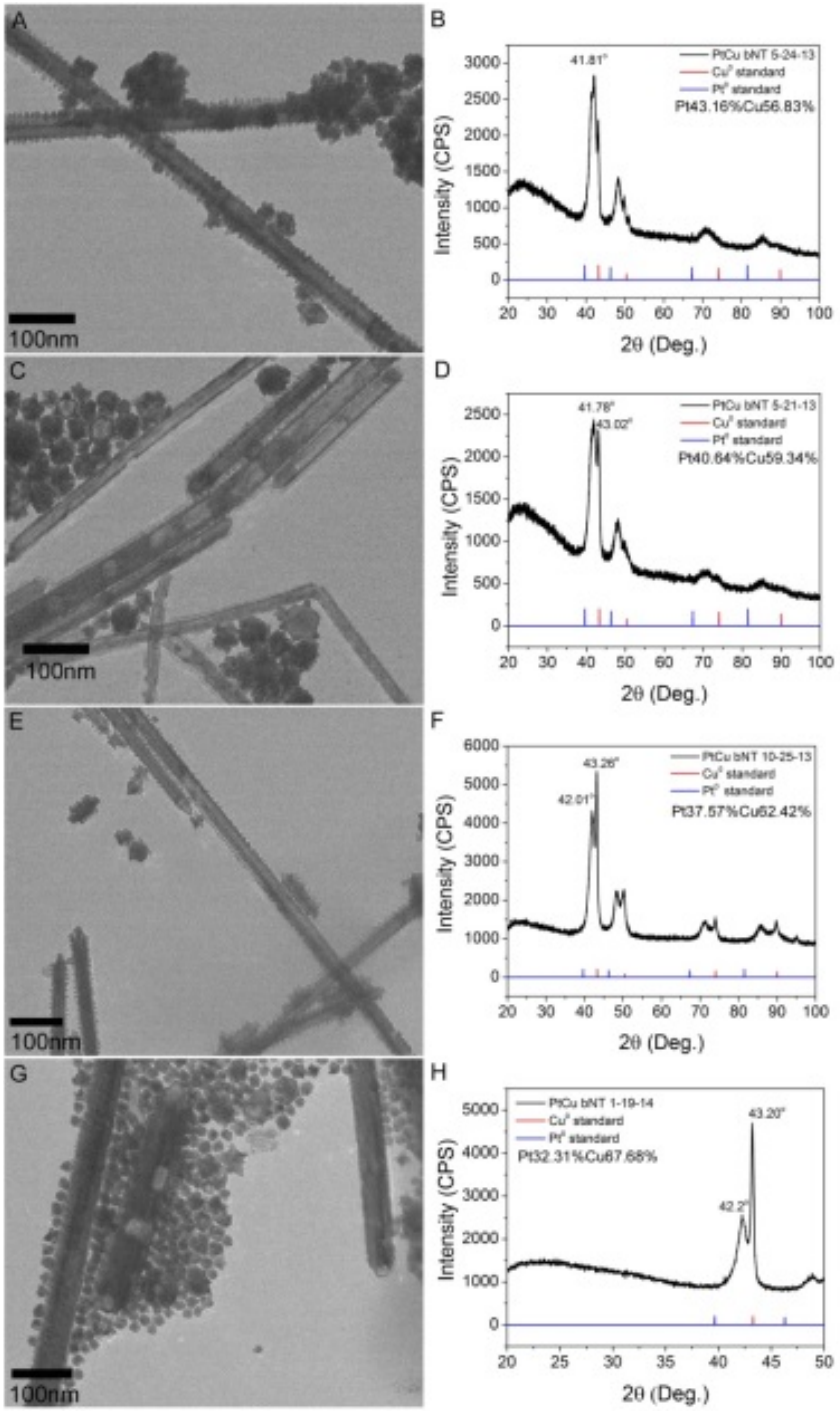

Figure S2: characterize the in situ optimization of the CuPt NT with rought surface morphology by concentration of platinum precursor. This synthetic optimization was completed by varying the secondary precursor amount and maintaining the reaction temperature suitable for the galvanic replacement reaction and coreduction processes (220 ˚C). The variations in platinum precursor concentration for each synthesis are as follows: (A & B) 0.153 (C & D) 0.102 mmol, (E & F) 0.076 mmol, and (G & H) 0.050 mmol of $Pt(acac)_2$ dispersed into 1ml OLA.

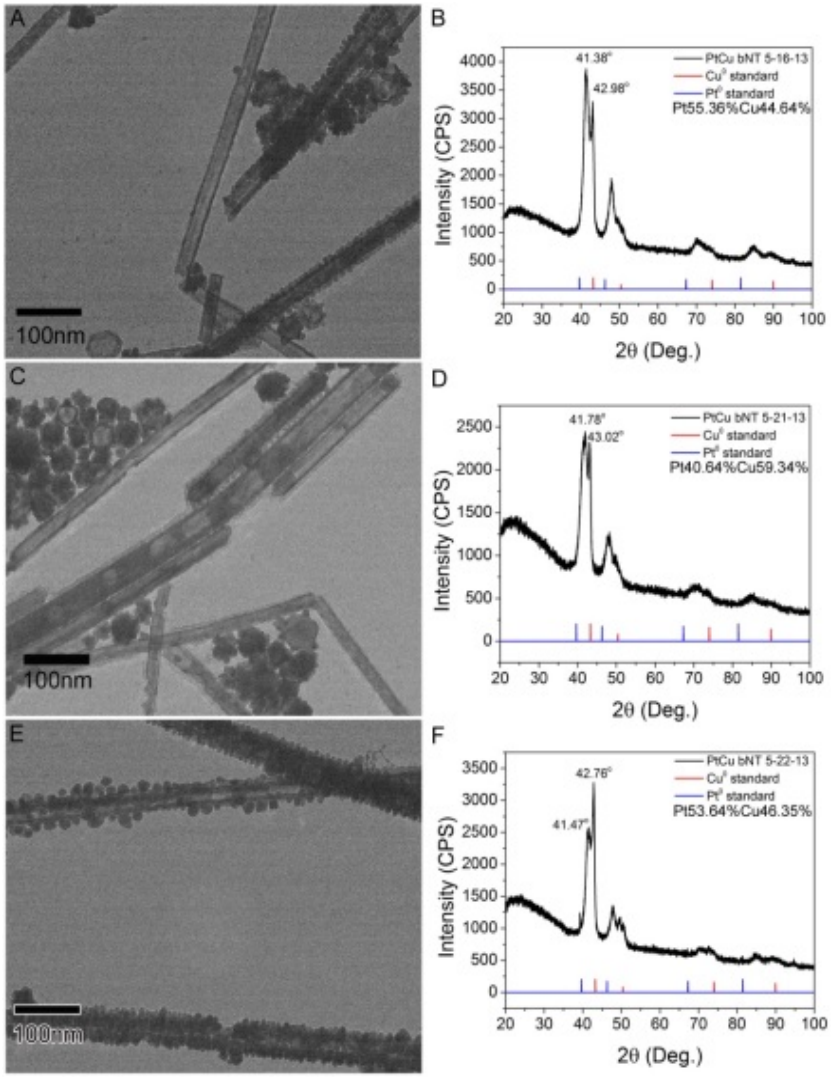

Figure S3: characterizes the in situ optimization of the CuPt rNT surface morphology by reaction time. This synthetic optimization was completed by varying length of reaction time and maintaining the reaction temperature suitable for the galvanic replacement reaction and coreduction processes (220 ˚C) and the initial platinum precursor amount. The variations in reaction time after the injection of the platinum precursor are as follows: 60 min (A & B), 90 min (C &D), and 120 min (E & F).

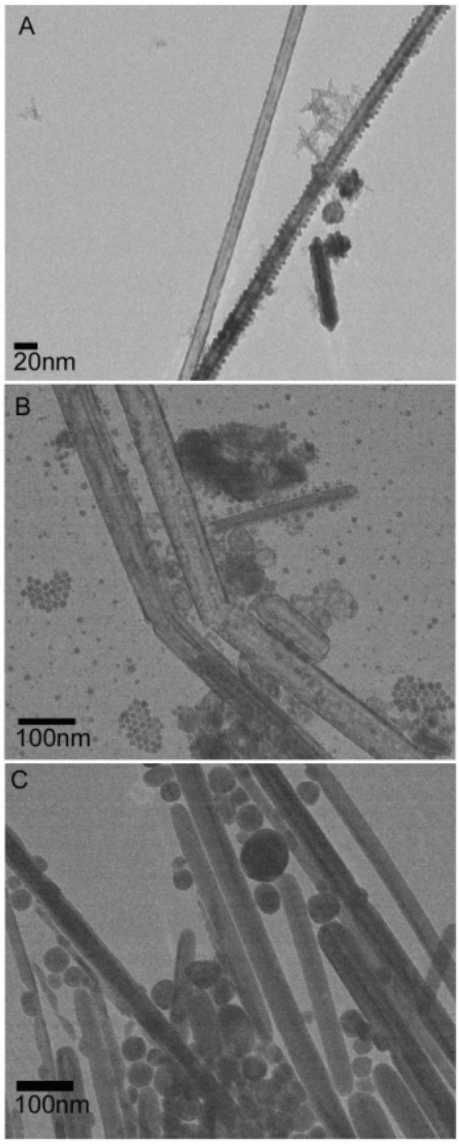

Figure S4: contains TEM images demonstrating the in situ and ex situ synthetic optimization of the platinum copper nanotubes with smooth surface structure.

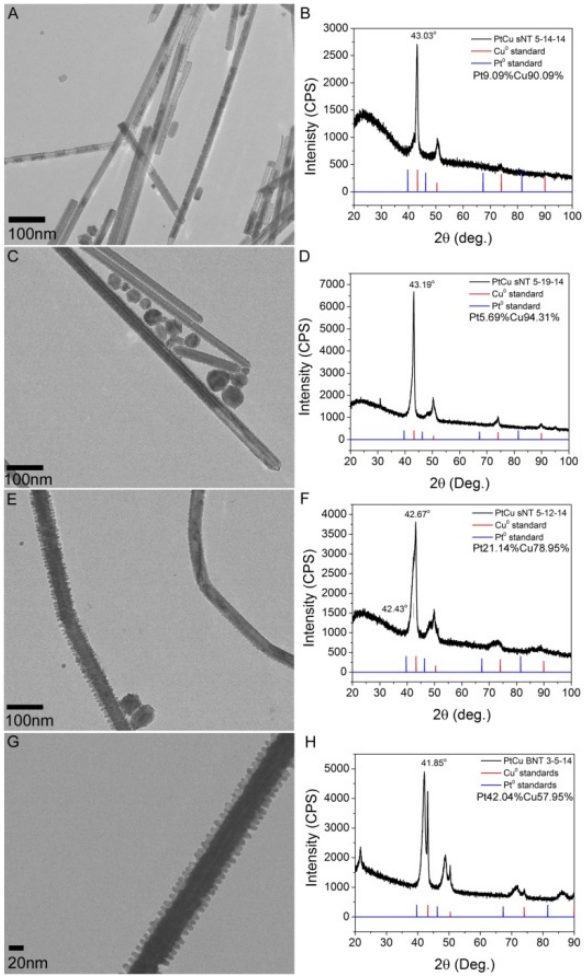

Figure S5: characterizes the in situ separation of the two mechanisms, galvanic replacement reaction and the coreduction process, which are responsible for the production of CuPt sNT and CuPt rNT. The in situ separation was completed synthetically by varying the reaction temperature, while maintaining the initial platinum precursor concentration and reaction time. The variations in reaction temperature after the injection of the platinum precursor are as follows: 190 ˚C (A & B), 195 ˚C (C & D), 200 ˚C (E & F), 220 ˚C (G & H).

4.7.3 ***The optimization of RuPtCu sNT synthesis based on separate precursor injection***.

The synthesis of CuPtRu sNT 10% was optimized, and the protocols can be found in **SI experimental.** Characterization of the synthetic attemps to form CuPtRu sNT 10% can be found in **Figure S6**, which contains TEM images of synthetic trials to develop ruthenium-platinum-copper nanotubes with smooth surface structure. The synthetic trials utilized copper templates with separate precursor injections and different alloying times in order to develop the smooth

nanotubes. Image A alloying with platinum for 3 hours and alloying with ruthenium for 2 hours. Image B provides results for synthetic trial alloying with platinum for 2 hours and ruthenium for 2 hours. Image C provides synthetic results for alloying with platinum for 3 hours and ruthenium for 1 hour. Each TEM image demonstrated the formation of copper-platinum-ruthenium nanotubes with smooth surface structure. The composition of these nanotubes was determined through ICP-MS, all of which demonstrated the presence of some ruthenium. The synthetic protocol that resulted in nanotubes with smooth surface structure and the highest content of ruthenium, while maintaining the copper and platinum content were chosen for this study. The chosen protocol & corresponding results can be found in the experimental and results section.

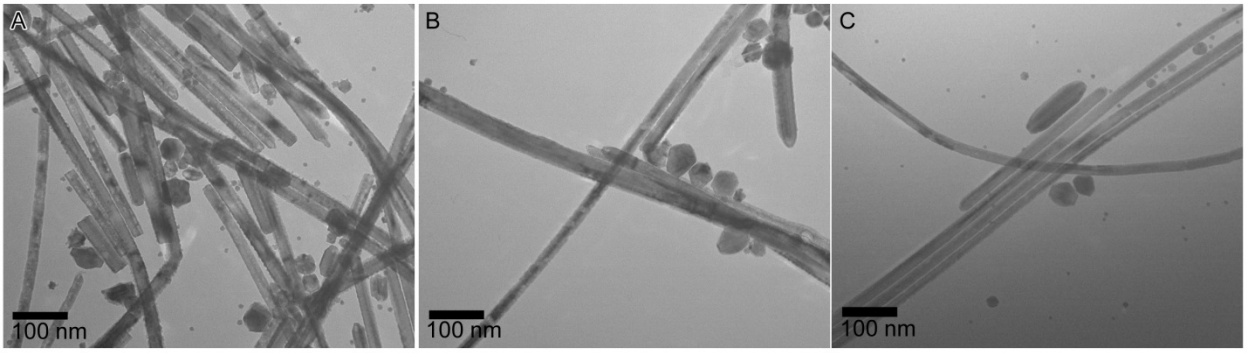

Figure S6: contains TEM images of synthetic trials to develop ruthenium-platinum-copper nanotubes with smooth surface structure. The synthetic trials utilized copper templates with separate precursor injections and different alloying times in order to develop the smooth nanotubes. Image A alloying with platinum for 3 hours and alloying with ruthenium for 2 hours. Image B provides results for synthetic trial alloying with platinum for 2 hours and ruthenium for 2 hours. Image C provides synthetic results for alloying with platinum for 3 hours and ruthenium for 1 hour.

Figure S7 characterized the electrochemical activity of CuPt sNT 10% and CuPtRu sNT 10%, with an enlarged axis. When considering the activity in electrolyte and analyte, both types of smooth nanotubes were significantly less activity than the RuPt/C standard. Additionally, both smooth nanotubes demonstrated activity for MOR and suppression of CO poisoning on the electrocatalyst's surface. The decrease in electrochemical activity can be related to the lower amount of platinum and ruthenium on the smooth nanotube's surface.

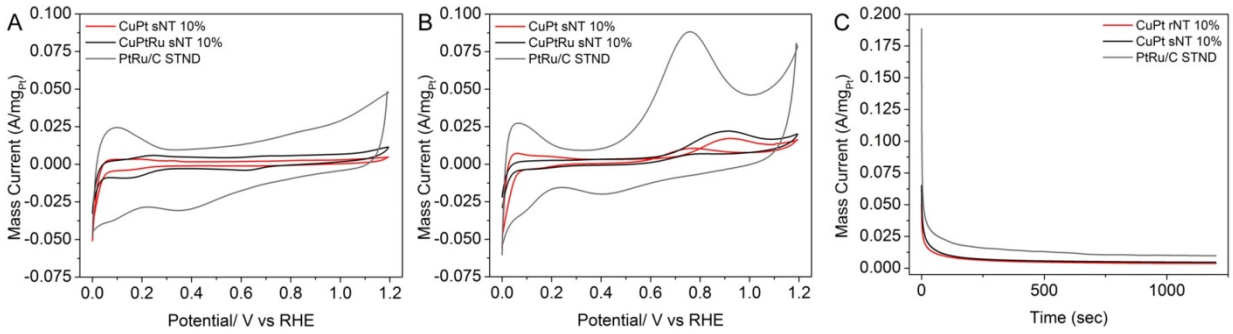

Figure S7: provides preliminary electrochemical activity results for the CuPt sNT 10% (red) CuPtRu sNT 10% (black). These smooth nanotubes were characterized by cyclic voltammetry (A & B) and chronoamperometry (C).

4.7.4 ***Comparison of rNT 10% and 20%***

SI Figure 7 compares the electrochemical activity of the CuPt rNT 10% and CuPt rNT 20% by cyclic voltammetry and chronoamperometry. Voltammograms A & D demonstrate the

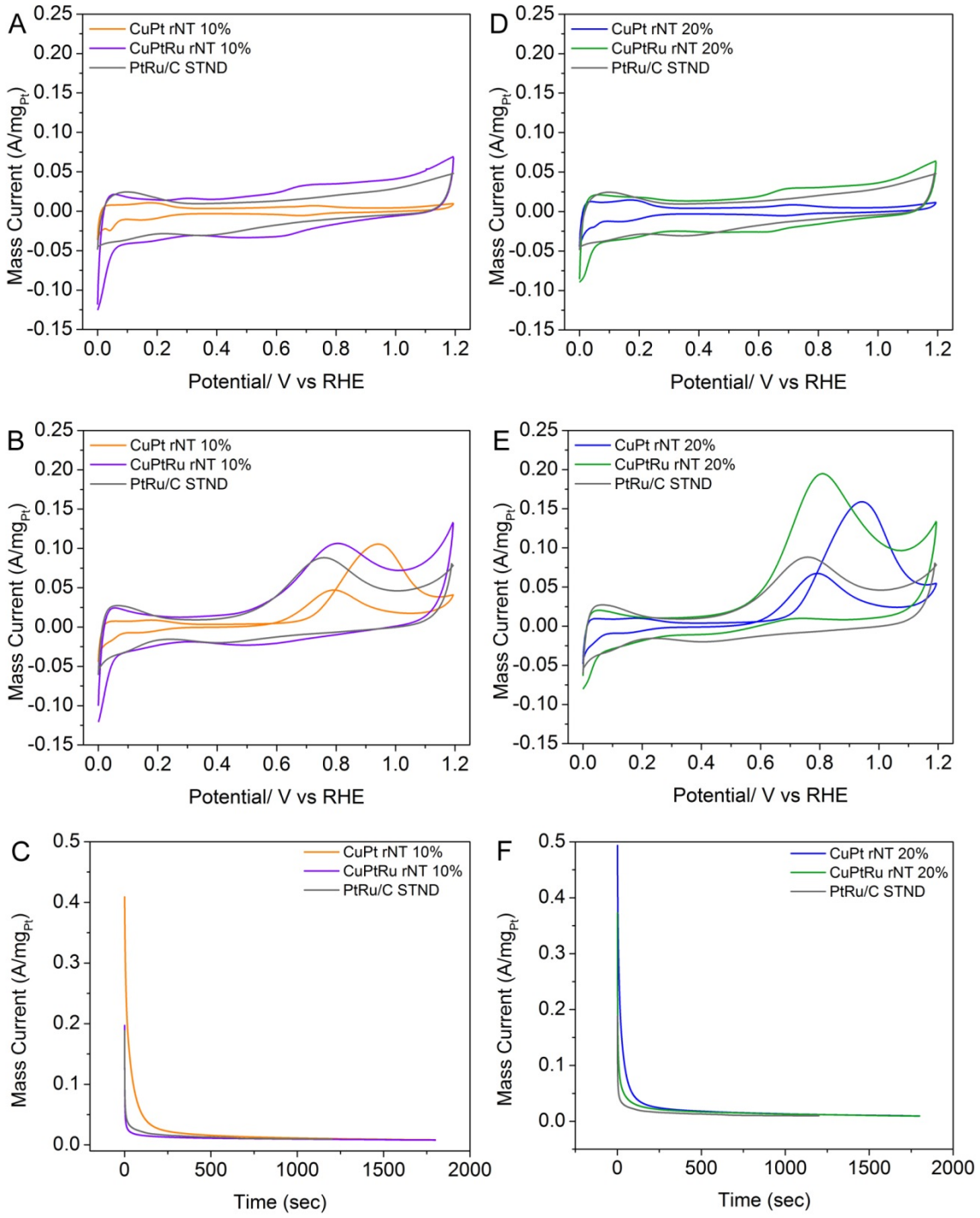

Figure S8: preliminary electrochemical characterization of CuPt rNT 10% & CuPtRu rNT 10% (A - C) and CuPt rNT 20% & CuPtRu rNT 20% (D – F). The electrochemical activity was studied through cyclic voltammetry in electrolyte (A & D) and analyte (B &E), as well as chronoamperometry (C & F). The results for each nanotube is denoted by color: CuPt rNT 10% (orange), CuPtRu rNT 10% (purple), CuPt rNT 20% (blue), CuPtRu rNT 20% (green).

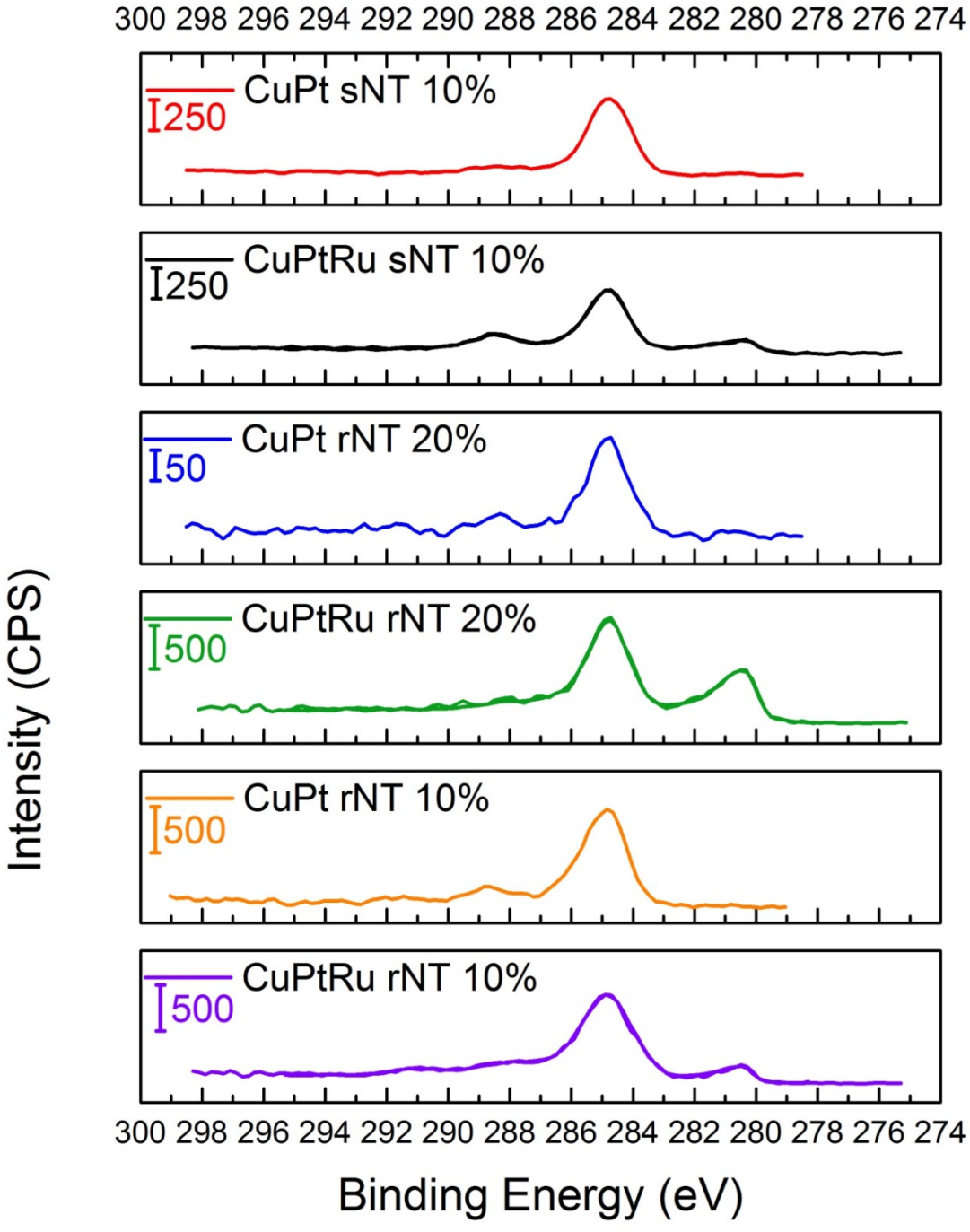

Figure S9: XPS characterization of the C 1s of all nanotube samples. CuPt sNT 10% (red), CuPtRu sNT 10% (black), CuPt rNT 20 % (blue), CuPtRu rNT 20% (green), CuPt rNT 10% (orange), CuPtRu rNT 10% (violet).

4.7.5 ***Peak deconvolutions of XPS data***

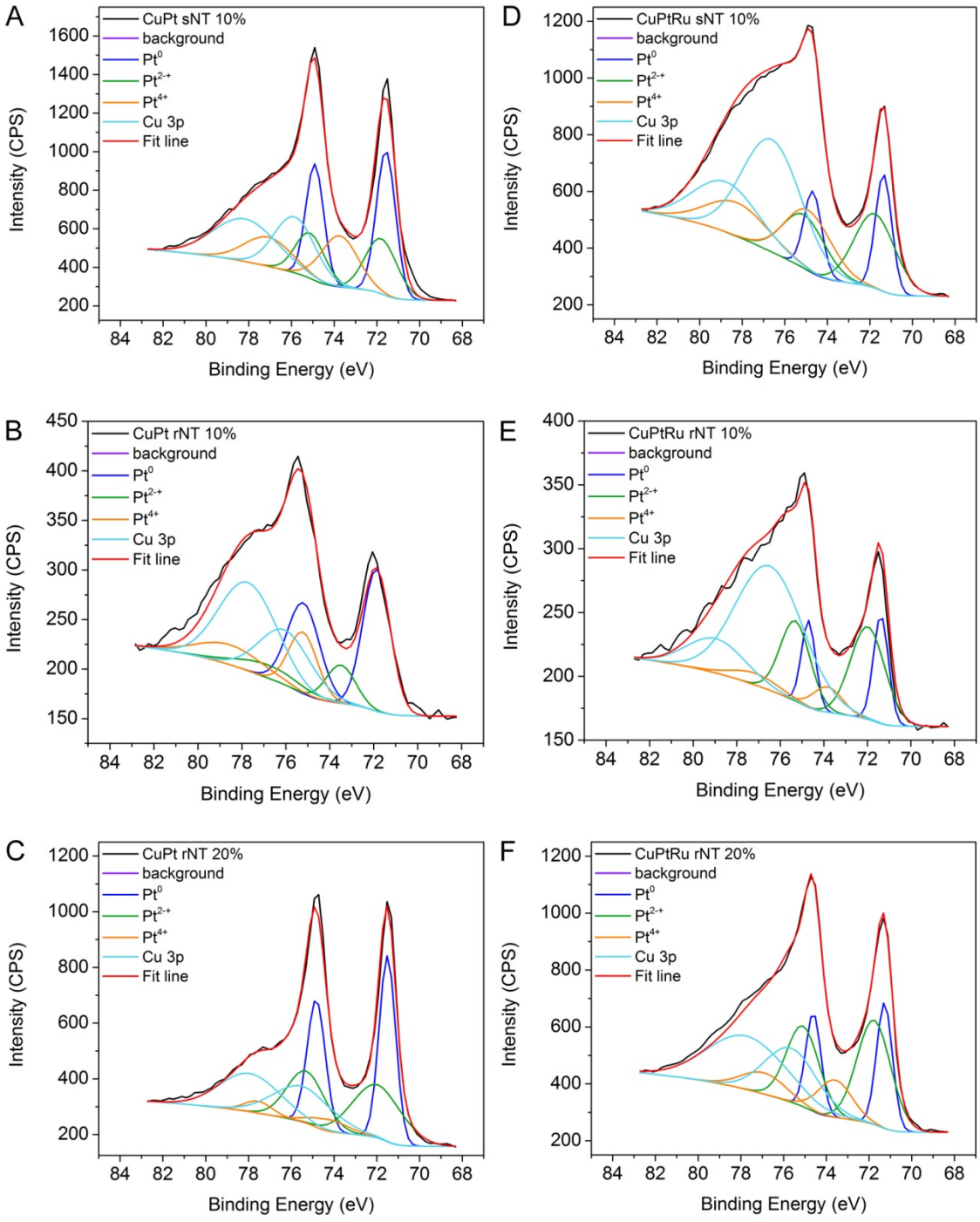

Figure S10: provides the XPS characterization of the Pt $4f_{5/2\ \&\ 7/2}$ photoelectron line as well as the peak deconvolution for the following nanotubes: CuPt sNT 10% (A), CuPt rNT 10% (B), CuPt rNT 20% (C), CuPtRu sNT 10% (D), CuPtRu rNT 10% (E), CuPtRu rNT 20% (F). The oxidation states of platinum are denoted by different colors, Pt^0 blue, Pt^{2+} green, Pt^{4+} orange, Cu 3p cyan. The fit line of the peak deconvolution is denoted by the red line.

	Pt^{0} ($4f_{7/2}$)		Pt^{2+} ($4f_{7/2}$)		Pt^{4+} ($4f_{7/2}$)		Cu^{0} $3p_{3/2}$	
Sample	Binding Energy (eV)	FWHM	Binding Energy (eV)	FWHM	Binding Energy (eV)	FWHM		FWHM
CuPt sNT 10%	71.57	1.05	71.79	1.75	73.74	2.01	75.85	2.25
CuPtRu sNT 10%	71.35	0.91	71.76	2.26	74.89	2.56	75.09	2.36
CuPt rNT 10%	71.86	1.47	73.49	1.55	75.19	1.72	76.61	3.27
CuPtRu rNT 10%	71.37	0.81	71.97	1.87	73.83	1.58	76.48	3.67
CuPt rNT 20%	71.5	0.91	71.98	2.69	74.23	2.07	75.45	3.26
CuPtRu rNT 20%	71.27	0.87	71.76	1.86	73.6	1.87	75.64	2.93

Table S1: provides the binding energy values of photoelectron lines Pt $4f_{7/2}$ and the corresponding peak deconvolution.

	Pt^{0} ($4f_{5/2}$)		Pt^{2+} ($4f_{5/2}$)		Pt^{4+} ($4f_{5/2}$)		Cu^{0} $3p_{1/2}$	
Sample	Binding Energy (eV)	FWHM	Binding Energy (eV)	FWHM	Binding Energy (eV)	FWHM		FWHM
CuPt sNT 10%	74.9	0.98	75.12	1.6	77.07	2.64	78.18	3.49
CuPtRu sNT 10%	74.68	0.97	76.03	2.77	78.22	3.44	78.76	3.6
CuPt rNT 10%	75.21	1.53	76.82	3.38	78.54	3.53	77.72	3.1
CuPtRu rNT 10%	74.7	0.76	75.3	1.62	77.16	2.57	78.95	3.12
CuPt rNT 20%	74.83	0.99	75.31	2.07	77.56	1.53	77.94	3.29
CuPtRu rNT 20%	74.6	0.83	75.09	1.81	76.93	2.47	77.74	4.34

Table S2: provides the binding energy values of photoelectron lines Pt $4f_{5/2\ \&\ 7/2}$ and the corresponding peak deconvolution.

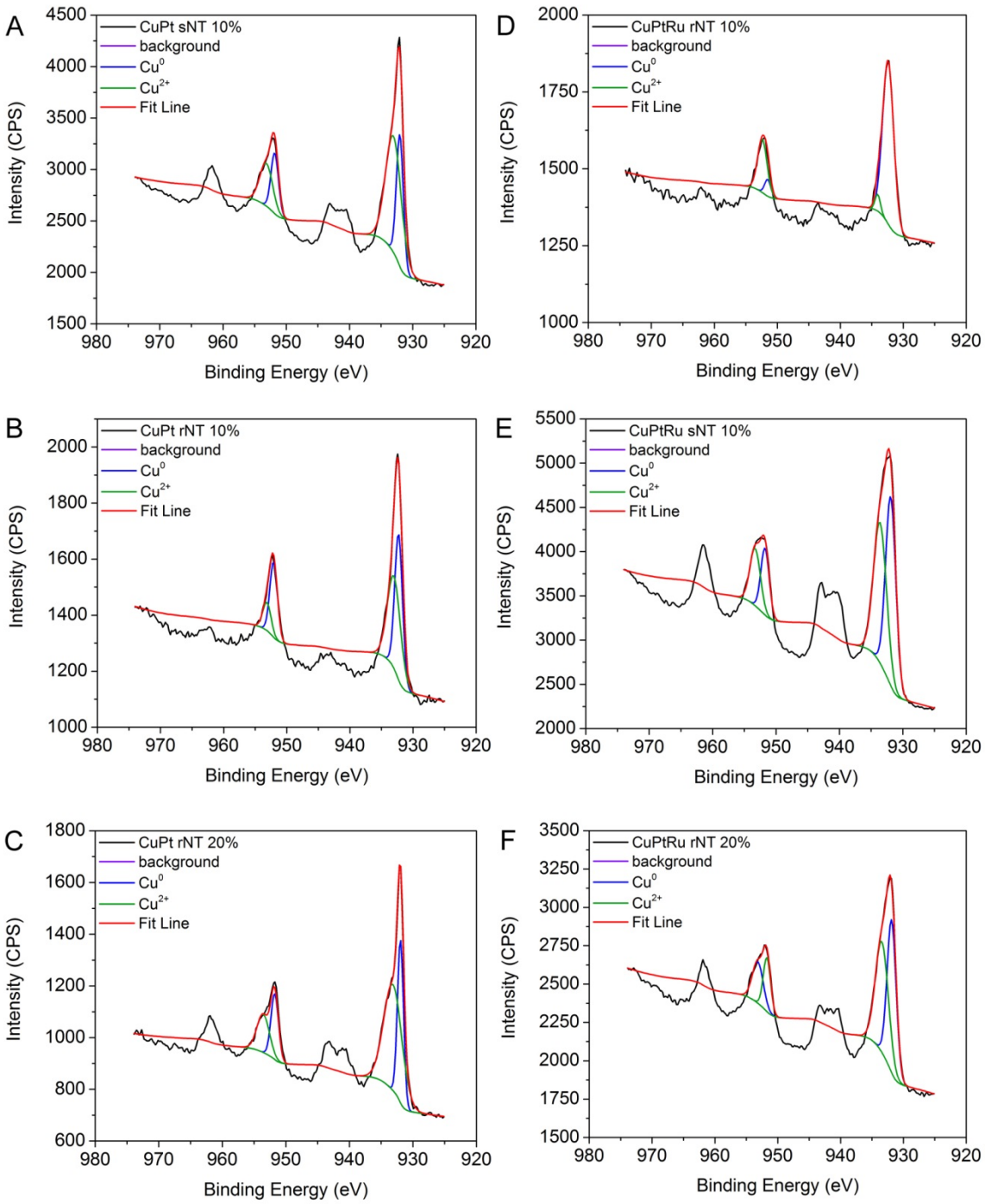

Figure S11: contains the XPS characterization of the Cu 2p $_{1/2\ \&\ 3/2}$ photoelectron line and peak deconvolution for CuPt sNT 10% (A), CuPt rNT 10% (B), CuPt rNT 20% (C), CuPtRu sNT 10% (E), CuPtRu rNT 10% (D), CuPtRu rNT 20% (F). The Cu^0 peak is denoted by the blue line, and the Cu^{2+} is denoted by the green line, and the red line provides the fit line of the deconvolution.

	Cu^0 ($2p_{3/2}$)		Cu^{2+}		Cu^0 ($2p_{1/2}$)		Cu^{2+}	
Electro-catalyst	Binding Energy (eV)	FWHM	Binding Energy (eV)	FWHM	Binding Energy (eV)	FWHM	Binding Energy (eV)	FWHM
CuPt sNT 10%	932.03	1.29	933.04	2.94	951.83	1.4	953.16	2.4
CuPtRu sNT 10%	931.9	1.9	933.59	2.42	951.74	1.55	953.3	1.94
CuPt rNT 10%	932.28	1.45	933.02	2.47	952.08	1.4	953.14	1.53
CuPtRu rNT 10%	932.39	2.08	934.05	0.97	951.52	1.16	952.38	1.76
CuPt rNT 20%	931.95	1.12	933.13	3.38	951.75	1.39	953.57	2.29
CuPtRu rNT 20%	931.86	1.7	933.41	2.44	951.72	1.38	953.17	2.02

Table S2: provides the values for the XPS characterization of Cu $2p_{1/2\ \&\ 3/2}$ and peak deconvolution of the rough and smooth nanotubes.

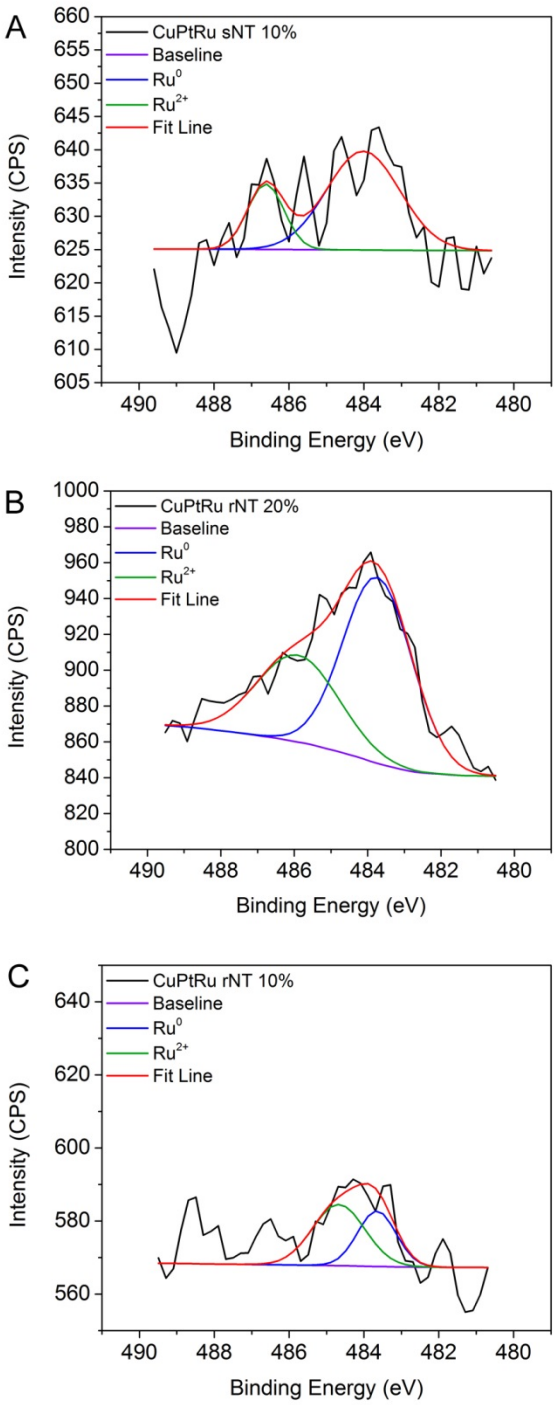

Figure S12: XPS characterization and peak deconvolution of the Ru $3p_{1/2}$ photoelectron line, which was obtained for CuPtRu sNT 10% (A), CuPtRu rNT 20% (B), and CuPtRu rNT 10% (C). The blue line denotes Ru^0, the green line denotes Ru^{2+}, and the red line denotes the sum line.

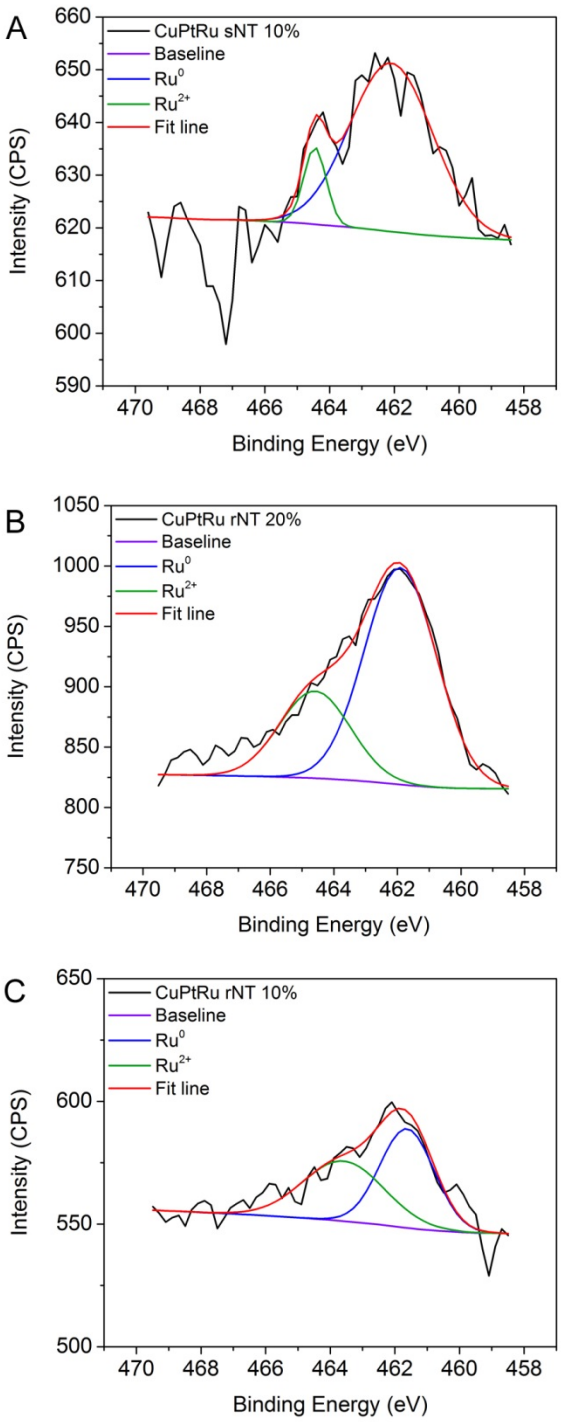

Figure S13: XPS characterization and peak deconvolution of the Ru $3p_{3/2}$ photoelectron line, which was obtained for CuPtRu sNT 10% (A), CuPtRu rNT 20% (B), and CuPtRu rNT 10% (C). The blue line denotes Ru^0, the green line denotes Ru^{2+}, and the red line denotes the sum line.

	Ru^{0} $3p_{1/2}$		Ru^{2+} $3p_{1/2}$		Ru^{0} $3p_{3/2}$		Ru^{2+} $3p_{3/2}$	
Electro-catalyst	Binding Energy (eV)	FWHM	Binding Energy (eV)	FWHM	Binding Energy (eV)	FWHM	Binding Energy (eV)	FWHM
CuPtRu sNt 10%	484.02	2.3	486.62	1.14	462.1	3.02	464.45	0.81
CuPtRu rNT 10%	483.66	1.2	484.67	1.64	461.62	1.97	463.59	2.96
CuPtRu rNT 20%	483.73	2.2	485.9	2.63	461.91	2.67	464.59	2.62

Table S3: provides the binding energy values and FWHM values for the peak deconvolution of the Ru $3p_{1/2\ \&\ 3/2}$ photoelectron lines.

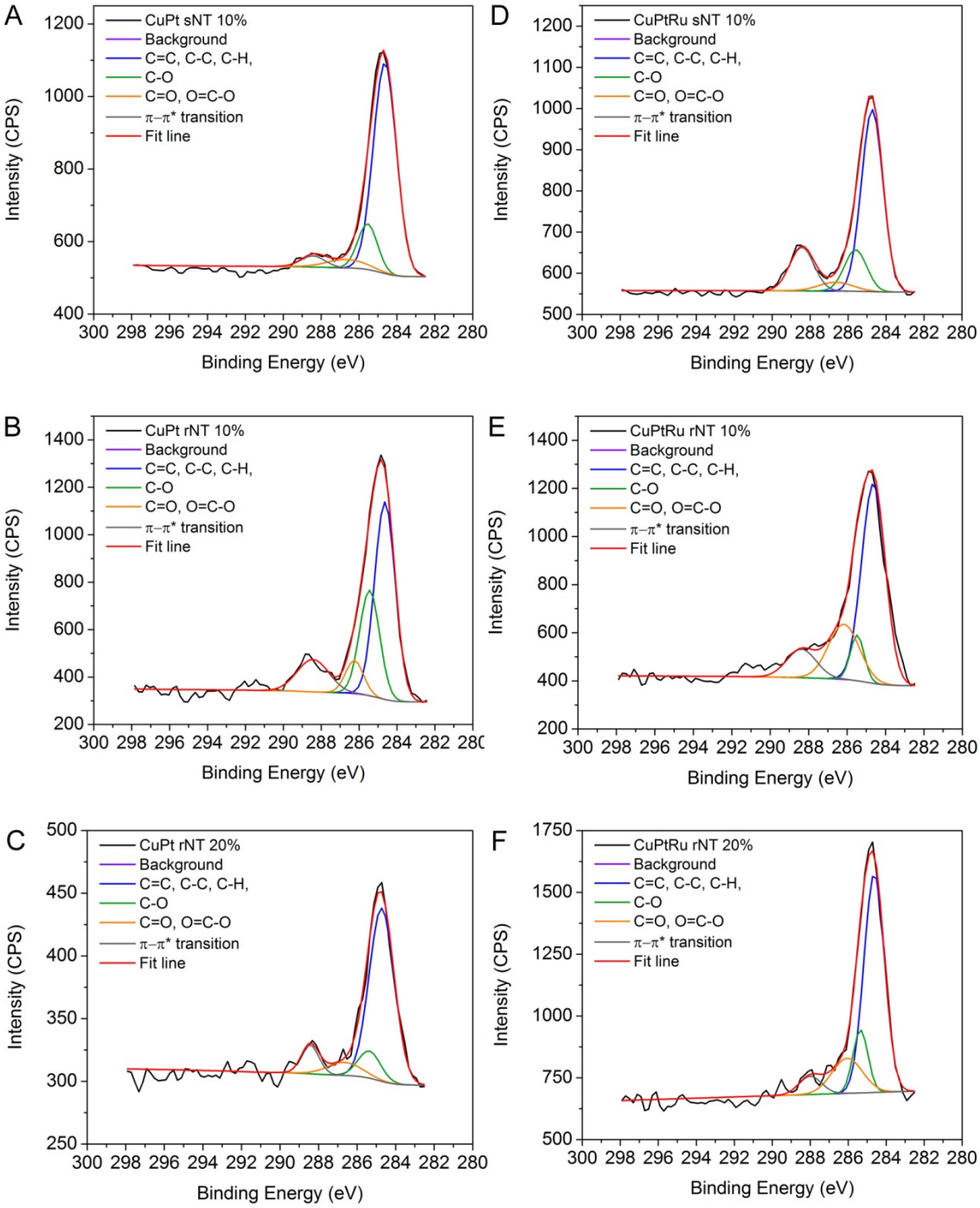

Figure S14: provides the peak deconvolution for the C 1s photoelectron line for the following nanotubes: CuPt sNT 10% (A), CuPt rNT 10% (B), CuPt rNT 20% (C), CuPtRu sNT 10% (D), CuPtRu rNT 10% (E), CuPtRu rNT 20% (F).

4.7.6 ***Compositional characterization of nanotubes***

The percentage of ruthenium, platinum, and copper in each type nanotube was determined by atomic absorption spectroscopy and inductively coupled plasmon mass spectrometry. The results of these studies can be found in table #. The concentration values were used to determine the % composition of each electrocatalyst. Could we possibly make a statement towards variation in composition of synthetic batches? The concentration values were utilized to normalize the concentration of each nanotube based electrocatalyst to 0.8 mg/ml.

intensity (CPS)	conc (PPB)	dilution factor (PPB)	conc ppm	conc mg/ml	mass %		Atomic %
884445.3063	25.02835	1802041	1802.041	1.802041443	67.613483	Cu	41.37598
797254.7352	11.08178	797888.5	797.8885	0.797888496	29.937169	Pt	56.24006
31842.09064	0.90667	65280.27	65.28027	0.065280274	2.449348	Ru	2.383963
				2.665210212	100	total	100

Table S4: provides the atomic ratio of the CuPt sNT 10% by ICP-MS

intensity (CPS)	conc (ppb)	dilution factor	conc (ppm)	conc (mg/ml)	mass %	mol	atomic %	
1188471	14.88297	1071574	1071.574	1.071574	33.11425	0.169749	13.8876	Pt
1292473	30.06133	2164416	2164.416	2.164416	66.88575	1.052556	86.1124	Cu
			total:	3.23599	100	1.222305	100	

Table S5: provides the atomic ratio of the CuPt rNT ~10% by ICP-MS

intensity (CPS)	conc (ppb)	dilution factor	conc (ppm)	conc (mg/ml)	mass %	mol	atomic %	
1207073	13.9602	1005135	1005.13	1.00513	24.3083	0.12461	9.80528	Pt
1675441	39.0547	2811937	2811.94	2.81194	68.0042	1.07016	84.2095	Cu
184891	4.41494	317876	317.876	0.31788	7.68755	0.07606	5.98521	Ru
			total:	4.13495	100	1.27083	100	

SI Table 6: provides the atomic ratio of the CuPtRu rNT ~10% by ICP-MS

intensity (CPS)	conc (ppb)	dilution factor	conc (ppm)	conc (mg/ml)	mass %	mol	atomic %	
2105858	24.6152	1772298	1772.3	1.7723	38.7214	0.19849	17.07	Pt
1671187	38.9548	2804749	2804.75	2.80475	61.2786	0.96432	82.93	Cu
			total:	4.57705	100	1.16281	100	

Table S7: provides the atomic ratio of the CuPt rNT ~20% by ICP-MS

intensity (CPS)	conc (ppb)	dilution factor	conc (ppm)	conc (mg/ml)	mass %	mol	atomic %	
1089636	16.1441	1162375	1162.38	1.16238	33.7232	0.17287	14.7959	Pt
747897	27.838	2004333	2004.33	2.00433	58.1503	0.91509	78.3223	Cu
103058	3.89036	280106	280.106	0.28011	8.12652	0.0804	6.88183	Ru
			total:	3.44681	100	1.16837	100	

Table S8: provides the atomic ratio of the CuPtRu rNT ~20% by ICP-MS

4.7.7 Preliminary electrochemical characterization in H_2SO_4 electrolyte

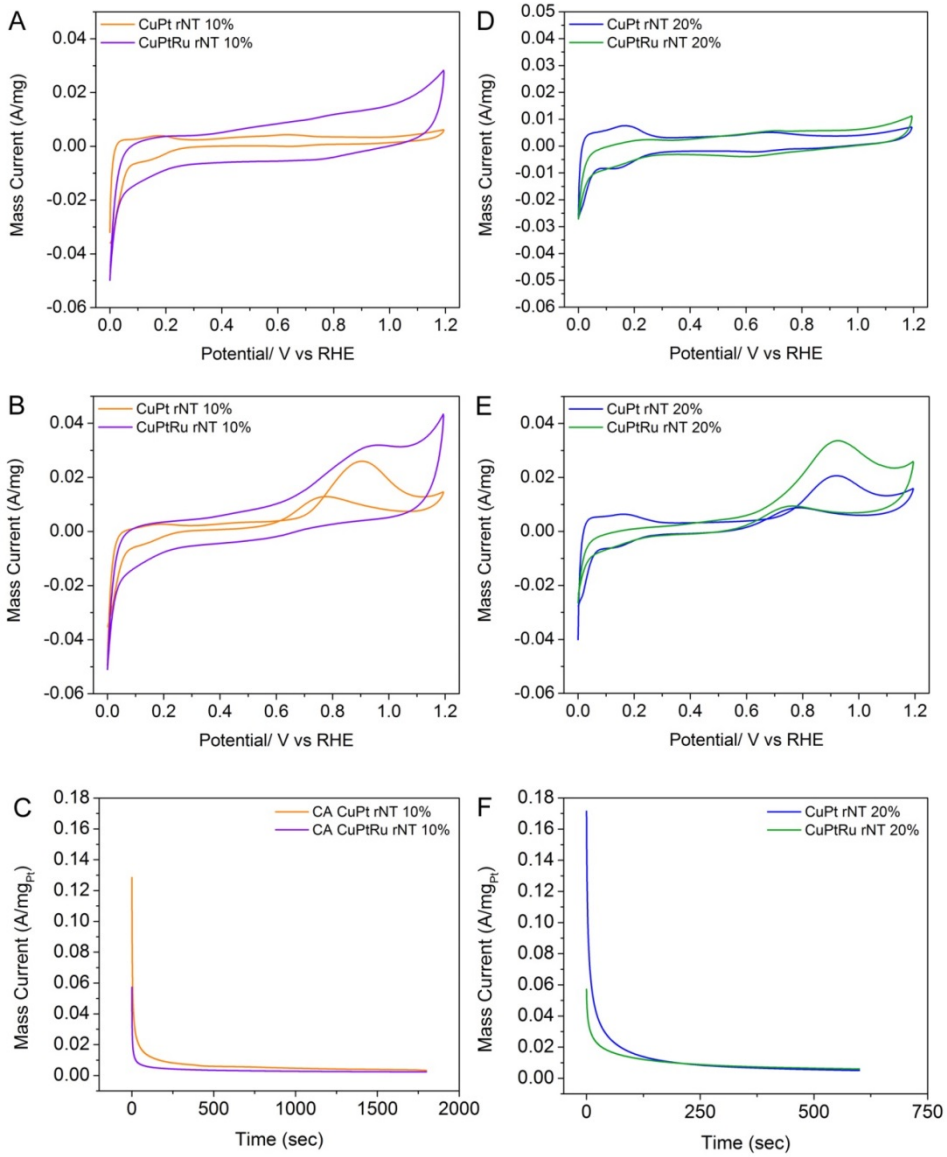

Figure S15 characterizes the electrochemical activity by CV (A, B, D, E) and CA (C and F) using a 0.1 M H_2SO_4 electrolyte, for the binary and ternary rough nanotubes 10% (A – C), and 20% (D – F).

4.8 **References**

1. (a) Chrzanowski, W.; Wieckowski, A., Surface Structure Effects in Platinum/Ruthenium Methanol Oxidation Electrocatalysis. *Langmuir* **1998,** *14* (8), 1967-1970; (b) Zhou, Z.-Y.; Huang, Z.-Z.; Chen, D.-J.; Wang, Q.; Tian, N.; Sun, S.-G., High-Index Faceted Platinum Nanocrystals Supported on Carbon Black as Highly Efficient Catalysts for Ethanol Electrooxidation. *Angewandte Chemie International Edition* **2010,** *49* (2), 411-414.

2. (a) Lee, S. W.; Chen, S.; Sheng, W.; Yabuuchi, N.; Kim, Y.-T.; Mitani, T.; Vescovo, E.; Shao-Horn, Y., Roles of Surface Steps on Pt Nanoparticles in Electro-oxidation of Carbon Monoxide and Methanol. *Journal of the American Chemical Society* **2009,** *131* (43), 15669-15677; (b) Zheng, J.; Cullen, D. A.; Forest, R. V.; Wittkopf, J. A.; Zhuang, Z.; Sheng, W.; Chen, J. G.; Yan, Y., Platinum–Ruthenium Nanotubes and Platinum–Ruthenium Coated Copper Nanowires As Efficient Catalysts for Electro-Oxidation of Methanol. *ACS Catalysis* **2015,** *5* (3), 1468-1474.

3. (a) Lim, B.; Jiang, M.; Camargo, P. H. C.; Cho, E. C.; Tao, J.; Lu, X.; Zhu, Y.; Xia, Y., Pd-Pt Bimetallic Nanodendrites with High Activity for Oxygen Reduction. *Science* **2009,** *324* (5932), 1302-1305; (b) Lim, B.; Yu, T.; Xia, Y., Shaping a Bright Future for Platinum-Based Alloy Electrocatalysts. *Angewandte Chemie International Edition* **2010,** *49* (51), 9819-9820.

4. (a) Chen, S.; Si, R.; Taylor, E.; Janzen, J.; Chen, J., Synthesis of Pd/Fe3O4 Hybrid Nanocatalysts with Controllable Interface and Enhanced Catalytic Activities for CO Oxidation. *The Journal of Physical Chemistry C* **2012,** *116* (23), 12969-12976; (b) Taylor, E.; Chen, S.; Tao, J.; Wu, L.; Zhu, Y.; Chen, J., Synthesis of Pt–Cu Nanodendrites through Controlled Reduction Kinetics for Enhanced Methanol Electro-Oxidation. *ChemSusChem* **2013,** *6* (10), 1863-1867; (c) Xu, D.; Bliznakov, S.; Liu, Z.; Fang, J.; Dimitrov, N., Composition-Dependent Electrocatalytic Activity of Pt-Cu Nanocube Catalysts for Formic Acid Oxidation. *Angewandte Chemie International Edition* **2010,** *49* (7), 1282-1285.

5. (a) Chen, C.; Kang, Y.; Huo, Z.; Zhu, Z.; Huang, W.; Xin, H. L.; Snyder, J. D.; Li, D.; Herron, J. A.; Mavrikakis, M.; Chi, M.; More, K. L.; Li, Y.; Markovic, N. M.; Somorjai, G. A.; Yang, P.; Stamenkovic, V. R., Highly Crystalline Multimetallic Nanoframes with Three-Dimensional Electrocatalytic Surfaces. *Science* **2014,** *343* (6177), 1339; (b) Xia, B. Y.; Wu, H. B.; Wang, X.; Lou, X. W., One-Pot Synthesis of Cubic PtCu3 Nanocages with Enhanced Electrocatalytic Activity for the Methanol Oxidation Reaction. *Journal of the American Chemical Society* **2012,** *134* (34), 13934-13937; (c) Guo, S.; Fang, Y.; Dong, S.; Wang, E., High-Efficiency and Low-Cost Hybrid Nanomaterial as Enhancing Electrocatalyst: Spongelike Au/Pt Core/Shell Nanomaterial with Hollow Cavity. *The Journal of Physical Chemistry C* **2007,** *111* (45), 17104-17109; (d) You, H.; Zhang, F.; Liu, Z.; Fang, J., Free-Standing Pt–Au Hollow Nanourchins with Enhanced Activity and Stability for Catalytic Methanol Oxidation. *ACS Catalysis* **2014,** *4* (9), 2829-2835.

6. Lou, Y.; Li, C.; Gao, X.; Bai, T.; Chen, C.; Huang, H.; Liang, C.; Shi, Z.; Feng, S., Porous Pt Nanotubes with High Methanol Oxidation Electrocatalytic Activity Based on Original Bamboo-Shaped Te Nanotubes. *ACS Applied Materials & Interfaces* **2016,** *8* (25), 16147-16153.

7. (a) Cohen, J. L.; Volpe, D. J.; Abruna, H. D., Electrochemical determination of activation energies for methanol oxidation on polycrystalline platinum in acidic and alkaline electrolytes. *Physical Chemistry Chemical Physics* **2007,** *9* (1), 49-77; (b) Chen, Y. X.; Miki, A.; Ye, S.; Sakai, H.; Osawa, M., Formate, an Active Intermediate for Direct Oxidation of Methanol on Pt Electrode. *Journal of the American Chemical Society* **2003,** *125* (13), 3680-3681.

8. Mavrikakis, M.; Hammer, B.; Nørskov, J. K., Effect of Strain on the Reactivity of Metal Surfaces. *Physical Review Letters* **1998,** *81* (13), 2819-2822.

9. Rossmeisl, J.; Ferrin, P.; Tritsaris, G. A.; Nilekar, A. U.; Koh, S.; Bae, S. E.; Brankovic, S. R.; Strasser, P.; Mavrikakis, M., Bifunctional anode catalysts for direct methanol fuel cells. *Energy & Environmental Science* **2012,** *5* (8), 8335-8342.

10. Wang, H.; Chen, S.; Wang, C.; Zhang, K.; Liu, D.; Haleem, Y. A.; Zheng, X.; Ge, B.; Song, L., Role of Ru Oxidation Degree for Catalytic Activity in Bimetallic Pt/Ru Nanoparticles. *The Journal of Physical Chemistry C* **2016,** *120* (12), 6569-6576.

11. (a) Marković, N. M.; Gasteiger, H. A.; Ross, P. N.; Jiang, X.; Villegas, I.; Weaver, M. J., Electro-oxidation mechanisms of methanol and formic acid on Pt-Ru alloy surfaces. *Electrochimica Acta* **1995,** *40* (1), 91-98; (b) Marković, N. M.; Gasteiger, H. A.; Ross, P. N.; Jiang, X.; Villegas, I.; Weaver, M. J., Surface Structure and Electrochemical ReactivityElectro-oxidation mechanisms of methanol and formic acid on Pt-Ru alloy surfaces. *Electrochimica Acta* **1995,** *40* (1), 91-98.

12. (a) Ávila-García, I.; Plata-Torres, M.; Domínguez-Crespo, M. A.; Ramírez-Rodríguez, C.; Arce-Estrada, E. M., Electrochemical study of Pt–Pd, Pt–Ru, Pt–Rh and Pt–Sn/C in acid media for hydrogen adsorption–desorption reaction. *Journal of Alloys and Compounds* **2007,** *434–435*, 764-767; (b) Wiltshire, R. J. K.; King, C. R.; Rose, A.; Wells, P. P.; Davies, H.; Hogarth, M. P.; Thompsett, D.; Theobald, B.; Mosselmans, F. W.; Roberts, M.; Russell, A. E., Effects of composition on structure and activity of PtRu/C catalysts. *Physical Chemistry Chemical Physics* **2009,** *11* (13), 2305-2313; (c) Poh, C. K.; Tian, Z.; Gao, J.; Liu, Z.; Lin, J.; Feng, Y. P.; Su, F., Nanostructured trimetallic Pt/FeRuC, Pt/NiRuC, and Pt/CoRuC catalysts for methanol electrooxidation. *Journal of Materials Chemistry* **2012,** *22* (27), 13643-13652.

13. (a) Stamenkovic, V. R.; Mun, B. S.; Mayrhofer, K. J. J.; Ross, P. N.; Markovic, N. M., Effect of Surface Composition on Electronic Structure, Stability, and Electrocatalytic Properties of Pt-Transition Metal Alloys: Pt-Skin versus Pt-Skeleton Surfaces. *Journal of the American Chemical Society* **2006,** *128* (27), 8813-8819; (b) Yuan, Q.; Huang, D.-B.; Wang, H.-H.; Zhou, Z.-Y., RhPt Flowerlike Bimetallic Nanocrystals with Tunable Composition as Superior Electrocatalysts for Methanol Oxidation. *Langmuir* **2014,** *30* (20), 5711-5715; (c) Suntivich, J.; Xu, Z.; Carlton, C. E.; Kim, J.; Han, B.; Lee, S. W.; Bonnet, N.; Marzari, N.; Allard, L. F.; Gasteiger, H. A.; Hamad-Schifferli, K.; Shao-Horn, Y., Surface Composition Tuning of Au–Pt Bimetallic Nanoparticles for Enhanced Carbon Monoxide and Methanol Electro-oxidation. *Journal of the American Chemical Society* **2013,** *135* (21), 7985-7991.

14. (a) Wanjala, B. N.; Fang, B.; Luo, J.; Chen, Y.; Yin, J.; Engelhard, M. H.; Loukrakpam, R.; Zhong, C.-J., Correlation between Atomic Coordination Structure and Enhanced Electrocatalytic Activity for Trimetallic Alloy Catalysts. *Journal of the American Chemical Society* **2011,** *133* (32), 12714-12727; (b) Sun, X.; Li, D.; Ding, Y.; Zhu, W.; Guo, S.; Wang, Z. L.; Sun, S., Core/Shell Au/CuPt Nanoparticles and Their Dual Electrocatalysis for Both Reduction and Oxidation Reactions. *Journal of the American Chemical Society* **2014,** *136* (15), 5745-5749.

Chapter V. Conclusion

5.1 Opening Statement:

This research focuses on the development of copper nanomaterials and multimetallic nanomaterials of unique morphologies. The variation in Cu NM morphologies was based on the halide, halide concentration, and reduction rate of the copper precursors utilized in the synthesis. Cu NM with specific morphologies, Cu RHD and Cu NW, were chosen to function as templates to form multimetallic nanomaterials. Alloying Cu RHD with platinum and ruthenium formed binary and ternary coreframe nanostructures, which were then etched into multimetallic frame nanostructures. The electrocatalytic activity of the coreframe and frame nanostructures were investigated, and it was determined that the trimetallic frame nanostructures enhanced MOR activity and durability. Cu NW were also alloyed with Pt and Ru forming bimetallic and trimetallic nanotubes. The multimetallic nanotubes' surface was synthetically tailored to possess a smooth or rough morphology. Additionally, the atomic ratio of platinum in the multimetallic rough nanotubes was synthetically increased. The electrocatalytic activity of these nanotubes was investigated. It was determined that the multimetallic nanotubes with rough surface structure possessed improved electrocatalytic activity for MOR. The MOR activity was further improved with the increase atomic ratio of platinum in the rough nanotubes. Incorporating ruthenium into the rough nanotubes led to enhanced electrocatalytic activity, lowered MOR onset potential, and improved resistance to CO poisoning.

5.2 Ch 2: shape control of copper nanomaterials & the influence of halides on growth

Cu NM with various structures was produced by altering the halide, concentration of the halide, and copper (II) precursor. The first copper precursor studied was $Cu(acac)_2$, and the combination of $Cu(acac)_2$ and $CuCl_2$ at different concentrations resulted in different

morphologies, including Cu NP, Cu RDH, Cu NW, and Cu NPL. When the chloride source varied from $CuCl_2$ to CTAC or CTAB, the resulting Cu NM formed the same morphology based on precursor ratio. The results of this study determined that the concentration of chloride in solution influenced copper nanomaterial growth, regardless of chloride source. Additionally, the cation in the external chloride source did not influence nanomaterial growth and structure.

In order to determine if the halide trend as a shape directing additive extends to other halides, the study was repeated with Br^- and I^-. When copper (II) chloride is exchanged for copper (II) bromide, the resulting nanomaterials differ in structure from the Cu NM produced with chloride. Varying the concentration of $CuBr_2$ and the precursor ratio produced Cu NM morphologies distinct to each synthesis. The Cu NM structures developed with $CuBr_2$ include nanospheres, nanopyramids, nanorods, nanooctahedra, and nanoplates. These syntheses were repeated with external bromide sources (CTAB and TBAB) some ratios demonstrated variations in Cu NM structure. Based on synthetic variation in the presence of Cl^- and Br^-, these morphological results suggest that the halides may bind to specific facets and direct morphology growth.

Cu NM structures formed with iodine were also studied in part 1, and it was determined that copper nanoplates are formed when iodine is utilized a shape directing additive. When the concentration of TBAI is increased the structure of Cu NPL alters from spherical to hexagonal. Additional studies are required to determine if the alteration in Cu NPL structure is related to I^- and TBA^+. An additional study completed in Part 1 observed Cu NM morphology without halide. In a synthesis without halide, Cu NM are formed without non-uniform polycrystalline structures. These results suggest the importance of the presence of a halide is important for crystal growth into distinct morphologies, and lends support to the facet selectivity of halides.

The final study for part 1 observed the influence of the copper precursor's oxidation state on Cu NM morphology. For this study the starting copper precursor oxidation state was altered from 2^+ to 1^+, which also varies the crystal structure of the copper precursor. This study was completed to determine if the copper precursor crystal structure influences nanomaterial morphology. The resulting nanomaterial morphologies remained similar to the shapes produced by the corresponding copper precursors with an oxidation state of 2^+. This suggests that the oxidation state of the starting precursor does not influence Cu NM morphology.

In order to determine if halides will function as shape directing additives in other copper precursor systems, $Cu(acac)_2$ is exchanged for $Cu(ac)_2$. This precursor system results in the formation of Cu NM that possess distinct morphologies, that differ from Cu NM formed from the corresponding $Cu(acac)_2$ precursor system. The structures developed when $Cu(ac)_2$ and $CuCl_2$ included copper nanowires, nanocubes, and nanospheres. External chloride sources the Cu NM morphology was studied. There was some variation in structure, suggesting that CTA^+ was a contributing factor to nanomaterial growth. When TBAC was utilized as an external chloride source for the $Cu(ac)_2$ study, the same Cu NM morphologies were formed as CTAC. This suggests that CTA^+ and TBA^+ can influence Cu NM growth. These structures varied from the nanomaterial morphologies developed with $Cu(acac)_2$, which could be due to the strength of binding ligand the corresponding copper reduction rate. Previous studies have determined that the stronger the binding ligand the slower the reduction rate, which influenced the nanomaterial seed & morphology. This lends support to the concept that the halogen is a facet specific protector that can influence nanomaterial formation.

This study was repeated with $Cu(ac)_2$ and $CuBr_2$, and the Cu NM morphologies varied from part 1. The nanomaterial shape did vary with concentration of bromide in solution,

supporting the concept of bromide as a shape directing additive. An external source of bromide (CTAB) was then combined with $Cu(ac)_2$, however, the morphologies slightly differed. This suggests that the corresponding cation CTA^+ contributes to nanomaterial growth and structure. TBAB was utilized as an external bromide source, which resulted in the same Cu NM morphologies as CTAB. This suggests that CTA^+ and TBA^+ can influence Cu NM growth. The morphological variations when $Cu(acac)_2$ verses $Cu(ac)_2$ are utilized in the synthesis suggest that reduction rate may influence the morphologies of the nanomaterials.

5.3 Ch 3: the development of multimetallic coreframe & frame nanostructures and their electrocatalytic activities for MOR

This research has developed ultra-fine, branched core-frame nanostructures containing binary (CuPt) and ternary (CuPtRu) compositions. Ultra-fine, branched frame nanostructures were developed from the core-frame nanostructures through an acetic acid etching process. During this process, the copper core was dissolved forming a porous, frame nanostructure. The alloyed frame composition was maintained forming binary (CuPt) and ternary (CuPtRu) frame nanostructures. The variation in the coreframe and frame nanostructures' morphology and composition elucidated the effects of composition, porosity, and morphology on electrochemical activity. The trimetallic coreframe nanostructures possessed an increase in MOR activity compared to the bimetallic coreframe nanostructures, indicating that Ru in the coreframe structure enhances MOR activity and resistance towards CO poisoning. The binary and ternary alloyed, frame nanostructures improved electrochemical activity and stability compared to the coreframe nanostructures. The improvement of electrochemical activity was based on the high surface area and alloying at the surface of the frame nanostructure.

The core-frame nanostructures electrolyte and analyte stability studies demonstrated a reduction in activity and an increase in CO poisoning after cycling. Morphology characterization of the core-frame nanostructures after stability studies demonstrates an alteration in morphology based on TEM image contrast. The alteration in morphology could rationalize the loss of electrocatalytic activity observed for the coreframe nanostructures. Alterations to composition could also contribute to loss of electrochemical activity after the stability studies. The electrolyte and analyte stability studies, completed on the frame nanostructures, demonstrated improved electrocatalytic activity for methanol oxidation, and maintained resistance towards CO poisoning. Based on the frame nanostructure characterization after the stability studies, the enhancement of electrochemical activity was not due to the morphology or overall composition of the binary and ternary frame nanostructures altering during the stability studies.

Based on the characterization results for CuPt frame nanostructures, the crystal structure of the binary frame nanostructure was rearranged during the stability study to contain Pt-rich surfaces and Cu-Pt pair sites. A similar reconstruction of the CuPtRu frame nanostructure's crystal structure occurred during the stability study. It was determined that the ternary frame nanostructure's alloy form both a phase segregated region that was ruthenium rich, in addition to increasing the number of Pt-M (M = Cu & Ru) present in the ternary frame nanostructure. The presence of both Ru and Cu in ternary alloyed frame nanostructures enhanced the durability of the electrocatalysts during electrolyte and analyte stability studies. When the stability studies were completed on the commercial standard, PtRu standard, there was a steady decrease in activity. Based on these studies, the ternary frame nanostructure is more active and more durable than the commercial standard. By optimizing the composition ratio and refining the morphology,

ternary nanostructured electrocatalysts may prove to be efficient electrocatalyst for MOR and more economically viable.

5.4 Ch 4: development of binary & ternary nanotubes with varying surface structure and their electrocatalytic activities for MOR

This research developed multimetallic nanotubes with synthetically tunable composition and surface structure. Copper platinum nanotubes smooth surface (CuPt sNT) structure were developed through the in situ separation of the galvanic replacement reaction and co-reduction mechanism. The rough copper platinum nanotubes were developed through both the coreduction mechanism and the galvanic replacement reaction. Ruthenium was incorporated into each nanotube to develop copper platinum ruthenium nanotubes with smooth and rough surface structure. The copper platinum ruthenium nanotubes with various surface structures were developed through the same growth mechanisms as copper platinum nanotubes. The composition of the binary and ternary rough nanotubes was synthetically tuned to contain a higher atomic ratio of platinum.

The electrocatalytic properties of the binary and ternary nanotubes with smooth and rough surface structure were investigated. It was determined that the binary nanotubes with rough surface structure were more electrocatalytically active for MOR than the smooth nanotubes, when the atomic ratio of platinum remained constant. The enhancement demonstrated by the rough nanotubes was observed for both the bimetallic and trimetallic nanotubes with rough surface structure. The rough nanotubes with ruthenium proved to be more electrocatalytically active for methanol oxidation, and the MOR overpotential is comparable to the PtRu STND. The electrocatalytic activity of binary and ternary rough nanotubes with an increase of platinum content was investigated, and the influence on MOR activity cause by

variation in atomic ratio was determined. The increase in platinum content on the rough nanotubes resulted in a more active electrocatalyst for MOR, as well as a more durable electrocatalyst during the stability studies.

6 Future Directions:

6.1 Ch 2: shape control of copper nanomaterials & the influence of halides on growth

Additional syntheses over $Cu(ac)_2$ and TBAI need to be completed in order to determine if Cu NPL structure is related to I^- concentration. Future directions for this research would include optimizing the syntheses developed in part 2. This research has observed Cu NM morphology control based on halide type and concentration. Characterizing the surface facets and facet selectivity of halides, may provide a rationale for the Cu NM morphologies developed by this research. This study has observed a variation in Cu NM structure based on the starting copper precursor. A future direction for this project would include elucidating the influence ligand binding strength has on copper nanomaterial growth and morphology. Additional ITC and reduction kinetics studies could determine the reduction rate of the copper salts, and determine if binding strength of the ligand in each copper salt influences nanomaterial growth. This could provide insight into the reduction kinetics, seed formation, and nanomaterial growth of the dual precursor system as well as the role of the halogen on these processes.

6.2 Ch 3: the development of multimetallic coreframe & frame nanostructures and their electrocatalytic activities for MOR

This project could be continued by forming an intermetallic alloy of the frame nanostructures. This could be completed by synthetically altering the frame nanostructures, either by increasing the temperature or by increasing the reaction time. Additionally platinum-copper intermetallic alloys spherical nanoparticles of similar diameter, could provide a

comparison point to highlight the importance of the frame structure as well as the surface facets present. Future directions of this project would include developing frame structures without copper, including platinum-ruthenium frame nanostructures, and platinum frame nanostructures, either synthetically or through an acetic acid etching process. The electrocatalytic activity for MOR and the durability of these frame structures could be investigated; this would provide additional support to the importance of a ternary electrocatalyst.

In-situ XPS studies or in-situ TEM studies could be completed on the multimetallic core-frame and frame nanostructures during the electrolyte and analyte stability studies to observe the alteration in crystal structure. This would elucidate the loss of current observed for the core-frame nanostructures, and the enhancement of electrocatalytic activity of the frame nanostructures. This project could be continued by studying by the products that are formed during methanol oxidation on the surface of respective electrocatalyst. The formed products would be collected and studied through GC-MS, which could provide insight into the specific methanol oxidation pathway. This project would ultimately be continued by incorporating these nanostructures into the anode of a direct methanol fuel cell. The durability of the nanostructures, the efficiency of the anode, and overall fuel cell would be studied.

6.3 Ch 4: development of binary & ternary nanotubes with varying surface structure and their electrocatalytic activities for MOR

Future directions for this project would include synthetically optimizing the binary and ternary smooth nanotubes to possess a higher concentration of platinum. The increase in percentage of platinum in the smooth nanotubes could influence electrocatalytic activity, and would need tobe investigated. The second future direction for this project would subject the multimetallic nanotubes with rough surface structure to an acetic acid treatment and then study the

electrochemical activity. This treatment could remove excess capping ligands, and possibly alter the alloying at the surface of the rough nanotube to increase the number of Pt-Cu or Pt-Ru pair sites present on the surface of the nanotubes. These acid treated nanotubes may enhance electrochemical results similarly as the frame nanostructures. Additional electrochemical studies for MOR in acidic media, would be the influence nafion content and electrocatalytic activity for MOR. The final future direction for this research would be synthetically tuning the composition of the rough nanotube to maintain the atomic ratio of copper and platinum, while increasing the atomic ratio of ruthenium on the surface. The atomic ratio between Pt and Ru, on a binary nanomaterial, influences the bifunctional mechanism and CO poisoning. Studying the electrocatalytic activity of a ternary rough nanotube, with increasing amounts of ruthenium, could determine the influence atomic ratio has on electrocatalytic activity and resistance towards CO poisoning in a ternary nanomate